eman ta zabal zazu

Universidad del País Vasco

Euskal Herriko Unibertsitatea

Doctoral thesis

Multifunctionality of membrane remodeling proteins Reticulon and Dynamin 2

Javier Espadas Moreno

Leioa 2021

Supervisors

Vadim Frolov Buyanov

Anna Shnyrova Zhadan

Gracias a todas aquellas personas que me he cruzado en este camino, habéis hecho que todo sea más divertido

Gracias Vadim y Anna, por guiarme en este proceso de aprendizaje

A mi familia, por vuestro amor y apoyo incondicional, por estar en los buenos momentos, y rescatarme en los malos, este trabajo va por vosotros

A Carmen, gracias por acompañarme todo este tiempo y por ser mi mejor amiga y compañera de vida

PREFACE

This thesis project has been carriet out in the Membrane Nanomechanics and Cellular Membrane Remodeling groups from the Biofisika Institute, Department of Biochemistry and Molecular Biology at the University of the Basque Country.

This thesis has been partially communicated at the following international meetings:

- EMBO-FEBS Summer School (2012). *Molecular architecture, dynamics and function of biomembranes.* Cargese, France
- Annual meeting of the Biophysical Society 2018. San Franciso, USA
- 12th EBSA-10th ICBP-IUPAP Biophysics congress (2019). Madrid, Spain
- EBSA 2019 Satellite Meeting. *Protein-lipid nanostructures: from domains to devices.* Bilbao, Spain

Publications:

- **J Espadas*,** D Pendin*, R Bocanegra*, Artur Escalada[1], Misticoni, Ariana Velasco del Olmo, Ibarra, Trevisan, Peter I. Kuzmin, P. V. Bashkirov, Anna V. Shnyrova[1], V Frolov[1,2,#], A Daga[#] **.** *Dynamic constriction and fission of endoplasmic reticulum membranes by reticulon.* ***Nature Communications*** (2019)10:5327
- **Javier Espadas**, Rebeca Bocanegra, Juan Manuel Martinez-Galvez, Eneko Largo, Soledad Baños-Mateos, Pedro Arrasate, Julene Ormaetxea Guisasola, Ariana Velasco-Olmo, Javier Vera Lillo, Borja Ibarra3, Anna V. Shnyrova* & Vadim A. Frolov*. *GTP and lipids control self-assembly and functional promiscuity of Dynamin 2 molecular machinery.* ***bioRxiv preprint*** (2021) (doi: https://doi.org/10.1101/2021.03.15.435402)

Financial support

This work has been supported by the National Institutes of Health, grant R01GM121725; the Spanish Ministry of Economy, grant BFU2015-70552-P. The author was a recipient of FPI pre-doctoral fellowship, grant BES-2016-077454, from the Spanish Ministry of Economy. Scientific stay in Dr. Tzviya Zeev-Ben Mordehai lab at the Utrecht University, Utrecht, The Netherlands, was supported by an EMBO Short-Term Fellowship, number 8639.

Index

Abbreviations

AlFx	Aluminum fluoride
amph	Amphiphysin
Atl	Atlastin
BAR	Bin-Amphiphysin-Rvs
BCA	Bicinchoninic acid
BDLP	Bacterial dynamin-like protein
BeFx	Beryllium fluoride
BSA	Bovine serum albumin
BSE	Bundle signaling element
Ca^{2+}	Calcium
CCP	Clathrin-coated pit
CFP	Cyan Fluorescent Protein
Chol	Cholesterol
CL	Cardiolipin
Climp63	Cytoskeleton-linking membrane protein 63
CME	Clathrin-mediated endocytosis
cryoEM	Cryo-electron microscopy
cryoET	Cryo-electron tomography
DAG	Diacylglycerol
DMEM	Dulbecco´s Modified Eagle Medium
DOPC	1,2-dioleoyl-sn-glycero-3-phosphatidylcoline
DOPE	1,2-dioleoyl-sn-glycero-3-phosphoethanolamine
DOPS	1,2-dioleoyl-sn-glycero-3-phospho-L-serine
DTT	Dithiothreitol
Dyn1	Dynamin 1
Dyn2	Dynamin 2
Dyn3	Dynamin 3
EDTA	Ethylenediaminetetraacetic acid
EGTA	Ethylene glycol-bis(β-aminoethyl ether)-N,N,N′,N′-tetraacetic acid
EM	Electron microscopy

EndoA2	Endophilin A2
ER	Endoplasmic reticulum
ET	Electron tomography
FAM134	Fam134 reticulon protein
FRAP	Fluorescence recovery after photobleaching
FRET	Fluorescence resonance energy transfer
G domain	GTPase domain
GABARAP	GABA Type A Receptor-Associated Protein
GDP	Guanosine diphosphate
GED	Guanosine triphosphate effector domain
GFP	Green fluorescent protein
GMPCPP	Guanosine-5'-[(β,γ)-methyleno]triphosphate
GSB	Giant Supported Bilayer
GST	Glutathione s transferase
GTP	Guanosine triphosphate
GTPase	Guanosine triphosphatase
GUV	Giant unilamellar vesicle
Hepes	4-(2-hydroxyethyl)-1-piperazineethanesulfonic acid
HS AFM	High-speed atomic force microscopy
I1	Interface 1
I2	Interface 2
I3	Interface 3
IP_3R	Inositol 1,4,5-triphosphate receptor
KCl	Potassium chloride
KDEL	KDEL endoplasmic reticulum protein retention receptor 2b
LC3	Microtubule-associated proteins 1A/1B light chain 3B
LDL	Low-density lipoprotein
Lnp	Lunapark
LUV	Large Unilamellar vesicle
lysoPC	1-oleoyl-2-hydroxy-sn-glycero-3-phosphocholine
MCS	Membrane contact site
mEGFP	Monomeric enhanced green fluorescent protein
Mg^{2+}	Magnesium

$MgCl_2$	Magnesium chloride
mGFP	Monomeric Green Fluorescent Protein
MLV	Multilamellar vesicle
MT	Microtubule
N_2	Nitrogen
NBD-DOPE	1,2-dioleoyl-sn-glycero-3-phosphoethanolamine-N-(7-nitro-2-1,3-benzoxadiazol-4-yl)
NT	Nanotube
ON	Overnight
p180	Ribosome-binding protein 1
PA	Phosphatidic acid
PC	Phosphatidylcoline
PDB ID	Protein Data Bank Identity Document
PDMS	Polydimethylsiloxane
PE	Phosphatidylethanolamine
PHD	Pleckstrin-homology domain
PI	Phosphatidylinositol
PI(3)P	Phosphatidylinositol-3-phosphate
$PI(3,5)P_2$	Phosphatidylinositol-3,5-biphosphate
PI(4)P	Phosphatidylinositol-4-phosphate
$PI(4,5)P_2$	Phosphatidylinositol-4,5-biphosphate
PRD	Proline-rich domain
PS	Phosphatidylserine
PSD	Phosphatidylserine decarboxylase
REEP5/6	Receptor Expression-Enhancing Protein 5 and 6
RHD	Reticulon-homology domain
Rh-DOPE	1,2-dioleoyl-sn-glycero-3-phophoethanolamine-N-(lissamine Rhodamine B sulfonyl)
ROI	Region of interest
Rtnl1	Reticulon-like-1
RTN	Reticulon
SDS-PAGE	Sodium dodecyl sulphate-polyacrylamide gel electrophoresis
Sec20p	Protein transport SEC20

Sec22p	Protein transport SEC22
Sey1p	Synthetic enhancer of Yop1p
SH3	SRC Homology 3
SLB	Supported lipid bilayer
SMFM	Single-molecule fluorescence microscopy
SNARE	Soluble NSF attachment receptor
STA	Streptavidin
TIRFM	Total internal reflection fluorescence microscopy
TMD	Transmembrane domain
TRH	Trehalose
TS	Transition state
TWJ	Three-way junction
VL1	Variable loop 1
WT	Wild-type
Yop1p	Yeast homolog of the polyposis locus protein 1

Symbols glossary

A	Area
f	Force
f_f	Frictional force
f_p	Pulling force
f_t	Tensile force
σ	Lateral tension of the membrane
k	Bending rigidity of the membrane
k_{eff}	Effective bending rigidity
k_p	Protein contribution to effective bending rigidity
k_l	Lipid contribution to effective bending rigidity
R_{NT}	Radius of the nanotube
v_t	Speed
t	Time
F	Fluorescence intensity
φ	Sorting coefficient
ρ_0	Fluorescence density of the membrane
J_s	Intrinsic curvature of the reservoir membrane
L_0	Lenght

Resumen

En cualquier aspecto de la vida tal y como la conocemos hoy, podemos darnos cuenta del gran nivel de compartimentalización que rodea a todo ser vivo. Sin embargo, mientras esta organización resulta inherente a organismos vivos, la capacidad de comunicación y asociación entre los distintos compartimentos es lo que hace que la vida sea tan dinámica e inesperada. Este fenómeno ha cautivado la atención de investigadores de todas las áreas en las que la curiosidad humana se puede manifestar. En este caso particular, la curiosidad sobre esa cuestión surgió en las escalas micro y nano, con la unidad mínima de vida esencial tal y como lo conocemos hoy en día, la célula.

Las células están segmentadas, al menos respecto a su medio exterior, como en el caso de las células procariotas, pero también, pueden estar segmentadas en su interior, como en el caso de las células eucariotas, en el que su propio interior celular está dividido en compartimentos membranosos denominados orgánulos. En cualquier caso, la función esencial de barrera se consigue mediante una membrana fluida, compuesta de moléculas lipídicas anfipáticas, y proteínas con la capacidad de estar ancladas en esas barreras, las proteínas transmembrana. El número, variedad y complejidad de dichas membranas es mucho más significativo en el caso de las eucariotas. Aquí, los compartimentos no son simples entes estáticos, sino que están continuamente sufriendo procesos de remodelación y adaptación.

Dentro de las diversas formas que tienen las células eucariotas para adaptarse al medio a través de los procesos de remodelación de sus “compartimentos” o membranas, se encuentran los procesos de fusión y fisión de las membranas (Fig. 1). En estos casos, el contenido completo de un compartimento delimitado por membrana es dividido completamente o unido a un compartimento idéntico o distinto (Fig. 1). Pero, dichos procesos de fusión y fisión de membranas no sólo ocurren entre el medio extracelular y el intracelular a través de la membrana plasmática, si no que ocurre en todos los orgánulos poseedores de membranas fluidas utilizadas como barreras.

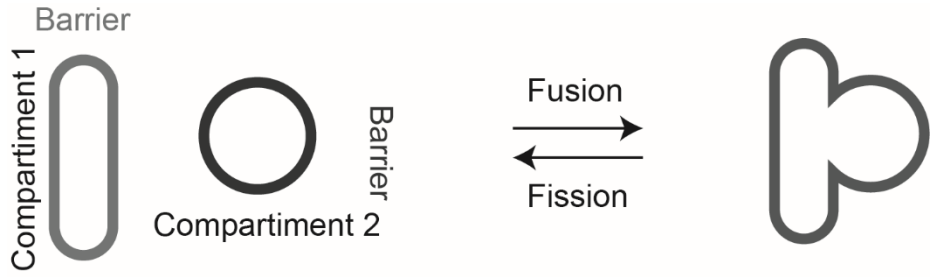

Figura 1. Representación esquemática de un proceso de fusión entre dos compartimentos membranosos (de izquierda a derecha) y un proceso de fisión (de derecha a izquierda).

Ambos procesos de remodelación de membranas, fusión y fisión, han sido ampliamente relacionados con la actividad específica de los miembros de una superfamilia de proteínas, las dinaminas. Las dinaminas son enzimas capaces de hidrolizar guanosin trifosfato (GTP), formadas por varios dominios proteicos, que se encuentran en todos los organismos vivos estudiados hasta la fecha, con un tamaño relativamente grande, y en comparación con otras proteínas con la capacidad de unión e hidrólisis de GTP, con poca afinidad por el GTP. En este contexto, las dinaminas interactúan tanto a nivel de orgánulos intracelulares, en procesos de fusión y fisión, como a nivel de membrana plasmática, permitiendo la comunicación con el medio extracelular mediante su participación en la endocitosis mediada por clatrina.

Con respecto a las dinaminas, las “clásicas” son las que más se han estudiado hasta la fecha (dinamina 1, 2 y 3) y son las que se relacionan con procesos de endocitosis mediada por clatrina. Gracias a la amplia investigación que se ha llevado a cabo durante las últimas tres décadas, sabemos cómo adquieren su especialización funcional mediante los distintos dominios pertenecientes a la dinamina (dominio de unión a membrana o PH, dominio de oligomerización o tallo, y dominio de hidrólisis de GTP). Las dinaminas clásicas tienen la habilidad de oligomerizar en estructuras helicoidales a través de sus regiones conocidas como tallos. Además, una vez oligomerizadas en estructuras helicoidales, los anillos resultantes interaccionan con los anillos adyacentes a través de los dominios de hidrólisis de GTP, lo que les hace convertirse en unidades funcionales para la remodelación de membranas.

Es generalmente aceptado que los procesos de fisión y fusión de membranas llevados a cabo por maquinarias moleculares, son complejos de pequeño tamaño, con la habilidad de interaccionar transitoriamente con la membrana que remodelan. Pero, siendo complejos de pequeño tamaño, sigue resultando discutible cual es la unidad mínima necesaria para producir los procesos de remodelación, y como las proteínas individuales en disolución son capaces de reaccionar ante estímulos externos para interaccionar entre ellas y convertirse en la potente maquinaria de remodelación.

Para llevar a cabo una caracterización completa de las unidades mínimas de dinamina implicadas en su actividad remodeladora de membrana, decidimos fijarnos en la dinamina “clásica” 2. La razón detrás de esta elección es que no sólo queremos centrarnos en un estudio estequiométrico de la reacción de remodelación por parte de la maquinaria molecular, sino que, además, queremos ver como dicha maquinaria es regulada a través de los distintos factores de los que depende la actividad de las dinaminas, como son la propia membrana y sus características físico-químicas, así como cofactores como GTP. En este contexto, la dinamina 2 parece *a priori* un candidato más susceptible para esta investigación, ya que su implicación en diversos procesos de membrana a nivel intracelular, así como su implicación clásica en la endocitosis mediada por clatrina, sugieren su gran adaptabilidad y capacidad reguladora en función de las propiedades del medio externo.

Para poder llevar a cabo tal estudio, durante la realización de esta tesis doctoral, llevamos a cabo la reconstrucción y análisis *in vitro* del comportamiento de oligómeros pequeños previamente caracterizados como unidades funcionales *in vivo*, de unidades inferiores a los complejos generalmente caracterizados en los sistema *in vitro*. En estudios previos llevados a cabo en distintas líneas celulares se observó que la media de unidades de dinamina 2 implicadas en procesos de endocitosis era de 26 moléculas (Fig. 2 a). Además, se cuantificó menos de 26 moléculas, en un 30% de los eventos de endocitosis. Este descubrimiento supuso un gran avance en el estudio de la remodelación de membranas por parte de la dinamina 2, ya que corresponden a una estructura menor a una vuelta helicoidal de dinamina 2 (Fig. 2 b). Es por ello, que teniendo en cuenta que la

dimerización a través de los dominios de hidrólisis de GTP es necesaria para la transición de dinamina 2 a una unidad funcional en remodelación de membranas, hipotetizamos como sería el complejo proteico en el 30% de los eventos demonstrando menos de una vuelta de hélice (Fig. 2 c). Así, decidimos evaluar la implicación del número de moléculas de dinamina 2 observadas *in vivo* y analizar su capacidad en procesos de fisión (Fig. 2).

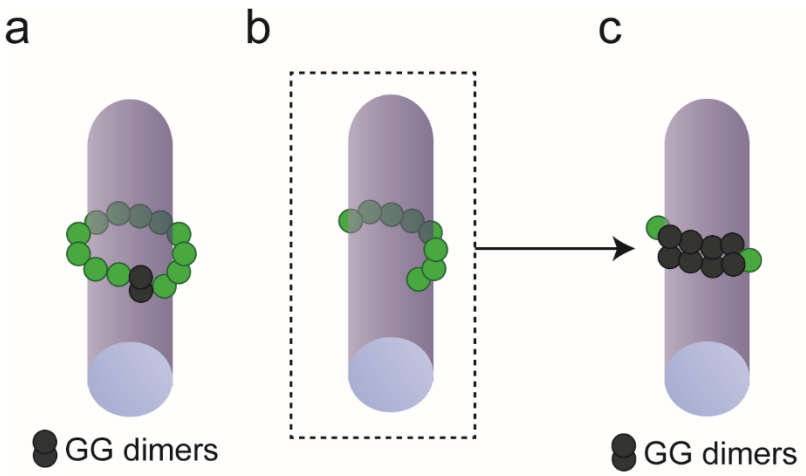

Figura 2. Representación esquemática de los complejos mecano-activos de dinamina 2 basada en los datos de microscopía de fluorescencia de unidades simples obtenidos *in vivo.* (a) Estructura correspondiente a 26 moléculas de dinamina 2. **(b)** Estructura correspondiente a menos de 26 moléculas (observado en los experimentos in vivo un 30% de las veces). **(c)** Mismo que en **(b)** pero formando la estructura correspondiente a la interacción con el dominio de hidrólisis de GTP.

Los objetivos perseguidos fueron la reconstitución de complejos menores de una vuelta helicoidal de Dyn2 *in vitro*, para poder determinar su adaptación a las características de la membrana durante los procesos de endocitosis, tanto físicas y químicas como de topología. Además, llevamos a cabo la caracterización de cómo los lípidos estructurales, moléculas esenciales para la morfología membranosa, afectan la actividad remodeladora de membrana por parte de la dinamina 2 y de sus unidades inferiores a una vuelta helicoidal. Por último, propondremos un mecanismo para la transición de unidades menores de dinamina 2 a complejos funcionalmente activos en procesos de remodelación de membranas.

Tras la consecución de dichos objetivos, obtuvimos resultados esclarecedores en cuanto a los mecanismos de preparación y acción de la

maquinaria molecular de dinamina 2. En primer lugar, observamos que los complejos inferiores de dinamina 2, los que podríamos asumir como unidades precursoras de la maquinaria funcionalmente activa, son capaces de sentir los cambios en cuanto a la topología de las membranas destino. Además, la transición desde estas unidades a las funcionalmente activas está favorecida mediante la presencia de lípidos específicos, especialmente de la fosfatidiletanolamina (PE), un lípido estructural con geometría de curvatura negativa.

Sorprendentemente, descubrimos la habilidad de la dinamina 2 de producir el efecto topológicamente contrario a su extensamente descrita actividad en la fisión de membranas, la agregación e incluso la fusión de vesículas. Para esta novedosa función, encontramos que era necesaria la presencia del lípido descrito anteriormente, PE, u otros lípidos con la misma geometría de curvatura negativa. De manera crucial, encontramos que esta actividad inesperada podía ser regulada por lípidos, GTP y proteínas conocidas por su interacción con dinamina 2 durante el proceso de endocitosis. Finalmente, aunque los resultados expuestos sobre la dinamina 2 en el contexto de agregación y fusión de membranas son púramente *in vitro*, y no está claro su relevancia fisiológica, pueden suponer un punto de inicio para futuras investigaciones sobre las actividades no canónicas de la dinamina 2 en el contexto del espacio intracelular.

Además del estudio en detalle de la dinamina 2, quisimos realizar un estudio mecanístico de un proceso de remodelación a nivel intracelular, como es el caso del retículo endoplasmático (ER). Mientras que la fusión homotípica en este orgánulo membranoso ha sido caracterizada extensivamente mediante la funcionalidad de uno de los miembros de las dinaminas, la atlastina, la existencia de un mecanismo molecular destinado a la acción opuesto, como por ejemplo la fisión de las membranas, continúa bajo debate. Sin embargo, la reconstrucción *in vitro* de una estructura membranosa en trabajos anteriores indicó evidencias de actividades polifuncionales, con una unidad proteica mínima capaz de llevar a cabo la creación y a su vez, la destrucción de esta estructura membranosa. En esta tesis, analizaremos estos efectos complejos y revelaremos que la capacidad

de llevar a cabo tareas múltiples es intrínseca de proteínas encargadas de procesos de remodelación de membranas, y que además, estas pueden ser reguladas por las membranas que remodelan.

Para diseccionar el mecanismo de la fragmentación de las membranas encontradas en el ER, utilizamos la proteína Reticulon-like-protein 1 (Rtnl1), proveniente de *Drosophila melanogaster*, gracias a las evidencias funcionales y genéticas encontradas por nuestro colaborador en Italia, el Doctor Andrea Daga, el cual descubrió como dicha proteína parece estar implicada en procesos de fragmentación en el ER. Además, Rtnl1 ha sido ampliamente descrita en los últimos 15 años como responsable de la generación de curvatura de membrana en el ER, y alguno autores han especulado previamente con su potencial implicación en procesos de fragmentación.

Con estas evidencias presentes, decidimos llevar a cabo la reconstitución de Rtnl1 en membranas modelo. Las principales hipótesis de nuestro trabajo se basan en primer lugar en la implicación de Rtnl1 en procesos de fisión mediante la generación de curvatura de membrana hasta límites donde dicha membrana se acaba fragmentando. Además, hipotetizamos que para que Rtnl1 se convierta en una maquinaria funcional de fisión de membranas, esta necesita el aporte de energía externa por parte de otros componentes celulares. Mientras que la dinamina 2 es capaz de proporcionarse dicha energía mediante la hidrólisis de GTP, en este caso, la unión de los túbulos del ER con motores moleculares, produciendo movimiento tras la hidrólisis de ATP, proporcionaría la energía necesaria (de manera no local si la comparamos con la dinamina 2) para llevar a cabo el proceso de fragmentación (Fig. 3).

Considerando tales hipótesis, llevamos a cabo la realización de los siguientes objetivos. En primer lugar, confirmaremos la implicación del Rtnl1 en la fisión de las membranas del ER en cultivo celulares. A continuación, reconstituiremos la proteína purificada de Rtnl1 en membranas tubulares *in vitro*. Posteriormente, identificaremos las potenciales implicaciones de la fuerza y la tensión en la transición de Rtnl1 en una maquinaria funcional de fisión. Por último, investigaremos como el equilibrio entre fusión mediada por atlastina y

fisión mediada por Rtnl1 es capaz de crear y mantener las estructuras membranosas características del ER.

Las conclusiones principales del estudio realizado sobre el Rtnl1 y su actividad en la curvatura de las membranes y la fisión fueron las siguientes: en primer lugar, confirmamos que el equilibrio entre atlastina y Rtnl1 es esencial para el correcto mantenimiento de las estructuras membranosas del ER. A continuación, caracterizamos cómo el Rtnl1 reconstituido en membranas modelo es capaz de sentir las propiedades topológicas de curvatura. Además, una vez reconstituido, el Rtnl1 es capaz de producir constricción severa y fisión mediante el acoplamiento a procesos dinámicos de membrana.

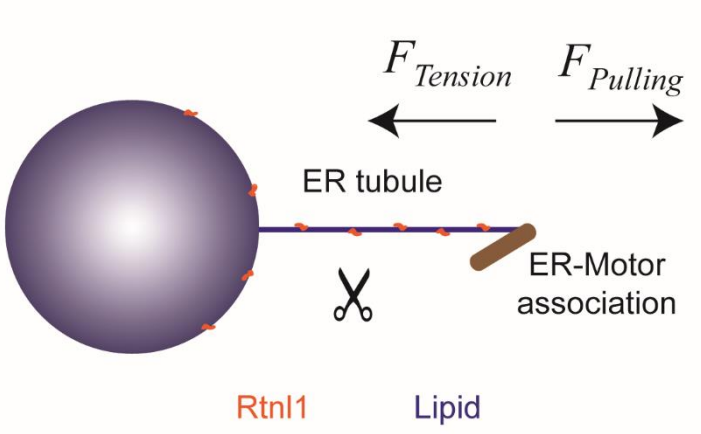

Figura 3. Mecanismo hipotético de la fisión de las membranas en el ER mediada por el acoplamiento entre el Rtnl1 y la movilidad de la membrana tras la asociación con motores moleculares.

1. General introduction

No matter where we look, it is evident that living matter is compartmentalized at all possible length scales. But while this is so, it is the ability to adapt and connect these compartments that makes life so unexpected and dynamic. This fact has intrigued many researchers from the various perspectives and disciplines in which human curiosity can manifest itself. In this particular case, curiosity arose at the micro and nano scales, with the minimal unit essential to life as we view it today, the cell.

Cells are compartmentalized, at least with respect to their environment, as in prokaryotes, but can also be elegantly segmented within, as in eukaryotes. In both, the barrier function is achieved by a fluid membrane composed of amphipathic lipid molecules and transmembrane proteins. The number, variety, and complexity of such membranes are much more significant in eukaryotes. The compartments are not static formations; they are visibly dynamic, constantly changing their shape and position. Most importantly, they interact. Multiple intracellular compartments cannot remain in isolation. They have to communicate to exchange information and materials. For that, they have to control the barrier function of the membrane to let the contents in and out. Out of multiple ways of trans-membrane communications and transport developed by eukaryotic cells throughout the evolution, membrane fusion and fission are the most radical. There, the entire content of compartments is either merged or split apart. This material exchange method is fundamental for cellular life, as it underlies cellular abilities to secrete and uptake, transport, and reseal the wounds. Nevertheless, during fusion and fission, the static barrier function of the membrane is completely compromised: the barrier between the fusing compartment essentially disappears while novel barriers are created upon fission. How have the cells learned how to remodel the membrane barriers without destroying the compartmentalization?

The intracellular membrane remodeling, both fusion and fission, is heavily linked to one protein superfamily, dynamins. They are multi-domain guanosine triphosphatase (GTPases), found in every living organism, that are essentially defined by their relatively big size, modular structure, and low affinity for guanosine triphosphate (GTP)[1]. They have emerged and evolved together with

the endomembrane system. Their functional and structural evolution has to reflect the complexity and robustness of intracellular membrane remodeling processes. Dynamins have been extensively studied. We understand the inner molecular mechanics of these mechano-enzymes. We know how they acquire functional specialization via dedicated membrane-interacting and residing domains. What we know less is that how they learned to appreciate membrane mechanics and dynamics. The fusion and fission processes are generally considered as extremely localized and transient membrane transformations. The protein machinery mediating those is thought about as a small protein complex, a ring or helix, transiently self-assembling to do the job[2]. Although the energy barriers for both fusion and fission are determined mainly by lipids[3,4], their resistance to bending and remodeling, the proteins are considered force-factors powerful enough to overcome lipid resistance. However, it´s become increasingly understood that inside the complex and dynamic endomembrane system, the fusion and fission proteins are to read and react to multiple mechanical and chemical cues. Accordingly, the mechano-activity of dynamins might be altered by lipids[5]. The efficiency of membrane remodeling by dynamins depends on global membrane forces, such as tension[6] as on local protein partners.

Furthermore, in the context of organelle maintenance, dynamin fusion and fission machinery are to work in concert, as seen in mitochondria[7]. Finally, multiple experimental evidences indicate that individual dynamins are multifunctional proteins operating as mechano-enzymes as regulators of membrane remodeling. How do they learn to do so many things? Can the functionality of a dynamin species or, in general, a membrane-remodeling protein be switched? Can membrane be a master controller of the function?

We decided to look at the membrane remodeling processes where protein multifunctionality might be revealed and analyzed to answer these questions. One particular case is Dynamin 2 (Dyn2), a ubiquitously expressed dynamin primarily implicated in membrane fission during endocytosis. Multiple works involved Dyn2 to other membrane remodeling processes, different from fission[8,9]. Another case is membrane remodeling in the endoplasmic reticulum (ER). While the homotypic fusion of the ER membranes is well documented and mediated by

Atlastin (Atl), a member of the dynamin superfamily, the existence of protein machinery behind the opposite fission process remains obscure. However, *in vitro* reconstruction of the ER network indicated polyfunctionality, the ability of a minimal protein set to create and destroy the network upon addition/removal of the nucleotide[10]. In this thesis, we will analyze some of these complex effects and reveal that multitasking is intrinsic for proteins mediating membrane remodeling and could be controlled by the membrane they remodel.

2. Mechanism of tubular ER membrane scission

2.1 Introduction

2.1.1 The ER topology and dynamics defines its biological functions

A century ago, the 1974 Nobel Prize George Palade observed for the first time the association of ribosomes with membranes using electron microscopy (EM)[11]. Later he named this structure the ER. Almost a century of extensive research later, we know that the ER membranous network spans the entire cytoplasm of eukaryotic cells. We learned that it consists of structural elements of varying curvature and topology, from flat sheets and reticular tubules to complex fenestrated structures (Fig. 2.1) enclosing a single lumen[12–14]. A similarly diverse biological functionality accompanies the structural complexity of the ER. Indeed, it is widely accepted that the shape of the ER elements defines the ER functions[15].

Flat sheets and curved tubules are associated with the major ER biological functions such as protein synthesis, calcium metabolism, and lipid biogenesis[15]. For example, protein synthesis and translocation are associated with ER sheets

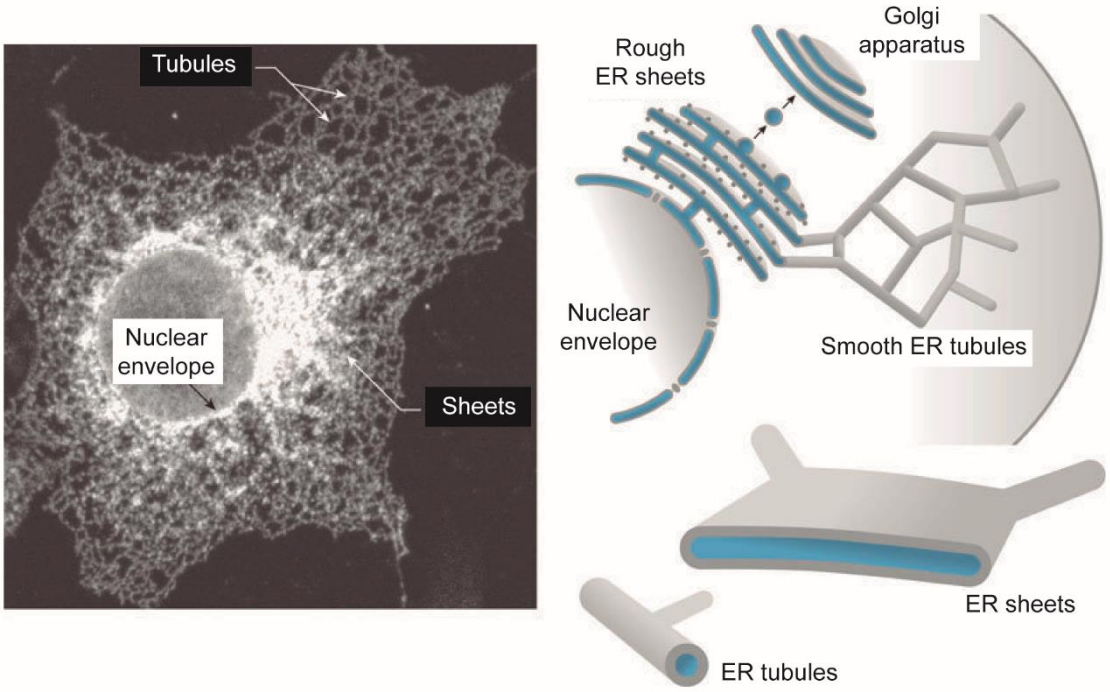

Figure 2.1. ER network is composed by elements of different membrane curvatures and topologies. The fluorescence micrograph shows a snapshot of the living ER network labeled with a fluorescent ER marker. The cartoon shows schematic representations of the different ER elements. Figure reprinted from "Further assembly required: construction and dynamics of the endoplasmic reticulum network"[16], Park and Blackstone, 2010. Copyright (2010) with the permission of WILEY.

rather than tubules[15]. Ribosomes localize to the outer flat leaflet of the ER sheets facing the cytosol and facilitate the production of transmembrane[17] and cytosolic proteins[18]. An example of this shape-based functionality in protein synthesis is seen in the pancreatic cells with high protein secretion capacity, where a higher number of flat ER sheets is detected[19] as compared to muscle cells or neurons with much lower protein synthesis capacity.

The cortical ER is structurally defined by tubular membranes and serves as a connection between the ER and the plasma membrane. In muscle cells and neurons, the lumen of the cortical ER functions as calcium (Ca^{2+}) storage[20,21]. Here, Ca^{2+} concentrations are three to four orders of magnitude higher as compared to cytosol[22]. When intracellular Ca^{2+} level drops, the ER starts to release Ca^{2+} through activation of Ca^{2+} channels, ryanodine receptors, and inositol 1,4,5-triphosphate receptors (IP_3R)[22]. Ca^{2+} release from the tubular ER is of critical importance for several physiological processes, such as the fertilization process upon sperm entry[23,24], muscle contraction[22] or neurotransmitter release during neuronal processes[25].

Lipid biogenesis is also one of the tubular ER main functions[26], not only to synthesize lipids for their insertion at the ER membranes but also to transport them to virtually all intracellular membranes. Regarding lipid production for the tubular ER, these highly curved membranes are mainly formed in their composition by two lipids, phosphatidylcholine (PC) and phosphatidylethanolamine (PE), both in mammals and yeast[27]. Both PC and PE come from a diacylglycerol (DAG) backbone in which the esterification of its phosphate group leads to either choline or ethanolamine[28]. Interestingly, although both lipids are synthesized from the same reaction, their mechanical influence on the membrane is different. On one hand, the prototypical version of PC, 1,2-dioleoyl-sn-glycero-3-phosphatidylcoline (DOPC), shows a cylindrical molecular architecture[29], which favors the formation of flat lipid bilayers. On the other hand, PE belongs to the group of non-bilayer lipids due to its cone-shaped structure, exhibiting preference for non-bilayer configurations with negative curvature[30] and reducing significantly the energy needed to produce membrane deformations (or membrane bending rigidity, k)[31]. Interestingly, molecular machineries involved in

local topological rearrangements of the membrane (i.e., membrane fusion or fission) rely precisely on the formation of non-bilayer structures and the lowering of k[32]. Therefore, the presence of high amounts of PE in the tubular ER would facilitate the deformation and remodeling of its membrane.

Although at lower abundance in the ER, phosphatidylinositol (PI) is also a fundamental lipid molecule essential for many remodeling processes. Analogously to PC and PE, PI also contains a DAG backbone. Once PI is produced, it can be stored at the ER or further transformed into phosphorylated species of PI, the phosphoinositides. Phosphoinositides act at different subcellular membranes in signaling and recognition. Some examples are phosphatidylinositol-4,5-biphosphate (PI(4,5)P_2) at the plasma membrane[33], phosphatidylinositol-3-phosphate (PI(3)P) on early endosomes, phosphatidylinositol-3,5-biphosphate (PI(3,5)P_2) on late endosomes, and phosphatidylinositol-4-phosphate (PI(4)P) on the trans-Golgi network[27]. Recognition and signaling of the phosphoinositides allow endocytic proteins recruitment at specific membrane locations involved in vesicle trafficking and cellular homeostasis[33].

While the ER parts have their respective distinct shapes, the development of advanced optical microscopy had allowed for the documentation of the highly dynamic nature of the ER membrane network[34]. The ER morphology and topology constantly change, with cortical ER being especially dynamic. New tubular branches being elongated and snapped, often at frenetic speeds[35]. Such dynamics are supported by the association of ER membranes with dynein/kinesin molecular motors and the microtubule cytoskeleton[34,36] (Fig. 2.2). ER tubules extend at considerable long distances in close alignment with the microtubules (MTs) (Fig. 2.2) or by single-point attachment to the MTs[37]. In the first case, motors pull the membranes along the MTs surface, whereas in the second case, the pulling is through MT polymerization upon the ER association with the MTs´ tip.

During the last decades, a surprising new link between the ER membrane dynamics and intracellular communication emerged with discovering the membrane contact sites (MCSs). MCSs form by close apposition of two

membranes from different organelles and allow for the limited and tightly controlled material exchange between the organelles, while the membrane integrity of the organelles is kept intact[38]. The constant movement of the ER network enables the formation of the MCSs with almost every organelle in the cell. One of the main functions of the MCSs is the lipid transport between organelles. Here, the formation of MCSs with the ER has emerged as an alternative to the classical vesicular transport[39–41]. The ER-associated MCSs promote the distribution of the core lipid species from the ER to the rest of the cellular membrane. For example, the ER produces the precursor of mitochondrial cardiolipin (CL), the phosphatidic acid (PA), which must be consistently transported to the outer and inner mitochondrial membranes for further modification[42,43].

Conversely, ER also receives lipids from organelles through MCSs. One example of this process is PE, which has an alternative synthesis pathway in the mitochondrion via decarboxylation of phosphatidylserine (PS) by the phosphatidylserine decarboxylase (PSD) enzyme[44]. The endogenous and mitochondrial PE may constitute up to 30% of total ER phospholipids[27]. Another example of lipid transfer through MCS is cholesterol (Chol), which is internalized into the cell by low-density lipoprotein (LDL) particles and stored at endosomes, to be further transported to ER via MCSs[38].

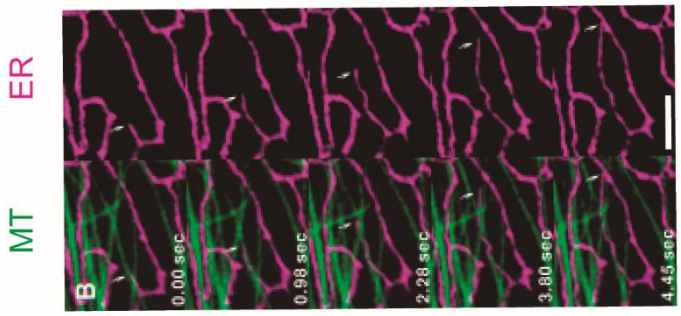

Figure 2.2. Elongation and fusion of an ER tubule (red, upper sequence, white arrows). The tubule sliding over the MT branch (green, lower sequence, white arrows) is driven by molecular motors. Scale bar 2 µm. Reprinted from "Visualizing Intracellular Organelle and Cytoskeletal Interactions at Nanoscale Resolution on Millisecond Timescales"[34] Guo et al. Copyright (2018), with permission from Elsevier.

Overall, our current understanding of the ER structure is based on a highly dynamic membrane network model. ER elements continuously change their shape and connectedness, constantly interacting with other intracellular organelles and the plasma membrane. It has become increasingly understood that structural and functional coherence of the ER network, its ability to change its shape and morphology during the cell cycle or upon external stimulation, is vital for intracellular homeostasis. Hence, molecular mechanisms underlying dynamic regulation of the ER shape and connectedness have attracted renewed attention.

2.1.2 ER morphology regulation and maintenance

In conventional fluorescence microscopy, the dynamics of the thin ER tubules might be contrasted to statics of less resolved amorphous structures corresponding to the stacks of sheets. The tube movements have been long associated with intrinsic dynamics of active filamentous networks, primarily microtubules, and the molecular motor movements along with such networks[45]. In a simplistic approximation, the ER tubules are pulled from perinuclear membrane reservoirs and pinned to contact points distributed over the cytoplasm, creating a tensed metastable network. Though lateral tension is indeed intrinsic for the ER network (as discussed below), its effects are balanced and regulated by various protein complexes responsible for the maintenance of the ER morphology. These proteins can stabilize tubular ER upon MT depolymerization and create complex fenestrated topologies of the ER elements revealed by modern super-resolution techniques[34,46].

Besides the shape dynamics, ER, like other intracellular organelles, has intrinsic means of fragmentation and reconnection[36,47]. These mechanisms constantly operate in the living ER, are synchronized with the cell cycle[36,48,49], and can be triggered in pathological scenarios, such as ER stress[50,51]. As in other organelles, ER maintenance relies on a dynamic balance between the membrane fusion conducted by the ER-specific protein machineries and fission processes. Below we review these two major ER-maintaining proteins: those responsible for shape and curvature stabilization and those dedicated to topological transformations.

2.1.2.1 Structural protein scaffolding

The first class of proteins responsible for maintaining the ER shapes operates via well-understood scaffolding mechanisms. The scaffolding form on and maintain as ER sheets as its tubular branches.

The ER sheets consist of closely spaced membrane layers. It has been suggested that the close interspace is stabilized by specialized proteins that form intra-membrane bridges through the luminal space[52,53]. One example of such membrane-bridging proteins is the Cytoskeleton-linking membrane protein 63 (Climp63), an abundant ER protein with a transmembrane domain (TMD) that accumulates in the sheets at the perinuclear ER[54,55]. Overexpression of Climp63 leads to the massive formation of ER sheets. However, partial removal of Climp63 does not significantly alter the sheet abundance[52], suggesting the existence of additional proteins involved in the stabilization. Indeed other proteins, such as ribosome-binding protein 1 (p180) and kinectin proteins, are also associated with the formation and structural maintenance of this structure in the ER[52]. These observations indicate that the sheet´s morphology is maintained by several redundant mechanisms which switch on and off under specific cellular requirements[26].

A different type of scaffolding is formed by reticulons (RTNs), a family of integral transmembrane proteins sharing the characteristic reticulon-homology domain (RHD)[56]. RTNs self-assemble into arc-shaped structures that act as structural scaffolds to maintain the highly curved membranes typical of the ER[52,57]. To date, RTNs are the best-described group of proteins responsible for generating and stabilizing membrane curvature in the ER[52,58,59] (Fig. 2.3 a). Unlike Climp63 and other membrane bridging proteins, RTNs are universal curvature generators involved in both ER sheets and tubes [52,58,59] (Fig. 2.3 a). In the ER sheets, RTNs concentrate at the curved edges, while in the ER tubules, their distribution is more homogeneous (Fig. 2.3 a). In both cases, the arc-shaped RTN scaffolds align along the radial curvature creating locally cylindrical shape[4] (Fig. 2.3 a). However, the RTNs are much more abundant in the tubular ER, the high membrane coverage by RTN arcs promoting creation and stabilization of the tubular network[60]. At a smaller coverage, a lower number of arcs accumulate

leading to the curvature stabilization at the edge of the ER sheet (Fig. 2.3 a). The RTN partitioning to both the sheets and tubules enables it to control the ER morphology, changing the ratio of sheets to tubules upon specific cellular demands.

Besides oligomerization into arc-like curved structures, the membrane curvature activity of RTNs are due to i) the hairpin-like structure of its two TMDs constituting the RHD[61] (Fig. 2.3 b) and ii) the C-terminal amphipathic helix[62]. Other proteins involved in the curved membrane topology of the tubular ER, such as Receptor Expression-Enhancing Protein 5 and 6 (REEP5/6) belonging to the yeast homolog of the polyposis locus protein 1 (Yop1) family of proteins[58], also contain the above membrane-wedging domains[62]. Although these proteins are not members of the RTNs family *per se*, they are considered to carry out similar structural functions to RTNs due to their RHDs. Furthermore, upon overexpression, these proteins, as well as RTNs, form immobile oligomers to the ER tubule, likely consisting of multiple arc-like structures oriented as previously explained for RTNs[56].

The ability of RTN family members to create and maintain tubular membrane topology has been tested *in vitro*[59] (Fig. 2.3 c). Purified RTNs and DP1/Yop1 transmembrane proteins were reconstituted into lipid vesicles using co-micellization approach[59,63]. The curvature of the resulting proteo-liposomes was assessed for different protein concentrations and lipid compositions using ultrastructural characterization techniques. The importance of the RHDs of RTNs in the generation of highly membrane curvature was further confirmed by the proteolysis of the RTN ectodomains, which did not affect the formation and maintenance of membrane tubules[59]. Notably, at high membrane concentrations, Reticulon-like-1 (Rtnl1) protein, the RTN member in *Drosophila melanogaster*, induced extremely high membrane curvatures[59] (Fig. 2.3 c), comparable of that produced by the fission dynamins[64].

While the scaffolding proteins support the local architecture of the ER elements, tubules and sheets, in dynamic ER and, upon changing their expression levels, mediate the ER shape transformations, they cannot account

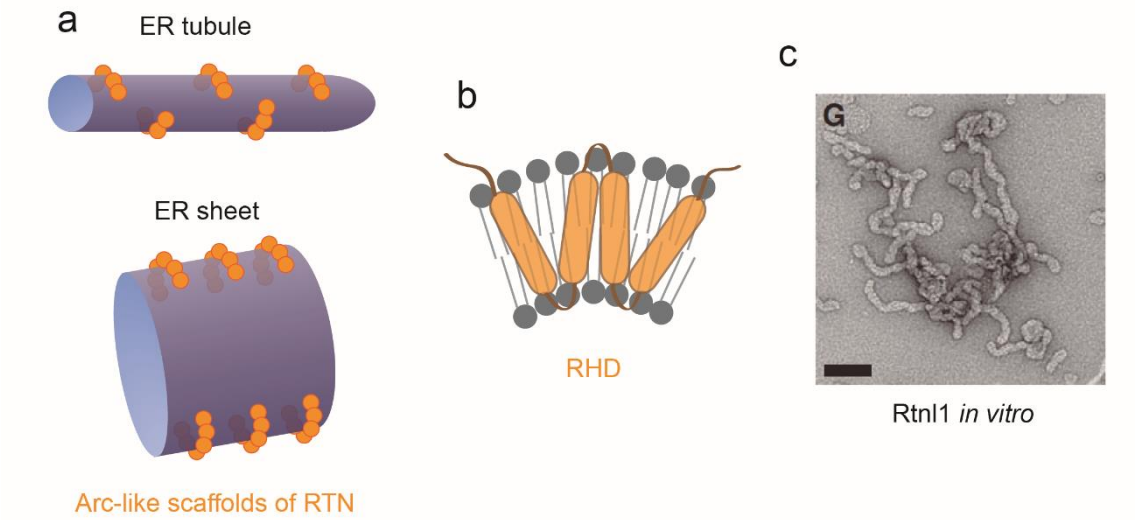

Figure 2.3. RTN generates and stabilizes membrane curvature through the curved arc-like shape and membrane wedging of its okigomers. (a) The cartoon showing RTN arcs covering an ER tubule (upper part) and edges on an ER sheet (lower part). **(b)** Schematics of membrane wedging by the transmembrane Reticulon Homology Domain (RHD). **(c)** EM micrograph of membrane tubulation by purified Rtnl1 reconstituted with *E. coli* polar lipids. Scale bar is 100 nm. From Hu et al.[59]/ Reprinted with the permission from AAAS.

for the ER maintenance during the topological transformations, ER fusion and fragmentation.

2.1.2.2 Dynamic balance of ER morphology

So far, the best-studied example of a membrane organelle that is morphologically maintained by the balance of fusion and fission is mitochondria[65]. Omission of either reaction results in a hyperfused[66] or fragmented[67,68] mitochondrial network. In both cases, mitochondria lose their structural and functional identity. Membrane fusion is essential for the creation and functioning of cortical ER. The ER fusion machinery has been identified and characterized, as described below. By analogy, it seems likely that the ER maintenance relies on a dynamic balance between fusion and fragmentation of the ER network, the latter going via still poorly defined mechanism.

2.1.2.2.1 ER homotypic membrane fusion

Homotypic membrane fusion in the ER has been extensively studied, both *in vitro* and in different cellular and organism models[69]. Atl GTPase was first identified as an ER fusogen in *Drosophila*[70]. Homotypic fusion in the tubular ER happens when a freshly cytoskeleton-elongated ER tubule encounters another

tubule on the way. At this point, Atl mediates initial membrane tethering of the membranes of both tubules resulting in a ¨T¨ shape structure called three-way junction (TWJ)[71]. Although the tethering activity of Atl was initially assumed as part of the fusion reaction, recent experimental observations confirmed that Atl´s tethering activity alone could play essential biological functions without necessarily leading to complete membrane fusion[72]. However, the initial membrane tethering step can be followed by Atl-mediated membrane fusion upon GTP hydrolysis[70]. Purified Atl retains its fusogenic activity and could produce the fusion of lipid vesicles[70]. Though fusion mechanism remains a subject of active debate, the basics of the mechano-chemical action of Atl are well understood. Atl belongs to the dynamin superfamily of large GTPases, the mechano-enzymes in charge of topological membrane remodeling, fusion and fission, in the cytoplasm[1]. Atl shares basic domain architecture and functional design elements with other dynamins, particularly with Dynamin1 (Dyn1), the founder of the superfamily.

Dyn1, the most studied dynamin, mediates synaptic vesicle scission during endocytosis. Dyn1 and Atl have a similar extended cytoplasmic part (Fig. 2.4 a, b, blue) responsible for the assembly-dependent GTP hydrolysis, a trademark of dynamins[73,74] and different membrane interacting domains. Atl is anchored to the membrane via two TMDs that are connected by a hydrophilic segment pointing towards the lumen of the organelle, suggesting that the N- and C-termini of Atl point in the same direction of the membrane[75,76] (Fig. 2.4 a, brown). Dyn1 is a cytoplasmic protein that transiently binds to the membrane through its pleckstrin-homology domain (PHD)[77] (Fig. 2.4 b, green). The GTP hydrolysis by Atl and Dyn1 requires dimerization of GTPase (G) domains of the proteins (Fig. 2.4 a, yellow)[75,78] (Fig. 2.4 a, c). The G domain of Atl is connected to the middle or stalk region of the protein via a flexible linker (Fig. 2. a), similarly to the bundle signaling element (BSE) observed in Dyn1[79].

Regarding their action on the membrane, both Atl and Dyn1 self-assemble into functional units for local membrane rearrangements upon GTP binding. However, whereas Atl self-interaction starts through the GG dimerization upon GTP binding[75,78] (Fig. 2.4 c), Dyn1 is already a tetramer consisting of two dimers upon

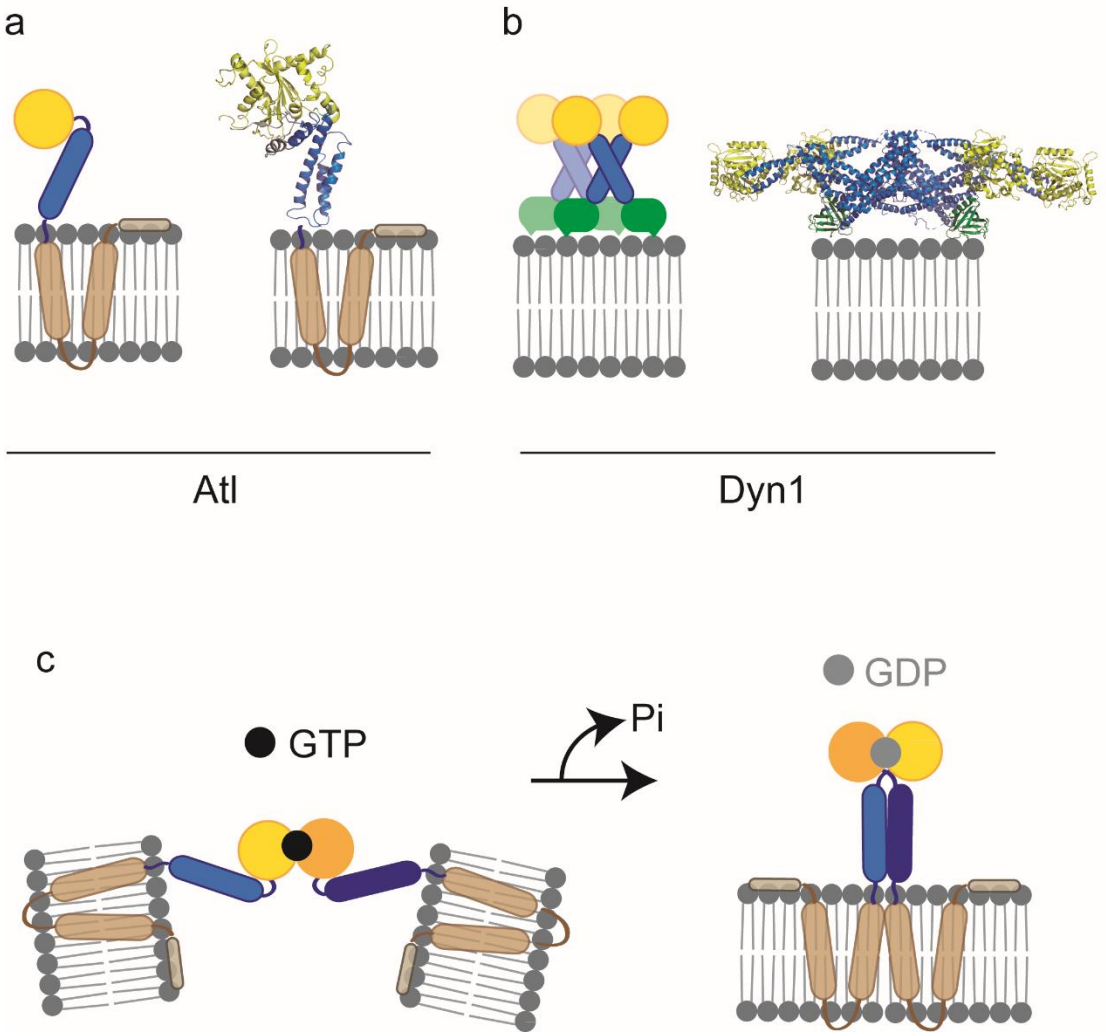

Figure 2.4. Atl shares structural similarities with Dyn1. (a) The left cartoon shows a schematic representation of Atl in the lipid bilayer (yellow = G domain; blue = stalk region; light brown = TMDs; light gray = N-terminal region. On the right, the crystal structure of the cytosolic C-terminal domains the Atl homolog from *Drosophila melanogaster* before the TMDs [Protein Data Bank Identity Document (PDB ID) 3X1D]. The color code is the same as in the schematic representation. **(b)** The left cartoon shows the transient interaction of Dyn1 tetramers with the lipid bilayer (yellow = G domains; blue = stalk regions; green = PH domains). On the right the crystal structure of the Dyn1 tetramer from *Homo sapiens* (PDB ID 5A3F). **(c)** Cartoon illustrating the initiation of Atl dimerization upon GTP binding (left), and the conformational change in the Atl dimer upon GTP hydrolysis leading to membrane fusion (right).

membrane binding even in the absence of nucleotides thanks to the polymerization of its stalks[80] (Fig. 2.4 b). Dyn1 assembles into helical structures[73], which are self-sufficient in membrane fission[81]. As Dyn1, purified Atl also forms self-sufficient fusion machinery upon reconstitution into lipid vesicles[82]. GTP-driven cross-dimerization between Atl molecules from different vesicles leads to stable tethering. The dimerization is followed by GTP hydrolysis driving conformational changes of the Atl dimers. The dimers pull the vesicular

membranes closer to each other until generated membrane stresses cause local membrane destabilization and fusion (Fig. 2.4 c).

The fusogenic activity of Atl is critical for the creation and maintenance of TWJ in the tubular ER network[70,83]. However, upon formation of a TWJ, RTNs could be rapidly recruited to the TWJ to further stabilize the curved membrane structure[84]. Therefore, it seems that RTNs can somehow sense membrane curvature changes happening in the ER. Aside from RTNs, it was recently discovered that Lunapark (Lnp) protein also accumulates at these structures[71,85], while its role in TWJ stabilization remains under debate. In fact, it was proposed that Lnp accumulation only affects the abundance of TWJs, while RTNs are the main responsible for structural stabilization. RTNs could bind to Lnp[85], suggesting that the mix of negative membrane curvatures brought by Lnp with the positive curvature imposed by RTNs is ideally suited for the structural maintenance of TWJs, which combines both types of geometries.

Of note, the fusogenic activity of Atl in the ER is likely supplemented by additional proteins. In *S. cerevisiae*, *in vitro* membrane and content mixing experiments with purified yeast microsomes demonstrated that the Soluble NSF attachment receptors (SNAREs) proteins, Protein transport protein SEC22 and SEC20 (Sec22p and Sec20p, respectively) are also involved in the production of effective membrane fusion in the ER[86]. However, the mechanism is less understood than with Atl alone. Therefore, it seems that other proteins, such as Lnp or Sec22p/Sec20p, may also be involved in ER network formation and maintenance *in vivo*.

2.1.2.2.2 Membrane fragmentation in the ER

As mentioned above, while the fusion of the ER tubules has been extensively documented, the experimental confirmation of ER membrane fission only emerged a few years ago thanks to the development of super-resolution fluorescence imaging techniques[34]. To preserve the morphology, by analogy with mitochondrial membrane dynamics, ER fusion should be counter-balanced by a reverse topological transformation, i.e., membrane fission. Following this hypothesis, partial inhibition of the fusogenic activity of Atl in the ER could potentially lead to a less connected ER. In agreement with this, suppression of

Atl GTPase activity in *Drosophila melanogaster* fruit flies resulted in fragmented ER[70].

In the physiological context, ER fragmentation was documented during mitosis[36,48,49] and prior to autophagic degradation[50,51]. Reversible fragmentation of the ER was reported as in neurons[87] as in other cell types[88,89]. Upon the fragmentation, the tubular ER network is transformed into a set of disconnected membrane structures, sheets, vesicles, and complex confined networks (Fig. 2.5). The fragmentation can be reversed, with de novo tubular branches emerge and connect via TWJ (Fig. 2.5, red arrow). Importantly, in cellular models and in *Drosophila*, the ER network fragmentation occurred upon suppression of membrane fusion activity by Atl[70]. Therefore, there is strong evidence for the existence of an endogenous mechanism aimed at reducing ER connectivity.

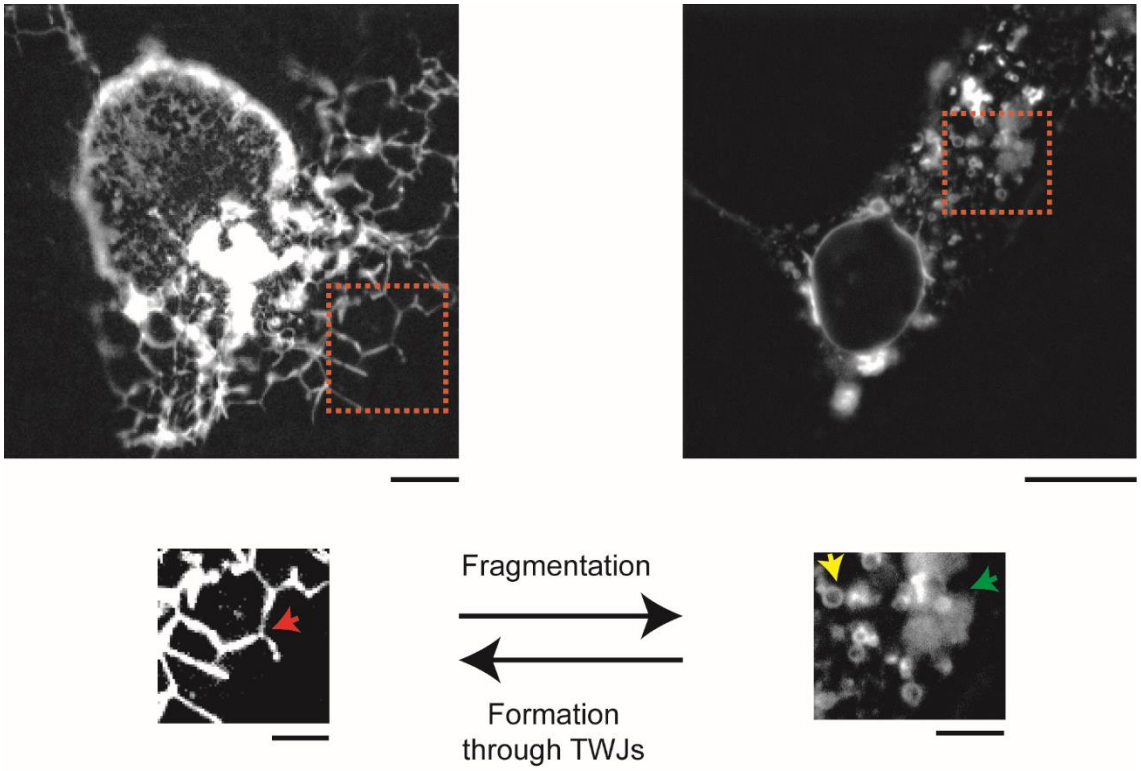

Figure 2.5. Fluorescence microscopy observation of the ER fragmentation. Upper images show epifluorescence snapshots of two COS-7 cells, the left image showing an interconnected ER periphery, and the right showing membrane fragmentation leading to sheet- and vesicle-like structures. The bottom images are regions of interest (ROIs) from the upper snapshots (indicated with the orange squares) showing the TWJs-connected ER tubules (left ROI, red arrow), vesicles (right ROI, yellow arrow) and sheets (right ROI, green arrow). Scale bars are 2 µm.

Though the ER fragmentation is well documented, the protein machinery behind the process remains largely unknown. The ER transformations have been long linked to the surface density of arc-liked RTNs promoting membrane curvature[4]. *In vitro* reconstitution of Yop1 and Rtnl1 into lipid vesicles generated tubular membrane structures (Fig. 2.3 c) and led to the formation of significantly smaller vesicles compared to the control ones[59]. Although this observation suggests that curvature activity by arc-like scaffolds might trigger membrane fragmentation, we cannot rule out the possibility that fragmentation occurs due to extremely high protein/lipid ratios (1 to 10) used in the reconstitution experiments[59]. However, other experimental observations and computational analysis also pointed to the involvement of RTNs in membrane fragmentation. The fam134 reticulon protein (FAM134) binds to the autophagy-specific proteins, such as microtubule-associated proteins 1A/1B light chain 3B (LC3) and GABA Type A Receptor-Associated Protein (GABARAP), inducing selective ER-phagy through membrane fragmentation[50,51,90]. Overexpression of these proteins resulted in complete fragmentation of the ER network[50,51,90]. Further indications of RTNs involvement in the ER fragmentation have come from the *in vitro* reconstruction of the tubular ER network[10].

2.1.3 Reconstitution of the ER network formation and fragmentation *in vitro*

Reconstruction of a membranous ER-like network with a few purified ER proteins reconstituted into lipid vesicles was successfully performed only recently by the group of Tom Rapoport[10]. The ingredients used for the reconstitution were the ER curvature-stabilizing proteins (such as RTNs and/or proteins containing the RHD) and the Atl fusion GTPases, including Atl from *Drosophila melanogaster* or its yeast homolog named Synthetic enhancer of Yop1p (Sey1p)[10,60] (Fig. 2.6). The network formed spontaneously upon mixing proteo-lipid vesicles in the presence of GTP. With the Sey1p fusogen, the presence of RTNs in the vesicles was found critical for the network formation. The RTN-driven curvature was needed to direct the vesicle fusion into tubules and stabilize the curved structures found at the ER periphery, specially at the newly formed TWJs, as we explain below. With *Drosophila* Atl, however, the network formed without

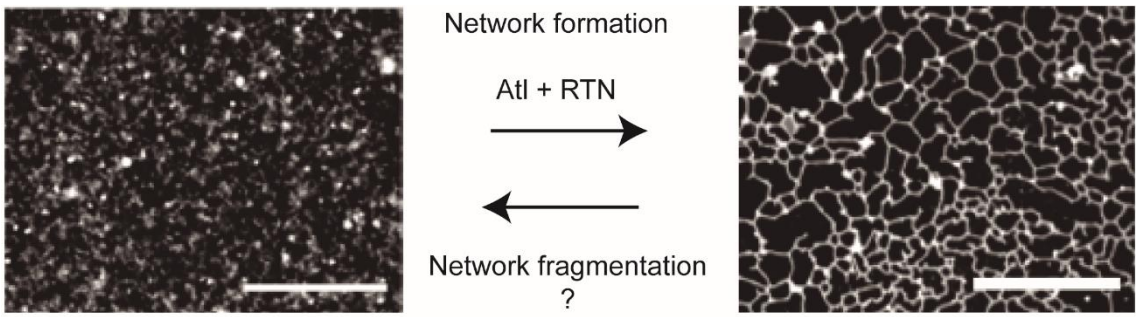

Figure 2.6. *In vitro* reconstitution of an ER-like membranous network. The fluorescence snapshot at the left shows the initial material for the reconstitution, the proteo-liposomes containing Sey1p (the fusogenic protein) and Yop1p (the RHD-containing protein). The right image shows the resulting interconnected membranous network through TWJs produced by proteo-liposomes incubation with GTP. Interestingly, the transition is reversible upon GTP removal (from right to left image), suggesting an embedded ER fragmentation mechanism based in the action of curvature-stabilizing proteins. Scale bars are 20 µm. Adapted by permission from Springer, Nature, "Reconstitution of the tubular endoplasmic reticulum network with purified components"[10], Powers et al. 2017,Copyright (2017).

the addition of RHD[10]. This finding led the authors to speculate on the bimodal functionality of Atl, which was proposed to be involved both in generating membrane curvature and in mediating membrane fusion[10].

Regardless of the protein composition, large ER-mimetic networks could be formed (Figure 2.6, right). Such a network provides an ideal model for further studies of dynamic regulation of ER shape and, specifically, of the mechanisms of ER fragmentation. As *in vivo*, the ER-mimetic network underwent fragmentation upon suppression of GTPase activity of the fusogen protein. As GTP is required for the membrane tethering activity of Atl and Sey1p[91,92], the fragmentation was associated with disruption of TWJ involving only membrane tethering but not fusion[69]. However, as the ER lumen is continuous throughout the tubular network, the cellular TWJ shall mainly support luminal connectivity and hence involve membrane fusion. The ER fragmentation in the cell is likely driven by specialized protein machinery operating in coordination with the fusogenic activity of Atl or Sey1p. The whereabouts of such machinery remain unknown.

2.1.4 Possible mechanisms and molecular machinery driving the ER fragmentation

If not via membrane detachment at TWJ, the network fragmentation would require scission of the tubular branches, the process known to demand the

creation of extremely high membrane curvatures[93]. Importantly, the ER-mimetic networks have a substantial amount of RHD proteins incorporated[10], and these proteins could generate extremely high membrane local curvatures[59]. Hence, the fission might be triggered by the local accumulation of RHD proteins. They might also operate in concert with other curvature-generating processes in the ER network. Such an example we can find in the members of the Bin-Amphiphysin-Rvs (BAR) domain family, in particular, in the member of such family called endophilin.

Endophilin has several well-defined functions, from recruitment of endocytic proteins via its SRC Homology 3 (SH3) domain to scaffolding and membrane deformation similar to that shown by Rtnl1. The link between generation of membrane curvature and membrane scission in clathrin-independent endocytosis was found for endophilin A2 (EndoA2). The membrane fission by EndoA2 was suggested to occur due to two main factors: the formation of EndoA2 scaffolds imposing its intrinsic curvature to the surrounded membrane and the influence of membrane traction forces[94]. The mechanism of membrane fission by EndoA2 was further analyzed *in vitro*[95]. The experiments carried out in that study demonstrated how intracellular components involved in membrane pulling by traction forces create a frictional barrier to lipid diffusion leading to membrane ruptures[95] (Fig. 2.7 a). Interestingly, membrane pulling did not result in the increment of the frictional barrier in the absence of endoA2 scaffolds, suggesting that the intrinsically curved scaffolds of endoA2, and potentially others as well, are directly involved in preventing lipid movement within the membrane upon coupling to membrane dynamics[95].

By analogy to endoA2, Rtnl1 could mediate membrane fission through additional force input coming from the Rtnl1 scaffolding, which induces membrane curvature and influences membrane dynamics (Fig. 2.7 b). Indeed, fluorescence visualization of both fusion and fission processes *in vivo* linked these two processes to membrane mobility through membrane extensions/retractions[34]. Hence, the sum of curvature sensing and creation by Rtnl1 and lipid mobility could constitute the core of the tubular ER scission mechanism. Moreover, the additional force applied during NT elongation, coupled

to the steady-state force of an ER tubule, would lead to higher membrane stresses and consequent membrane fission.

The steady-state force of the ER tubule can be explained through membrane tension. The retraction of individual nascent ER branches is constantly happening in the living tubular ER[34], indicating lateral membrane tension as the retraction force[96]. Tensile forces in the ER were measured using optical tweezers on *in vitro* membrane network reconstructions obtained from chicken embryo fibroblasts purified components[97]. To form the networks, the isolated components were enriched in molecular motors, such as dynein and kinesin, and incubated in the presence of ATP to promote the formation of an interconnected membrane network. Tensile force values of 18.6 ± 2.8 pN were measured when mimicking the network growth phase via molecular motors by pulling membrane nanotubes (NTs) from the existing ER branches with an optically trapped bead[97]. When the bead was released from the optical trap, the NT was rapidly snapped back to the network´s reservoir membrane, confirming that the ER tubules are under tension. In the cylindrical membrane geometry, tension operates as a constriction factor. The radius of a membrane tube (R_{NT}) pulled from a lipid membrane reservoir is reversely proportional to the tension

$$R_{NT} = \sqrt{k/\sigma} \qquad \text{(Eq. 2.1)}$$

where k is the bending rigidity modulus, and σ is the lateral tension of the reservoir membrane[93]. Hence, the tension could operate in concert with RTN in constriction of the ER tubules.

But, where does ER tension come from? The answer is pretty complex. On one side, ER has a pool of attached lipid droplets, the storage of cellular lipids. Such droplets can be considered oil lenses in the membrane, working as lipid solvent and thus setting the membrane tension[98]. On the other hand, the ER has many attachment points through MCS with other organelles[99]. Finally, the constant interaction of the ER with the cytoskeleton has a major contribution to ER membrane tension[100]. All these parameters sum up to define the ER membrane mechanical parameters for membrane remodeling events (Fig. 2.7 b).

Taking all of the about into account, this thesis project aims at unraveling the specific mechanisms controlling ER network fragmentation considering the possible involvement of RTNs and the ER membrane tension in the process (Fig. 2.7 b).

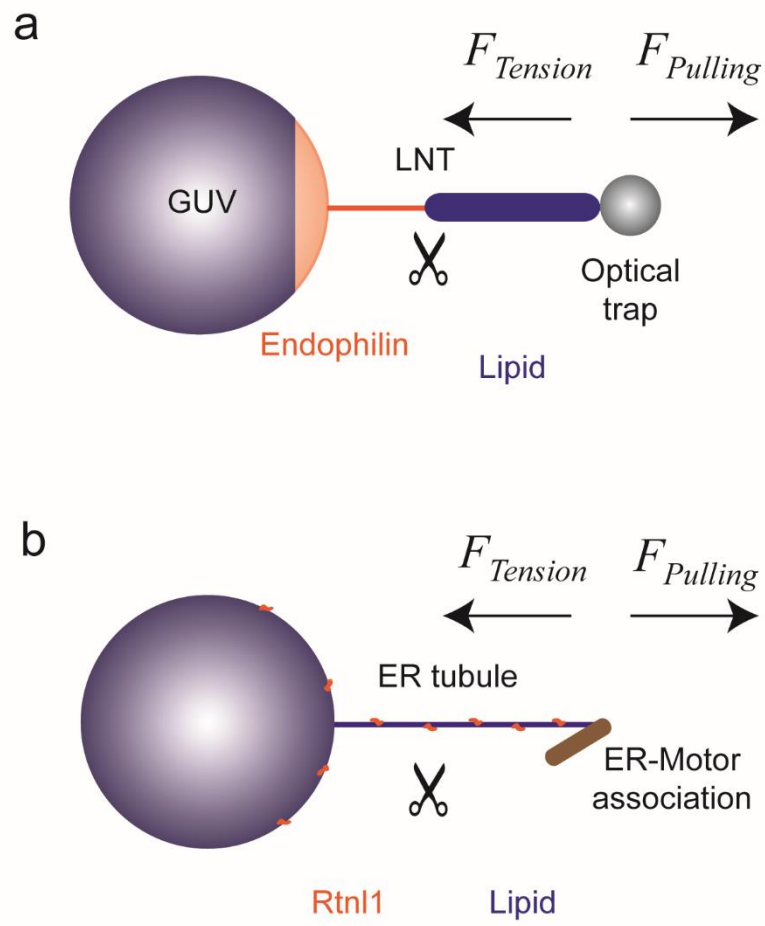

Figure 2.7. Comparison between endoA2-driven membrane fission and the hypothetical mechanism of RTN-mediated membrane fission in the ER tubules (a) Schematic representation of the *in vitro* experimental design in[95], showing the coupling of curvature creation with pulling forces leading to membrane fission. **(b) Hypothetical mechanism** of Rtnl1-driven membrane fission upon coupling to intrinsic ER membrane dynamics. The curvature of the ER tubules shaped by RTN (*Drosophila* Rtnl1) has a dynamic component related to the tensile force acting along the tubule axis. The force constricts the tubule acting synergistically with RTNs and helping to bring the curvature close to the values associated with spontaneous membrane fission[93]

2.2 Problem statement and objectives

To dissect the mechanism of the ER fragmentation, we first needed to identify the suitable model systems. *Drosophila melanogaster* seems to be the best candidate to test antagonistic interactions between ER proteins involved in the generation and the rupture of the network. It has only one functional gene for Atl (*atl*) and for RTN (*Rtln1*), which are in genetic and functional balance among them. In collaboration with Dr. Andrea Daga group (Univ. of Padova, Italy), the experts in *Drosophila* genetics, we planned to test genetical and functional relations between Atl and Rtnl1 *in vivo*, in cellular expression systems, and *in vitro*, via quantitative reconstitution of the proteins into membrane vesicles and tubes. Based on the sum of experimental observations reviewed above, we hypothesize that **Rtnl1 mediates ER membrane fission**. Besides, **Rtnl1 needs additional force input to do fission (Fig. 2.7b)**, as the curvature induced by Rtnl1 *in vitro* has never been directly resolved into membrane fission. Finally, we hypothesize **a dynamic balance between Atl induced fusion and Rtnl1 induced fission** which controls the ER morphology.

Considering the above hypotheses, we will pursue the following specific goals:

1. Confirm the role of Rtnl1 in ER membrane fission in cells
2. Reconstitute the Rtnl1 into membrane tubules *in vitro*
3. Identify the possible force and mechanical switches that transform Rtnl1 into a fission protein
4. Investigate how Atl and Rtnl1 create and maintain a tubular membrane network

2.3 Results and discussion

2.3.1 Functional and genetic interactions between Atl and Rtnl1

We start by describing the analysis of the genetic interaction between *Reticulon* and *atlastin* genes in *Drosophila melanogaster* obtained in collaboration with Dr. Andrea Daga´s group. They found a robust interaction between the two genes. The homozygous *Rtnl1*^{1}-null *Drosophila melanogaster* flies are viable and normal, while homozygous *atl*^{2}-null individuals die at the pupa stage with a 2% rate of escapers (Fig. 2.8 a). Combining these two null mutations in homozygosity resulted in an 84% adult survival rate (Fig. 2.8 a). Thus, the removal of *Rtnl1*^{1} substantially mitigates the lethality associated with depletion of *atl*^{2}, indicating antagonistic interaction between *atlastin* and *Reticulon* genes in *Drosophila*.

Further 3D-reconstruction of the ER network of individual neuronal cells from *Drosophila* brains by electron tomography (ET) revealed that in *atl*^{2}-null neurons, the ER periphery appeared disconnected (Fig.2.8 b), supporting previous observations of ER fragmentation following the loss of *atlastin*[70]. Remarkably, deletion of *Rtnl1*^{1} in the *atl*^{2}-null background restored a normal ER structure similar to the control neurons, with interconnected tubular and sheet-like elements (Fig.2.8 b). The fact that the removal of *Rtnl1*^{1} in the *atl*^{2}-null cells resulted in viable individuals with normal ER morphology strongly suggests that Rtnl1 is the driving force behind the morphological changes and fragmentation of the ER caused by loss of fusogenic activity of Atl. Furthermore, this dataset indicates that a balance of the Atl and Rtnl1 activities would be required not only for the maintenance of the ER architecture but also for the organism´s survival.

Quantitative EM-based analysis of *Rtnl1*^{1} mutant neurons showed elongated ER profiles, as previously reported for a different cell type[101] (Fig. 2.8 c, d). Of note, the ER profile of Rtnl1 overexpression in the wild-type (WT) cells resulted in reduced profile length (Fig. 2.8 c, d). EM-analyses further showed that this length reduction was typically compensated by Atl activity. The profile length was substantially shortened in neurons lacking *atl*^{2}, indicating that loss of *atl*^{2} or *Rtnl1*^{1} alters the profile length in the opposite direction. These results confirm that Atl counteracts the reduction in ER profile length mediated by either endogenous

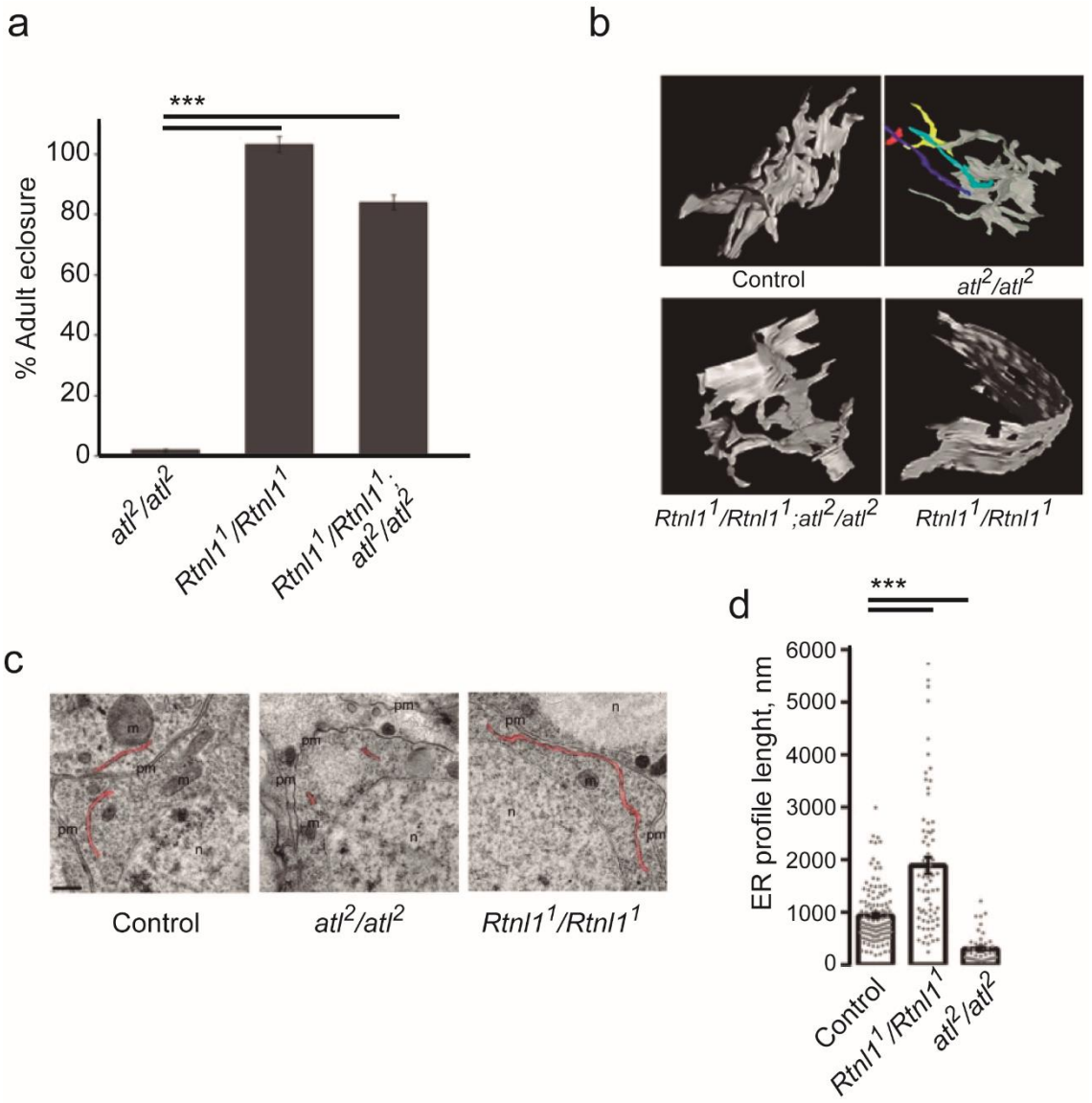

Figure 2.8. Genetic and functional antagonism between *Rtnl1* and *atlastin* in *Drosophila melanogaster* leads to morphological alterations of the ER. (a) The histogram displays the percentage of surviving adults, expressed as the ratio of observed over expected individuals, for the indicated genotypes (n = 3 independent experiments, statistical significance: unpaired two-tailed *t* test, ***$p < 0.001$; error bars represent SEM). **(b)** EM tomography-based 3D reconstruction of portions of the ER network from neurons of the indicated genotypes. ER elements not connected are shown in color. Scale bar is 200 nm. **(c)** Representative EM images of ventral ganglion neuronal bodies of the indicated genotypes highlighting ER profiles in red. Scale bar is 0.5 µm (pm = plasma membrane; m = mitochondria; n = nucleus). **(d)** Average length of ER profiles measured on thin EM sections shown in **(c)** (n > 100 ER profiles). Statistical significance: unpaired two-tailed *t* test, ***$p < 0.001$. Error bars represent SEM.

or transgenic Rtnl1 and that the ratio of Atl/Rtnl1 controls ER profile length, a parameter that can thus be used as a measure of functional antagonism between Rtnl1 and Atl *in vivo*.

2.3.2 Rtnl1 mediates constriction of ER tubules *in vivo*

The ER transformations seen upon genetic manipulations in *Drosophila* corroborate our hypothesis that Rtnl1 has a role in ER membrane fragmentation. To detect individual fragmentation events, we resorted to fluorescence microscopy observations of the ER network in COS-7 cells expressing Rtnl1. COS-7 cells with their widely spread tubular ER network provide a convenient and typically used model to study real-time ER membrane dynamics.

One of the main limitations to interpret the data from protein overexpression is the difficulty in assessing the extent of protein expression to a specific cellular phenotype. Thus, in collaboration with Dr. Daga´s group, we applied a pcDNA3 plasmid with two cytomegalovirus transcription units, one with a vector with a targeting construct for nuclear Cyan Fluorescent Protein (CFP) and another one for WT Rtnl1. This way, we could quantify the extent of Rtnl1 overexpression in the ER by measuring the CFP fluorescence signal from the nucleus. Additionally, we used a pcDNA3 plasmid for mammalian expression of monomeric Green Fluorescent Protein (mGFP) Rtnl1 to further compare the effects of both constructs upon overexpression and to directly visualize if mGFP-Rtnl1 co-localize with the ER luminal marker mCherry KDEL endoplasmic reticulum protein retention receptor 2b (KDEL).

We detected that mGFP-Rtnl1 overexpression in COS-7 cells transformed the continuous ER network into bright, visibly disconnected spots (Fig. 2.9 a). By comparison with WT Rtnl1 construct, we found that the extent of such transformation was proportional to the amount of Rtnl1 in the cell, as assessed by the CFP reporter fluorescence from the nucleus (Fig. 2.9 b). However, due to the intrinsic resolution limits of conventional fluorescence microscopy, such a “fragmented” phenotype of the ER tubules could be attributed both to the tubular scission or to the high constriction of the tubules by Rntl1 completely expelling the luminal fluorescence marker mCherry-KDEL from the constricted parts of the network.

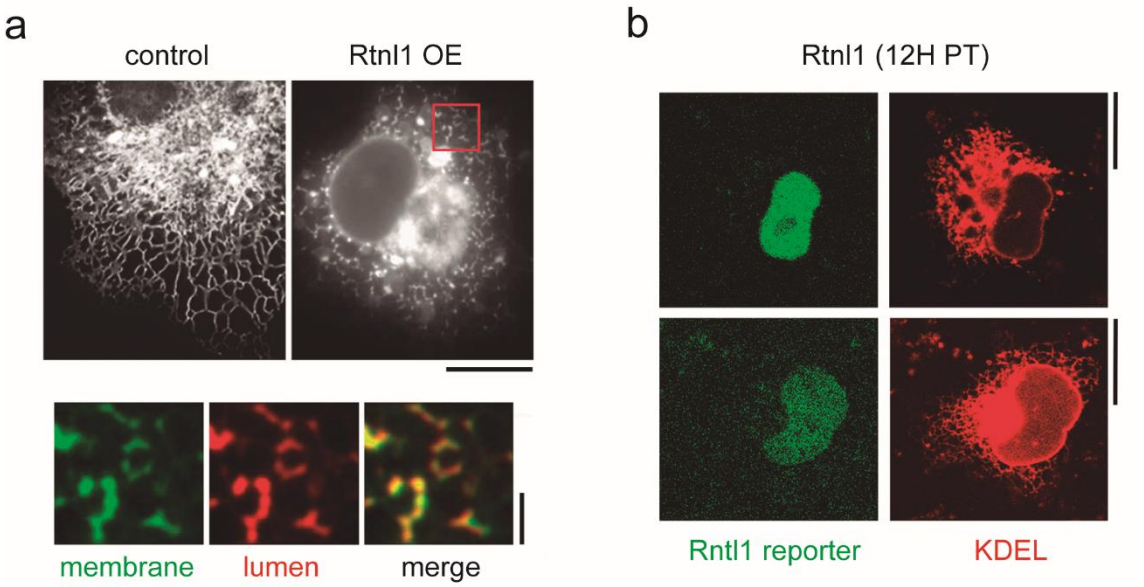

Figure 2.9. Constriction-driven fragmentation of the tubular ER network by Rtnl1. (a) Upper panel: ER network in control COS-7 cells (left) and in cells expressing mGFP-Rtnl1 at 24 hours post-transfection (right). mCherry-KDEL (ER luminal marker) fluorescence is shown. Scale bar 10 µm. Bottom panel: blow-up of the region marked with a red square in the upper right image. mGFP-Rtnl1 (membrane) and mCherry-KDEL (lumen) fluorescence is shown. Scale bars is 2 µm. **(b)** Comparison of cell phenotypes with high (top) and low (bottom) overexpression of WT Rtnl1 12 hours post-transfection. The CFP (nuclear marker, green) and mCherry-KDEL (ER lumen, red) fluorescence is shown. Scale bar is 5 µm.

ER transformation became visible as early as 12 h post-transfection (Fig. 2.9 b, 2.10) when the tubular network was still visible and dynamic. This transformation switched to the fragmented-like state at 17-24 h post-transfection (Fig. 2.10). However, we noticed that when mGFP-Rtnl1 was overexpressed, the resultant phenotype was significantly less fragmented compared to the phenotype upon WT Rtnl1 overexpression (Fig. 2.10). Thus, attachment of a mGFP tag to Rtnl1 likely impairs its membrane action compared with WT Rtnl1.

The dependence of the Rtnl1-driven ER fragmentation on the Rtnl1 amount in the cell (Fig. 2.9b) and on the presence of the mGFP tag (Fig. 2.10 b) confirms that the Rtnl1-driven constriction of the ER tubes depends upon the intrinsic curvature activity and amount of Rtnl1 in the ER. These data are in agreement with the ER transformation phenotypes described for other RTNs[58,59]. To obtain further insight into the mechanism of the fragmentation, we applied live-cell imaging.

2.3.3 Observation of Rtnl1-driven membrane fission of ER tubules

Based on the timing of the ER fragmentation (Fig. 2.10), we performed live-cell observations of ER in COS-7 cells at 12 h post-transfection with Rtln1. We detected scission-like events with individual ER tubules breaking near their ends and in their middle part (Fig. 2.11 a, red arrow). The scission led to the rapid retraction of the broken tubules (Fig. 2.11). However, the nascent ER tubules are highly dynamic and could undergo stretching/retraction cycles (Fig. 2.11 b. lower panel) prior to getting fully incorporated into the tubular network via the formation of a stable TWJ (see Fig. 2.2 and 2.5). To avoid scoring the tubule retraction not related to scission, we considered only those events that began with a localized constriction of a stable ER branch, followed by the snapping of two separated parts of the branch in opposite directions (Fig. 2.11 b, upper panel). The criteria we introduced for the detection of ER fission events could lead to underestimation

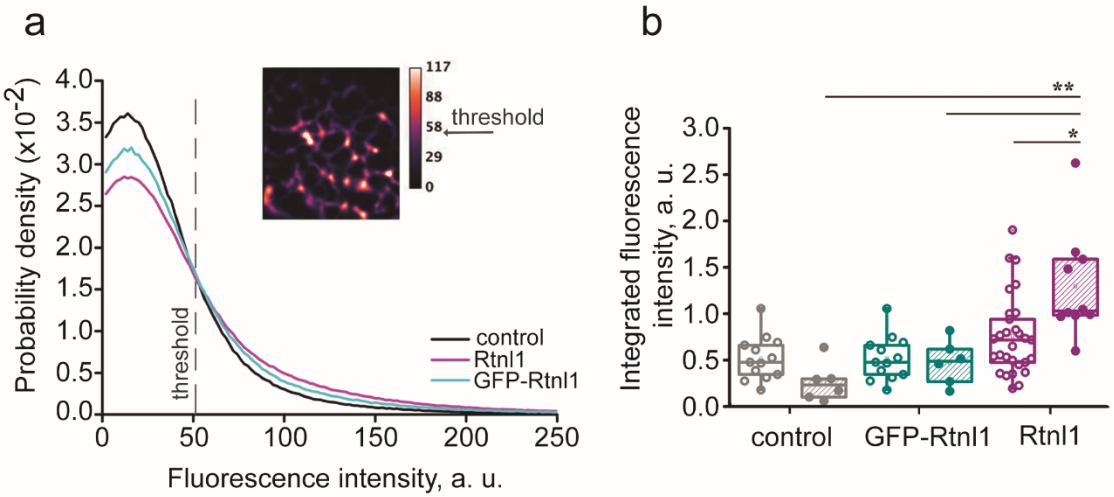

Figure 2.10. Progression from normal to constricted state in the peripheral ER begins as soon as 12 hours after transfection. (a) Probability density of mCherry-KDEL fluorescence intensity per pixel measured at 12 h post-transfection in COS-7 cells at different conditions in randomly selected ROIs covering the peripheral ER. Low intensities (below threshold) correspond to the tubular ER network, whereas high intensities (above threshold) correspond to the bright fluorescent punctae resultant from ER constriction by Rtnl1. The inset shows ER regions 24 hours post-transfection where the fluorescence is below (connected tubules) and above (puncta due to constriction or fission) the threshold. The threshold was calculated by determining the crossing point of the fluorescence profiles within the three conditions. **(b)** ER constriction measured as the integral increase in fluorescence intensity above the threshold (shown in **(a)**). 12h and 17h post-transfection are shown as empty and dashed boxes, respectively. The tested conditions are: control mCherry-KDEL (grey, n=13 cells at 12h post-transfection and n=5 cells at 17h post-transfection), mGFP-Rtnl1+mCherry-KDEL (cyan, n=8 cells at 12h pots-transfection and n=6 cells at 17h post-transfection) and Rtnl1+mCherry-KDEL (purple, n=12 cells at 12h post-transfection and n=8 cells at 17h post-transfection) cells.

of the true extent of fission in the ER. For example, one of the two separate parts of the branch would not snap in the opposite direction after scission if it is attached to another cytoskeleton component. Nevertheless, we could systematically score the fission events upon Rtnl1 overexpression.

Importantly, our results of membrane scission occurring in visibly transforming parts of the ER network indicated the involvement of axial forces and dynamic membrane stress. These force factors are intrinsic to actively remodeling, dynamic regions of the peripheral ER network[102], where Rtnl1-driven fragmentation is most evident (Fig. 2.9). As we hypothesized earlier (Fig. 2.7), the axial forces contribute to the constriction of membrane tubules and hence facilitates the creation of the membrane curvature by Rtnl1. However, overexpression of Rtnl1 also caused a significant deceleration in the retraction of detached ER branches (Fig. 2.11 c), consistent with stabilization of tubular ER

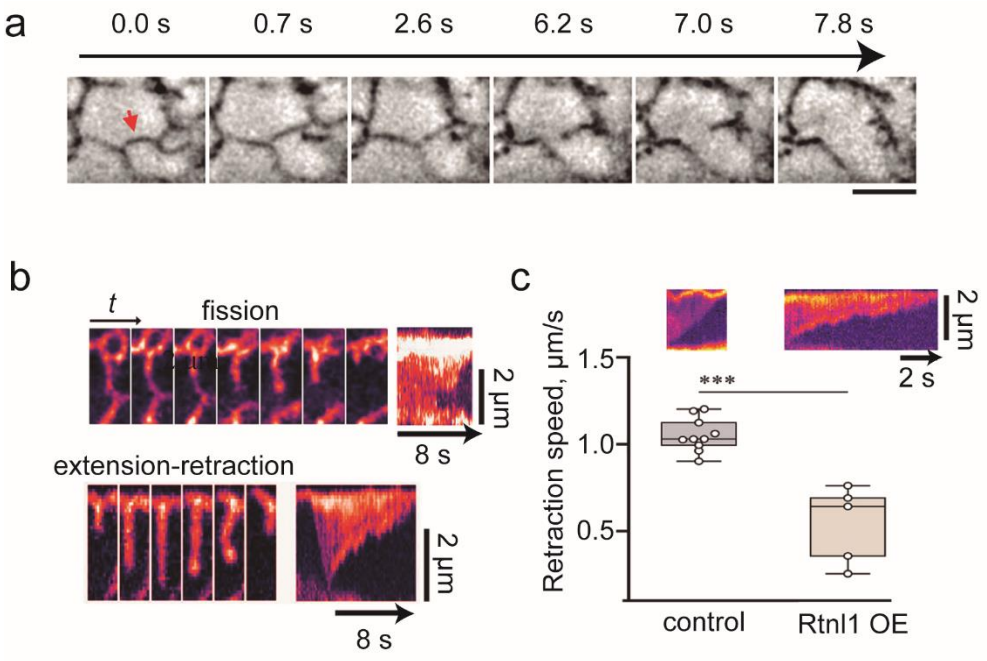

Figure 2.11. Real-time observation of Rtnl1-driven fission of tubular ER branches. (a) Image sequence showing membrane cleavage (red arrow) of an ER branch in a Rtnl1-expressing COS-7 cell. Scale bar 2 µm. **(b)** Image sequences showing fission (upper sequence, corresponding to that shown in (a)) and transient extension/contraction (lower sequence) of the ER branch. The sequences are followed by the corresponding kymographs. The pseudocolor plot highlights the local constriction that precedes membrane fission. **(c)** Kymographs showing retraction of ER branches in control (n = 10 branches) and Rtnl1-expressing (n = 5 branches) cells. Box plot shows retraction velocity of branches. Statistical significance: unpaired two-tailed t-test, ***$p < 0.001$. Box plots show IQR, whiskers show minimum and maximum of the dataset.

branches by Rtnl1. The stabilization is apparently inconsistent with the direct involvement of Rtnl1 in membrane scission. To untangle this apparent contradiction, we relied on the reconstitution of the process in a minimal *in vitro* system.

2.3.4 Reconstitution of purified Rtnl1 into lipid membrane templates

To resolve the aforementioned issue, we reconstituted purified WT Rtnl1 and mGFP-Rtnl1 into lipid NTs, thus mimicking dynamic ER branches. To this end, we first reconstituted the purified protein into large unilamellar vesicles (LUVs) to generate Rtnl1 proteo-liposomes. Although several methods are available nowadays for this purpose, we opted for a detergent-assisted protein insertion procedure often called co-micellization[63,103] (see Materials and methods: Atl, Rtnl1 and mGFP-Rtnl1 reconstitution into LUVs). Upon reconstitution, we first confirmed the successful membrane insertion of WT Rtnl1 and mGFP-Rtnl1 into LUVs by a density-based flotation assay (Fig. 2.12), followed by sodium dodecyl sulphate-polyacrylamide gel electrophoresis (SDS-PAGE) analysis of the fractions (See Materials and methods: Determination of reconstitution efficiency on Rtnl1 and Atl proteo-liposomes; Fig. 2.12). The coexistence of each protein and fluorescently labeled LUVs with 1,2-dioleoyl-sn-glycero-3-phophoethanolamine-N-(lissamine rhodamine B sulfonyl) (Rh-DOPE) in the gradient was adopted as the proof of successful protein reconstitution in the proteo-liposomes. For that, upon centrifugation, we measured the fluorescence intensity of the collected fractions for each preparation of proteo-liposomes (Fig. 2.12 a). Once we determined which fractions of the flotation assay contain the membranes, we ran an SDS-PAGE analysis to confirm the presence of protein in the fluorescent fractions (Fig. 2.12 b).

We then followed a recently developed protocol for the formation of giant supported bilayers (GSBs)[104], which consists in the rehydration of previously dehydrated proteo-liposomes over silica beads. Dehydration and rehydration of the proteo-liposomes were performed in the presence of the sugar trehalose (TRH), a natural protectant of membrane´s and proteins´ structure[105]. Upon rehydration, we obtained the proteo-GSBs. The proteo-GSBs were perfused with

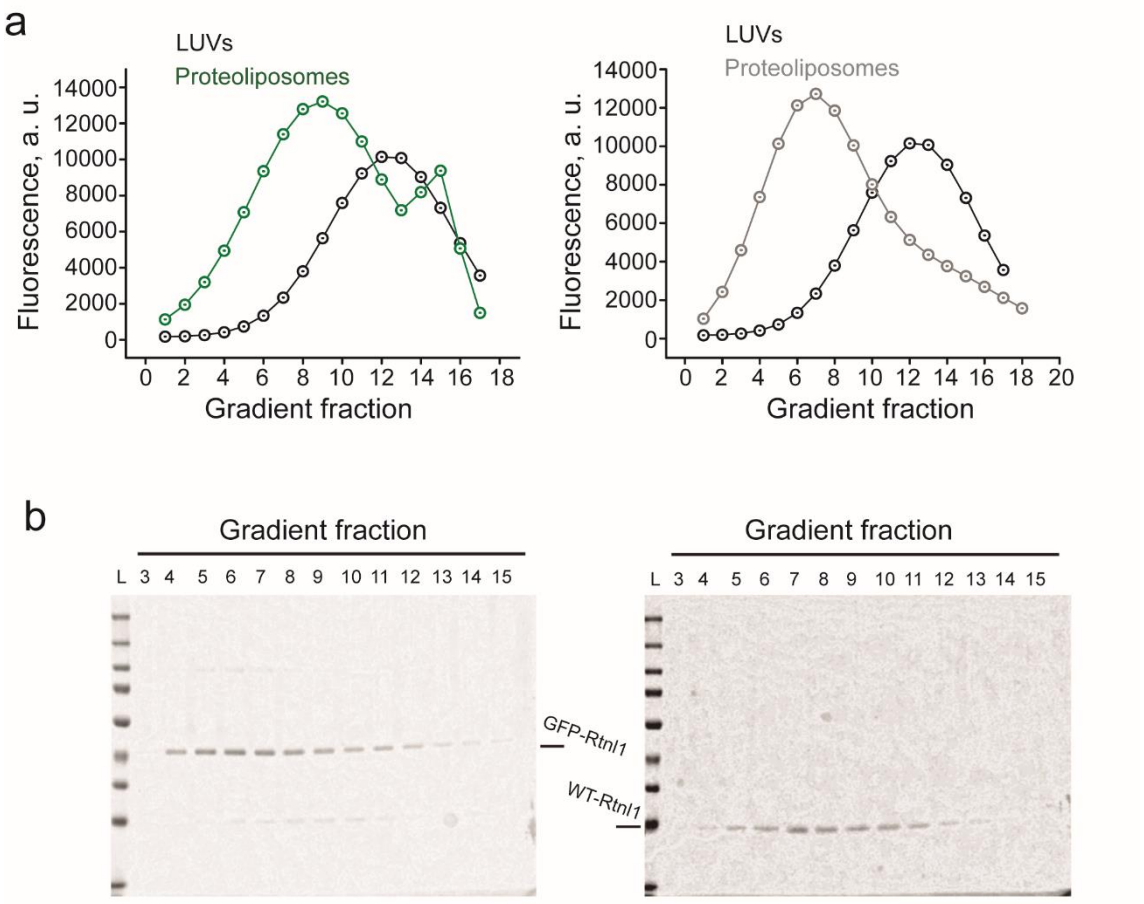

Figure 2.12. WT Rtnl1 and mGFP-Rtnl1 reconstitution in LUVs. (a) Lipid fluorescence intensity measured in the fractions collected upon the density-based flotation assay of mGFP-Rtnl1 (left plot, green curve) and WT Rtnl1 (right plot, gray curve) proteo-liposomes. Each population of proteo-liposomes is compared with the control LUVs without reconstituted protein (right and left plots, black curves). **(b)** SDS-PAGE gels show the presence of mGFP-Rtnl1 (left gel) and WT Rtnl1 (right gel) in the fluorescent fractions of the flotation assay containing the proteo-liposomes shown in **(a)**. The LUVs´ lipid composition is DOPE:DOPC:DOPS:Chol:Rh-DOPE 40:39:10:10:1 mol%.

the working buffer as described in Materials and methods (Formation of GSBs on silica and polystyrene beads). Importantly, upon proteo-GSB formation, mGFP-Rtnl1 fluorescence was uniformly distributed on the GSB´s membrane (Fig. 2.13), confirming the successful incorporation of Rtnl1 into the proteo-GSBs.

The proteo-GSBs doped with traces of biotin-PC were further used as the parent membrane to form the NTs, extended from the GSBs by pulling with a streptavidin-covered (STA) bead either 1) suctioned into the tip of a micropipette controlled by a micromanipulator or 2) trapped by optical tweezers, as described in Materials and methods (in collaboration with Dr. Borja Ibarra lab, IMDEA,

Madrid, see Fig. 5.6). This way, we could obtain the proteo-lipid NTs, mimicking the ER branches of COS-7 cells expressing Rtln1. Furthermore, we could change the NT length, thus imitating the extension/retraction cycles of the ER branches and measure the associated axial forces and changes in the NT curvature.

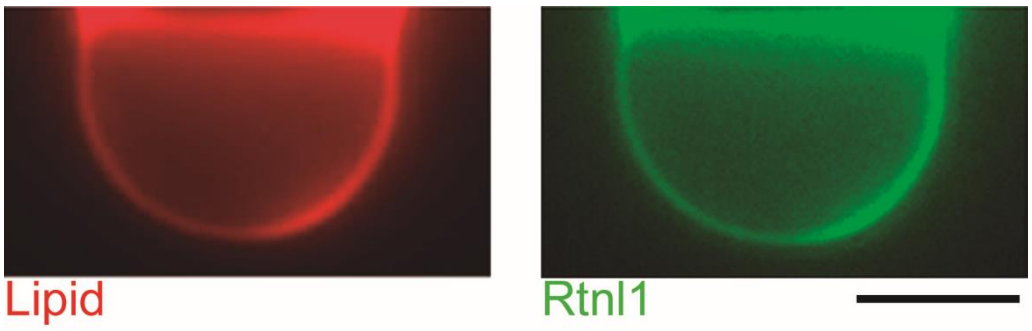

Figure 2.13. Rtnl1 incorporation into GSBs was confirmed by direct visualization with fluorescence microscopy. The fluorescence micrographs show a proteo-GSB observed in the Rh channel (red, Rh-DOPE) and mGFP channel (green, mGFP-Rtnl1). The lipid composition is DOPE:DOPC:DOPS:Chol:Rh-DOPE 40:39:10:10:1 mol%. Scale bar is 5 µm.

The NT produced from the GSB reservoir are under substantial lateral tension determined by the amount of lipids deposited on the silica bead [104]. As the amount of lipids in the reservoir is much higher than in the NT, the tension remains constant during the NT extension/contraction. The tension defines the stationary radius of the NT (see Eq. 2.1 in the introduction). To mimic the curvature of the ER tubules (20-40nm diameter)[59,97], we systematically varied the amount of lipids on the silica bead to obtain the NTs of similar curvature. The procedure was repeated for each new lipid composition, as for pure lipid vesicles as for the proteo-liposomes, to facilitate the discrimination of the lipid and Rtnl1 effects on the NT curvature and stability.

2.3.4.1 Static membrane constriction and curvature sensing by Rtnl1

We began from the analysis of the RTnl1 effect on the stationary curvature of the proteo-lipid NT. The incorporation of mGFP-Rtnl1 into the NT could be monitored and quantified by fluorescence microscopy. The Rtnl1-containing NTs appeared non-uniform, with visibly constricted regions separated by vesicle-like membrane bulges (Fig. 2.14 a). We quantified the NT radius (R_{NT}) in the constricted regions using a fluorescence intensity calibration as previously

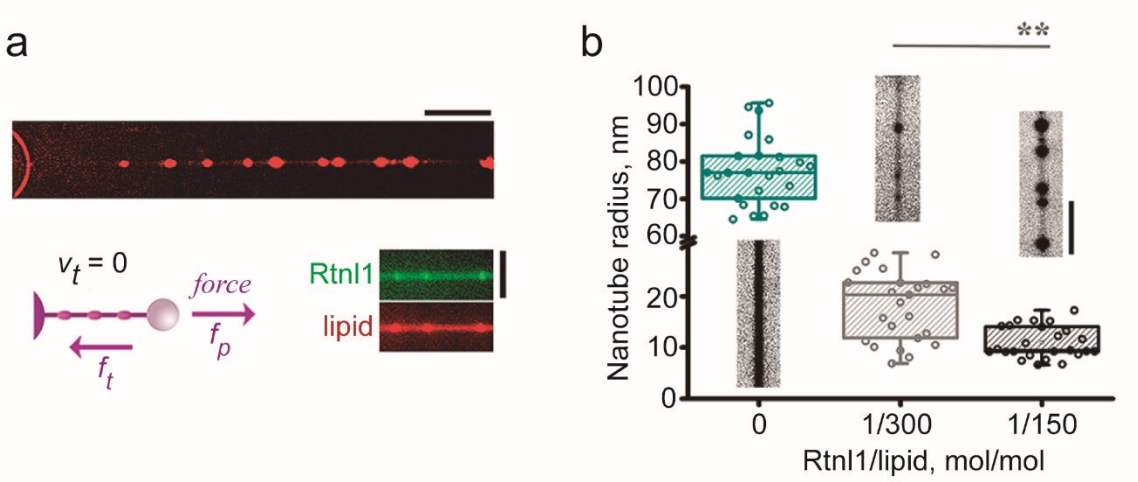

Figure 2.14. Rtnl1 produces static membrane curvature proportional to the protein concentration. (a) Representative image of Rtnl1-narrowed lipid NTs (Rh-DOPE fluorescence is shown) obtained at 1:150 Rtnl1/lipid ratio (mol/mol). Scale bar is 10 μm. The cartoon shows the static force balance $f_p = f_t$, where the pulling force (f_p) is equal to the tensile force (f_t). The inset shows the mGFP-Rtnl1 (green) incorporation into the NT (red) at 1:150 protein/lipid ratio. Scale bar is 2 μm. **(b)** Boxplots showing the radii of control NTs (n = 25 NTs) and NTs constricted by Rtnl1 at 1:300 (n = 25 NTs) and 1:150 (n = 25 NTs) protein/lipid ratio; 3 independent proteo-lipid preparations were used. The insets show the representative images of the NTs for each condition (Rh-DOPE fluorescence, scale bar 2 μm). Boxplots represent IQR, whiskers indicate minimum and maximum of the dataset. Statistical significance: unpaired two-tailed t test, **p < 0.01. The lipid composition is DOPE:DOPC:DOPS:Chol:Rh-DOPE 40:39:10:10:1 mol%.

described[104,106] (see Materials and methods: Radii quantification of NTs). Calculations revealed that Rtnl1 generated static membrane curvature ($1/R_{NT}$) in the range of 0.1-0.3 nm^{-1} proportional to protein concentration (Fig. 2.14 b), confirming the involvement of Rtnl1 in the membrane curvature´s generation in the NT. These curvature values are in good agreement with the ones previously measured in cells, where radii of 12-50 nm have been reported for the ER tubules [59,107–109]. In addition, the highest curvature measured at 1:150 Rtnl1/lipid ratio is consistent with that measured in cultured cells overexpressing RTN [59]. Importantly, we observed that at a higher Rtnl1/lipid ratio (1:80), pulling out the NT from the GSB membrane became completely impaired (12 of 12 cases), suggesting insurmountable viscous resistance of the membrane during NT pulling. This effect may be due to the large membrane RHD that completely spans the outer and, to some extent, the inner lipid leaflet, likely generating the viscous resistance, which is exacerbated by curvature-induced sorting and reticulon oligomerization[56]. Therefore, for further analysis, we used the protein/lipid ratio of

1:150, which showed the strongest membrane constriction in static NTs measurements.

The ratiometric comparison of mGFP-Rtnl1 fluorescence intensity in the reservoir and constricted portions of the NT revealed that Rtnl1 was accumulated in the constricted parts of the NT (Fig. 2.15 a). This curvature-driven sorting of Rtnl1 was coupled to the NT constriction (Fig. 2.15 b, 2.14 b). The constriction, in turn, was accompanied by a reduction in the axial tensile force (f_t, Fig. 2.15 c), indicating the NT stabilization against retraction to the GSB reservoir by Rtln1. This stabilization effect is consistent with the slower retraction of ER tubules observed upon Rtnl1 overexpression in COS-7 cells. This finding might also explain the Rtnl1-mediated inhibition of ER retraction upon prolonged microtubule depolymerization[56].

We further combined force and fluorescence datasets to calculate the mechanical parameters of the proteo-lipid NT. Pulling a tube from a pure lipid GSB reservoir requires a force more significant than the tensile force driving the NT retraction back to the reservoir. In the stationary situation, the force equals[110]:

$$f_t R_{NT} = 2\pi k \qquad (\text{Eq. } 2.2)$$

where f_t is the tensile force and R_{NT} and k are the NT radius and the bending rigidity modulus of the reservoir membrane, respectively (see Eq. 2.1). Upon the Rtnl1 incorporation into the reservoir, the Eq. 2.2 changes as:

$$f_t R_{NT} = 2\pi k_{eff} (1 - R_{NT} J_s) \qquad (\text{Eq. } 2.3)$$

where k_{eff} is the effective bending rigidity due to Rtnl1 curvature-driven sorting and J_s is the intrinsic curvature of the reservoir membrane. The incorporation of RHD into the curved NT membrane alleviates the curvature stress, effectively reducing the work of membrane bending. It follows that k_{eff} shall be significantly lower than k. At 1:150 protein:lipid ratio, J_s is negligible, explaining Rtnl1

incorporation into the relatively flat GSB membrane. The Eq. 2.3 can be rewritten as:

$$f_t R_{NT} \cong 2\pi k_{eff} \qquad \text{(Eq. 2.4)}$$

The ~6-fold decrease in $f_t R_{NT}$ (Fig. 2.15 d) reflects the dramatic reduction of the effective bending rigidity of the NT membrane due to curvature-induced sorting of Rtnl1[110,111]. We note the dynamic nature of the NT "softening" by Rtnl1. The softening effect is based upon the slow influx of Rtnl1 into the NT membrane (Fig. 2.15 c). The NT deformations faster than the characteristic time of the curvature-composition coupling are limited by the instant bending rigidity defined by lipid k. The slow deformations enabling for dynamic adjustment of the Rtnl1 concentration in the membrane are limited by the effective bending rigidity k_{eff}.

We conclude that membrane constriction in the static NT is driven by the accumulation of curved RHD of Rtnl1[90,112] in the NT membrane. The formation of Rtnl1 arc-like scaffolds upon Rtln1 sorting and accumulation in the tubular ER promotes the generation of membrane curvature and stabilizes the curved membrane architecture characteristic of the ER periphery[59]. At the 1:150 Rtnl1/lipid ratio, the static membrane curvature (Fig. 2.14 b) only approaches that associated with membrane fission (R_{NT} = 4-5nm)[3]. Further increase of the Rtnl1/lipid ratio interferes with the NT pulling, suggesting that high Rtnl1 incorporation would interfere with membrane dynamics in the ER. Indeed, we observed the slowing down of the ER branch dynamics by Rtnl1 in COS-7 cells (Fig. 2.11 c). Hence, instead of amassing Rtnl1 in the membrane, additional sources of membrane constrictions might account for the final curvature push causing instability and scission of Rtnl1-containing membrane tubules.

2.3.4.2 Combination of static Rtnl1 activity with membrane dynamics

The necessity of a final power-stroke-like action of the fission machinery has been documented earlier for Dyn1. High membrane constriction by static Dyn1 helices is insufficient to mediate membrane fission unless additional dynamic energy input is provided by the GTP hydrolysis [81,106,113]. We turned

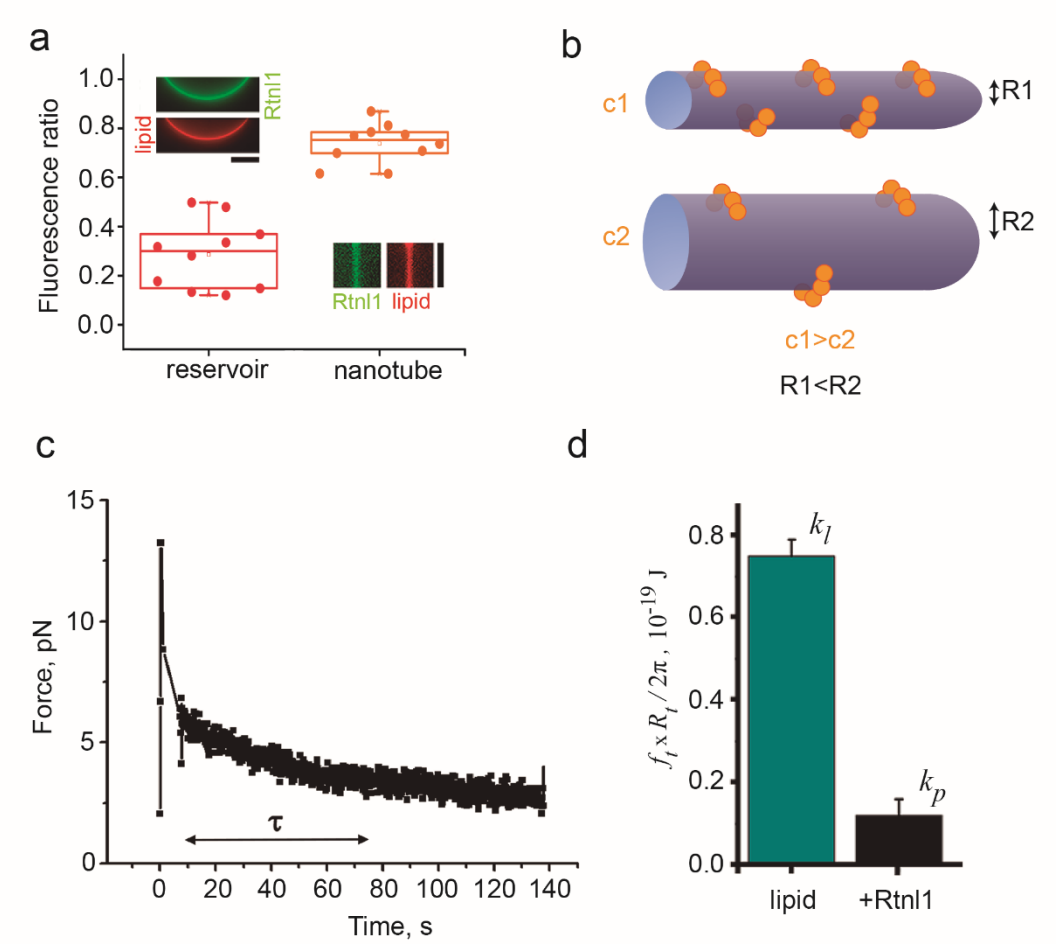

Figure 2.15. Stabilization of Rtnl1-containing NTs and reduction of effective bending rigidity by membrane curvature-driven Rtnl1 sorting. (a) Differential incorporation of mGFP-Rtnl1 into reservoir and NT membranes (n = 8 independent NT/reservoir pairs). Incorporation was measured as the ratio of mGFP-Rtnl1 to lipid (Rh-DOPE) fluorescence. Representative fluorescence microscopy images of the reservoir membrane and a constricted portion of the NT membrane used for the calculations are shown. Scale bars 4 μm. Statistical significance: unpaired two-tailed t test, **p < 0.01. **(b)** The cartoon illustrates how the accumulation of Rtnl1 in the NT promotes membrane constriction in a Rtnl1 concentration-dependent manner. **(c)** Kinetics of the axial force reduction upon a short stepwise stretch of the tube. The slow decrease (τ = 63.2 ± 8.7s) corresponds to the diffusional exchange of Rtnl1 between the NT and the reservoir ($D \sim L^2$ / τ ~10^{-9} cm^2 /s). **(d)** Rtln1 stabilization of constricted NTs (1:150 protein/lipid) measured as a decrease in $f_t R_{NT}$. The values of mean R_{NT} and f_t values are taken from fluorescence and force measurements, respectively: for lipid-only NTs R_{NT} = 77.4 ± 1.8 nm (n = 25), f_t = 6.9 ± 0.4 pN (n = 26); for Rtnl1-containing NTs R_{NT} = 10.9 ± 0.6 nm (n = 25), f_t = 7.6 ± 2.6 pN (n = 10), where n is the number of independently formed NTs and errors represent SEM. Error bars are SD (n = 25 tubes for lipid column, n = 10 tubes for +Rtnl1 column). The lipid composition is DOPE:DOPC:DOPS:Chol:Rh-DOPE 40:39:10:10:1 mol%.

towards the ER dynamics linked to the cytoskeleton activity observed *in vivo* as a possible fission cofactor for Rtln1-mediated fission. In this scenario, the additional force to rupture the membrane would be triggered by the coupling of

Rtnl1 curvature-driven sorting with membrane mobility. Therefore, the energy supply would also be derived from ATP hydrolysis, which is required for NT pulling by molecular motors.

Crucially, pulling at constant speed v_t resulted in a linear increase in NT curvature (Fig. 2.16 a) until it reached a plateau, while a similar time pattern was recorded for the pulling force (Fig. 2.16b). This behavior was not observed in the control experiments with purely lipid NTs (Fig. 2.16, cyan curves). The dynamics of the force growth are indicative of the frictional barrier for the NT pulling from the GSB reservoir[114]. During the initial growth state, the pulling force remains smaller than the friction resistance, and hence no material is retrieved from the GSB. The NT extension happens at a fixed membrane area, leading to the NT constriction requiring progressively higher puling force. The constriction dynamics is defined by the constancy of the NT area:

$$A = 2\pi R_{NT}(L_0 + v_t t) = 2\pi R_{NT}^0 L_0 \qquad (\text{Eq. } 2.5)$$

where R_{NT}^0 and L_0 are the radius and length of the NT before the extension, and t is time. For small L_0, $R_{NT} \sim const/t$. Substituting this into Eq. 2.4, we see that the pulling force indeed should increase linearly with time. At a certain point, the growing pulling force becomes comparable with the frictional drag so that additional lipid and protein material could be retrieved from the GSB reservoir. The balance of the pulling and the friction forces defines the constant force (plateau, Fig. 2.16 b) regime of the NT pulling.

Corroborating the viscous nature of the force increase during the NT elongation (Fig. 2.16 b), the plateau force increased with the velocity reaching 27.4 ± 3.9 pN at v_t = 0.1 μm/s and 62.1 ± 10.1 pN at v_t = 8 μm/s, comparable to forces reported for NTs pulled from the ER and Golgi membrane networks (20-40 pN)[97]. The simultaneous increase in curvature and force implies increased membrane stress, ultimately causing the NT scission[95] (Fig. 2.17 a, inset). As in COS-7 cells, the scission cut the NT into two parts snapping in the opposite directions (Fig. 2.17. a, inset). At v_t = 0.1 μm/s, nearly half of the NTs (15 of 32) ruptured at 32.4 ± 2.6 s after the onset of elongation, corresponding to an average

tube elongation of 3.2 μm before scission. Thus, *in vitro*, Rtnl1 causes NT fission at physiological tension, velocities, and forces normally found in the ER network[97].

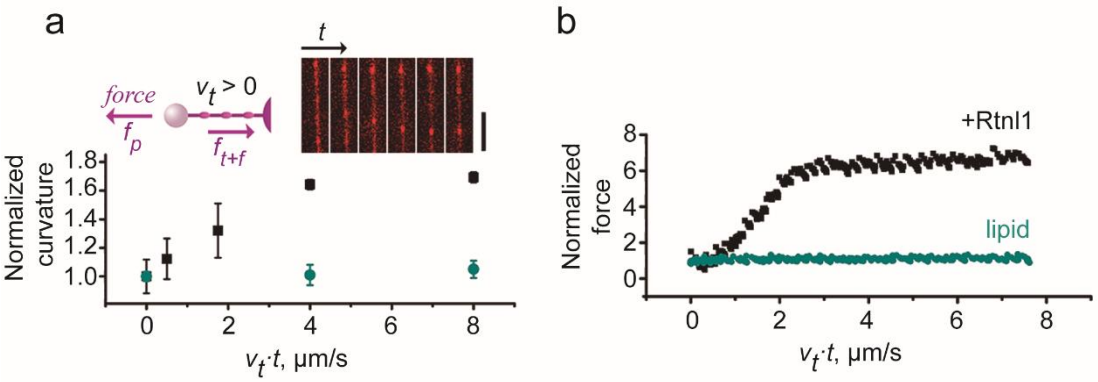

Figure 2.16. Simultaneous constriction and force increase during NT pulling leads to the increase in membrane stresses. (a) NT curvature values change (normalized to initial static values) upon pulling force application at a constant speed v_t on control (cyan, n = 3 NTs) and Rtnl1-containing (black, n = 3 NTs) NTs. Error bars represent SEM. Image sequence shows one NT ROI used for curvature calculations. Rh-DOPE fluorescence is shown. Scale bar 5 μm. The cartoon illustrates the dynamic force balance ($f_p = f_t + f_f$), where the pulling force is equal to the sum of the tensile (f_t) and frictional forces (f_f). **(b)** Increase in the pulling force (normalized to its initial static value) upon pulling control NTs (cyan, n = 3 NTs) and Rtnl1-containing NTs (black, n = 3 NTs) at constant velocity v_t, as measured by optical tweezers. Error bars represent SEM. The lipid composition is DOPE:DOPC:DOPS:Chol:Rh-DOPE 40:39:10:10:1 mol%.

As the plateau force, the curvature increase during the NT elongation depended on the pulling speed. In the fluorescence microscopy experiments, pulling at 20-30 μm/s caused an almost two-fold decrease of the NT radius (Fig. 2.17 b, red). The combination of this dynamic effect with the static constriction produced by Rtnl1 brings the NT curvature close to the threshold values associated with membrane hemifission[3] (Fig. 2.17 b). The reduction of the R_t can be also recalculated from the amplitude of the force during the initial linear growth phase[115] (Fig. 2.16b) using:

$$\Delta R_{NT} = 2\pi k \Delta(1/f) \qquad (\text{Eq. } 2.6)$$

The ΔR_{NT} calculated with the forces measured upon NT rupture (f) (Fig. 2.17 b, black) agreed with those measured directly by fluorescence microscopy (Fig. 2.17 b, red). Notably, the coupling of static and dynamic Rtnl1-driven

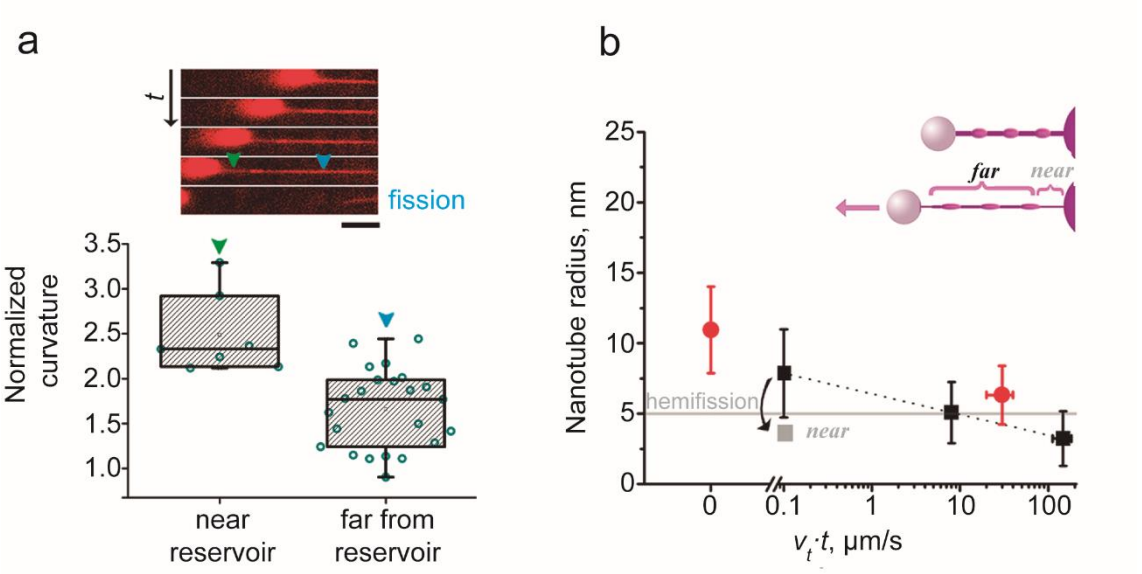

Figure 2.17. Rtnl1-driven constriction and fission of the elongating NTs. (a) Image sequence (100 ms/frame) showing Rtnl1 NT scission (arrow). Scale bar 2 μm. The histogram shows more prominent membrane curvature near the membrane reservoir on the pulling pipette (green arrow, n = 7 NTs) than NT curvature far from the reservoir (blue arrow, n = 20 NTs). The boxplots show IQR, whiskers indicate minimum and maximum of the dataset. **(b)** Radial constriction of the membrane NT measured by fluorescence microscopy (red, error bars show SD, n = 25 NTs for both static and dynamic constriction) and recalculated from the force increase using either k_l (black) or k_p (gray). The lipid composition is DOPE:DOPC:DOPS:Chol:Rh-DOPE 40:39:10:10:1 mol%.

membrane constriction was not homogeneous across the NT, as we found that local membrane constriction was more pronounced in the regions connecting the proteo-lipid NT to the reservoir (Fig. 2.17 a). The NT scission always happened in these regions. We associate the additional constriction with the diffusional influx of Rtnl1 into elongating NTs driven by the increasing curvature of the NTs. As shown above (Fig. 2.15 d), this curvature-composition coupling leads to reduction of k_{eff} facilitating the NT constriction. The k_{eff} reduction explains the NT fission at extremely slow elongation rates (Fig. 2.17 b, arrow). In the ER network, the dynamic incorporation of Rtnl1 into elongating tubules should facilitate their fission near membrane reservoirs, such as ER sheets, explaining their predominance in the late stages of Rtnl1 overexpression.

The static membrane curvature generated by mGFP-Rtnl1 was significantly smaller than that caused by the WT protein (Fig. 2.18, a). This finding is consistent with the lower occurrence of membrane fragmentation of tubular ER in COS-7 cells upon mGFP-Rtnl1 overexpression. Remarkably, *in vitro*, the

scission probability was also significantly higher for WT Rtnl1 than for mGFP-Rtnl1 when reconstituted at similar concentrations in the membrane (Fig. 2.18 b). Thus, we confirm that mGFP tag fused to Rtnl1 leads to a partial loss-of-function phenotype. A similar impairment of the *in vitro* and *in vivo* activities was previously reported for Yop1p upon modification of the N-terminal region of the protein [59]. We associated the functional impairment of mGFP-Rtnl1 with the downregulation of Rtnl1 self-assembly into curved structures of the membrane surface NTs (Fig. 2.18 a, cartoon).

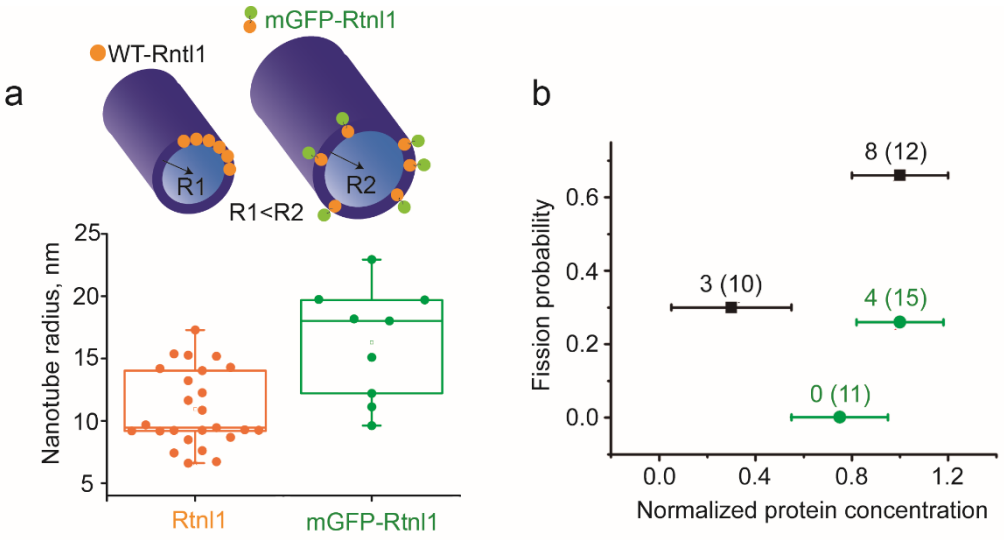

Figure 2.18. Membrane constriction and fission of NT with reconstituted WT Rtnl1 and mGFP-Rtnl1 (a) Static (v_t = 0) NT constriction by Rtnl1 (black, n=25 NTs) and mGFP-Rtnl1 (green, n=9 NTs). Boxplots show IQR, with whiskers at 1.5 IQR, square represents mean. **(b)** Fission probability at different membrane concentrations of WT Rtnl1 (WT Rtnl1) and mGFP-Rtnl1. The NTs were pulled at v_t = 20-30μm/s, the elongation length ΔL= 35 μm; the total number of NTs undergoing fission is indicated on the graph above each data point. The lipid composition is DOPE:DOPC:DOPS:Chol:Rh-DOPE 40:39:10:10:1 mol%.

Importantly, even significant increases in force measured during high-speed pulling (v_t above 100 μm/s) were insufficient to trigger fission of control lipid NTs[93]. High-speed pulling produced a similar increase in force in Rtnl1-containing and lipid-only NTs but did not cause scission in control NTs (in 21 of 21 cases), whereas it caused rupture in 12 of 12 proteo-lipid NTs. To directly compare the stress effect, we subjected lipid NTs to increased forces (above 30 pN) for the same time (0.74 ± 0.23 s) as Rtnl1 NTs were elongating at 8 μm/s. None of the 15 lipid tubes ruptured, whereas a 30% rupture rate was observed

for the proteo-lipid NTs. We concluded that the physical presence of Rtnl1 in the constricted NTs facilitates the scission.

To summarize, the mechanism of the membrane fission by Rtnl1 is based upon the following four key elements. First, Rtnl1 is a potent curvature creator producing and stabilizing highly bent membrane tubes (Fig. 2.14 b). Second, Rtnl1 senses membrane curvature and migrates towards membrane areas of high curvature (2.15 a). Third, the presence of the large membrane residing RHD of Rtnl1 in the membrane increases the membrane viscosity. Forth, in highly constricted membrane tubes Rtnl1 triggers membrane instability leading to the tube scission. The first three elements underlie the specific visco-elastic properties of membrane tubules containing Rtnl1. When such a tubule is pulled from a low-curved membrane reservoir (such as an ER sheet), Rtnl1-related viscous drag sets the pulling force threshold. If exceeding the tensile force, the pulling leads to substantial constriction of the tube (Fig. 2.16). The constriction, in turn, triggers additional recruitment of Rtnl1 due to dynamic curvature-composition coupling (Fig. 2.17 a). This self-enhanced membrane constriction process leads to progressive accumulation of the curvature stress causing membrane scission. Importantly, the constriction cascade depends on the Rtnl1 concentration in the reservoir membrane. Both the static constriction and the viscous drag are proportional to the concentration. As the scission relies on both the static and dynamic constriction, the scission probability becomes a function, likely very steep, of the Rtnl1 concentration. In the context of the ER network, the steep concentration dependence might explain the RTN bifunctionality in the ER network maintenance. At low concentrations, RTN predominantly stabilizes the ER tubules with rare fission events balanced by Atl-mediated membrane fusion. Upon increasing the RTN concentration above a threshold value, the scission function becomes dominant, causing ER fragmentation.

But how do Rtnl1s in the highly constricted NT trigger the scission? To obtain more information on the membrane-remodeling pathway, we resorted to testing the influence of the lipidome in Rtnl1-driven membrane rupture. As explained in the introduction, the ER plays a pivotal role in lipid biosynthesis and distribution to the entire cell. Hence, we decide to focus on PE, due to its high

concentration in the ER[27] and its established role in membrane remodeling, fusion and fission[2].

2.3.4.3 Lipidome sensing enhances Rtnl1-driven membrane fission

In the earlier assessment of the friction-related fission of the elongating NTs, it was suggested that the presence of proteins in the NT might facilitate the formation of a pore under even moderate tensile stress, leading to the NT scission via membrane poration[95]. However, our data suggest that in Rtnl1-containing tubes, force-driven constriction is enhanced by the intrinsic curvature and curvature-driven sorting of Rtnl1, which brings the NT curvature close to the hemi-fission threshold[93]. Hemi-fission, or local self-merger of the inner monolayer of the NT membrane, allows to severe the NT without producing a trans-membrane pore[81,116]. PE is a known inhibitor of pore formation, while it also facilitates local membrane rearrangements leading to hemi-fusion and hemi-fission. Consistent with the hemi-fission scenario, we found that adding 1,2-dioleoyl-sn-glycero-3-phosphoethanolamine (DOPE) to the NT membrane increased the fission probability (Fig. 2.19) without changing the membrane stress defined by the

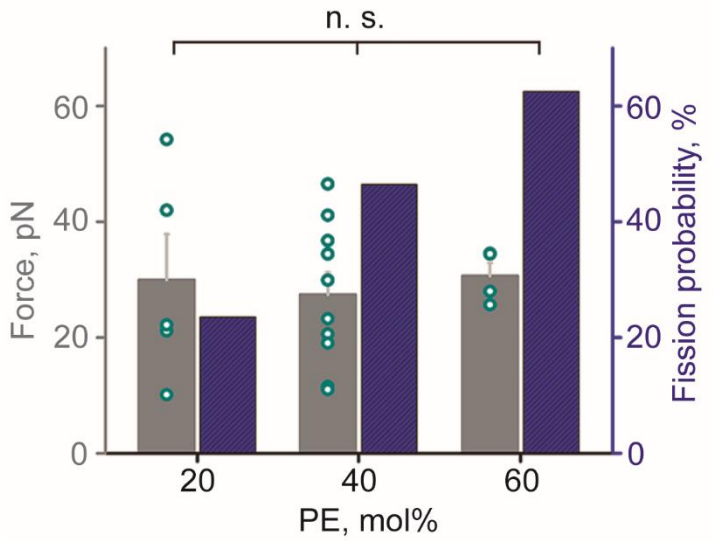

Figure 2.19. Stimulation of Rtnl1-driven membrane fission by PE. NT fission probability and pulling force changes at different PE concentrations in the NT membrane. Data correspond to DOPE:DOPC:DOPS:Chol:Rh-DOP: 20:59:10:10:1 mol% (n = 17 NTs, fission in 4 out of 17 cases), DOPE:DOPC:DOPS:Chol:Rh-DOPE 40:39:10:10:1 mol% (n = 28 NTs, fission in 13 out of 28 cases), and DOPE:DOPC:DOPS:Chol:Rh-DOPE 60:19:10:10:1 mol% (n = 8 NTs, fission in 5 out of 8 cases). Statistical significance: one-way ANOVA with multiple comparison.

magnitude of the pulling force (Fig. 2.19). The PE effect and also the ability of Rtnl1 to accumulate in the NT and create locally high membrane curvature strongly indicate that Rtnl1-driven membrane scission proceeds via the hemi-fission route.

2.3.5 Atl-Rtnl1 synergy analyzed *in vitro*

The capability of Rtnl1 to promote ER tubules fission in a concentration-dependent manner made us think further about the interactions between Atl and Rtnl1 and their implications for ER structural regulation. Although Rtnl1 has been identified in *Drosophila* as responsible for ER membrane fragmentation and thus an antagonist of Atl-driven membrane fusion, *in vitro* analysis has revealed apparent synergism between RTNs and the GTPase[10]. Then, the question remained on how this observed synergy may affect ER morphology.

2.3.5.1 Functional characterization of Atl-containing proteo-liposomes

We began by purification of *E. coli* expressed Atl and its reconstitution into LUVs using the same protocol we used for Rtnl1. Following reconstitution, we first measured the fusogenic activity of reconstituted Atl by fluorescence resonance energy transfer (FRET)-based lipid mixing assays. For that, we used two Atl-containing LUV populations (see Materials and methods: Lipid mixing), one with 1,2-dioleoyl-sn-glycero-3-phosphoethanolamine-N-(7-nitro-2-1,3-benzoxadiazol-4-yl) (NBD-DOPE) (donor) and Rh-DOPE (acceptor), constituting the FRET pair, and the other LUV population unlabeled. Upon progression of membrane fusion, the dilution of fluorophores by the unlabeled membrane should induce an NBD fluorescence increase. This process can be followed by measuring the NBD fluorescence emission (see Materials and methods: Lipid mixing). The extent of lipid mixing at each point can be quantified by normalizing against total NBD fluorescence upon adding a detergent to the cuvette (Fig. 5.9 b, see Materials and methods: Lipid mixing).

We observed a low degree of membrane fusion promoted by Atl in our lipid mixing experiments (Fig. 2.20, black curve) typically seen with purified *Drosophila* Atl[70,117]. We wondered whether the low fusion efficiency of purified Atl could be

ascribed to the lack of post-translational modifications during protein expression in the *E. coli* system. Thus, we decided to investigate the functionality of purified Atl from a different expression system, the Sf9 insect cells. Crucially, we found that Atl expression in Sf9 cells produces significantly higher levels of lipid mixing in reconstituted Atl proteo-liposomes (Fig. 2.20, red curve). Such lipid mixing levels have previously been achieved only with bacteria-purified Atl reconstituted into liposomes with 30% ergosterol in their membrane[118]. Thus, both lipid composition and post-translational modifications could have an essential role in Atl functionality.

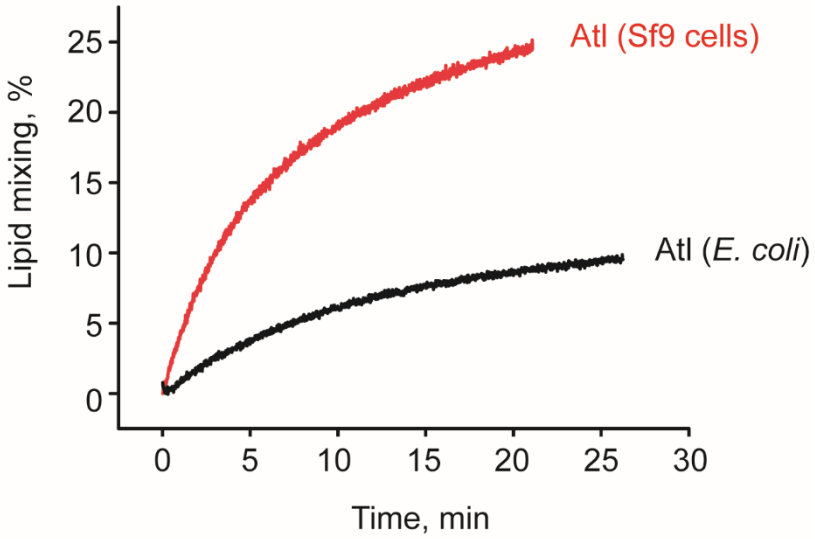

Figure 2.20. Atl-driven membrane fusion is more favorable when Atl is expressed in Sf9 cells than with *E. coli* Atl expression. Representative lipid mixing curves for each condition are shown. In both cases, the protein/lipid ratio is 1:400. Lipid composition is DOPC:DOPS:Rh-DOPE:NBD-DOPE 85:12:1.5:1.5 mol% for the labeled population and DOPC:DOPS 85:15 mol% for the unlabeled. The mixing ratio between both populations is 1:1.

Crucially, the efficiency of Atl production in *E. coli* was low. To increase the protein concentration in the stock, we had to spin it down, which might have further affected protein functionality. With Sf9 cells, the protein yield was 100 times bigger than with *E.coli*, making the protein detection in the proteo-liposome fractions of a flotation assay feasible. Atl was detected by SDS-PAGE in density gradient fractions showing a strong Rh-DOPE fluorescence signal coming from the LUVs (Fig. 2.21). Hence, we could conclude that Atl was successfully inserted into the LUVs membrane (Fig. 2.21).

2.3.5.2 Structural characterization of Atl proteo-liposomes by EM

We turned to cryo-electron microscopy (cryoEM) for visualization of the insertion of Atl into the model membranes. CryoEM has become an extremely powerful tool for the visualization and structural characterization of proteins by single-particle analysis with spatial resolution comparable to X-ray crystallography. In this context, single-particle analysis has been used to determine the structure of soluble proteins and protein complexes with membrane-interacting capabilities. However, the structural characterization of transmembrane proteins by EM remains a major challenge. The stabilization of

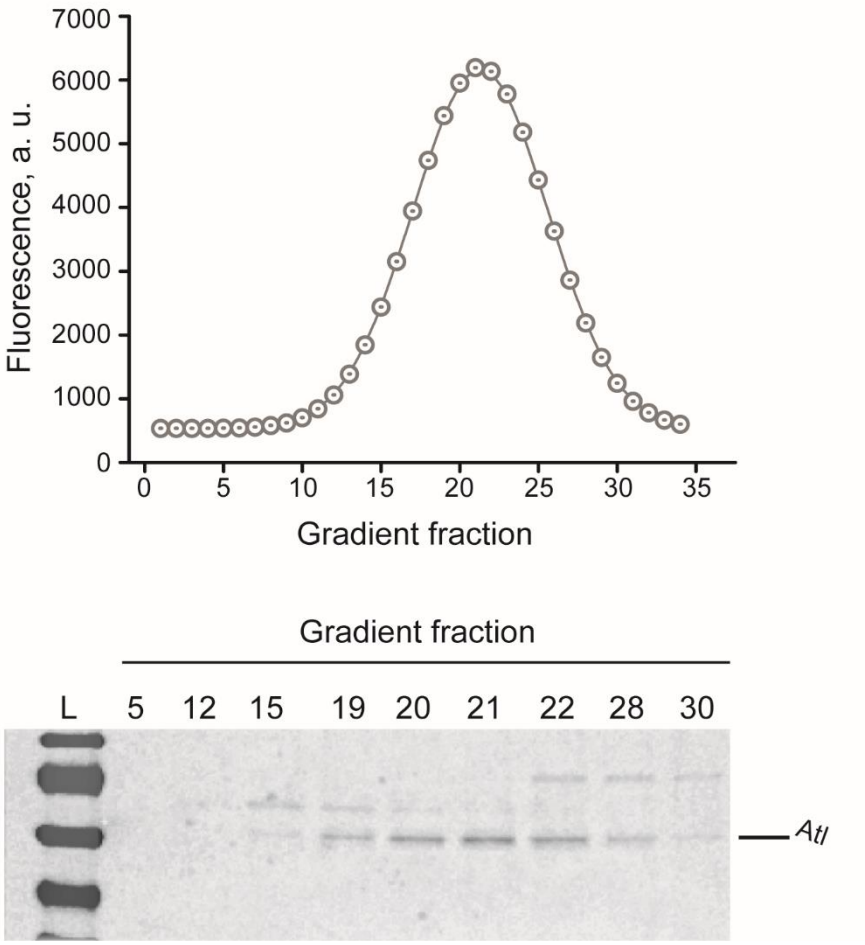

Figure 2.21. Density gradient-based flotation assay for Sf9-expressed Atl reconstituted into LUVs. Upper panel: measurement of Rh-DOPE fluorescence intensity of each fraction of the density gradient. The peak corresponds to the fractions containing the LUVs (lipid composition is DOPC:DOPS:Rh-DOPE 84:15:1 mol%). Lower panel: SDS-PAGE analysis of the gradient fractions shown in the upper panel. Only the fractions from 19 to 22 were added consecutively. The other fractions were randomly picked to the SDS-PAGE as representative points of the density gradient. Lipid composition is DOPC:DOPS:Rh-DOPE 86.5:12:1.5 mol%.

TMDs in model membranes, such as LUVs or lipid nanodiscs, is technically challenging, considering the high level of sample homogeneity needed for high-resolution structural studies. To dodge such experimental limitation, structural analysis is often based on protein truncation, i.e., the removal of the TMDs.

However, in the case of Atl, it has been shown that its TMDs become essential during Atl-driven membrane fusion[119]. With this in mind, we decided to perform EM structural characterization directly on our proteo-liposomes containing Atl. CryoEM visualization revealed that the proteo-liposomes were surrounded by a dense cloud around the membrane, probably indicating the presence of the protein (Figure 2.21, black arrows). However, previous attempts of EM visualization of Atl proteo-liposomes showed no clear evidence of the presence of the protein in the LUVs´ membrane[120].

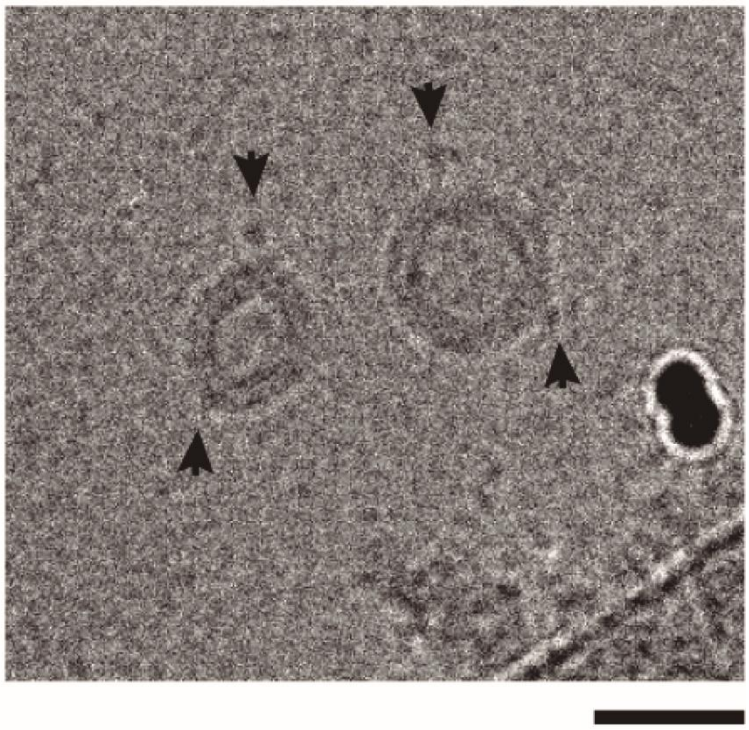

Figure 2.22. Single cryoEM micrograph of Atl-containing LUVs. Arrows indicate presumable Atl ectodomains (Scale bar 10 nm). Lipid composition is DOPC:DOPS:Rh-DOPE 86.5:12:1.5 mol%.

Such lack of detection in previous works could be due to the difficulty in observing individual proteins located outside the membrane in single images, especially considering the small volume of the cytosolic Atl region. Therefore, we

decided to perform cryo-electron tomography (cryoET) series to test whether the contradiction above was related to technical limitations rather than an unsuccessful reconstitution. CryoET revealed spots within the lipid bilayer of the model membranes (Fig. 2.23 a), which could correspond to the cytosolic regions of the reconstituted Atl, thus confirming that the reconstitution was indeed successful. Further subtomogram averaging allowed obtaining the preliminary structure of the Atl molecule sticking from the membrane (Fig. 2.23 b). Although we are far from obtaining the fine structure of Atl in its native environment on the membrane, these preliminary results demonstrate the overall feasibility of cryoET analysis of Atl-mediated membrane tethering and fusion.

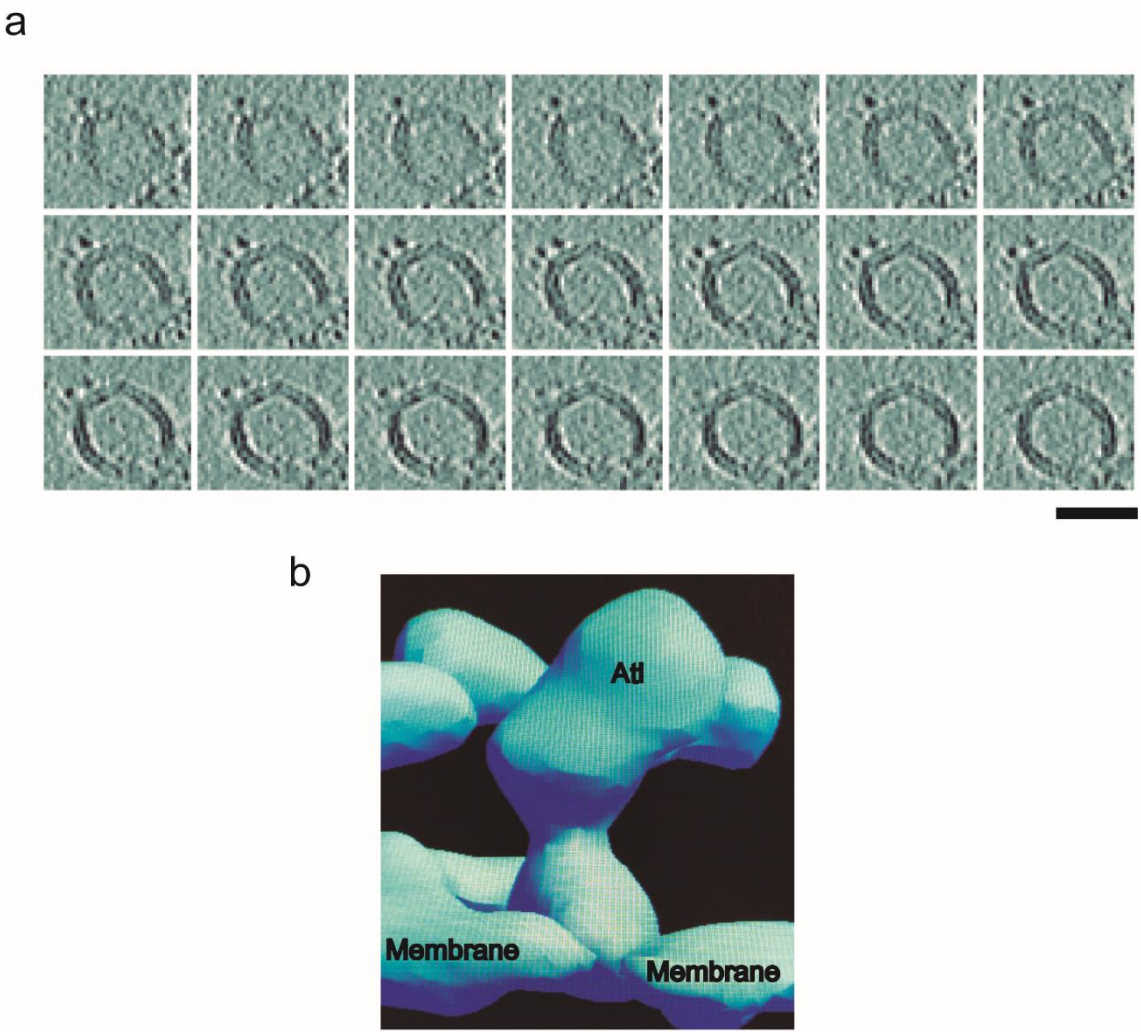

Figure 2.23. CryoET detection and visualization of Atl into the LUVs´ membrane (a) Tomographic 3D-reconstruction of Atl-containing LUVs. The image sequence goes from the bottom to the upper part of the liposome (Scale bar is 100 nm). **(b)** Preliminary structural data of membrane-inserted Atl done by subtomogram averaging with EMAN2. The membrane and Atl are identified within the reconstruction. Lipid composition is DOPC:DOPS:Rh-DOPE 86.5:12:1.5 mol%.

2.3.5.3 Atl and Rtnl1 complementarity in membrane network maintenance

Upon confirming the successful incorporation of Atl into the LUVs, we made a co-reconstitution of Atl and Rtnl1 into the vesicles and further compare the lipid mixing efficiency between Atl- and Atl/Rtnl1 proteo-liposomes. Interestingly, we found that lipid mixing was faster when both proteins were reconstituted together into the lipid bilayer (Fig. 2.24). The ability of Rtnl1 to generate high static membrane curvature might facilitate the Atl-mediated membrane fusion via pre-stressing the fusing membrane[121] and increasing the size of the Atl fusion complex. Indeed, for the best-known fusogen complex SNARE, its size varies from a single complex on extremely curved membranes[122,123] to 10-15 fusion complexes on weakly curved membranes[124]. Also, we cannot rule out a direct interaction between Rtnl1 and Atl. The observed synergetic action of the two proteins in membrane fusion might be related to their ability to sense membrane curvature and rearrange in membrane curvature gradients. This subject, however, requires further investigation.

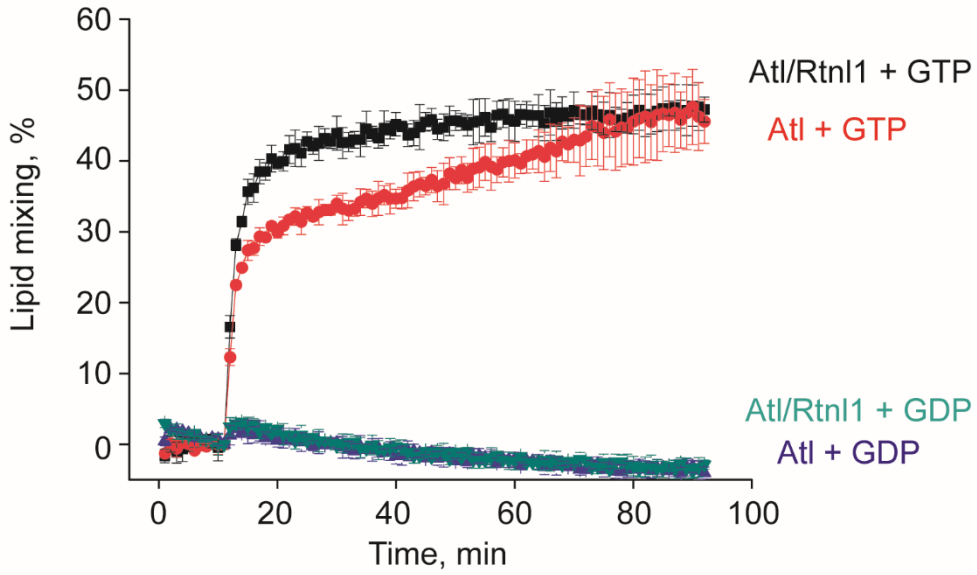

Figure 2.24. Rtnl1 enhances the rate of Atl-driven membrane fusion reaction. The curves show the rate of lipid mixing in the presence of GTP (red and black, respectively) and of non-hydrolyzable guanosine diphosphate (GDP) (cyan and purple, respectively) for Atl and Atl/Rtnl1 proteo-liposomes. Errors are SD. Lipid composition is DOPC:DOPS:Rh-DOPE:NBD-DOPE 85:12:1.5:1.5 mol%.

Next, we asked if Atl or its combination with Rtnl1 would promote the formation of a membranous network resembling the ER. For that, we incubated Atl- or Atl/Rtnl1 proteo-liposomes in the presence of GTP in a specially designed chamber composed of a cover glass and a polydimethylsiloxane (PDMS) lid with a small cell for the reaction mixture. Interestingly, we found that after 12 h of incubation, only the co-reconstituted Atl/Rtnl1 proteo-liposomes were able to transform into the membranous network (Fig. 2.25). Notably, the reaction time was far beyond the steady-state point in lipid mixing reached by each protein individually.

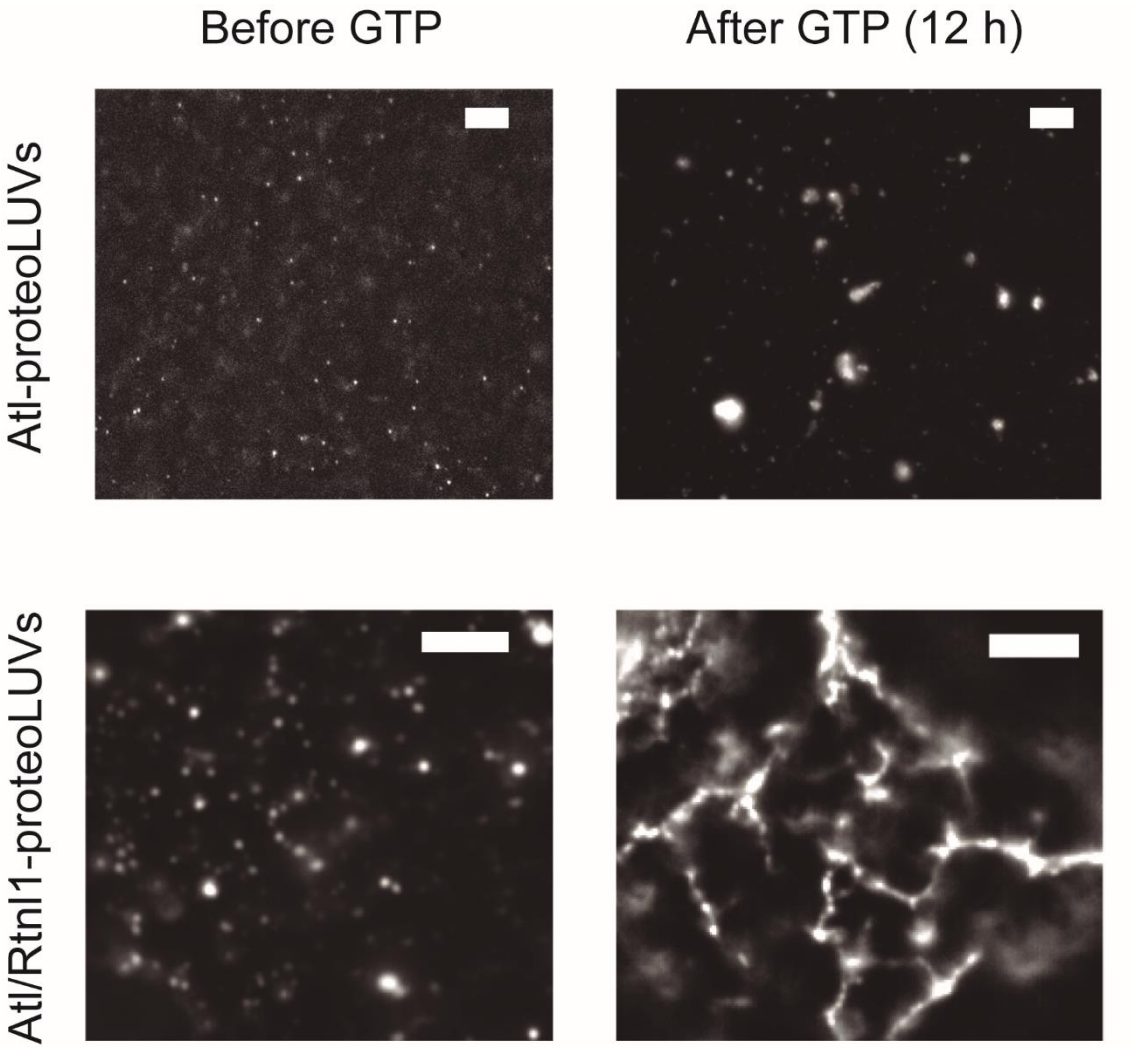

Figure 2.25. Rtnl1 and Atl are required for the formation of an ER-like membranous network. The images show proteo-liposomes (with reconstituted Atl- (upper images) or Atl/Rtnl1 (lower images)) before (left images) and 12 h after (right images) the addition of GTP to the incubation chamber. Rh-DOPE fluorescence is shown. Scale bars are 5 µm.

We conclude that Atl and Rtnl1 act synergistically during the *de novo* formation of the ER network *in vitro* from purified components. Significantly, this result does not contradict the earlier analysis of the functional antagonism between Atl and Rtnl1 in the maintenance ER. While Rtnl1 might be involved in creating and breaking the ER tubules, these processes likely depend differently on the Rtnl1 concentration and membrane motility. Steep dependence of the scission on the Rtnl1 concentration indicated by our analyses explains that Rtnl1 over-expression is likely to cause the ER fragmentation[84], while suppression of the Rtnl1 activity would lead to the appearance of distinct unbranched ER network[117]. The ER maintenance and fragmentation then can be governed by the balance of Atl and Rtnl1 expression, consistently with the genetic analysis presented here (Fig. 2.8).

3. Membrane remodeling by Dyn2 GTPase

3.1 Introduction

3.1.1 Dynamins in membrane fission

Dynamin superfamily of proteins is sometimes subdivided into membrane fission and fusion proteins[1]. While the dynamins specialized in membrane fusion, such as Atl described in the previous chapter, are generally anchored to the membrane via TMDs, dynamins implicated in membrane scission are cytosolic proteins that transiently and reversibly interact with the target membrane. The best-described group of these dynamins is the classical dynamins involved in membrane fission at the plasma membrane[125]. Three tissue-specific isoforms, Dyn1, Dyn2, and dynamin 3 (Dyn3) form this group of the so called ¨classical¨ dynamins[126,127], which are universally involved in membrane fission during vesicle internalization by clathrin or caveolin-mediated endocytosis[126]. Dyn1 is often considered as the paradigm fission dynamin. The mechanism of Dyn1-mediated membrane scission has been dissected into stages and extensively characterized in minimal *in vitro* systems[81,113,128], enabling detailed characterization of the fission mechanism.

Classical dynamins are mainly involved in orchestrating and mediating membrane scission in endocytosis. Endocytosis is fundamental for cellular life and is tightly linked to various physiological and pathological processes, such as mitosis, cell migration, many intracellular signaling cascades[129] or pathogen internalization[130]. During endocytosis, the extracellular cargo is internalized into membrane vesicles budding from the plasma membrane into the cytoplasm. While the vesicle budding and maturation are conducted and regulated by various protein machineries, including classical dynamins themselves, dynamins become the major player at the latest stage of the process. The mature endocytic vesicles are connected to the plasma membrane via a thin membrane neck[131]. Dynamins bind to the neck and self-assemble into a machinery that performs the neck scission. During the scission, the barrier function of the plasma membrane should be kept intact to avoid harmful leakage of contents to and from the cell. Hence dynamin mechano-enzymes have evolved to use the energy from GTP hydrolysis to acutely constrict and cut the neck without the leakage[125]. This ability resides in

the complex structure of the dynamin fission machinery, which remains a subject of debates[132].

Dyn1 homolog from *Drosophila melanogaster* was the first dynamin associated with the clathrin-mediated endocytosis (CME) *in vivo*[133,134] (Fig. 3.1). Since then, extensive research by many groups showed that dynamins´ recruitment to the endocytic vesicle neck results from their interactions with adaptor proteins containing SH3 domain[135,136] and from their ability to sense the high membrane curvature of the vesicle´s neck[137]. It is precisely the membrane curvature that triggers dynamins´ self-assembly into higher-order oligomeric structures that ultimately drive membrane fission[137].

While many research groups have well-characterized dynamin´s role in the endocytic vesicle neck scission upon GTP hydrolysis, the controversy remains at which stage of the endocytic pathway dynamin is recruited to the nascent vesicle. Crucially, recent data situated dynamins at the beginning of the CME process, before the emergence of the highly curved membrane neck[138,139]. Yet, we lack a clear understanding of the function and state of dynamin molecules at the slightly curved membrane of the emergent endocytic vesicle. Besides, it is unclear whether membrane curvature is implicated in the transition from small dynamin oligomers at the begging of CME to the fully assembled dynamin fission machinery.

Aside from endocytosis, classical dynamins, particularly Dyn2, have been implicated in other membrane remodeling processes inside the cell[140]. Particularly, Dyn2 has been localized at the trans-Golgi network in several cell types[9], where it mediates the secretion of newly formed proteins to the plasma membrane[141]. Dyn2 is also implicated in early endosome recycling[142] and the transport from late endosomes to the Golgi complex[143]. In addition, during the last few years, several studies have pointed to Dyn2 as a possible mediator of mitochondrial membrane fission[144,145] alongside with DRP1. Therefore, while the canonical action of classical dynamins is related to membrane fission during CME, Dyn2 has emerged as a specialized fission protein involved in membrane remodeling events throughout the entire cell.

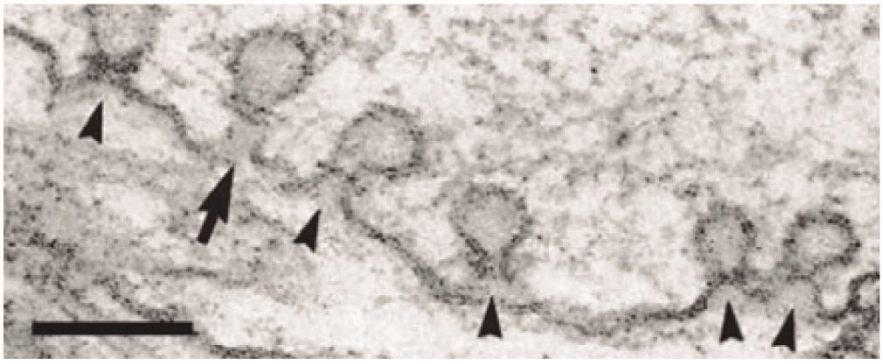

Figure 3.1. EM visualization of CME by electron microscopy revealed the temperature-sensitive mutant of dynamin in Drosophila, Shibire, at the membrane necks of the CCPs. Scale bar is 100 nm. Image adapted from Koening and Ikeda, 1989 [133], with the permission of The Journal of Neuroscience ("Copyright (1989) Society for Neuroscience").

3.1.1.1 Structural organization of classical dynamins

All three isoforms of the classical ¨fission¨ dynamins, especially Dyn1 and Dyn2, are approximately 80% identical[146] and share the same structural organization into five functionally defined domains[147,148] (Fig. 3.2 a) as follows:

- The *GTPase (G) domain,* or protein´s head, is responsible for dynamin-mediated GTP binding and hydrolysis [149,150] (Fig. 3.2 b). Compared to other GTPases in nature, dynamin is not a molecular switch but a mechano-enzyme. GTP analogs with impaired GTP hydrolysis fully arrest membrane fission *in vitro*[151]. Thus, the energy input required for local membrane rearrangements is provided by GTP hydrolysis. The GTP hydrolysis is stimulated upon dimerization of G domains in the context of high order oligomerization of dynamins. The GG dimer constitutes the minimal GTPase unit [152,153], as their formation stimulates the GTPase activity of Dyn1 about 100 times as compared to the basal GTPase activity of dynamin in solution [154].

- The *GTPase effector domain (GED)* and *middle domain* form the stalk of the protein (Fig. 3.2 b). GED, as follows from the name, is also essential for the GTPase activity of G-domain dimers. The GTPase-GED fusion protein is a minimal unit capable of forming a catalytic machinery via GG dimerization [152].

- The *bundle signaling element (BSE)*, which is not strictly a protein domain, is a three-helix bundle acting as a flexible linker that is located at the interface between the G domain and the GED. It is an intramolecular signaling module formed by the N-GTPase, C-GTPase, and C-GED termini that link the G-domain to the stalk [79,150,152,155]. BSE flexibility is represented as different conformations of the G domains depending on the catalytic cycle state [156].

- The *proline-rich domain (PRD)* mediates dynamin interactions with SH3-protein partners[135]. This domain is exclusive to the classical dynamins and allows for dynamin recruitment to endocytic sites by SH3-containing proteins[136]. Recently published data[138,139] showed how this interaction could mediate dynamin binding to the planar plasma membrane at the initial stages of CME. However, structural information on the PRD is scarce as truncated PRD-less dynamins were generally used for crystallographic and cryoEM analyses.

- The *pleckstrin homology domain (PHD)* is a domain that occurs in a wide range of proteins involved in the intracellular signaling and formation of the cytoskeleton. Similar to PRD, it is exclusive to the classical dynamins[125,157] (Fig. 3.2 b), functioning as the membrane anchor selective to highly charged phosphatidylinositol lipid species, particularly to the $PI(4,5)P_2$ lipid [158]. While dynamin´s PHD has a specific $PI(4,5)P_2$ binding pocket, PHD´s recruitment to the membrane is also possible through electrostatic interactions, albeit less efficient, with monovalent charged lipids in the absence of phosphatidylinositoles, [e.g., with 40% of negatively charged 1,2-dioleoyl-sn-glycero-3-phospho-L-serine (DOPS) in the membrane, see[81]]. To complement the electrostatic interactions, the short amphipathic variable loop 1 (VL1) located in the PHD might wedge into the hydrophobic core of the lipid bilayer and enhances membrane binding through hydrophobic interactions[159,160] (Fig. 3.2 b).

In addition to structural similarities, classical dynamins share the ability to self-assemble into collar-like helical structures in solution and on a membrane

template. The mechanisms of helical self-assembly and mechano-action are usually extrapolated from the Dyn1 helix, which has been studied more extensively and which we will review in the following subsections.

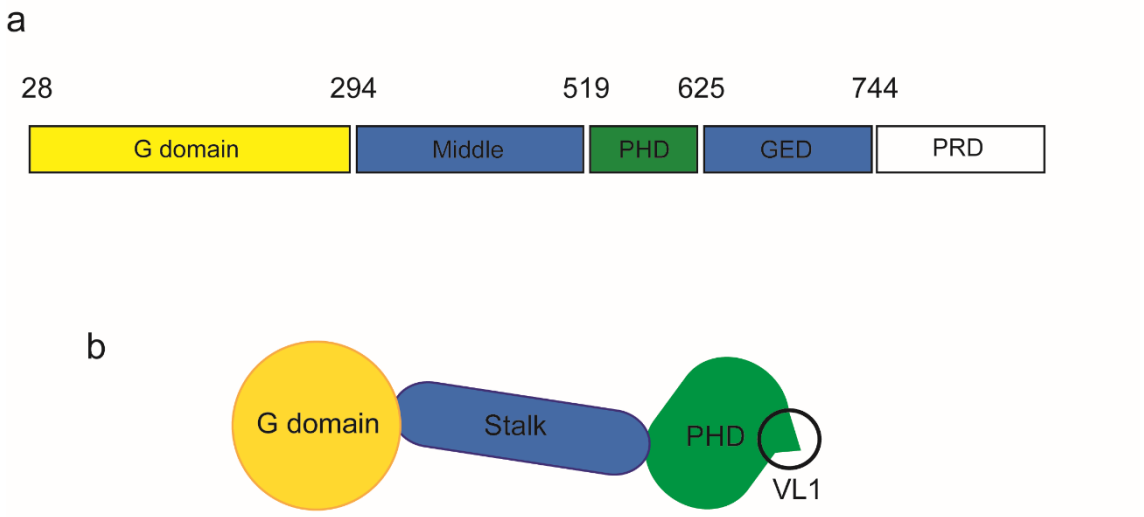

Figure 3.2. Structural characterization of Dyn1 and Dyn2 isoforms. (a) Schematics of the domain´s distribution of Dyn2 based on the primary amino acid sequence. **(b)** Schematics of the ternary structure of Dyn1, which shares 80% homology with Dyn2.

3.1.1.2 Dynamin self-assembly in solution

At physiological ionic strength, dynamin is generally considered to form tetramers in solution[161]. Lowering the buffer´s salt content to below 50 mM induces the exposure of previously buried residues leading to the protein self-assembly into helical scaffolds. Such self-assembly was first observed by Hinshaw and Schmid in 1995[147]. They found that the self-assembly in low salt was a reversible process, indicative of a specific self-assembly mechanism rather than denaturation or aggregation of the protein[147]. Formation of higher-order dynamin oligomers, rings and helices observed by EM, correlated with an increase in dynamins´ GTPase activity[73]. Thus, dynamin´s mechano-enzymatic activity is activated by dynamin´s oligomerization rather than by additional upstream factors, as happens with small GTPases[73]. Dynamin also polymerizes into rings and helices at physiological ionic strength in the presence of GDP and aluminum or beryllium fluorides (AlFx or BeFx, respectively)[162]. Both fluorides promote binding of guanosine diphosphate (GDP) to the catalytic center of various GTPases, stabilizing the center in the conformation closely resembling

the transition state (TS) of the hydrolysis reaction[162]. It remains unclear whether the low salt and the TS mimics stimulate the same self-assembly pathway. AlFx-GDP induces stable GG dimerization[152] and thus promotes the interaction between G domains of dynamin tetramers. The low salt, in turn, might stimulate the generic helical self-assembly pathway generally observed in the presence of a membrane template[163].

3.1.1.3 Dynamin self-assembly on the membrane

Dynamin tetramers have different conformation in solution[164,165] and on a highly curved membrane template[166] (Fig. 3.3). In solution, the PHDs of the dynamin tetramer are located close to the protein´s stalks, which prevents further polymerization of the protein (Fig. 3.3 a). When the tetramer approaches the membrane, the PHDs are released from the stalk due to the electrostatic and hydrophobic interaction with the membrane[166] (Fig. 3.3 b). Such PHD release allows for further helical self-assembly of the tetramers. This interaction is achieved through interface 1 (I1) in the upper part of the stalk region and interface

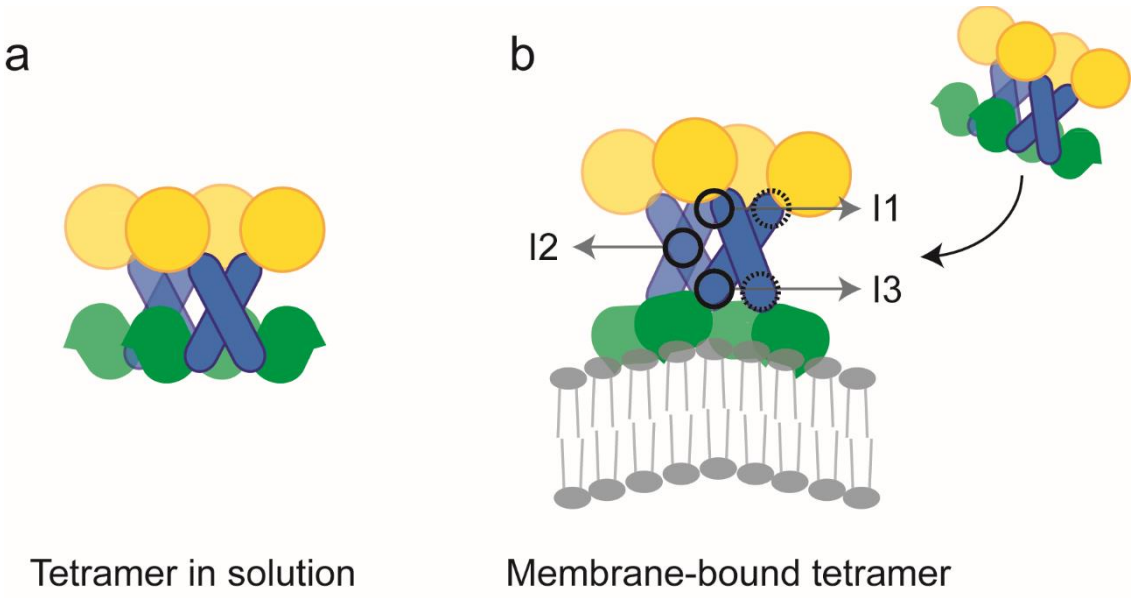

Figure 3.3. Structural rearrangement of Dyn1 tetramer upon membrane binding. (a) PHDs of Dyn1 tetramer in solution are locked to the stalks, preventing the stalk-driven interaction between the tetramers. **(b)** On a curved membrane, the PHDs reconfigure to bind and wedge into the lipid layer, making the self-assembly I1 and I3 available for the helical oligomerization of Dyn1. The self-assembly interface 2 (I2) is crucial for the formation of the X-shaped Dyn1 dimer, the basic structural unit of the Dyn1 helix.

3 (I3) in the lower part[80,156,167] (Fig. 3.3 b). Therefore, upon initial binding to the lipid substrate, lateral interaction between dynamin tetramers mediated by the stalk region of the protein leads to the helical self-assembly.

CryoEM of Dyn1-ΔPRD on lipid NTs and X-ray crystallography analyses of Dyn1-ΔPRD have provided us with the pseudo-atomic models of the dynamin helix configurations and the geometries of the enclosed lipid NTs at different points of the GTP hydrolysis cycle[163,166] (Fig. 3.4 a). The hydrolysis cycle of dynamin begins with the tight GTP binding to the G domains of adjacent helical turns, mediating the GG dimerization at the ground state of the cycle (Fig. 3.4 a). GG dimerization upon GTP binding triggers GTP hydrolysis through the transition state of the enzymatic cycle[125] (Fig. 3.4 a). Upon GTP hydrolysis, GDP and Pi are released from the GG dimer, potentially leading to the scaffold disassembly[125,165] (Fig. 3.4 a).

The oligomerization and the GTPase activity of the Dyn1 oligomer are tightly coupled to membrane deformations. Already in the apo state, the oligomerization through the stalks provides sufficient energy to transform spherical lipid vesicles into thin tubules that has to fit inside the dynamin helix[64,166]. The helical pitch in the apo state varies from 104 to 120 Å, with ~14 dimeric subunits (~28 dynamin monomers) making the helical turn of the right-handed 1-start helix[64,166]. GTP binding leads to to the compaction of the dynamin polymer (Fig. 3.4 c), resulting in further membrane constriction[166]. In the ground state, stabilized by non-hydrolyzable GTP analog Guanosine-5'-[(β,γ)-methyleno]triphosphate (GMPPCP), the Dyn1-ΔPRD polymer needs ~13 dimeric subunits (~26 monomers) to complete one helical turn, while the pitch between different rungs of the helix at this stage is 99.3 Å. In the ground state, the enclosed membrane tube reaches 7 nm in diameter[153,168] (Fig. 3.4 c). While the membrane curvature achieved in the ground state is relatively high, it is insufficient to promote spontaneous membrane fission. Thus, further rearrangements of the dynamin polymer are required to complete the fission reaction.

The final transition due to GTP hydrolysis leads to the switch between the constricted and super-constricted helix states. CryoEM analysis revealed that

coordinated GTP hydrolysis by multiple GG dimers in the helix results in robust compactization of the helix and the constriction of the enclosed membrane[168] (Fig. 3.4 d). Conformational differences between the crystallized GG dimer in the presence of GMPPCP and GDP/AlFx (TS mimic) pointed to the existence of a hydrolysis-dependent powerstroke[152,153] responsible for the structural transition from the constricted to the super-constricted state. The helical polymer structure for the super-constricted state was first obtained using the K44A dynamin mutant and GTP. This mutant allows for GTP binding, while being deficient in hydrolysis[169]. Further analyzes using WT dynamin and GTP showed identical structural conformations as for K44 mutant[168]. The structural rearrangement of the Dyn1-ΔPRD polymer is more pronounced in the super-constricted state. Here, computational docking of the cryoEM data indicated a 2-start helical symmetry as the most efficient packing of the dynamin polymer[168,169] (Fig. 3.4 d). The transition between the 1-start helix predicted for the ground state and the 2-start helix in the TS requires a transient disassembly of the dynamin polymer, as well as conformational changes in the G domain and the flexible BSE linker to make more room for the assembly of the second strand[168].

Importantly, in the super-constricted state the lipid NT lumen reaches 3.4 nm[168], the curvature sufficient to trigger spontaneous membrane fission[93]. However, stabilization of dynamin in its transition state by chemical cross-linking arrested the membrane nanotube at the hemi-fission state, without further progression to membrane scission[170]. Completing the fission reaction seemingly requires an additional force input linked to asymmetric PHD tilting or twisting of Dyn1 helix upon GTP hydrolysis[166,170–172].

The helical disassembly postulated by structural analyses was confirmed by real-time analyses of membrane constriction by Dyn1. Various and often sophisticated experimental techniques have been applied, ranging from confocal fluorescence microscopy and optical tweezers to high-speed atomic force microscopy (HS AFM) and conductance measurements[81,128,170,171,173]. While dynamics of preformed Dyn1 driven by GTP hydrolysis have been documented, the bulk of the data indicates that long dynamin scaffolds are inhibitory for the fission process, with fission linked to GTP-driven disassembly of the helices[81,128].

The GTP-driven disassembly of the preformed Dyn1 scaffold into small pieces having different orientations on the membrane tube was unequivocally shown by HS AFM[171]. Hence, while the GTP-driven helical constriction is seemingly intrinsic

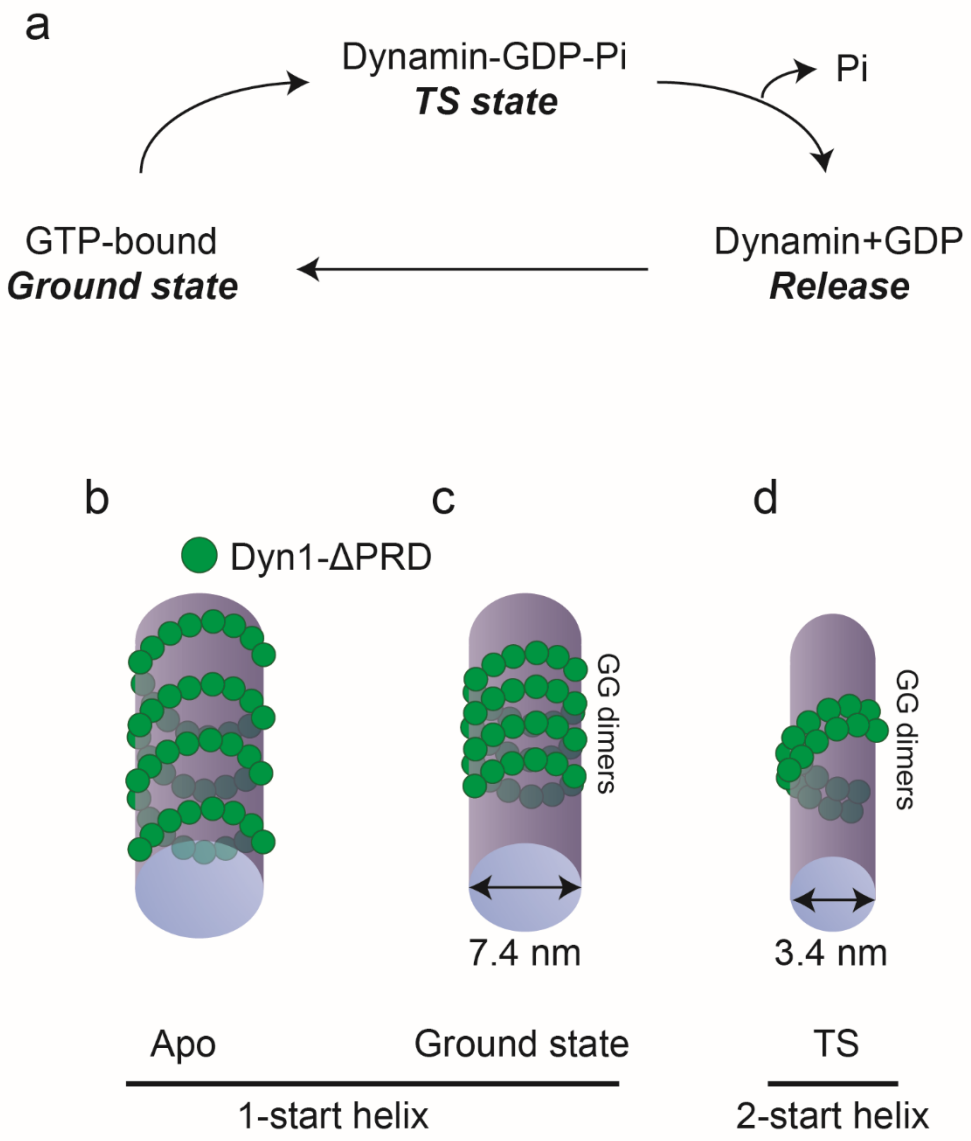

Figure 3.4. Progressive membrane constriction by Dyn1-ΔPRD helix at different stages of the GTPase cycle. (a) Schematic representation of the GTP hydrolysis cycle of classical dynamins. **(b)** Schematics of the formation of the membrane tubules (termed membrane tubulation) by the Dyn1-ΔPRD helix in the nucleotide-free (apo) state. **(c)** Compactization of the Dyn1-ΔPRD helix upon GTP binding causes further membrane constriction. **(d)** The super-constricted state is produced upon the initiation of GTP hydrolysis by Dyn1-ΔPRD, which results in the formation of a two-start protein helix that constricts the NT to an internal luminal diameter of 3.4 nm.

for Dyn1, the size and the structure of the helical machinery emerging from GTP-driven cyclic reassembly of Dyn1 preceding the fission remains unknown.

Importantly, while dynamin self-assembles into long helical collar-like structures on model membranes[151,162,174], it seems that such big-scale assembly is absent *in vivo*. Indeed, the single-molecule quantification performed with fluorescently labeled Dyn2, another isoform of the classical dynamins, revealed that the fission was produced by on an average of 26-40 Dyn2 molecules, roughly corresponding to 1 to 1.5 helical turns[175,176]. (Fig. 3.5 a). In addition, in around 30% of the event, the fission machinery was smaller than a single helix turn[175] (Fig. 3.5 b). The 2-start helix assembly in the presence of GTP[166,177] might help to explain this observation, as GG dimerization even for small sub-helical Dyn2 complexes facilitates the transition from small complexes to a fully functional Dyn2 fission machinery (Fig. 3.5 c).

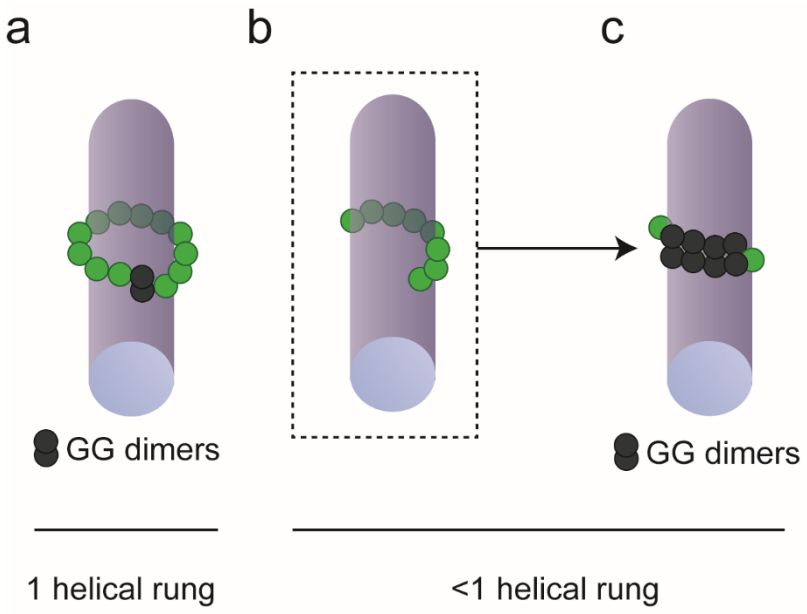

Figure 3.5. Schematic representations of the Dyn2 mechano-active complexes based on single-molecule fluorescence data from[175]. (a) The average number of Dyn2 molecules involved in fission during CME is of 26-40, corresponding to 1-1.5 helical rungs. **(b)** In 30% of the CME events, the number of Dyn2 molecules at the CCP is below one helical rung, indicating that a complete helical rung is unnecessary to form a fission active Dyn2 machinery **(c)** An hypothetical mechanism of GG dimerization with sub-helical dynamin units.

The HS AFM data and fluorescence microscopy quantification combined indicate that sub-helical dynamin oligomers might be not a byproduct of the helix

disassembly but rather active elements of the fission machinery. On the other hand, membrane curvature seems to trigger the assembly of a functional dynamin fission complex. While small amounts of likely sub-helical oligomers of both Dyn1 and Dyn2 have been detected on the relatively flat membrane of a nascent endocytic vesicle [139], it is only after the vesicle is fully assembled and ready to pinch-off when dynamins become active in mediating fission. This feedback loop between membrane curvature and the activation of the dynamin fission function was linked to the helical polymerization of Dyn1[137]. However, in the cell, the loop could also involve the oligomers residing on the vesicle membrane if those oligomers could feel membrane curvature and migrate towards the emergent vesicle neck. Importantly, this feedback loop seems to operate differently in Dyn1 and Dyn2, indicating a possible functional adaptation mechanism[139,146].

3.1.2 Different functional activation of Dyn1 and Dyn2 fission complexes

The expression of Dyn1 and Dyn2 in the organism varies between tissues[138]. While Dyn1 is a neuron-specific isoform, Dyn2 is ubiquitously present. Both isoforms are thought to rely on helical oligomerization for the function. In order for the helix to form on a membrane, dynamin must overcome the bending resistance of the membrane. Despite the large structural homology, it appears that purified Dyn1 and Dyn2 perform differently in bending. Dyn1 is a robust self-sufficient membrane bending machinery that can convert flat biomimetic lipid membranes into tubules during self-assembly, a process known as membrane tubulation[146]. While this happens in the micromolar range, at physiologically relevant nanomolar concentration, Dyn1 sense membrane geometry and assembles into helices only on membranes with high membrane curvature (>1/20 nm^{-1})[137].

Similar curvature sensing is present in the Dyn2 polymer[146]. However, even at micromolar concentrations, Dyn2 failed to produce membrane tubulation[146], indicating that the polymerization energy of Dyn2 is not sufficient to overcome the elastic energy barrier of the membrane. Such "sensing" of membrane curvature may have special significance in a physiological context. If the dynamin fission machinery can only form at a sufficiently curved vesicle neck,

cleavage of the neck cannot occur prematurely, e.g., before the clathrin-coated pit (CCP) has matured. Interestingly, compared to Dyn1, Dyn2 is more frequently localized to the plasma membrane prior to the maturation of the CCP[138] (Fig. 3.6). Since Dyn2 is generally defined as a curvature sensor rather than a creator, its apparently incongruent recruitment to the planar membrane could be triggered by strong interactions with the SH3 partners (Fig. 3.6). In agreement with this, Dyn2 has a stronger relationship with SH3 partners *in vitro* than Dyn1[146]. These data, combined with the poor performance of Dyn2 in the tubulation assays, suggest that Dyn2 functionality resides more in the small, sub-helical oligomers than in the full-flesh helical formations generally associated with tubulation[132]. However, the membrane activity of small Dyn2 oligomers operating on the CCP membrane prior to the fission has not been directly investigated.

In addition to Dyn2 function at the scission stage of the CME, the curvature activity of sub-helical Dyn2 oligomers may also play a role at the earlier stages of the process. We already mentioned that the sub-helical oligomers of both, Dyn1 and Dyn2, first appear on low-curvature membranes of early CCPs, including transient non-productive CCPs[178]. The progressive association of sub-helical dynamin oligomers with budding CCPs observed by fluorescence microscopy[138] is consistent with their intrinsic membrane curvature sensing capabilities. If the sub-helical oligomers retain the inherent high curvature activity of the dynamin helix, their local curvature effect should be profound, comparable to that of clathrin adaptor proteins. Since Dyn2 is a hub protein strongly involved in the CCP proteome, the curvature activity of oligomers could be an important mechanical factor in CCP maturation. Moreover, the curvature-controlled sorting of dynamin oligomers toward the nascent vesicle neck might be responsible for the timely self-assembly of the dynamin fission machinery.

The differences between Dyn1 and Dyn2 in the *in vitro* tubulation assays were ascribed to a single point mutation in the membrane-interacting PH domain[146]. This finding indicates that the functional differences between the isoforms shall be considered in the context of the membrane lipidome. Both membrane bending and protein binding strongly depend on the mechanical

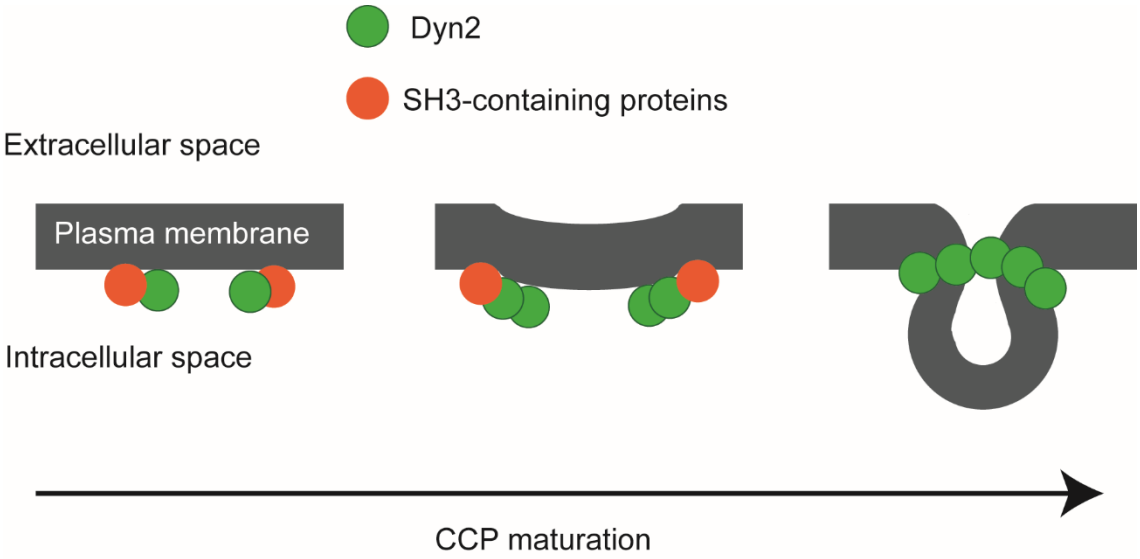

Figure 3.6. Dyn2 recruitment at the planar plasma membrane at the early stages of the CME. The scheme shows the progression from the initiation (left) to the fully mature CCPs (right).

parameters and membrane defects that may affect protein interaction with the membrane. Particularly important here is the role of non-bilayer lipid species, as we will explore in the following subsection.

3.1.3 Membrane mechanics as a trigger for dynamin action

Lipidome regulation of Dyn1 has been already researched both *in vivo* and *in vitro*[5]. As dynamins use membrane substrates to carry out their functions, the lipid composition and geometry seem suitable for potentiating dynamin mechano-chemical activity and their ability to remodel membranes. The lipid species enriched in the specific habitat of Dyn1 at synaptic membranes, polyunsaturated phospholipids, significantly increase the GTPase activity of Dyn1, as their presence on model membranes increases the GTPase activity rates up to 7.5-fold[5]. The increase in mechano-chemical activity of Dyn1 is likely induced by the reduction in the membrane bending energy[5], which reduces the elastic energy barrier of the membrane being deformed and favors the formation of membrane defects that facilitate the shallow incorporation of Dyn1 into the membrane.

While the influence of the lipidome on the recruitment and activity of Dyn2 remains largely unexplored, its presence at different cellular locations, such as the plasma membrane, the Golgi apparatus, or even the mitochondrion, all with

different lipid compositions, indicate that membrane mechano-chemistry should have a decisive role in Dyn2 functional regulation. PE is a major phospholipid component in virtually all membrane organelles found in the cell. In the plasma membrane of mammalian cells, PE constitutes about 20-25% of total phospholipids, while this value increases up to 30 mol% in the endosomes or the mitochondria[27], locations where Dyn2 has been proposed to mediate membrane fission. PE has an intrinsic negative curvature, which underlies its role in membrane remodeling. It has been observed to promote lipid membrane fusion by decreasing the energy barrier to form the so-called hemifusion stalk[179]. It also reduces the membrane´s bending resistance[31], similarly to the action of polyunsaturated lipids found to modulate the activity of Dyn1 *in vivo* and *in vitro*.

The negative curvature of PE could promote the formation of membrane defects. A similar type of membrane defects induced by polyunsaturated lipids has been shown to promote Dyn1 binding by supporting the shallow protein insertions into the lipid bilayer. Therefore, PE could upkeep Dyn2-mediated remodeling by promoting Dyn2 binding via membrane defects and lowering the membrane´s bending rigidity during Dyn2 self-assembly. Thus, PE could be the critical co-factor for Dyn2 function in membrane fission.

Additionally, other lipids might favor Dyn2 functionality inside the cell. In this context, CL, the lipid mainly found in the inner mitochondrial membranes constituting approximately 20 mol% of their lipid composition[27], share the geometric features with PE. CL shows more substantial intrinsic negative curvature in the nanometer range[180–182]. Moreover, CL carries two negative charges[183]. Hence, CL seems to satisfy dynamin´s requirements for successfully membrane binding, i.e., the membrane defects through the presence of conically shaped lipid molecules and the electrostatic interaction.

3.2 Problem statement and objectives

In the previous sections, we highlighted the subtle functional differences between Dyn1 and Dyn2 isoforms, with the latter likely relying more on small sub-helical oligomers and membrane lipidome for its function. This thesis project aims at **reconstructing and analyzing *in vitro* the behavior of small, sub-helical Dyn2 oligomers** observed to mediate membrane fission *in vivo*. We will further investigate how factors such as lipid composition and nucleotide presence affect the **transition from these sub-helical units towards a fully functional fission apparatus.**

In this context, the objectives proposed for this part of the thesis project were:

5. To reconstitute the sub-helical Dyn2 oligomers *in vitro* to assess their membrane curvature sensing/creation capabilities.
6. To characterize how lipid factors, mainly PE, membrane curvature, and nucleotides, affect the membrane remodeling activity of the sub-helical dynamin complexes.
7. To propose a mechanism for the transition from sub-helical Dyn2 complexes to fully functional fission machinery.

3.3 Results and discussion

3.3.1 The nucleation step in Dyn2 helical self-assembly

One of the preferred approaches to study protein dynamics is through real-time visualization by fluorescence microscopy. Either Green Fluorescent Protein (GFP) or mGFP are usually the molecules of choice for such kind of visualizations due to its resistance to photobleaching, high quantum yield and 1:1 labeling ratio. However, in the previous chapter, we already discussed that addition of mGFP to Rtnl1 severely altered the functional phenotype of the protein. Thus, we wondered if a similar inhibitory effect will occur with Dyn2 after its C terminus is tagged with monomeric Enhanced Green Fluorescence Protein (mEGFP). mEGFP is an enhanced variant of mGFP, exhibiting stronger emission fluorescence in the absence of dimerization through A206K point mutation[184] (Fig. 3.7).

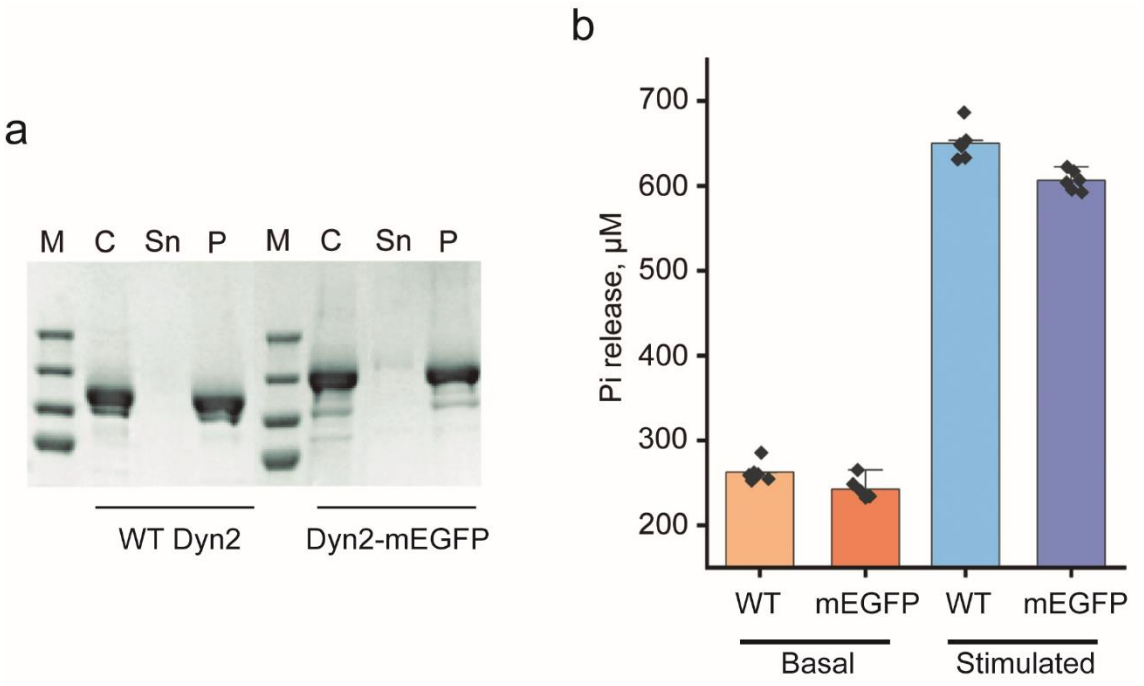

Figure 3.7. Comparison of membrane binding and GTPase activity of WT Dyn2 and Dyn2-mEGFP. (a) SDS-PAGE analysis of the pellet (P) and supernatant (Sn) fractions of a binding assay performed by pulling down 0.5 µM WT Dyn2 or Dyn2-mEGFP in the presence of 0.2 mM LUVs (100 nm) upon 30 min incubation. The LUVs´ lipid composition is DOPE:DOPC:DOPS:Chol:Rh-DOPE:PI(4,5)P_2 25:52:10:10:1:2 mol%. **(b)** Comparison of GTPase activity between WT Dyn2 and Dyn2-mEGFP (0.5 µM in each condition) in the absence (basal) or presence (stimulated) of lipid templates. Lipid templates are the same as described in **(a).** Error bars are SD, and n=3 independent experiments.

Both the WT and the Dyn2-mEGFP constructs showed similar membrane binding in pull-down assays (see Materials and methods:Determination of Dyn2 membrane binding efficiency) performed on LUVs with the same lipid composition (Fig. 3.7 a). In addition to the binding assay, we performed a GTPase assay to measure the release of free inorganic phosphate upon GTP hydrolysis by the enzyme (see Materials and methods: Dyn2 GTPase activity measurements) in the absence (basal) or presence of LUVs (assembly stimulated)[73]. Both constructs exhibited similar GTPase activity on identical lipid templates (Fig. 3.7 b). Since the mechanochemical activity of Dyn2 is related to its ability to oligomerize and tubulate membranes[185], these results also suggest that both proteins share the same membrane tubulation capability.

Since Dyn2-mEGFP showed no evidence of functional inhibition, we proceeded with analyzing the dynamics of Dyn2 self-assembly. For that, we first produced NTs from GSBs as described in the previous chapter and then added 0.5 μM Dyn2-mEGFP to the experimental chamber. Interestingly, upon Dyn2-mEGFP addition, we observed a clear nucleation process similar to that previously reported for Dyn1[137]. We first detected the appearance of a weak and uniform mEGFP signal on the NTs, indicating the binding of the individual Dyn2-mEGFP oligomers. This initial stage was followed by the rapid appearance of brighter mEGFP spots (Fig. 3.8 a, white arrows), indicating the formation of Dyn2 helices. The formation of protein helices on longer incubation times was further confirmed by cryoEM observation of LUVs incubated with Dyn2 (Fig. 3.8 b). Comparison of the Dyn2-mEGFP fluorescence signal from the helices and the regions in between revealed that the fluorescence density was on average five times lower, consistent with membrane coverage by the dispersed Dyn2 oligomers (Fig. 3.8 a). Thus, Dyn2 fission machinery emergence is precluded by protein binding to the membrane, as was also observed previously for Dyn1[137].

To assess the mechanical action of Dyn2 on the NT during the protein binding and helical self-assembly, we (in collaboration with Dr. Borja Ibarra lab, IMDAE, Madrid) used lipid membrane NTs pulled from GSBs by optical tweezers, as described above for Rtnl1-containing NTs. A similar mechanistic assessment

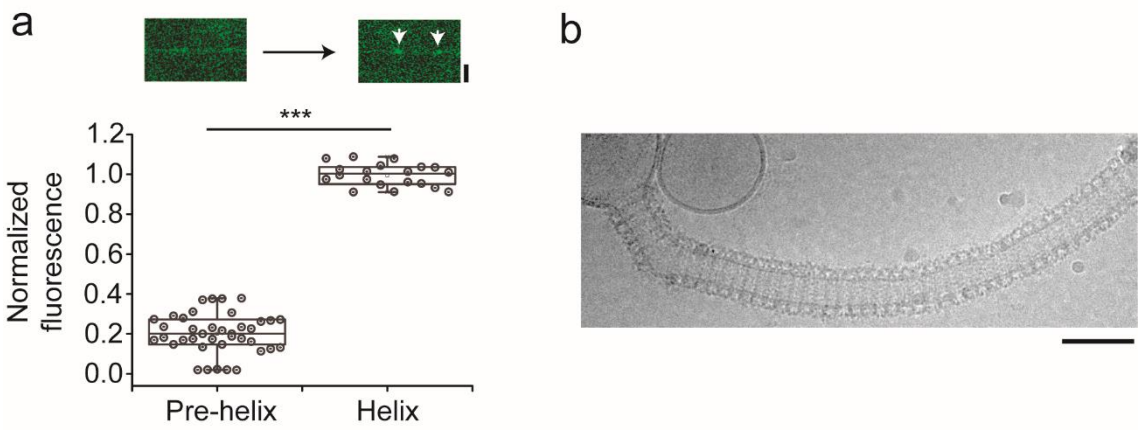

Figure 3.8. Nucleation of Dyn1-mEGFP helical self-assembly on lipid NTs. (a) Fluorescence microscopy images (above) show representative snapshots of Dyn2-mEGFP fluorescence distribution around the NT after the addition of 0.5 μM Dyn2-mEGFP to the bulk. White arrows show the emergence of Dyn2-mEGFP scaffolds. Scale bar is 2 μm. Boxplot shows the measured fluorescence intensity per unit length of the lipid NT of the bound Dyn2-mEGFP inside the scaffolds of Dyn2 (n=21) and in the regions in between the scaffolds (n=40). In each case 5 independent NTs were analyzed. Statistical significance: paired-sample *t*-test, *** < 0.001. The boxplots show IQR, and the whiskers indicate the maximum and the minimum of the dataset. **(b)** CryoEM micrograph showing a tubulated LUV decorated with Dyn2 after incubation of 400 nm LUVs with 0.5 μM of Dyn2 for 30 min. The lipid composition is DOPE:DOPC:DOPS:Chol:Rh-DOPE:PI(4,5)P_2 25:52:10:10:1:2 mol%. Scale bar is 50 nm.

was made earlier for Dyn1 isoform[137]. In this work, it was demonstrated that helical polymerization of Dyn1 led to the axial force decrease due to the NT stabilization by the protein scaffold. Indeed, the addition of Dyn2 to a preformed lipid NT resulted in the expected drop in force from its initial value (Fig. 3.9, f_0) to the background level, indicating a rapid formation of rigid protein scaffold constraining the NT (Fig. 3.9, f_{final}). This effect is reminiscent of the membrane tubulation activity observed for Dyn2 (Fig. 3.8 b).

Importantly, the force decrease had a clear intermediate step (Fig. 3.9, adsorption) in about half of the experiments (29 out of 59 total cases), suggesting that another process affecting NT elasticity precedes that of helical polymerization. Comparison to the fluorescence microscopy observation of Dyn2-mEGFP binding to the NT (Fig. 3.8 a) indicates that the initial step corresponds to the protein adsorption to the NT membrane before the nucleation of the helical polymerization. We next asked whether the small pre-helical Dyn2 complexes can recognize membrane curvature before complete oligomerization, as we observed in the case of Rtnl1.

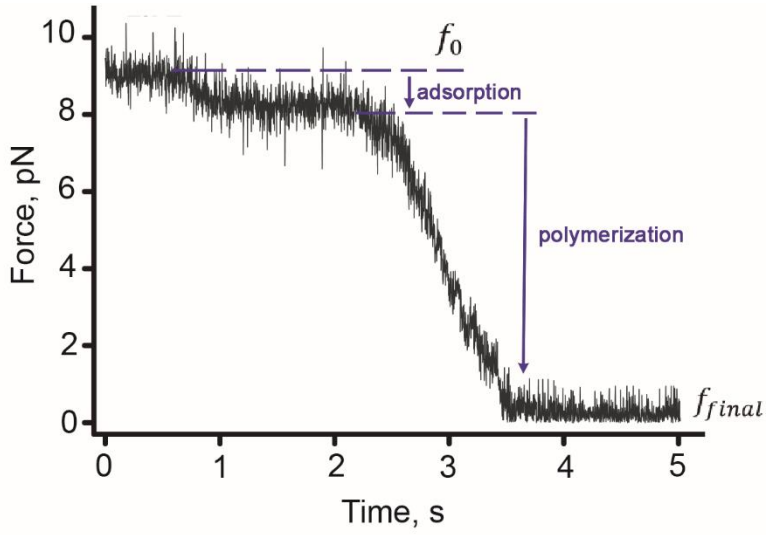

Figure 3.9. Two-stage kinetics of the pulling force decrease upon Dyn2 addtion to a lipid NT. The plot shows a representative example of the force measurement experiment, showing the changes in the force acting on the streptavidin bead pulling the NT (referred to as the axial force) upon the addition of 0.5 μM of Dyn2 the bulk. The initial force decrease is caused by the adsorption of small Dyn2 oligomers to the NT. The final force decreases to the background level due to Dyn2 helical polymerization leading to the NT stabilization. The lipid composition is DOPE:DOPC:DOPS:Chol:Rh-DOPE:PI(4,5)P_2 25:52:10:10:1:2 mol%.

3.3.1.1 Membrane curvature sensing by non-polymerized Dyn2 oligomers

To measure the curvature sensing capabilities of pre-helical oligomers of Dyn2, we first attempted the experimental toolbox we used to measure the curvature-driven sorting of Rtnl1. Although we could produce pulled NTs from GSBs with bound Dyn2-mEGFP (Fig. 3.10 a), we found that the pulling of NTs from the GSBs was affected by the background tubulation activity of Dyn2, which made it impossible to pull the NTs. Therefore, we decided to measure the curvature-driven sorting of Dyn2 as surface mEGFP fluorescence density on preformed NTs of different curvatures (Fig. 3.10 b).

We found that the mEGFP surface density increased with the NT curvature, in agreement with curvature-driven sorting towards the NT (Fig. 3.10, blue). To further confirm the curvature sensing by small pre-helical Dyn2 complexes, we suppressed Dyn2 self-assembly by the addition of 10 mM GDP[154]. While GDP prevented helical polymerization (Fig. 3.10 b, inset), the mEGFP density increased with the NT curvature as in the absence of the nucleotides (Fig. 3.10 b, magenta). In turn, the mEGFP signal from long helical scaffolds of Dyn2-mEGFP showed no systematic dependence on the NT curvature (Fig. 3.10 b,

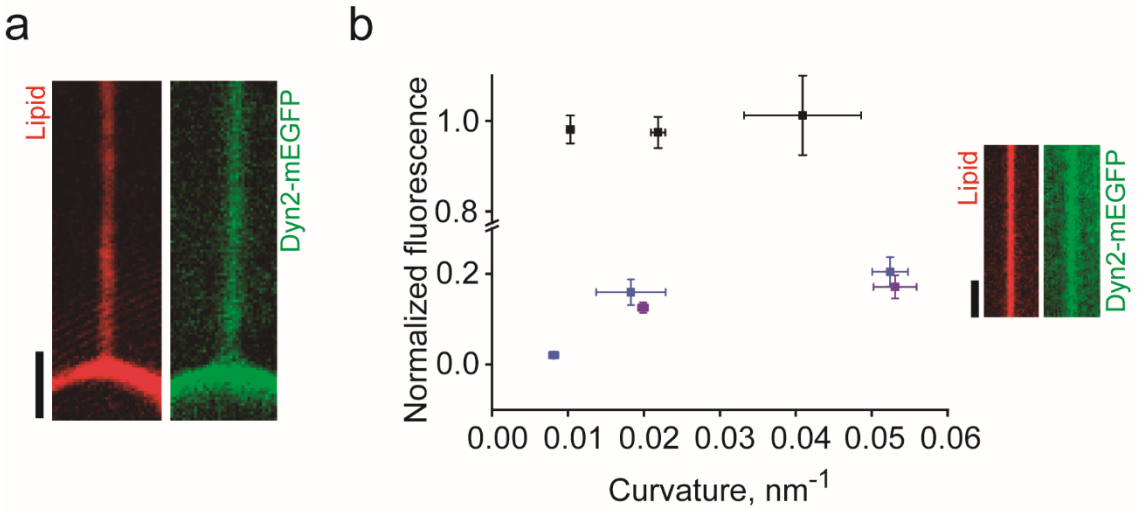

Figure 3.10. Small Dyn2 oligomers, the precursors of helical self-assembly, sense membrane curvature. (a) Micrographs of a pulled lipid NT from a GSB covered by Dyn2-mEGFP. Rh-DOPE and mEGFP fluorescence signals are shown in the left and right images, respectively. Scale bar is 4 µm. **(b)** Dyn2-mEGFP surface density dependence on the NT curvature for the scaffold regions (black) and in the regions between the scaffolds (blue). For the normalization of the fluorescence signal, the NT radius´s mEGFP integrated fluorescence per unit length was divided by the NT radius and then normalized to the mean fluorescence density measured in the scaffold regions. The fluorescence density of Dyn2-mEGFP also decreased in the presence of 10 mM GDP (magenta), an inhibitor of the scaffold formation, dependently on the NT curvature, in a similar manner as in the apo state before Dyn2 helical self-assembly. Dyn2-mEGFP concentration was 0.5 µM. Mean values and SD are shown. At least three different NTs were used per each data point. The inset shows a lipid NT covered by Dyn2-mEGFP before its self-assembly through the addition of 10 mM GDP. Rh-DOPE and mEGFP fluorescence signals are shown in the left and right images, respectively. The lipid composition is DOPE:DOPC:DOPS:Chol:Rh-DOPE:PI(4,5)P_2 25:52:10:10:1:2 mol%.Scale bar is 2 µm.

black). This finding suggests that membrane curvature is relevant for the membrane recruitment of small Dyn2 complexes, which then self-assemble into a functional mechano-active Dyn2 helix. Since Dyn2 membrane coverage is regulated by charged lipids, we hypothesize that other lipids (e.g., conical lipids, previously shown to enhance Rtnl1 membrane fission) may also be critical for regulating the emergence of Dyn2 fission machinery.

3.3.1.2 Lipidome sensing by Dyn2

Dyn2 interacts with various membrane organelles in the cell. The diversity of these interactions suggests that Dyn2 adapts to the specific target lipidome. However, this aspect of Dyn2 functionality in the cell has been overlooked in the *in vitro* studies. Particularly, as Dyn2 interacts with membranes through electrostatic attraction and partial PHD membrane insertion, the role of lipids

creating local packing defects, the hotspots for protein insertion[5], has not been assessed. We already observed the stimulating effect of PE on Rtln1 activity. So, we decided to test whether increasing the PE content in the membrane could also enhance the Dyn2 binding to membranes with low levels of negative charge. Indeed, at 0.5 mol% PI(4,5)P_2, Dyn2 membrane binding is almost negligible in membranes lacking PE (Fig. 3.11 a, b). The addition of PE stimulates the Dyn2

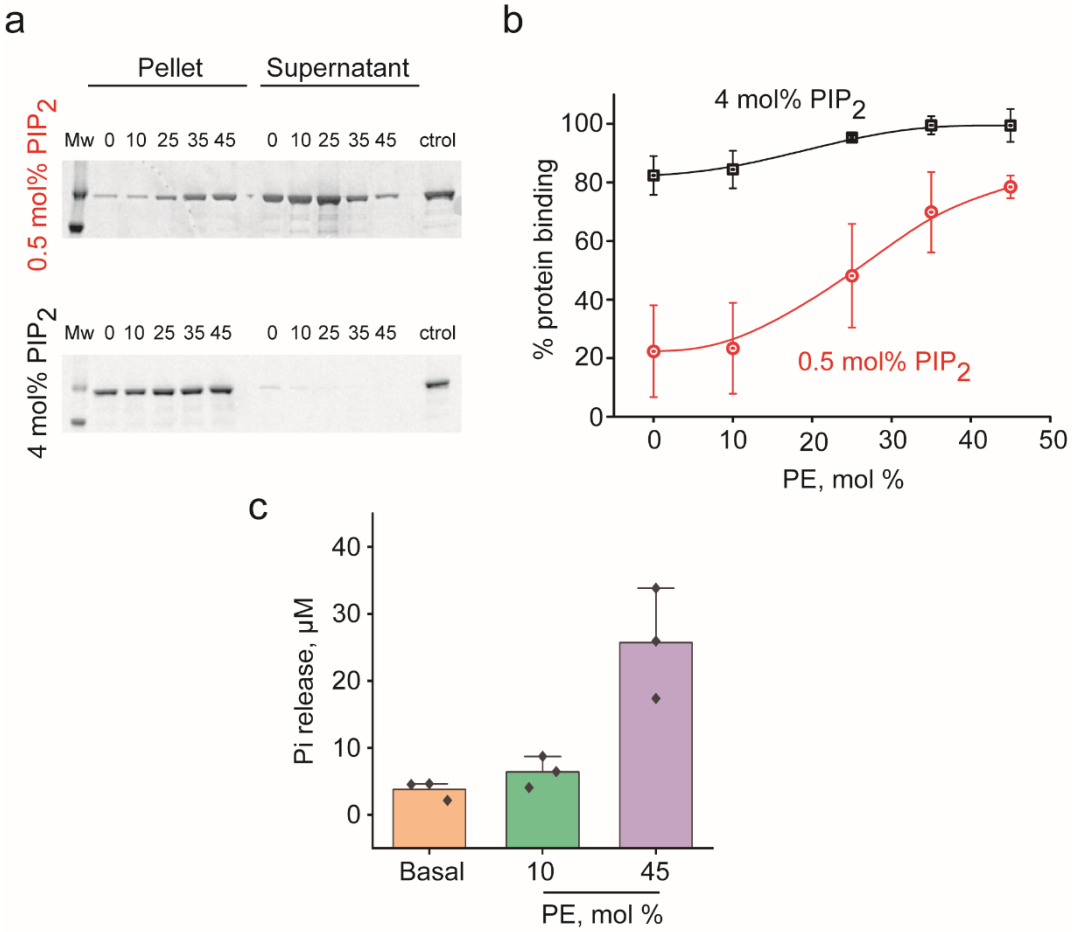

Figure 3.11. Control of Dyn2 membrane binding by PE and PI(4,5)P_2. (a) Representative SDS-PAGE analysis of Dyn2 binding "pull-down" assay showing the pellet and supernatant fractions at different concentrations of PE and PI(4,5)P_2. **(b)** Quantification of Dyn2 binding extension calculated from three different gels. The quantification was done by measuring the protein in the pellet fractions and normalizing it against the total protein used in each assay, multiplied by 100. **(c)** The graph shows the Pi released after 30 min of GTP addition in the absence (basal) and presence of 400 nm LUVs containing 4 mol% of PI(4,5)P_2 and different PE concentrations. Mean values and error bars of the SD are shown, three independent experiments per condition. Statistical significance: unpaired two-sample t-test, *p < 0.05. Each lipid composition used contained fixed amounts of Chol:DOPS:Rh-DOPE of 10:10:1 mol%. The molar proportions of DOPE and PI(4,5)P_2 were added accordingly to each condition used, as shown in the figure. To compensate the changes of either DOPE and/or PI(4,5)P_2, the molar proportion of DOPC was varied accordingly.

binding proportionally to PE in the membrane (Fig. 3.11 a, b). We next determined whether the electrostatic attraction could compensate for the PE effect. We found that the protein binding saturates at 4 mol% PI(4,5)P_2 virtually independently on the amount of PE in the membrane (Fig. 3.11 a, b). We finally asked whether, under these saturation conditions, PE still affects the Dyn2 activity. We measured the GTPase activity after incubating 0.5 μM Dyn2 with LUVs containing 10 or 45 mol% PE at a fixed amount of 4 mol% PI(4,5)P_2 (Fig. 3.11 c). Remarkably, we found that at 45 mol% PE in the membrane, the GTP hydrolysis rate was much higher than at low PE levels (Fig. 3.11 c). Therefore, the PE not only promotes Dyn2 binding but also facilitates membrane remodeling by Dyn2, likely, via facilitating LUV tubulation coupled to the helical self-assembly of Dyn2.

To test the conjecture that PE facilitates the helical self-assembly, we compared the axial force behavior (Fig. 3.9) in the NTs containing 10 and 25 mol% PE (Fig. 3.12). We found that Dyn2 failed to self-assemble and bring the axial force to the background level on the membranes with low PE content, while it robustly produces such force reduction at high but physiologically relevant

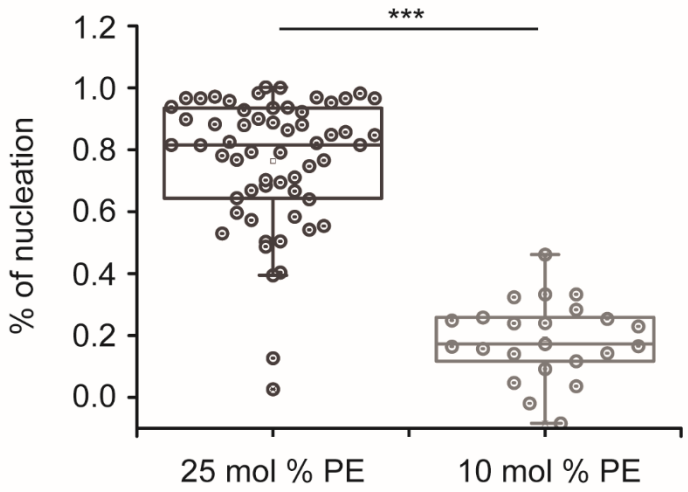

Figure 3.12. PE facilitates Dyn2 full-scale helical self-assembly by favoring its nucleation on the lipid NTs. The data set was obtained by normalizing the ratio between f_{final} and f_0 (as in the graph from the Fig. 3.9) against the maximum ratio value. Analyzed force curves are 59 and 23 for DOPE:DOPC:DOPS:Chol:Rh-DOPE:PI(4,5)P_2 25:52:10:10:1:2 mol% and DOPE:DOPC:DOPS:Chol:Rh-DOPE:PI(4,5)P_2 10:67:10:10:1:2 mol%, respectively. Statistical significance: one-way ANOVA with post hoc Bonferroni test, *** $p < 0.001$. Boxplots show IQR, whiskers indicate the maximum and minimum of the dataset.

levels of PE (25 mol%, Fig. 3.12). Thus, functional conversion of the small curvature-active Dyn2 oligomers into the long helical fission machinery requires moderate PE amounts (e.g., 25 mol%, Fig. 3.12) or other lipid factors providing the membrane with similar mechanical behavior. Overall, the data presented here demonstrate that membrane lipidome could control the emergence and the function of the Dyn2 fission machinery. To obtain further mechanistic insight into the machinery emergence, we turned to single-molecule fluorescence microscopy (SMFM).

3.3.1.3 Single-molecule analysis of Dyn2 self-assembly

To perform SMFM characterization of the Dyn2 helix precursors on the membrane, we used the Dyn2-mEGFP construct. By measuring the fluorescence coming from the mEGFP molecule on the NT and normalizing it towards the single mEGFP molecule fluorescence, we can approach the process quantitatively. Single mEGFP fluorescence was measured in a separate experiment as described in the Materials and methods (Single-molecule fluorescence calibration). To reduce possible background and limit the protein self-assembly on the NTs, we lowered the concentration of Dyn2 to 20 nM Dyn2. Upon addition of the protein to the preformed lipid NTs the unbound Dyn2 molecules were quickly washed out from the system via perfusion. This approach allowed us to detect the initial ensemble of the smallest Dyn2 precursors on the membrane (Fig. 3.13 a). Consistent with the predictions of the above analysis, we found that Dyn2 adsorption began with the formation of small mobile clusters (Fig. 3.13 a, kymograph).

Further quantitative analysis revealed that the size of the smallest Dyn2 clusters detected on the NT membrane were consistent with a half of a Dyn2 helical rung (i.e., 12-16 molecules, Fig. 3.13 b). These data indicate that curvature recognition by Dyn2 occurs prior to full helical self-assembly and is intrinsic to small oligomers. It follows that the small Dyn2 oligomers located on the emergent CCPs are curvature active. Moreover, their inherent curvature generation and sensing capabilities may underlie their regulatory role in CCP maturation. The sorting of small oligomers to the neck could also form the core for subsequent

helical self-assembly, providing a plausible mechanism behind the timely emergence of the Dyn2 fission machinery in the cell.

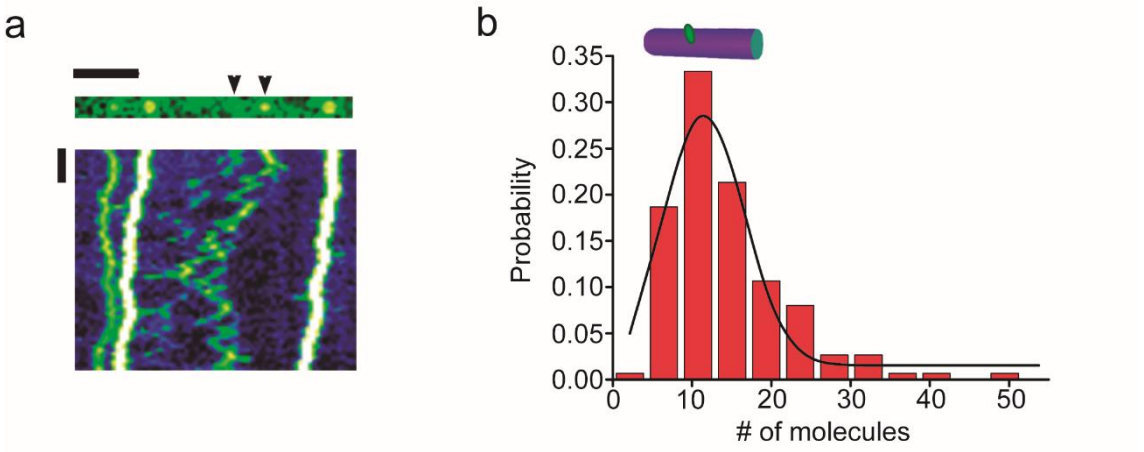

Figure 3.13. Visualization and quantification of small Dyn2-mEGFP oligomers on the lipid NTs. (a) Top: Fluorescence microscopy snapshot of the NT with bound Dyn2-mEGFP oligomers seen as bright spots. Bottom: Kymograph showing lateral mobility of Dyn2-mEGFP oligomers on the NT. The horizontal length scale is 500 nm. The vertical time scale is 2 s. **(b)** Histogram showing the size distribution of Dyn2-mEGFP oligomers (n=150). Maximum probability corresponds to half a ring of the Dyn2 helix shown in the schematic cartoon. The lipid composition is DOPE:DOPC:DOPS:Chol:Rh-DOPE:PI(4,5)P_2 25:52:10:10:1:2 mol%.

We then tested how these sub-helical Dyn2 oligomers self-assemble into fission machinery in the presence of GTP. The GTP (1-2 mM) addition caused rapid clustering of Dyn2 "half-ring" oligomers sitting on top of the lipid NT into structures containing 26-40 dynamin molecules. This number correlates with the number of Dyn2 molecules in a complete helical rung (Fig. 3.14 a), traditionally associated with a full-length fission apparatus[175,186]. However, the observed clustering of oligomers after GTP addition is likely due to GTP-driven dimerization between the GTPase domains of the sub-helical Dyn2-mEGFP oligomers[152] (Fig. 3.14 b). Notably, such small Dyn2-mEGFP oligomers could produce the NT underwent fission, albeit at a lower frequency than at a higher (0.5 μM) Dyn2 concentration (Fig. 3.14 c).

Crucially, the observed size increase of the Dyn2 complex in the presence of GTP suggests that Dyn2 nucleation is influenced not only by membrane curvature, as shown previously, but also by the GTP. This process is consistent with previous observations of GG dimerization, as dynamins have been widely

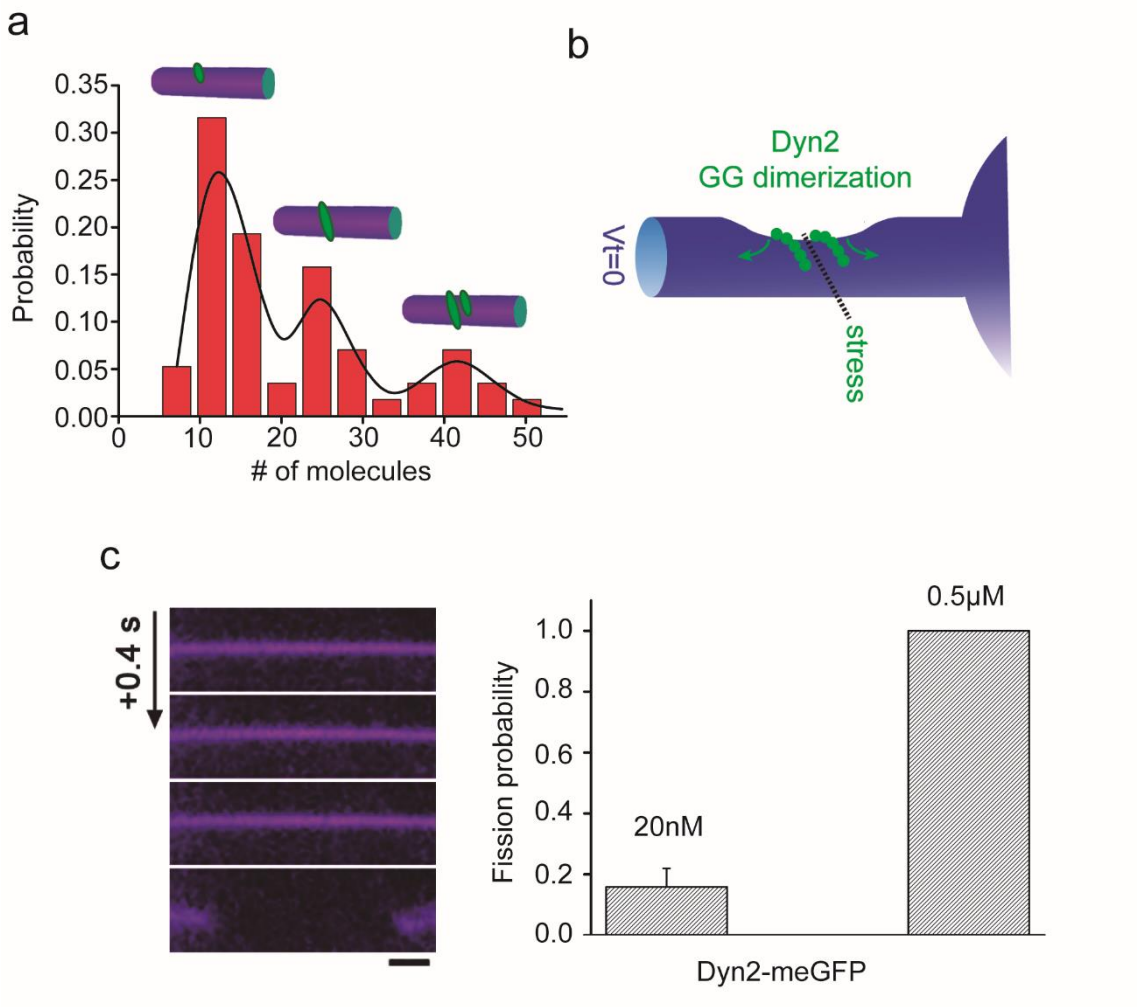

Figure 3.14. Quantification of the NT fission driven by small Dyn2-mEGFP oligomers. (a) Probability density histogram of the number of Dyn2 molecules in the protein complexes after GTP addition. The cartoon shows a schematic representation of the most probable Dyn2 structures as found in the peaks of the histogram. **(b)** Schematic representation of the minimal complex required for membrane fission after GG dimerization. **(c)** Dyn2 compaction by GG dimerization favors the formation of mechano-active Dyn2 oligomers capable of membrane fission. The left panel shows an image sequence of a NT, which undergoes membrane cleavage at 20 nM Dyn2. The right plot shows that fission still occurs at 20 nM in the bulk, albeit with much less extent than at 0.5 μM Dyn2 in the bulk. The lipid composition is DOPE:DOPC:DOPS:Chol:Rh-DOPE:PI(4,5)P_2 25:52:10:10:1:2 mol%. Scale bar is 1 μm.

described to oligomerize through GG interactions across the G2 interface when arrested in the catalytic transition state of the GTPase cycle[162,174]. Indeed, the recently proposed 2-start helix model of Dyn1, in which two helical turns of Dyn1 interact directly through their GTPase domain[166,177], implies dynamin self-assembly in the physiological context where GTP is always present in the cell. Therefore, we speculate that GTP may promote the lateral interaction of small sub-helical Dyn2 complexes, facilitating the transition from a curvature sensor to

a mechano-active fission machinery. In this context, while PE crucially facilitates such a transition, GTP acts as a master regulator of the fission activity of Dyn2.

3.3.2 PE triggers functional promiscuity of Dyn2

Surprisingly, we found that PE not only facilitates the transition of Dyn2 into a functional, fission competent machinery, but also favors other, non-canonical behaviors of the protein. Apart from well-defined protein helices surrounding the membrane (Fig. 3.8 b), cryoEM analysis of samples with high PE content revealed that Dyn2 was forming irregular patterns on the NTs (Fig. 3.15) as well as bridging adjacent LUV membranes together (Fig. 3.15, red arrow). Crucially, this finding is reminiscent of the previous analysis of bacterial dynamin-like proteins (BDLPs) mediating membrane tethering[187].

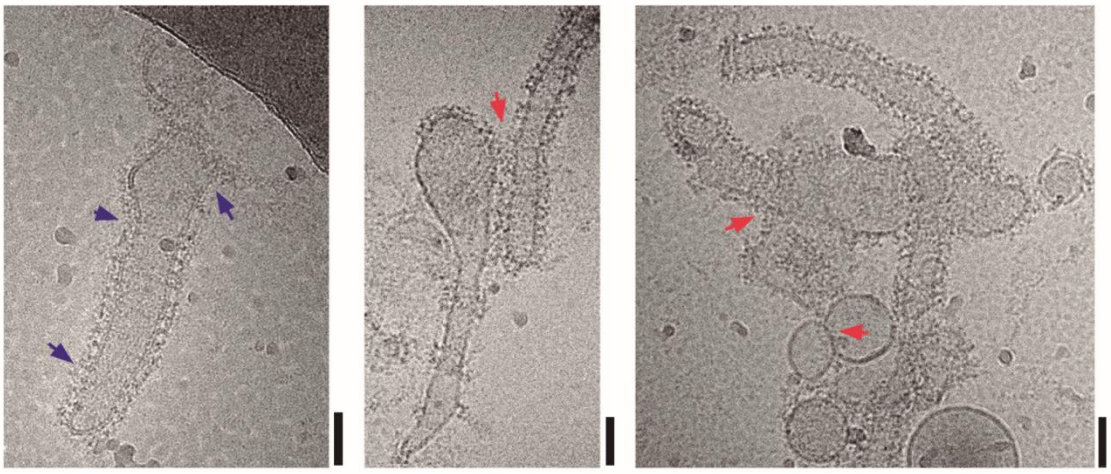

Figure. 3.15. PE provokes non-canonical behavior in Dyn2. Representative cryoEM micrographs of Dyn2 assemblies on the membrane containing 40 mol% PE. Blue arrows indicate irregularities in Dyn2 packing on the membrane, and red arrows indicate trans-membrane contacts induced by Dyn2. The lipid composition is DOPE:DOPC:DOPS:Chol:Rh-DOPE:PI(4,5)P_2 40:37:10:10:1:2 mol%. Scale bars are 20 nm.

Therefore, we wondered whether the stacked protein observed by CryoEM mediates the stabilization of contacts between membranes, as previously suspected for BDLPs. With this in mind, we relied on fluorescence microscopy to test this hypothesis. Crucially, in the absence of GTP, WT Dyn2 produced robust aggregation of LUVs containing 40 mol% PE (Fig. 3.16 a), confirming the phenotype observed by EM. We then used Dyn2-mEGFP to directly monitor the behavior and co-localization of the protein in the membrane tethering process.

The fluorescence data analysis (Fig. 3.16 b) further confirmed the active role of Dyn2 in the process of membrane tethering between LUVs.

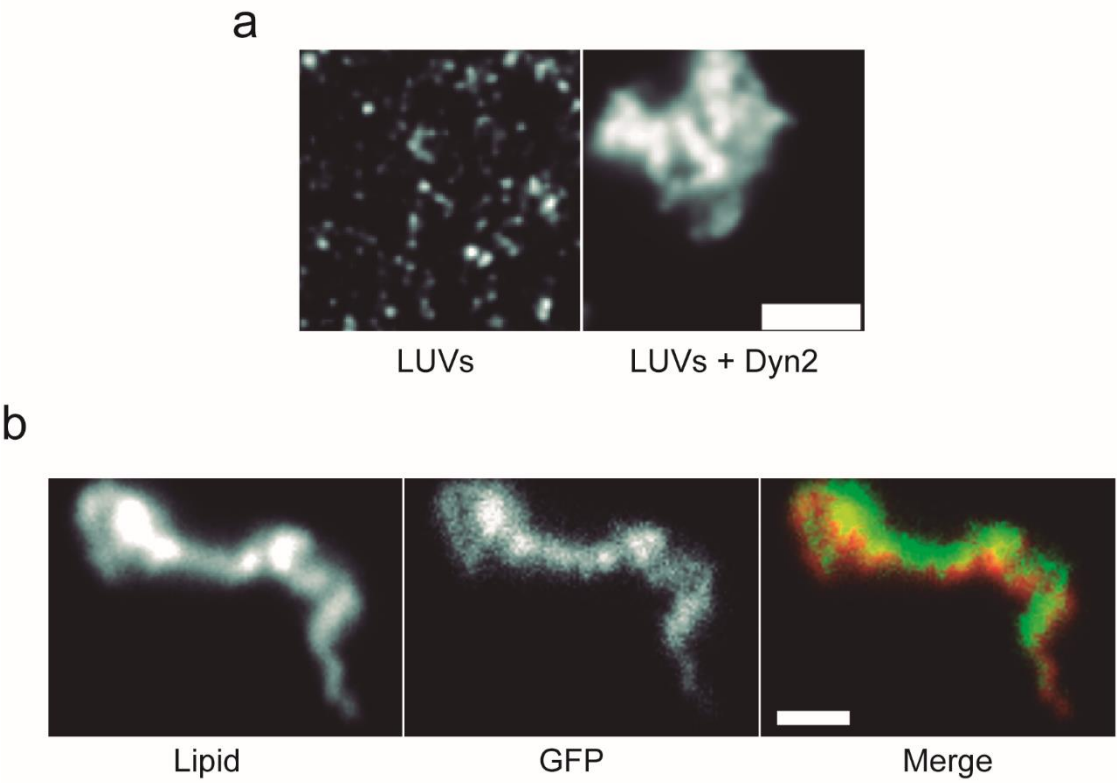

Figure 3.16. Dyn2-driven membrane aggregation observed by fluorescence microscopy. (a) Representative images of LUVs without protein (left) and LUV aggregates upon 20 min incubation with WT Dyn2 (right). Scale bar is 2 µm. **(b)** Colocalization between the LUV membranes and Dyn2-mEGFP. The lipid composition is DOPE:DOPC:DOPS:Chol:Rh-DOPE:PI(4,5)P_2 40:37:10:10:1:2 mol%. Scale bar is 4 µm.

Interestingly, we found that removing PE from LUVs´ membrane resulted in complete inhibition of membrane tethering by Dyn2 (Fig. 3.17). This inhibition was not due to a decrease in binding efficiency between Dyn2 and the model membrane, as at 2mol% of PI(4,5)P_2 both WT Dyn2 and Dyn2-mEGFP showed strong binding to 100 nm LUVs without PE (Fig. 3.17 a, top panel). Furthermore, we quantified the extent of membrane tethering observed by fluorescence microscopy in LUV membranes with and without PE (Fig. 3.17 a, lower panel). Quantification was performed by measuring the total fluorescence intensity of the under-diffraction spots as a metric for cluster size[188]. Quantitative analysis showed that at 0.5 µM Dyn2, the clustering process progressed rapidly to massive LUV aggregates only in membranes containing PE, whereas in membranes lacking PE, the tethering effect was completely abolished (Fig. 3.17

b). These results suggest that Dyn2 mediates the tight contacts between LUV membranes and that membrane mechanics is likely an important regulator of the observed tethering.

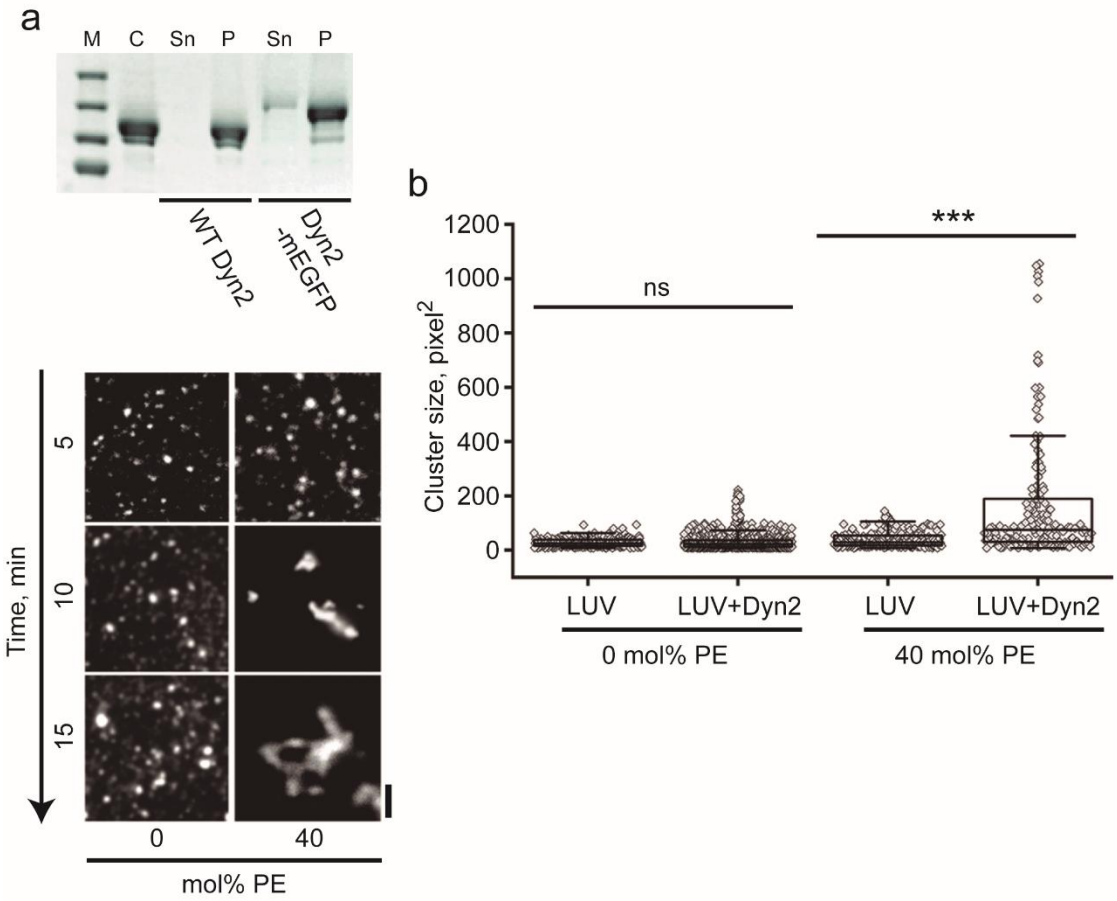

Figure 3.17. Lipid-dependent membrane tethering by Dyn2. (a) Upper panel: sedimentation assay measuring Dyn2-membrane binding between 100 nm LUVs without PE in the lipid composition. Proteins used were WT Dyn2 and Dyn2-mEGFP (binding efficiency between Dyn2 and 40 mol% PE LUVs is shown in Fig. 3.7 a). Lower panel: The time sequence illustrates the clustering effect upon the addition of Dyn2 (0.5 µm, time 0) to LUVs without PE and with 40 mol% PE. Rh-DOPE fluorescence is shown. Scale bar is 2 µm **(b)** Quantification of the size of LUV aggregates shown in **(a)**. The area of the clusters was measured 10 to 15 min after the incubation of Dyn2 with LUVs. The data set represents three independent experiments for each condition. Statistical significance: Wilcoxon signed ranks test, ****p*<0.001, ns- not significant. Boxplots show IQR, whiskers indicate the minimum and maximum of the dataset. The lipid composition is DOPE:DOPC:DOPS:Chol:Rh-DOPE:PI(4,5)P_2 40:37:10:10:1:2 mol% or DOPC:DOPS:Chol:Rh-DOPE:PI(4,5)P_2 77:10:10:1:2 mol%

To further confirm how intrinsic curvature of the lipid species affects the functional promiscuity shown by Dyn2, we decide to measure the tethering effect on membranes containing lipids with different inherent curvatures.

3.3.2.1 The lipidome regulates Dyn2-driven membrane tethering

As explained earlier, several lipid species, such as PE, PC, or even CL, are synthesized from a common DAG backbone. Structurally, PE, CL, and DAG exhibit intrinsic negative curvature, being the biggest for DAG. Therefore, we wondered whether DAG or CL have a similar effect on Dyn2, as the one previously shown on PE-containing membranes in the LUV tethering context.

For that, we prepared LUV from membranes containing 15 mol% PE or DAG and measured membrane tethering by fluorescence microscopy as described above (Fig. 3.18). As expected, Dyn2 was able to induce similar

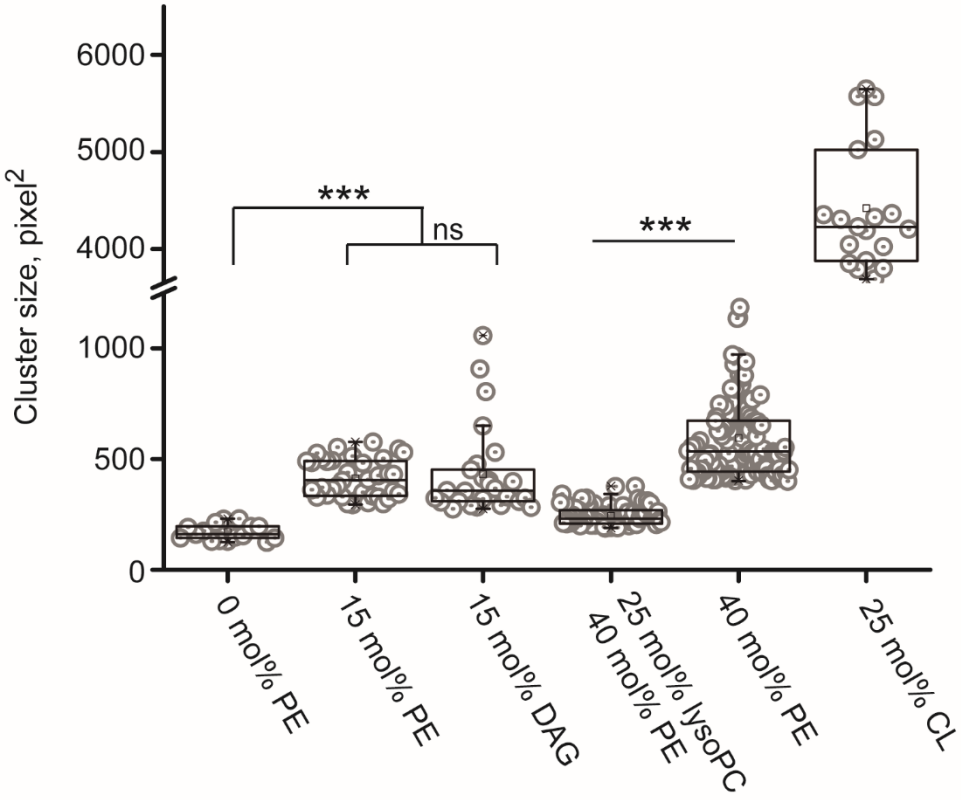

Figure 3.18. Lipidome influence on Dyn2-driven membrane tethering. Quantification of the area of the membranous clusters induced by the 10-15 minute incubation of 0.5 μM Dyn2 with LUVs containing different amounts of intrinsically curved lipids as indicated. The dataset represents at least three independent experiments. Statistical significance: Wilcoxon signed ranks test, ***p<0.001, ns- not significant. Boxplots show IQR, whiskers indicate the maximum and minimum of the dataset. The lipid compositions are DOPC:DOPS:PI(4,5)P_2:Rh-DOPE 87:10:2:1; DOPE:DOPC:DOPS:PI(4,5)P_2:Rh-DOPE 15:72:10:2:1; DAG:DOPC:DOPS:PI(4,5)P_2:Rh-DOPE 15:72:10:2:1;1-oleoyl-2-hydroxyl–sn–glycerol–3-phosphocholine(lysoPC):DOPE:DOPC:DOPS: PI(4,5)P_2:Rh-DOPE 25:40:22:10:2:1; DOPE:DOPC: DOPS:PI(4,5)P_2:Rh-DOPE 40:47:10:2:1; CL:DOPC:DOPS:PI(4,5)P_2:Rh-DOPE 25:62:10:2:1, respectively.

membrane tethering in both types of LUVs (Fig. 3.18). Since the ability of Dyn2 to recognize membrane curvature for further self-assembly was described previously, and that it binds to lipid bilayers thanks to a combination of membrane defects caused by curved lipids and electrostatics, we decided to test how functional promiscuity is affected by the negatively charged and also negatively curved CL. Therefore, we further tested membrane tethering by Dyn2 at membranes containing 25 mol% CL. Interestingly, we found that the tethering effect produced by Dyn2 in the presence of CL was 10 times stronger than the one detected on membranes containing 40 mol% PE (Fig. 3.18). This result may have a physiological significance as Dyn2 was proposed to function at the mitochondria fission site, which is believed to be enriched with CL[189].

As negatively curved lipids promote membrane tethering by Dyn2, we then tested if lipids with the opposite curvature would have an inhibiting effect on tethering. When 25 mol% of positively curved 1-oleoyl-2-hydroxy-sn-glycero-3-phosphocholine (lysoPC) was added in a membrane containing 40 mol% PE, we observed an inhibition of Dyn2-mediated tethering (Fig. 3.18). Therefore, local membrane curvature promoted by lipid species with different intrinsic curvature regulates the functional promiscuity of Dyn2.

3.3.2.2 Differential regulation of membrane tethering by GTP and lipid mechanics

Since we have only considered the membrane tethering activity of Dyn2 in the nucleotide-free state, we wondered how GTP would affect the aforementioned process. We focused on testing the two lipid compositions showing the stronger membrane tethering effect, 40 mol% of PE and 25 mol% of CL. We found that the addition of GTP to the chamber inhibited Dyn2-mediated membrane tethering on PE-containing membranes. Remarkably, the inhibition decreased only gradually with GTP concentration. Thus, at a low but physiological concentration of 0.2 mM GTP[190], both activities of membrane fission[128] and membrane tethering (Fig. 3.19 a) can coexist in membranes containing substantial amounts of PE, such as the mitochondrion. In contrast, we found that neither 0.2 mM nor 2 mM GTP blocked tethering activity in CL membranes (Fig. 3.19 b). This effect could be due to the higher extent of

membrane aggregation compared to PE-containing membranes. Thus, the Dyn2-mediated tethering in CL-containing membranes cannot be reversed by GTP (Fig. 3.19 b).

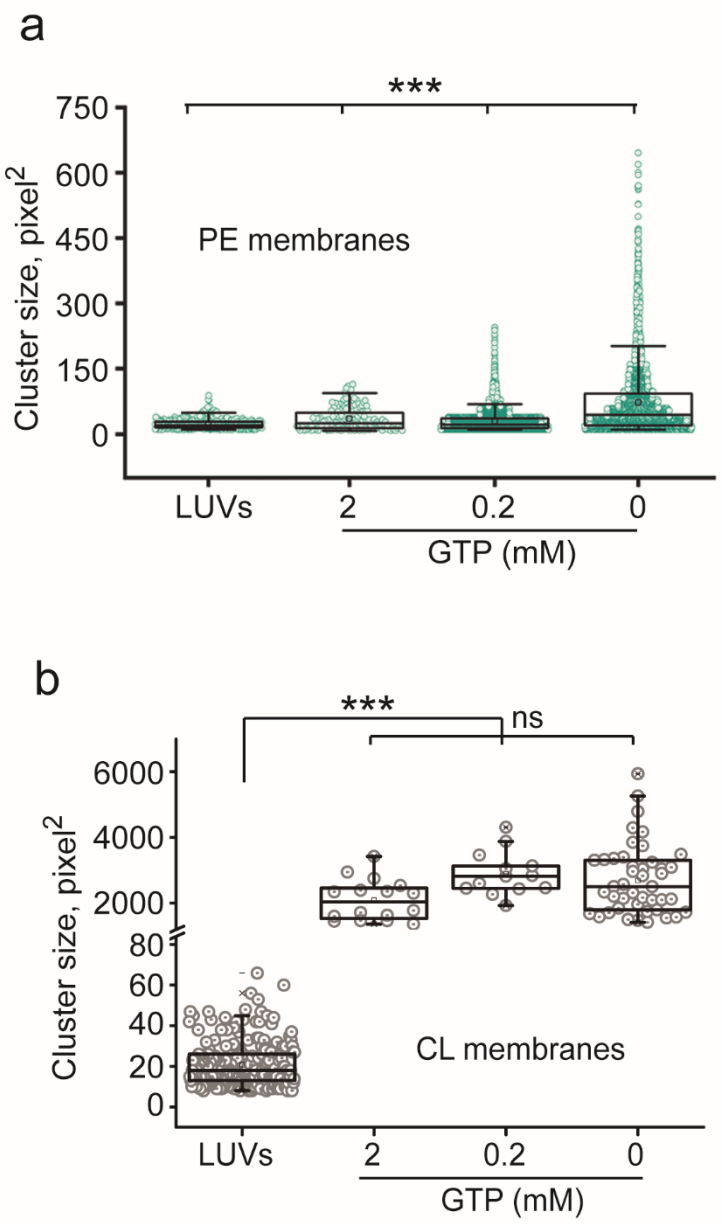

Figure 3.19. GTP regulation of Dyn2 induced membrane tethering. (a) GTP affects cluster formation in LUVs containing 40 mol% PE. Boxplots show IQR, whiskers indicate the minimum and maximum of the dataset. Statistical significance: Kruskal-Wallis ANOVA, ****p*<0.001. The lipid composition is DOPE:DOPC:DOPS:Chol:Rh-DOPE:PI(4,5)P_2 40:37:10:10:1:2 mol%. **(b)** GTP does not affect Dyn2-induced clusterization of LUVs with 25 mol% CL in their composition. Boxplots show IQR whiskers indicate the maximum and minimum of the dataset. Statistical significance: Kruskal-Wallis ANOVA, ****p*<0.001, ns- not significant. The lipid composition is CL:DOPC:DOPS:PI(4,5)P_2:Rh-DOPE 25:62:10:2:1 mol%

3.3.2.3 Dyn2-driven lipid mixing between LUVs

We decided to focus on membranes containing 40 mol% PE as we have previously shown Dyn2 self-assembly on these membranes in the context of membrane fission. CryoEM micrographs of samples with PE containing LUVs and Dyn2 indicate the formation of local trans-membrane bridges reminiscent of the stalk intermediate of membrane fusion[191] (Fig. 3.20 a). PE is expected to promote the formation of such membrane structures as well as lipid exchange between the tethered membranes[179]. To directly test if there is lipid mixing in the presence of Dyn2, we employed the lipid mixing assay using FRET, as previously applied to study Atl and Atl/Rtnl1 proteo-liposomes interactions.

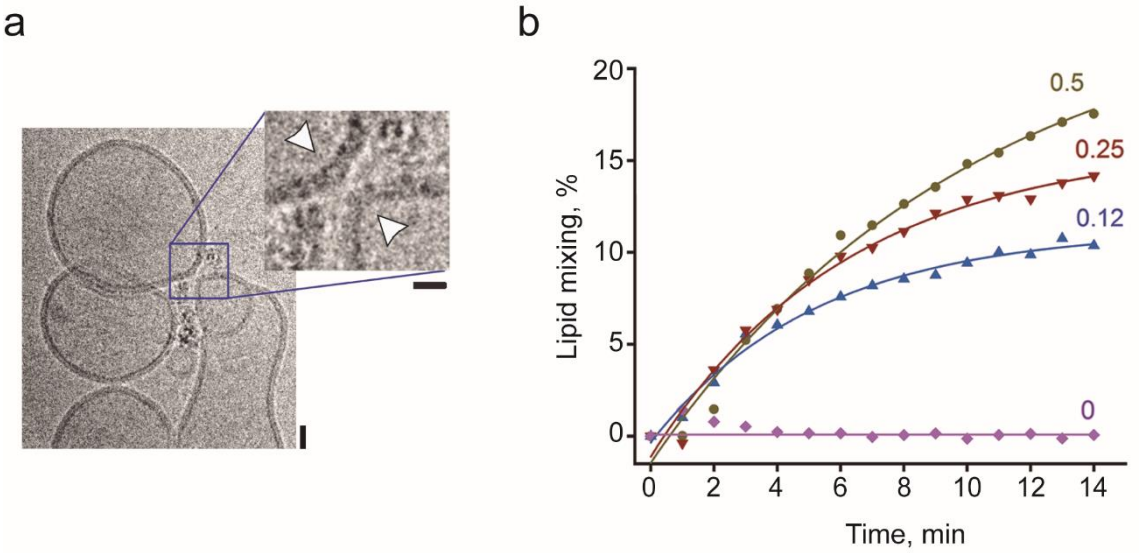

Figure 3.20. PE- and Dyn2-driven membrane aggregation leads to lipid exchange between the membranes. (a) Representative cryoEM micrograph showing the dimple-like structure formed upon Dyn2 tethering of the membranes containing 40 mol% of PE (white arrowheads). **(b)** Representative kinetic curves of the lipid mixing between LUVs measured by a FRET assay upon addition of different concentrations of Dyn2 as indicated in the graph. The pair Rh-DOPE and NBD-DOPE were used as donor-acceptor, respectively (see Materials and methods: Lipid mixing). NBD-DOPE fluorescence is shown. The lipid composition is DOPE:DOPC:DOPS:Chol:Rh-DOPE:NBD-DOPE:PI(4,5)P_2 40:35:10:10:1.5:1.5:2 mol%.

In the LUVs containing high amounts of PE, lipid mixing occurred quickly upon Dyn2 addition (Fig. 3.20 b), clearly indicating that Dyn2, in a concentration-dependent manner, could promote lipid exchange between tethered lipid membranes. In contrast, although CL-containing LUVs were much more efficient in membrane attachment by Dyn2, they did not undergo lipid exchange under conditions similar to PE membranes. Therefore, while lipid curvature and

electrostatics promote membrane tethering and clustering, only PE appears to be the specific trigger for lipid exchange. However, further systematic analysis is required to confirm these conclusions and link them to the *in vivo* scenario.

So far, we analyzed the lipid mixing in the buffers containing divalent ions, such as Magnesium (Mg^{2+}) or Ca^{2+}, as Dyn2 relies on the Mg^{2+} ion to carry out its enzymatic activity during GTP hydrolysis[192]. We next systematically analyzed the effect of divalent on lipid mixing. We found that although lipid mixing depends on the electrostatic interactions triggered by Mg^{2+} or Ca^{2+}, Mg^{2+} has a greater impact on the efficiency of the process (Fig. 3.21 a). Besides, we did not detect lipid mixing in the absence of Dyn2 at 5 mM Mg^{2+} or 5 mM Ca^{2+} (Fig. 3.21 b). Therefore, lipid mixing by Dyn2 results from a convolution of lipid geometry, electrostatics, and protein-driven membrane tethering, the combo long associated with membrane fusion mediated by SNAREs[188,193].

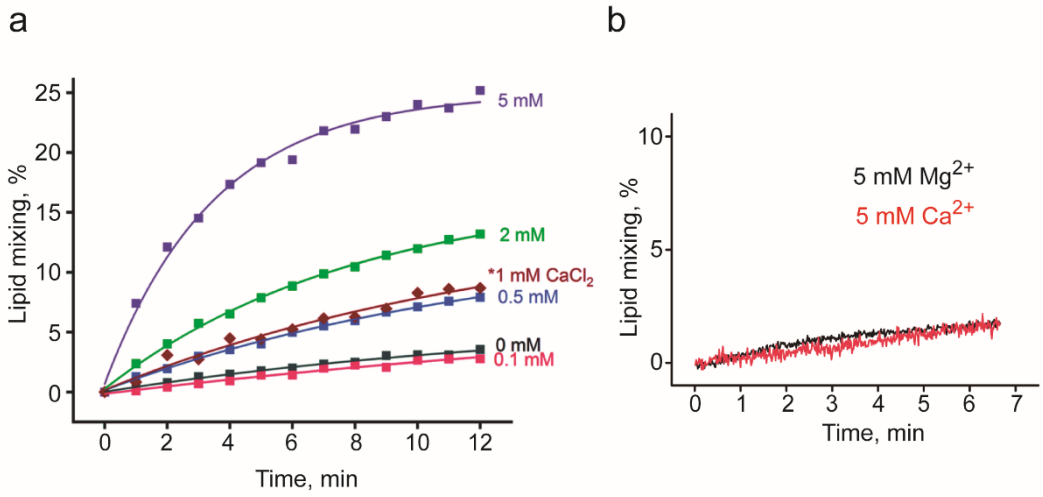

Figure 3.21. Divalent Mg^{2+} or Ca^{2+} are required to trigger Dyn2-driven lipid exchange between tethered membranes. (a) Effect of Mg^{2+} on lipid mixing induced by 0.5 µM of Dyn2 between two populations of LUVs, as measured by FRET. The brown curve shows the impact of the addition of Ca^{2+} instead of Mg^{2+}. NBD-DOPE fluorescence is shown. **(b)** Effect of 5 mM Mg^{2+} (black) or Ca^{2+} (red) on lipid mixing measured as in (a), but in the absence of Dyn2. The lipid composition is DOPE:DOPC:DOPS:Chol:Rh-DOPE:NBD-DOPE:$PI(4,5)P_2$ 40:35:10:10:1.5:1.5:2 mol%.

These results were initially unexpected for Dyn2, as it is generally classified as a protein specialized in membrane fission in endocytosis. The functional specialization of Dyn2 is in part due to its interaction with other proteins

implicating in membrane remodeling during endocytosis. The interaction is mediated by the PRD domain of Dyn2 specifically recognizing SH3 domain proteins. One of the SH3-containing partners of Dyn2 is amphiphysin (amph), which regulates membrane interactions of Dyn2 during CME[185,194]. The addition of amph to the reaction inhibited Dyn2-driven lipid mixing (Fig. 3.22 a). Indeed, at a molar ratio of 1:2 Dyn2:amph, the inhibition is comparable to that produced by the addition of GTP (Fig. 3.22 a). Therefore, in the intracellular context, the functional promiscuity of Dyn2 found *in vitro* would be strongly inhibited by its canonical partners (such as amph) and cofactors (GTP).

However, in scenarios involving GTP depletion, Dyn2 in combination with conical lipids could become a potent trigger of membrane tethering and even fusion. The overall results shown here prompted us to analyze in search of functional promiscuity the behavior of a known fusogen from the dynamin superfamily, Atl. We have previously demonstrated that GTP is required for Atl mediated membrane tethering and lipid mixing, but the membrane we used were different from the one employed for Dyn2. Thus, we began by reconstituting Atl into model membranes containing 40 mol% PE. As expected, we found that, in the presence of GTP, Atl produced an effective lipid exchange independent of the presence of PE in the membrane (Fig. 3.22 b). However, as previously shown for Dyn2, the presence of PE was critical for lipid mixing in the absence of GTP (Fig. 3.22 b). Therefore, both Dyn2 and Atl were shown to promote membrane tethering and lipid mixing upon removal or depletion of GTP in membranes containing a substantial amount of PE, indicating the ability of dynamins to form primitive membrane contact sites.

We further asked whether the curved lipids, such as PE, could mediate membrane tethering and lipid mixing due to irregular protein accumulation (crowding) or whether this process could be related to the previous findings on Dyn2 activity before or after helical self-assembly. With this in mind, we relied on single-molecule fluorescence microscopy as previously used.

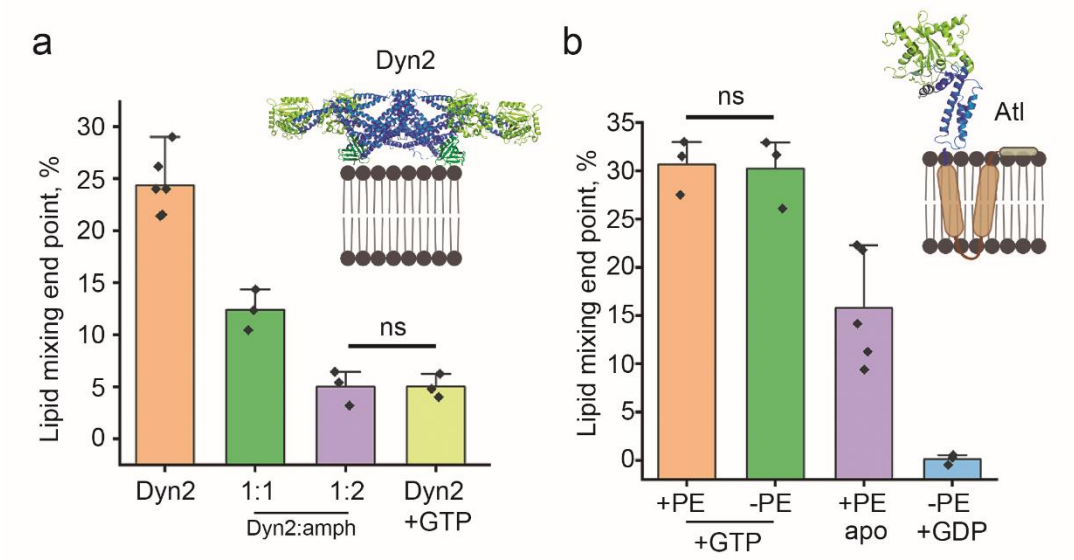

Figure 3.22. Functional promiscuity of dynamins is controlled by membrane lipidome, GTP, and protein partners. (a) The effect of amph and GTP on the efficiency of the Dyn2-induced lipid mixing in the LUV system. 0.5 μM of Dyn2 and 5 mM of Mg^{2+} were used in all the experiments. Statistical significance: ns- not significant. **(b)** Effect of GTP (5 mM) and PE (40 mol%) on the lipid mixing between proteo-liposomes containing Atl at 1:400 protein to lipid ratio, in the presence of 5 mM Mg^{2+}. Error bars are SD in at least three independent experiments for each condition. Statistical significance: one-way ANOVA with post hoc Bonferroni test, ***p<0.001. The lipid composition is DOPE:DOPC:DOPS:Chol:Rh-DOPE:NBD-DOPE:PI(4,5)P_2 40:35:10:10:1.5:1.5:2 mol%.

3.3.2.4 Single-molecule analysis of Dyn2-driven membrane tethering

To test whether protein crowding, as suggested by the cryoEM images, is responsible for mediating membrane tethering, we turned to the previously developed *in vitro* system to perform single-molecule counts over lipid NTs. To observe membrane tethering, this time, we added fluorescently labeled LUVs (0.1 mol% of Rh-DOPE to avoid fluorescence crosstalk) in the presence of 20 nM protein to the chamber to capture the membrane-membrane interactions between the LUVs and the NT. After washing away the unbound material, we observed the colocalization of the LUVs, NTs, and Dyn2-mEGFP oligomers (Fig. 3.23 a), indicating formation of the tethering complex. The NT-tethered LUVs moved along the tubule axis (Fig. 3.23 a, kymograph), indicating that the tethering complex is small and does not restrict the lateral mobility of the vesicles. Further quantification of the fluorescence of Dyn2-mEGFP colocalized with the moving vesicles showed that the tethering complex contains 38±16 Dyn2 molecules. The size of the lower group of the Dyn2 cluster (Fig. 3.23 b, left peak) approached a complete turn of the Dyn2 helix, a structure suitable for stabilization. The structure

is about twice the size of the sub-helical Dyn2-mEGFP oligomers at the NT without the LUV (Fig. 3.13 b). Therefore, this difference in size likely means that the Dyn2 tethering complex is formed by the interaction between sub-helical oligomer precursors bound at each membrane.

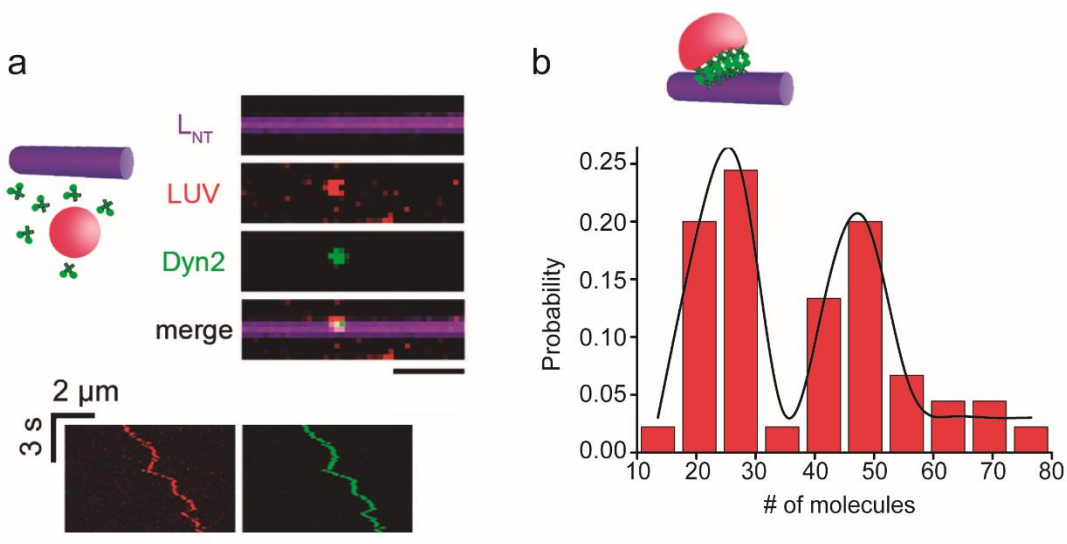

Figure 3.23. Sub-helical Dyn2 oligomers promote membrane tethering between LUVs and lipid NTs. (a) Tethering of 100 nm LUVs (red) to the lipid NT (magenta) by Dyn2 (10-2 nM, green) in the absence of GTP. The kymograph shows how Dyn2 (green) colocalizes with the liposome (red), moving synchronously on the NT axis. **(b)** Histogram showing the number of Dyn2 molecules involved in the tethering process between the LUV and the lipid NT. The cartoon represents the hypothetical configuration of the protein complex mediating membrane tethering for the number of Dyn2 molecules counted on the left peak. The data was obtained by single-molecule fluorescence counting, as described in the previous chapter. The lipid composition is DOPE:DOPC:DOPS:Chol:Rh-DOPE:PI(4,5)P_2 40:37:10:10:1:2 mol%.

To summarize, our results identify small sub-helical Dyn2 oligomers as common precursors of the membrane tethering and fission complexes formed by Dyn2. We propose that GTP, lipidome adaptation, and protein partners regulate Dyn2 self-assembly along these two pathways, controlling the functional promiscuity of Dyn2 in the intracellular context. We believe that further efforts based on the data presented in this dissertation will lead to exciting findings on new Dyn2 functions in the cellular context.

4. Conclusions

We have demonstrated that both Rtn1 and Dyn2 are multitasking membrane remodeling proteins capable of switching between different functional modalities upon receiving mechanical cues from the membrane. They both create and sense membrane stresses and act in accordance with their assessment of the membrane, its mechanics, dynamics and topology. They both can produce seemingly opposing membrane transformations. Rtnl1 could mediate both formation and destruction of the tubular membrane network. Dyn2 could both produce membrane fission and mediate membrane tethering and lipid mixing. We believe that this multifunctional nature of membrane remodeling proteins suits well to complex and dynamic membrane architecture of the intracellular space and enables the proteins not only to perform a particular task but also communicate with other membrane remodeling systems and processes, ultimately ensuring the coherent working of the intracellular interior. Below, we detailed the major conclusions of this PhD project:

Rtnl1 part

1. Balancing of membrane remodeling activities of Rtnl1 and Atl control the morphology of the endoplasmic reticulum in *Drosophila* cell

2. Purified Rtnl1 reconstituted into biomimetic lipid membranes senses and creates membrane curvature

3. Purified Rtnl1 mediates constriction and fission of membrane nanotubes pulled from Rtnl1-containing biomimetic membranes

4. Rtnl1-driven membrane fission is coupled to membrane motility

5. Rtnl1 and Atl work synergistically in creating ER-mimetic tubular membrane network from proteo-liposomes containing both proteins

Dyn2 part

6. Small non-helical Dyn2 oligomers, the precursors of helical self-assembly, sense membrane curvature

7. Helical self-assembly of Dyn2 is controlled by phosphatidylethanolamine (PE), a cone-shaped lipid abundant in cellular membranes

8. Dyn2 can mediate tethering and lipid mixing between lipid vesicles containing cone-shaped lipids

9. The functional promiscuity of Dyn2 is controlled by lipids, GTP and protein partners containing SH3 domains

10. Minimal membrane fission and tethering complexes of Dyn2 are formed via dimerization, on-membrane, or trans-membrane, respectively, of sub-helical Dyn2 oligomers.

5. Materials and methods

5.1 General buffers, equipment and materials

Stock solutions

Calcium Chloride solution, $CaCl_2$	1M, # J63122, Fluka, Sigma-Aldrich, USA
Chloroform for HPLC	#366927, Sigma-Aldrich, USA
D-(+)-Trehalose dihydrate	#T9449, Sigma, Sigma-Aldrich, USA
Dithiothreitol, DTT	#GE17-1318-01, Sigma, Sigma-Aldrich, USA
Ethanol (≥99,5%)	EMSURE, #100983, Merk Millipore, USA
Ethylene glycol-bis(2-aminoethylether)-N,N,N′,N′-tetraacetic acid, EGTA	#E3889, Sigma, Sigma-Aldrich, USA
Ethylenediaminetetracetic acid solution, EDTA	0.5M, pH 8.0 #03690, Fluka, Sigma-Aldrich, USA
Hepes Buffer	1M solution pH 7.3, #BP299, Fisher Bio reagents, ThermoFisher Scientific, USA
Magnesium Chloride solution, MgCl2	1M, #63069, Fluka, Sigma-Aldrich, USA
Methanol (≥99,8%)	NORMAPUR, #20847, VWR, USA
Phosphate-buffered saline, PBS	Phosphate-buffered saline 10X, #BP399-1, Fisher BioReagents™, USA
Potassium Chloride, KCl	#P9333, SigmaUltra, Sigma-Aldrich, USA

SDS-Running buffer	Tris-Glycine SDS Running Buffer (10X) # LC26754, Invitrogen™ Novex™, USA
Triton X-100	#T8787, Sigma, Sigma-Aldrich, USA

Buffers

Buffer A	20 mM Hepes, pH 7.4, 150 mL NaCl, 1 mM DTT
Buffer A100	25 mM Hepes, 100mM KCl, 10% glycerol, 2mM DTT, 1mM EDTA
Buffer A200	25 mM Hepes, 200 mM KCl, 10% glycerol, 2 mM DTT, 2 mM EDTA, 4% Triton-X100
Buffer B	20 mM PIPES, pH 6.1-6.5, 1.2 M NaCl, 10 mM CaCl2, 1 mM DTT
Working buffer	20 mM Hepes pH 7.4, 150 mM KCl, 5 mM MgCl2, 1 mM EDTA
Lysis buffer	50 mM NaH2PO4, 0.3 mM NaCl, 10 mM imidazole, 10% glycerol, 4% Triton-X100
Washing buffer 0	50 mM NaH2PO4, 0.3 mM NaCl, 10 mM imidazole, 1 mM EDTA, 10% glycerol, 4% Triton-X100
Washing buffer 1	50 mM NaH2PO4, 0.3 mM NaCl, 10 mM imidazole, 1 mM EDTA, 10% glycerol, 1% Triton-X100
Washing buffer 2	50 mM NaH2PO4, 0.3 mM NaCl, 10 mM imidazole, 1 mM EDTA, 10% glycerol, 0.1% Triton-X100

Elution buffer	50 mM NaH2PO4, 0.3 mM NaCl, 250 mM imidazole, 10% glycerol, 0.1% Triton-X100
Dialysis buffer for model membranes	1 mM TRH, 1 mM Hepes pH 7.4
Hydration buffer	1 M TRH, 1 mM Hepes pH 7.4

General materials

Dialysis cassettes	Slide-A-Lyzer™, 10K MWCO, 3 ml # 66380, ThermoFisher Scientific, USA
pH paper strips	Macherey-Nagel, Germany
SDS marker	PageRuler™ Plus Prestained Protein Ladder, 10 to 250 kDa # 26620, ThermoFisher Scientific, USA
Blue Safe Protein Stain	GelCode™, #24594, ThermoFisher Scientific, USA
Black Bottom Plate 96-Well	#165305, ThermoFisher Scientific Inc., USA
Nunc™ MicroWell™ 96-Well	Nunclon Delta-Treated, Flat-Bottom Microplate, #167008, ThermoFisher Scientific, USA
SDS-PAGE Electrophoresis Gel	Novex™ 4-20% Tris-Glycine Mini Gels, WedgeWell™ format, 12-well, #XP04202BOX, ThermoFisher Scientific, USA
Guanosine 5´-triphosphate lithium salt, Li GTP	#G5884, Sigma, Sigma-Aldrich, USA

Guanosine 5´-triphosphate sodium salt, Na GTP	#G5884, Sigma, Sigma-Aldrich, USA
Guanosine 5´-diphosphate sodium salt, Na GDP	#G7127, Sigma, Sigma-Aldrich, USA
Parafilm	4" Parafilm ® M Barrier Film, SPI supplies, USA
Cover glass	No.1, 25mm diameter glass covers, #41001125, Waldemar Knittel Glasbearbeitungs, Germany
Coverslip chamber 25mm	QR-40LP, Warner Instruments, USA
Triton X-100	Triton™ X-100 Surfact-Amps™ Detergent Solution, #85111, TermoFisher Scientific Inc., USA

General equipment

Balance	CP32025, CP225D and ME36S-0CE, Sartorius, Germany
Bath sonicator	FB15049, Fisher Scientific, Thermo Fisher Scientific, USA
Bench centrifuge	Biocen 22R, Ortoalresa, Spain
Electrophoresis tank	Mini Gel Tank #A25977, Invitrogen™, USA
Microplate reader	Synergy HT, BioTek Instruments Inc., USA
Peristaltic Pump	2C 7.0 mbar, Vacuumbrand, Germany

Ultrapure water purification system	Ultrapure Direct-Q® 3 UV, Merck-Millipore, Germany
Variable Volume Single Channel Pipettes	0.1-2, 2-20, 20-200, 100-1000, Discovery Comfort, HTL, Germany
Sonicator	Soniprep 150, MSE, UK
Rotating mixer	Benchmark Scientific, R5010-ES, Sigma, Sigma-Aldrich, USA
Thermostatic Bath	CBN 18-30, Heto-Holten, Germany
Vortex	2x3, Velp Scientifica, Italy
Cell culture incubator	Galaxy® 48 R, Eppendorf, Germany
Epifluorescence microscopy	
IX-71 inverted microscope, Olympus, Japan	
Andor Camera	iXon EM+, Andor, Ireland
Fluorescence filter cube set for FITC	485/505 ex/em, Semrock, USA
Fluorescence filter cube set for TRITC	560/585 ex/em, Semrock, USA
Fluorescence filter cube set for CY-5	649/662 ex/em, Semrock, USA
Fluorescence Lamp	Series 120PC Q, X-Cite, Lumen dynamics, USA
Lense	UAp o 150X/1,45 Oil TIRFM, Olympus, Japan

Microscope stage-top incubator	Tokai Hit Stage Top Incubator INUG2-GSI2-SET, Japan
Optical table	Newport, USA
PC workstation	Dell Inc., USA
Eclipse Ti-e inverted microscope, Nikon, Japan	
Zyla Camera	Zyla 4.2 sCMOS, Andor, Oxford Instruments, UK
Fluorescence filter cube set for FITC	485/505 ex/em, Semrock, USA
Fluorescence filter cube set for TRITC	560/585 ex/em, Semrock, USA
Fluorescence filter cube set for CY-5	649/662 ex/em, Semrock, USA
Fluorescence Lamp	pE-4000, Cooled, UK
Lense	CFI Apo TIRF 100X Oil (NA=1.49), Nikon, Japan
Optical table	Newport, USA
PC workstation	Dell Inc., USA
General data acquisition and analysis softwares	
µManager	version 1.4, µManager, NIH, USA
Image J	64, 1.50n, NIH, USA
Origin 8	SR4, OriginLab Inc., USA

5.2 Live-cell imaging in COS-7 cells

5.2.1 Equipment and materials

Cell culture

Automated Cell Counter	TC20™ Automated Cell Counter, BioRad, USA
Cell Culture Imaging Dish	Glass bottom Dish 35mm, #81218-200, Ibidi®GmbH, Germany
COS-7 cells	ATCC® CRL-1651™, ATCC®, USA
Counting Slides	Dual Chamber for cell counter, #145-0011, BioRad, USA
DMEM	HyClone, Thermo Scientific, USA
Flask	TC Flask T25, Stand. Vent. Cap, #83.3910.002, Sarstedt, Germany
Medium	DMEM (1X), high glucose, GlutaMAX™ Supplement, #10566016, Gibco® by life technologies, USA
Transfection reagent	Lipofectamine 2000 Transfection Reagent, #11668027, Thermo Scientific, USA
Trypan Blue Solution	Trypan Blue Stain (0,4%), #15250-061, Gibco® by life technologies, USA
Trypsin	Trypsin-EDTA 0,05% (1X), #25300-062, Gibco® by life technologies, USA

5.2.2 Methodology

COS-7 cells were transfected with mGFP-Rtnl1 or Rtnl1-myc. Controls were transfected with mCherry-KDEL. mGFP-Rtnl1 cloned in pcDNA3 for mammalian cell expression (appendix) and a pcDNA3 plasmid containing two tandem CMV transcription units containing nuclear-CFP, and the other expressing Rtnl1-myc were kindly provided by Prof. Andrea Daga. For transfection, 2 µg of each DNA type were mixed with 200 µL of Opti-MEM™. Separately, 4 µL of Lipofectamine 2000 were mixed with 200 µL of Opti-MEM™. After 5 min incubation at room temperature, both solutions were mixed and incubated for 20 min at room temperature. Then, the mixture was taken to 1 mL of Dulbecco´s Modified Eagle Medium (DMEM) and gently added to the cell culture dish containing the COS-7 cells. After 6 h, the medium was replaced with fresh DMEM.

Live-cell imaging was performed at the desired time post-transfection, using a microscope stage-top incubator equipped with a lens heater to maintain the cell culture dishes at 37 °C and 5% CO_2. The incubator was located on the stage of an epi-fluorescence inverted microscope equipped with a 150X/1.45 numerical aperture (NA) total internal reflection fluorescence microscopy (TIRFM) objective, an iXon-EMCCD camera, and BrightLine filter sets for the specific wavelengths. The image sequences were acquired using the open-source µManager software at 10 or 30 fps[195]. The images were further processed using ImageJ to crop, subtract background and adjust brightness/contrast[196].

To quantify Rtnl1-driven constriction of the peripheral ER network in COS-7 cells, the images were acquired at different time points after transfection. Two to three 30-40 μm^2 regions of interest (ROIs) covering the peripheral ER were selected for analysis. All histograms of pixel fluorescence intensity were obtained from ROIs of control COS-7 cells and cells expressing Rtnl1-myc and mGFP-Rtnl1 proteins.

5.3 Protein expression, purification and biochemical characterization

5.3.1 Equipment and materials

Expression, purification and characterization

Bacteria cells	M15 *E.coli* cells, kindly provided by Prof. Andrea Daga
Sf9 insect cells	Cell Line from Spodoptera frugiperda pupal ovarian tissue, #89070101, Sigma, Sigma-Aldrich, USA
BCA Protein Assay Kit	Pierce™ BCA Protein Assay Kit, #23227, ThermoFisher Scientific Inc., USA
Centrifuge	Ultra Optima L90K Beckman Coulter, Beckman Coulter Inc., USA
Rotor	Ti70, Beckman Coulter, Beckman Coulter Inc., USA
Gravity Chromatography Column	Econo-Pac® Chromatography Column, Bio-Rad, Bio-Rad Laboratories Inc., USA
Ni-NTA resin	Sigma-Aldrich, USA
GST resin	Pierce™ Glutathione Agarose #16102BID, TermoFisher Scientific Inc., USA
Heating magnetic stirrer	ARE, Velp Scientifica, Italy
HRV 3C protease	Pierce™ HRV 3C protease, TermoFisher Scientific Inc., USA
Protease Inhibitor Cocktail	Complete Tablets EASYpack, #04693116001, Roche, Germany

Centrifuge	Optima Max Ultracentrifuge, Beckman Coulter, Inc, USA
MLS50 rotor	Beckman Coulter, Inc, USA
OptiPrepTM density gradient	92339-11-2 Sigma, Sigma-Aldrich, USA
Ultracentrifuge tubes	Open-Top Thinwall Polypropylene Tube, Beckman Coulter, Inc, USA
GTPase Activity Assay Kit	MAK113-1KT, Sigma, Sigma-Aldrich, USA

5.3.2 Protein expression and purification

Dyn2, Dyn2-mEGFP, and Atl were expressed in Sf9 cells transiently transfected with pIEX6 constructs (Appendix) previously designed for each specific protein.

The cell pellets of Dyn2 and Dyn2-mEGFP were resuspended in buffer A and lysed by sonication. To isolate purified Dyn2 and Dyn2-mEGFP, the SH3 domain of amphiphysin-II, tagged with glutathione s transferase (GST) in the expression construct, was previously purified from *E. coli*. Then, the lysate was clarified by ultracentrifugation, and the supernatant was purified by affinity chromatography using immobilized GST-tagged SH3 domain of amph-II as an affinity ligand. After incubation with amphiphysin-SH3 beads, the protein-bound resin was washed extensively with buffer A. Proteins were eluted in buffer B and dialyzed overnight (ON) in buffer containing 20 mM 4-(2-hydroxyethyl)-1-piperazineethanesulfonic acid (Hepes) (pH 7.2), 150mM potassium chloride (KCl), 1 mM dithiothreitol (DTT), 1mM ethylenediaminetetraacetic acid (EDTA), 1 mM ethylene glycol-bis(β-aminoethyl ether)-N,N,N′,N′-tetraacetic acid (EGTA). Protein aliquots were then supplemented with 5% glycerol and flash-frozen in liquid nitrogen for storage at -80°C.

Atl was purified with an N-terminal GST tag. The cell pellet was resuspended in buffer A200 and broken by sonication. The lysate was then purified by centrifugation twice. After incubation with glutathione agarose beads, the resin was washed first with A100-high-detergent (buffer A100 + 1% Triton-X100) and then with A100-low-detergent (buffer A + 0.1% Triton-X100) buffers. The protein was eluted in A100-low-detergent buffer by cleaving the tag with HRV 3C protease ON. The cleaved protein was aliquoted, flash-frozen in liquid nitrogen, and stored at -80°C.

His-Rtnl1 or His-mGFP-Rtnl1 were expressed in M15 bacteria previously transformed with pQE-30 constructs (Appendix). Bacteria were lysed in lysis buffer. The lysate was incubated with Ni-NTA resin and washed successively with decreasing concentrations of Triton X-100 until reaching a concentration of 0.1 % (washing buffers 0, 1 and 2). His-Rtnl1-HA or His-mGFP-Rtnl1 were then eluted in elution buffer and used immediately. Alternatively, the proteins were aliquoted and frozen in liquid nitrogen for storage at -80°C.

Proteins purity was determined by SDS-PAGE with Blue Safe Protein staining. Upon measuring protein purity, the concentration was quantified by bicinchoninic acid (BCA) assay according to the manufacturer´s instructions.

Before functional *in vitro* experiments with purified proteins, the proteins were subjected to a 2 h dialysis in working buffer. Upon dialysis, the protein aggregates were removed by centrifugation at 22,000xg for 20 min.

5.3.3 Determination of reconstitution efficiency on Rtnl1 and Atl proteo-liposomes

The incorporation of purified Rtnl1 and Atl transmembrane proteins into 100 nm LUVs was verified by a flotation assay based on a density gradient as follows:

a) A density gradient was prepared based on a 3-6-9-12-15-20-30-40% OptiPrep™ density gradient diluted with working buffer. 100 µL of the reconstituted proteo-liposomes sample with either Rtnl1 or Atl at the desired protein/lipid ratio were added to the bottom of a 5 mL

ultracentrifuge tube. 500 µL of each fraction of the density gradient were layered on top, starting from the 40% fraction.

b) The gradient was centrifuged at 45,000xg for 2 hours at 4°C.

c) Upon centrifugation, 150-200 µL fractions were collected sequentially from the bottom of the gradient using a peristaltic pump.

d) Each collected fraction was analyzed by SDS-PAGE and by fluorescence spectroscopy using a 96-well plate reader to establish the protein and liposome content in each of the gradient´s fractions.

5.3.4 Determination of Dyn2 membrane binding efficiency

To test Dyn2 binding efficiency, we performed a sedimentation assay using the following protocol:

a) 400 nm LUVs prepared in working buffer at 0.2 mM at the desired lipid composition were incubated for 20 min with 0.5 µM Dyn2 in 20 µL total volume.

b) The sample was centrifuged at 18,000xg in a bench centrifuge for 20 min to sediment the LUVs to the pellet.

c) The pellet and supernatant were separated, and the pellet fraction was resuspended in 20 µL working buffer to equal the volume of the supernatant. Both, pellet and supernatant were subjected to SDS-PAGE analysis. An additional well of the gel contained the total amount of Dyn2 initially added for each condition.

d) The total membrane-bound Dyn2 was quantified by image processing of the pellet and supernatant fractions in the electrophoretic gel stained with Blue Safe Protein Stain. The normalization was done against the total protein per condition.

5.3.5 Dyn2 GTPase activity measurements.

We measured the catalytic activity of Dyn2 and Dyn2-mEGFP by a GTPase assay. GTP hydrolysis rates of basal and assembly-stimulated activity of Dyn2 or Dyn2-mEGFP were measured by detecting the inorganic phosphate released during the time course of the reaction using a Malachite Green-based colourimetric assay[197]. Briefly, 0.5 µM of either Dyn2 or Dyn2-mEGFP were incubated at 37 °C in the absence or presence of 400 nm LUVs (0.2 mM) (basal and assembly-stimulated, respectively) in a buffer containing 20 mM Hepes (pH 7.5), 150 mM KCl, 5 mM magnesium chloride ($MgCl_2$) and 2 mM GTP. 20 µL aliquots were drawn from the reaction mixtures after 30 min of incubation and transferred to wells of a 96-well microplate containing 5 µl 0.5 M EDTA to finish the hydrolysis reaction. 150 µL of Malachite Green stock solution were added to each well, and then the absorbance at 650 nm was measured using a microplate reader. Free phosphate was determined from the absorbance values using a standard calibration curve obtained with the inorganic phosphate stocks.

5.4 Generation of model membranes

5.4.1 Equipment and materials

Lipid stocks

1,2-dioleoyl-sn-glycero-3-phosphocholine, 18:1 (Δ9-cis) PC, DOPC	#850375, Avanti Polar Lipids Inc., USA
1,2-dioleoyl-sn-glycero-3-phosphoethanolamine, 18:1 (Δ9-Cis) PE, DOPE	#850725, Avanti Polar Lipids Inc., USA
1,2-dioleoyl-sn-glycero-3-phosphoethanolamine-N-(Cyanine 5), Cy5-DOPE	#810335, Avanti Polar Lipids Inc., USA
1,2-dioleoyl-*sn*-glycero-3-phosphoethanolamine-N-(lissamine rhodamine B sulfonyl), 18:1 Rh-DOPE	#810150, Avanti Polar Lipids Inc., USA

1,2-dioleoyl-sn-glycero-3-phospho-L-serine, 18:1 PS, DOPS	#840035, Avanti Polar Lipids Inc., USA
1,2-dipalmitoyl-*sn*-glycero-3-phosphoethanolamine-N-(7-nitro-2-1,3-benzoxadiazol-4-yl), NBD-DPPE	#810144, Avanti Polar Lipids Inc., USA
1´,3´-bis[1,2-dioleoyl-sn-glycero-3-phospho]-glycerol, CL	#710335, Avanti Polar Lipids Inc., USA
1-2-dioleoyl-sn-glycerol, DG	#800811, Avanti Polar Lipids Inc., USA
1-oleoyl-2-(12-biotinyl(aminododecanoyl))-sn-glycero-3-phospho-L-serine, Biotin PS	#860560, Avanti Polar Lipids Inc., USA
1-oleoyl-2-[12-biotinyl(aminododecanoyl)]-sn-glycero-3-phosphocoline, Biotin PC	#860563, Avanti Polar Lipids Inc., USA
1-oleoyl-2-hydroxy-sn-glycero-3-phosphocholine, Lyso PC	#845875, Avanti Polar Lipids Inc., USA
Cholesterol (ovine wool, >98%), Chol	#700000, Avanti Polar Lipids Inc., USA
L-α-phosphatidylinositol-4,5-bisphosphate (Brain, Porcine), $PI(4,5)P_2$	#840046, Avanti Polar Lipids Inc., USA

Model membranes

Streptavidin-coated polystyrene bead, Ø=2 µm	Microspheres-Nanospheres, USA
Polystyrene Microspheres, Ø=5 µm	#100243 Corpuscular, USA

Silicon Oxide Microspheres, Ø=40 µm	#140256 Corpusc ular, USA
Detergent removal Bio-Beads	Bio-Beads SM-2 Adsorbent, 20-50 mesh, 100g, Bio-Rad Laboratories, Inc., USA
Liposome Extruder	Lipex Extruder,Transferreda, Canada
Liquid nitrogen	Air Liquide, France
Microcentrifuge tubes	Safe-Lock Tubes, 1.5mL, Eppendorf, Germany
Micropositioning system	High-resolution NanoPZ actuators, Newport, USA
P-1000 micropipette puller	Sutter Instruments, USA
Piezo-actuator	ESA-CXA µDrive three-axis controller, Newport, USA
Polycarbonate membranes	Whatman® Nucleopore Track-Etched Membranes, 25mm diameter, pore size 0.1 µm, #110605 or pore size 0.4 µm, #110607, Merck-Millipore, Germany
Teflon® film	Teflon® film 0.02" thick, 24" wide, VS002X24, Fluoro-plastics Inc., USA
35mmPetrii dishes	S01775, Thermo Fisher Scientific, USA
Argon compressed gas	Alphagaz™, Air Liquide, France
Borosilicate glass capillaries	GB 150-10, Science Products, Germany
Sodium dithionite	#7775-14-6, Sigma-Aldrich, USA

5.4.2 Formation of MLVs

The experimental procedure for multilamellar vesicles (MLVs) production was as follows:

a) Lipid stocks in chloroform were mixed in the desired proportions in a glass vial (Fig. 5.1 a).

b) The lipid mixtures were dried under vacuum for 30-45 minutes to obtain a uniform lipid film (Fig. 5.1 b). For lipid mixtures containing PI(4,5)P_2 the dried lipid film was resuspended in a 9:1 mixture of chloroform:methanol and then dried again to ensure uniform distribution of this particular lipid, which is not soluble in pure chloroform solvent.

c) The lipid films were then hydrated in working buffer to the desired final lipid concentration and vortexed to complete the MLV formation (Fig. 5.3 b).

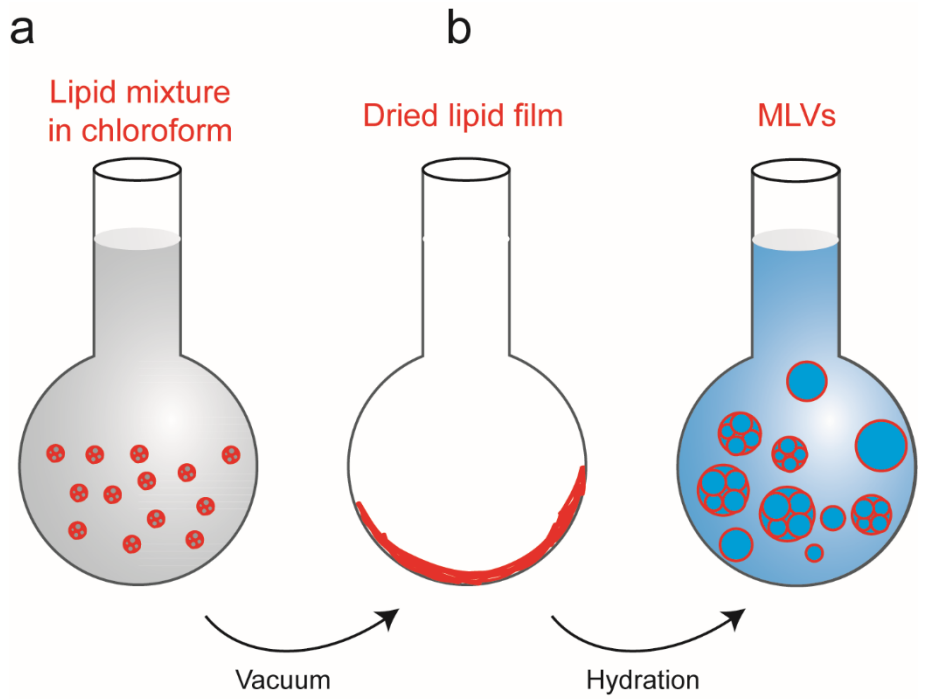

Figure 5.1. Schematic representation of MLVs formation protocol. (a) The lipids are mixed in chloroform in the desired molar proportions. **(b)** Upon their mixture in chloroform, the lipid mixture is dried in a vacuum for at least 30 min. The dried lipid film is then hydrated in working buffer, leading to the formation of MLVs.

5.4.3 Preparation of LUVs

LUVs were formed from MLVs as follows:

a) First, the MLVs were subjected to 10 freeze-thaw cycles in liquid nitrogen (N_2) (Fig. 5.2 a).

b) To obtain a homogeneous size of LUVs, the MLVs were extruded through polycarbonate filters with either 100 or 400 nm pore size (Fig. 5.2 b). The desired LUVs concentrations for each experiment were obtained by diluting the LUV stock in the working buffer.

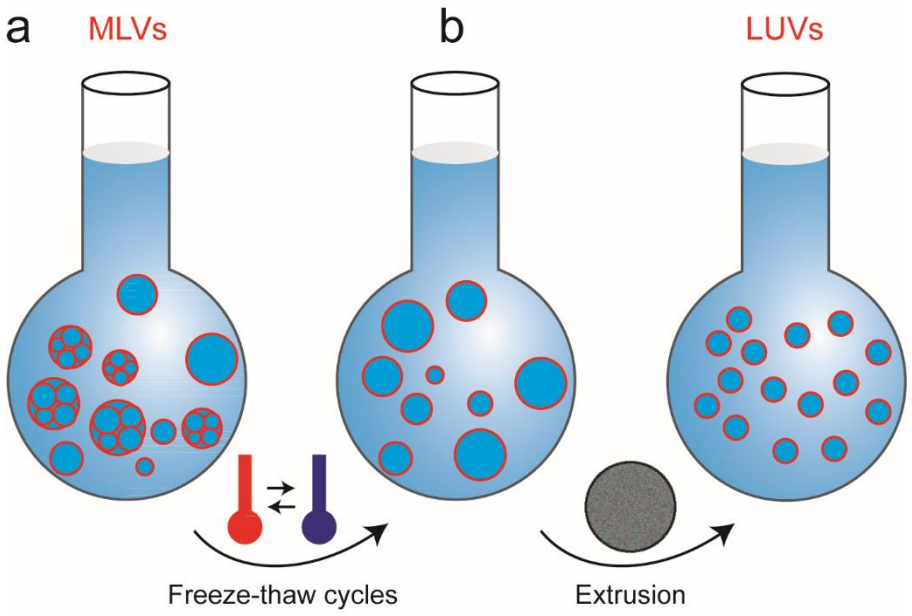

Figure 5.2. Schematic representation of the protocol to produce LUVs from MLVs. (a) The MLVs are subjected to 10 cycles of freeze and thaw. **(b)** Upon completion of the cycles, the sample is extruded through 100 nm or 400 nm polycarbonate filters, leading to forming a homogeneously sized population of LUVs.

c) To confirm the lamellarity of the 100 nm or 400 nm LUVs, the emission fluorescence of Rh-DOPE intensity was measured before and after adding 5 mM dithionite quencher to 0.2 mM LUVs (Fig. 5.3). Assuming that the Rh-DOPE is symmetrically distributed, the fluorescence signal from unilamellar LUVs should decrease 50% of its initial value. Total fluorescence intensity of each LUV sample was established upon the

addition of 1% v/v final concentration of Triton X100 to the LUV sample upon experiment completion.l

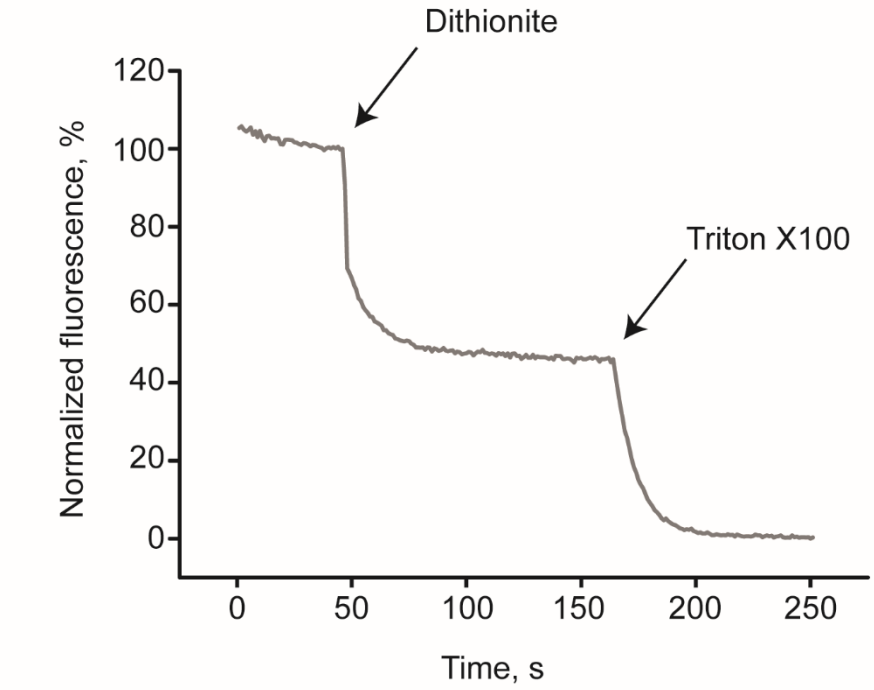

Figure 5.3. Characterization of the LUVs´ lamelarity by measurements of Rh-DOPE quenching. Upon addition of dithionite, the Rh-DOPE fluorescence coming from the molecules in the outer monolayer of the LUVs gets quenched. Hence, the 50% decrease in fluorescence intensity indicates the unilamelarity of the membrane. The addition of Triton X100 promotes the micellization of the sample so that now all Rh is exposed to the dithionite, making the fluorescence signal decrease to the background level.

5.4.4 Atl, Rtnl1, and mGFP-Rtnl1 reconstitution into LUVs

The transmembrane proteins Atl, Rtnl1 and mGFP-Rtnl1 were reconstituted into the LUVs as follows:

a) The 100 nm LUVs performed from the desired lipid compositions as explained above were diluted with working buffer to a final concentration of 0.5-1 mM. To facilitate transmembrane protein insertion into the model membranes, the LUVs were destabilized via the addition of a small amount of detergent that intercalates into the lipid membrane and makes defects that help protein incorporation. For that, the LUVs were titrated with an increasing concentration of Triton X100. The optical density of titrated

LUVs was measured at 540 nm to find the optimum point of LUV destabilization[198] before micellization of the membrane.

b) The detergent-destabilized LUVs (final concentration ~0.2 mM) were mixed with purified Atl, Rtnl1, or mGFP-Rtnl1. For Atl and Rtnl1 co-reconstitution, the LUVs were mixed directly with both purified proteins.

c) After 15 min incubation at room temperature with gentle shaking, the detergent was removed with BioBeads® SM-2 adsorbent, which was added to the proteo-lipid mixture five times (at time 0, +30 min, +90 min, and +150 min and ON)[63,103]. To replace the BioBeads® at each time point, the mixture was gently centrifugated to settle down the beads in the pellet. Then, the supernatant was transferred to a new vial containing fresh BioBeads®.

d) The sample was then centrifuged for 1 h at 15,000×g in a bench centrifuge to remove the BioBeads® and unincorporated protein.

e) Control samples for proteoliposome experiments were produced following the same protocol, replacing the proteins with an identical volume of working buffer.

5.4.5 Formation of GSBs on silica and polystyrene beads

The protocol for GSBs formation was based on a previously published protocol by our lab[104] with slight modifications as follows:

a) 50-100 µL of LUVs or proteo-liposomes at the desired concentrations were dialyzed against 1 L of dialysis buffer for 30 min (TRH, present in the dialysis buffer, has been shown to prevent protein degradation even at high temperatures and/or in the absence of hydrogenating molecules[105].

b) 10-15 µL of the dialyzed LUVs or proteo-liposomes were applied as 4-5 small drops onto a Teflon sheet. 2 µl of a 40 µm silica or 5 µm polystyrene beads solution (for fluorescence-based experiments and force

measurements, respectively) were deposited over each droplet containing the LUVs (Fig. 5.4 a). The droplets were dried in vacuum for 20 min to form the dried lipid or proteo-lipid film over the silica or polystyrene beads (Fig. 5.4 b).

c) To hydrate the lipid or proteo-lipid films and form the GSBs, a 10 µL plastic tip was cut from the bottom to about 2/3 of its original length and used to collect 5-6 µL of the hydration buffer. Beads covered by dried lipid or proteo-lipid films (Fig. 5.4 b) were picked up with a fire-sealed glass capillary and deposited into the hydration buffer of the cut tip. The tip was then incubated for 15 min at 60ºC in a homemade humidity chamber to facilitate the GSBs hydration.

d) After hydration, the lipid or proteo-lipid GSBs were formed by transferring the beads to the observation chamber, previously filled with the working buffer (Fig. 5.4 c).

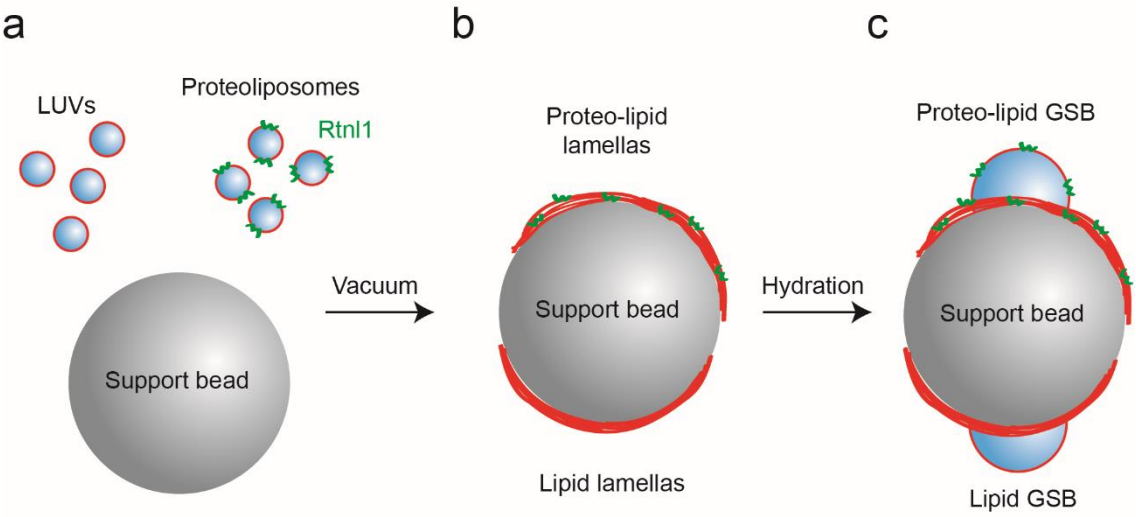

Figure 5.4. Lipid or proteo-lipid GSBs formation protocol. (a) Either LUVs or reconstituted proteo-liposomes were mixed with silica or polystyrene beads. **(b)** The mixture of LUVs or proteo-liposomes with the beads was dried in vacuum for >20 min. **(c)** The lipid and proteo-lipid films over the beads were pre-hydrated in TRH 1 M 15 min (step c)) and hydrated in working buffer in the observation chamber (step c) and d)), leading to the formation of lipid or proteo-lipid GSBs.

5.4.6 Formation of SLBs from lipid films on silica beads

Two types of supported lipid bilayers (SLBs) were produced in this dissertation. In the first case, SLBs were produced to obtain the fluorescence calibration curves for NT radii quantification (see Radii quantification of NTs). In that case, SLBs had the same membrane composition as the experiment of interest. Alternatively, SLBs were produced to block the coverslip surface. In this case, SLBs were produced from the neutral DOPC lipid in order to avoid electrostatically driven membrane-protein interactions. The SLBs were formed as elsewhere reported[199] with some modifications, as follows:

a) The cover glass of the observation chamber was subjected to a cycle of plasma cleaning to delete any biological contaminants and make the surface hydrophobic.

b) Dried lipid films over the silica beads, obtained as explained above (see Formation of GSBs on silica and polystyrene beads, steps a) and b)), were picked up with a fire-sealed glass capillary and directly deposited in an observation chamber filled with working buffer (Fig. 5.5). After 5-10 min, the SLBs formation was observed on the coverslip surface as the spilling of the lipid membrane from the silica beads (Fig. 5.5).

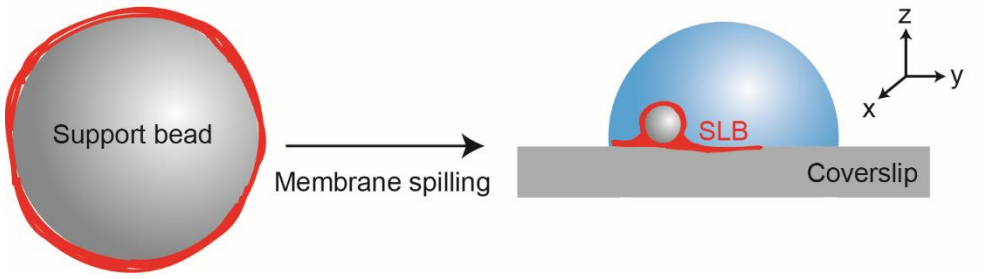

Figure 5.5. Formation of SLBs. Lipid-covered silica beads were deposited in the microscopy observation chamber filled with working buffer. SLBs formed spontaneously upon 5-10 min incubation, as the membrane from the beads spilled onto the coverslip surface.

c) Once the SLBs formed, the beads were removed from the observation chamber by several washing cycles with the working buffer.

5.4.7 NT formation by micromanipulation of GSBs

The P-1000 micropipette puller was used to prepare the glass micropipettes. A micropositioning system based on a 461xyz stage and high-resolution NanoPZ actuators was used to position the micropipette over the microscopy observation chamber. Following, a 2 µm streptavidin-coated polystyrene bead was captured by aspiration with the tip of the micropipette (Fig. 5.6). To pull lipid NTs from formed GSBs or proteo-GSBs doped with either 0.2% biotinylated-DOPS or biotinylated-DOPC, the GSB supporting bead was either fixed in the chamber bottom by gravity (40 µm silica bead for fluorescence microscopy experiments) or trapped with an optical trap (5 µm polystyrene bead for force measurements). The streptavidin bead was then displaced by moving the micropipette until it contacted the GSB membrane. The NT was pulled by displacing the streptavidin bead away from the GSB membrane. Constant velocity NT stretching and/or retraction experiments were performed with a calibrated piezo-actuator controlled by an ESA-CXA µDrive three-axis controller.

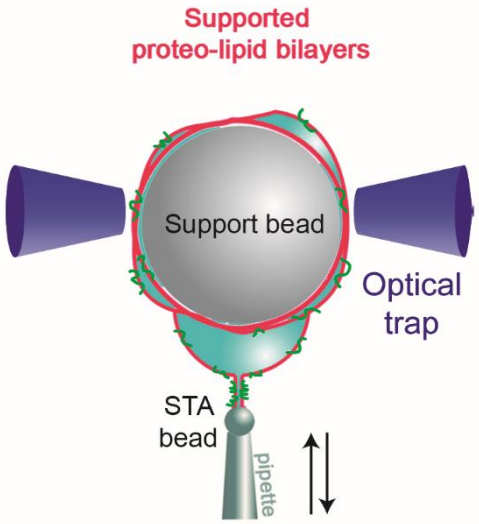

Figure 5.6. Formation of proteo-lipid NTs from the GSB system. First, the 40 µm silica beads that supported the GSBs were immobilized on the coverslip by gravity. Alternatively, the 5 µm polystyrene beads supporting the GSBs were trapped with an optical trap (purple cones). Upon immobilization of the supporting bead, a 2 µm streptavidin-coated bead (STA-bead) was trapped into a micropipette tip by aspiration and brought into close proximity to the GSB membrane. The tight contact between the STA bead and the GSB membrane was established trough the STA-biotin covalent interaction (the GSBs membrane was doped with 0.2% of biotinylated lipid). The membrane NTs were pulled from the GSB reservoir membrane by micromanipulation of the pipette with the trapped STA-bead.

5.4.8 NT formation by GSB rolling

A simplified protocol for NT formation was used to produce NTs as follows:

a) Microscopy coverslips were cleaning for 30 min with EtOH in a sonication bath and then plasma-cleaned for 30 s with air plasma.

b) The coverglass was passivated via the formation of DOPC SLBs as previously described.

The lipid-film-covered beads (see Formation of GSBs on silica and polystyrene beads, steps a) and b)) were added to the observation chamber and rolled over the SLBs applying liquid flux (Fig. 5.7). Upon rolling, the hydrated membranes lamella attached to the hotspots on the cover glass, and the NTs formed between these anchor points (Fig. 5.7).

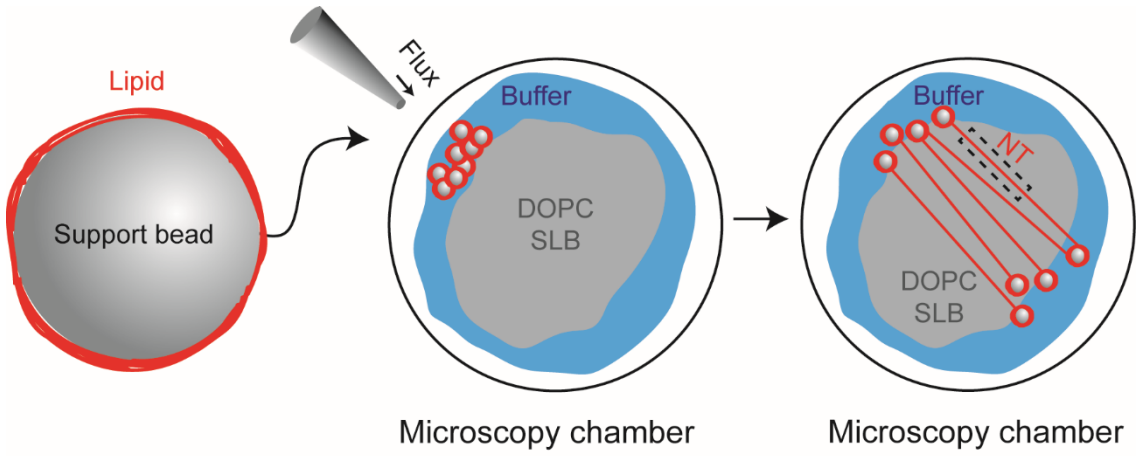

Figure 5.7. Schematic representation of the generation of preformed lipid NTs. Lipid-covered beads were deposited over a passivated coverslip. Upon addition, the beads were either rolled by shaking the coverslip, or moved by application of a flux with a micropipette filled with working buffer, leading to the formation of the lipid NTs over the SLBs.

5.4.9 Radii quantification of NTs

Radii quantification of either lipid or proteo-lipid NTs was done as reported elsewhere[106] (Fig 5.8 a). First, a fluorescence calibration curve was made using SLBs prepared with the same composition as the sample. The SLBs were used to find the density of the membrane fluorescence signal (Fig. 5.8 b, ρ_0).

The total fluorescence intensity (I_{ROI}) of a given membrane area (A) can be described as follows:

$$I_{ROI} = \rho_0 A \qquad \text{(Eq. 5.1)}$$

The NT images were taken at the same lamp excitation intensity as the one used for the calibration curve, and the background was subtracted. Following, a ROI along the NT axis was used to calculated the NT integrated fluorescence intensity using the ImageJ software. The measured fluorescence is directly proportional to the NT area through the constant calibration ρ_0, which corresponds to the fluorescence density of the membrane. Considering that the NT geometry can be approximated by a cylinder, and by considering the length of the selected ROI used to measure the NT´s fluorescence (L_{ROI}), the NT radius is obtained as:

$$R_{NT} = \frac{I_{ROI}}{2\,\pi\,\rho_0\,L_{ROI}} \qquad \text{(Eq. 5.2)}$$

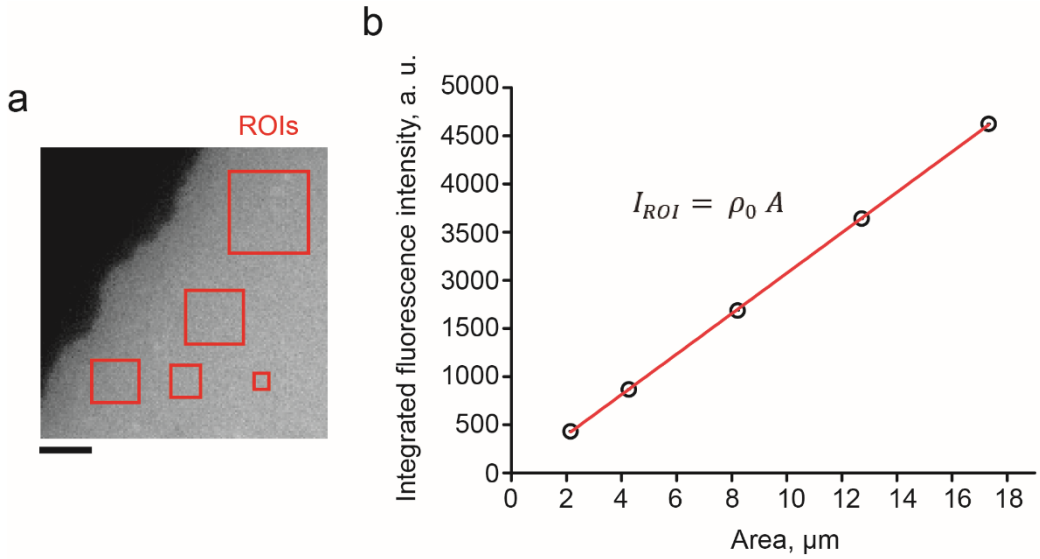

Figure 5.8. Fluorescence-based calibration for NT radius calculation. (a) Micrograph showing an SLB on a coverslip. Scale bar is 2 µm. Rh-DOPE fluorescence is shown. **(b)** Graph representing the integrated fluorescence per area of each ROI shown in **(a)**. The slop of the linear fit of the data corresponds to ρ_0, the fluorescence density of the membrane.

5.5 Functional assays

5.5.1 Equipment and materials

PTI Fluorometer	HORIBA Scientific, Japan
Polydimethylsiloxane (PDMS)	SYLGARD™ 184 Silicone Elastomer Kit, Dow, Spain
Monomeric Enhanced Green Fluorescent Protein, mEGFP	#14-392, Merck Life Science S.L.U, Spain
Low volume spectroscopy cuvette	Thomas Sub-Micro Cells, Thermo Fisher Scientific, USA
Bovine Serum Albumin (BSA)	#10829410, Thermo Fisher Scientific, USA
Plasma cleaner	Plasma cleaner PDC-002-CE, Harrick Plasma, USA
Mini Twizeers	Patent N°0146718 A1, USA
Diode lasers	Lumics (LU0808 M250-FBG), Berlin, Germany
Lense 1 and 2	UPLASAPO 60X Water, Olympus, Japan
Data acquisition softwate	
Fluorimetry FelixGX Software	HORIBA Scientific, Japan

5.5.2 Lipid mixing

Lipid mixing experiments were based in the FRET between two fluorophores (Fig. 5.9 a). Initially, when both fluorophores co-exist in the same membrane at identical proportions, the acceptor fluorophore is excited by the emission fluorescence from the donor fluorophore upon its excitation. After hemi-

fusion or complete membrane fusion with an unlabeled proteoliposome, the distance between the fluorophores increases, and the donor is no longer quenched by the acceptor (Fig. 5.9 a, cartoon).

The experiment was performed by mixing a population of fluorescently labeled proteo-liposomes containing the FRET pair (1.5 mol% of both Rh-DOPE as the acceptor and NBD-DOPE as the donor fluorophores) with a population of unlabeled proteo-liposomes at approximately 0.2 mM of each lipid mixture (Fig. 5.9 a, cartoon). Lipid mixing experiments on Atl- or Atl/Rtnl1 proteo-liposomes were started by GTP addition of 2 mM to a final volume of 100 µL in working buffer. For Dyn2-driven lipid mixing measurements, each labeled and unlabeled LUV population was added at 0.2 mM. Then, Mg^{2+} or Ca^{2+} and Dyn2 were added at the desired concentration depending on the experiment (specified for each experiment in the Results section).

Emission fluorescence of NBD was recorded at 530 nm and excited at 467 nm either on a black bottom 96-well using a microplate reader or in a PTI fluorometer (Fig. 5.9 b). Experiments were performed at constant temperature (37ºC). To determine total NBD fluorescence, 1% TritonX-100 stock solution was added to each reaction to a final concentration of 0.1%. The maximum NBD fluorescence was established once the plateau was reached (Fig. 5.9 b). For the calculation of total lipid mixing percentage, the maximum NBD fluorescence after the addition of Triton X-100 was considered as 100% lipid mixing and the fluorescence baseline before the addition of GTP as 0% lipid mixing. Lipid mixing extent (LM) was then calculated by applying the following equation:

$$LM = \frac{(F - F_0)}{(F_{max} - F_0)} \times 100 \qquad \text{(Eq. 5.3)}$$

where F is the fluorescence signal at any given moment, F_0 is the baseline fluorescence signal and F_{max} is the maximum fluorescence signal upon addition of the detergent.

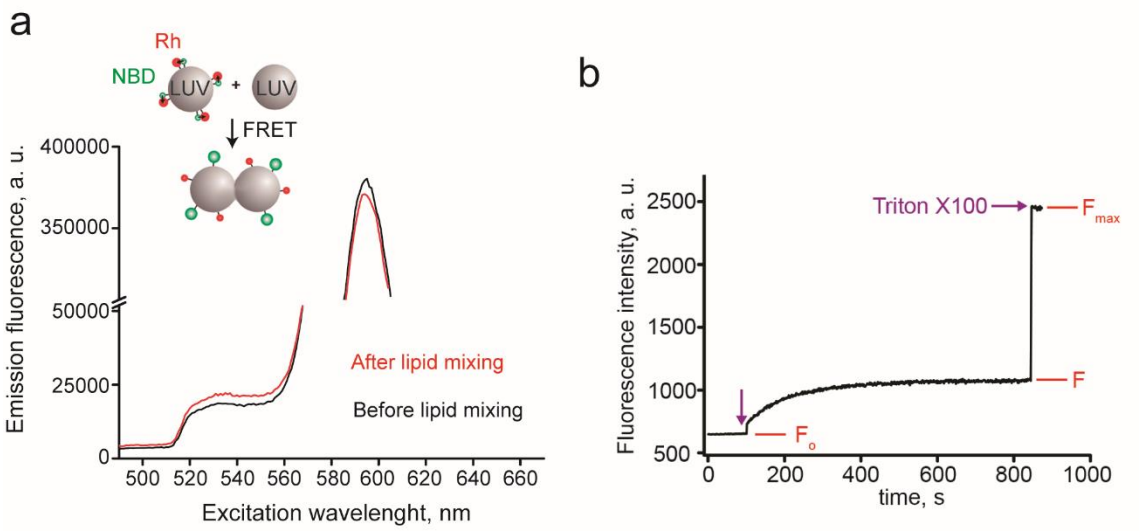

Figure 5.9. Experimental design of a lipid mixing-based FRET experiment. (a) The cartoon shows the physical principle behind the lipid mixing experiment based on the FRET pair Rh-DOPE/ NBD-DOPE (acceptor/donor, respectively). Upon initiation of the lipid mixing reaction (red curve), the distance between the two fluorophores of the FRET-pair increases, resulting in the NBD emission fluorescence signal increase (left peak) and Rh emission fluorescence signal decrease (right peak). The black curve shows the emission fluorescence signals before the lipid mixing reaction. **(b)** Representative raw data of a lipid mixing experiment.

5.5.3 Quantification of curvature-driven sorting of mGFP-Rtnl1

The relative change in membrane area occupied by mGFP-Rtnl1, which defines the sorting coefficient (φ), was calculated by measuring the mGFP-Rtnl1/Rh-DOPE fluorescence ratio ($F_{mGFP-Rtnl1}/F_{Rh-DOPE}$) between the planar reservoir and curved membranes of the proteo-lipid NTs/GSB system at low protein concentrations[111], as follows:

$$\varphi = \frac{(F_{mGFP-Rtnl1}/F_{Rh-DOPE})^{reservoir}}{(F_{mGFP-Rtnl1}/F_{Rh-DOPE})^{nanotube}} \qquad \text{(Eq. 5.4)}$$

$F_{mGFP-Rtnl1}/F_{Rh-DOPE}$ was measured as the ratio of total fluorescence intensities obtained from a ROI after subtracting the background and neglecting the polarization factor[111]. Two different circular ROIs (with a diameter of 2 µm) were used for each reservoir/NT membrane.

5.5.4 Characterization of Dyn2-mEGFP membrane curvature-sensing

Dyn2-mEGFP curvature-driven sorting was not measured as previously described for mGFP-Rtnl1 due to pronounced membrane tubulation of the GSB

promoted by Dyn2-mEGFP on high PE-containing membranes. Instead, curvature-driven sorting was calculated as the increase of fluorescence surface density from Dyn2-mEGFP upon the increase in the lipid NT curvature.

Dyn2-mEGFP was added to the microscopy chamber and incubated until the protein binding to the lipid NT was detected. The integrated fluorescence intensity of the protein scaffolds (F_{helix}) and of the helical precursors ($F_{pre\text{-}helix}$) were determined by calculating the area under the fluorescence intensity peaks of cross-sections at the NTs (Fig. 5.10 a). Integrated mEGFP fluorescence signal was then normalized against the Rh-DOPE fluorescence signal of the bare NT

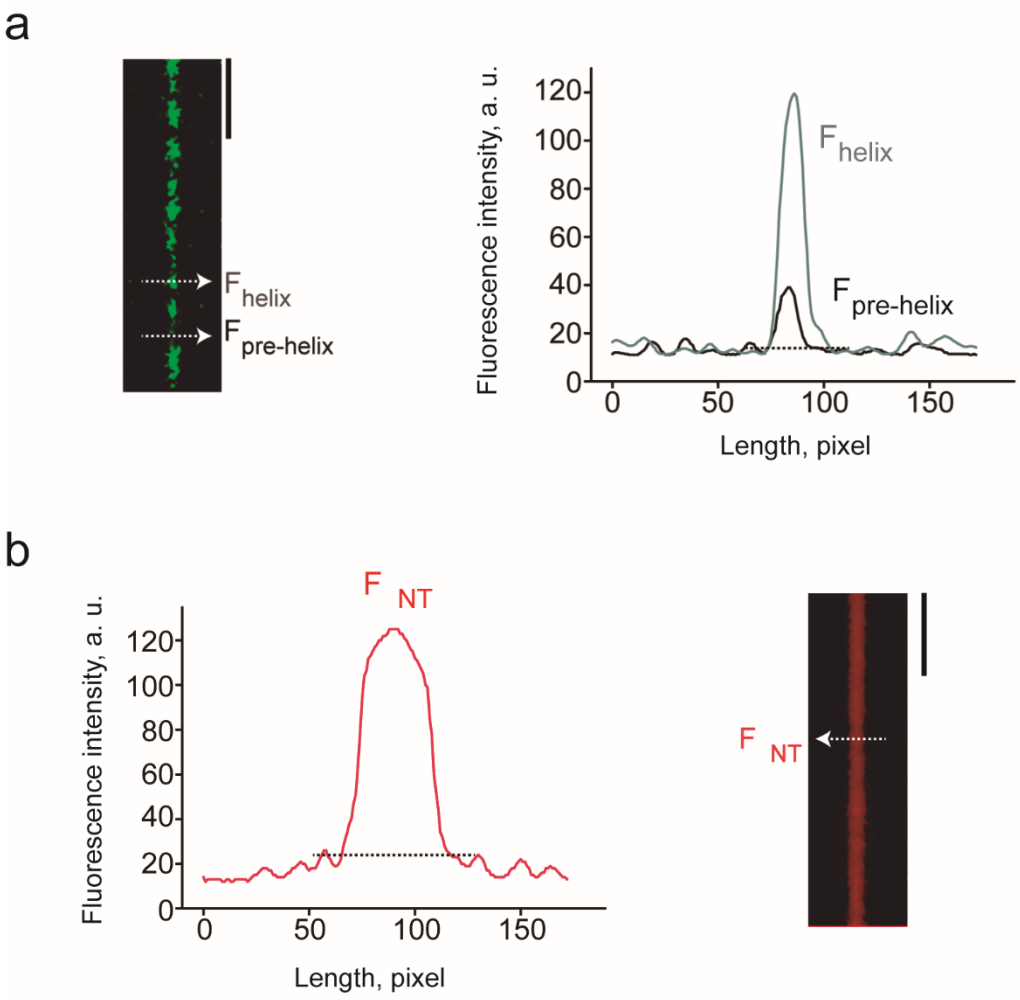

Figure 5.10. Data analysis workflow to detect curvature-driven sorting of Dyn2-mEGFP on lipid NTs. (a) Fluorescence micrograph shows Dyn2-mEGFP scaffolds and Dyn2 helical precursors as observed in the mEGFP channel. The plots show the fluorescence intensity per pixel unit of NT cross sections (white lines in the micrograph) of the Dyn2-mEGFP scaffolds and the helical precursors (F_{helix} and $F_{pre\text{-}helix}$, respectively). Scale bar is 4 µm. **(b)** The plot shows the fluorescence signal of Rh-DOPE of the bare NT before Dyn2-mEGFP binding (from the right fluorescence micrograph, F_{NT}). Scale bar is 4 µm.

before Dyn2-mEGFP binding (Fig. 5.10 b, F_{NT}) neglecting the polarization factor[111]. In the case of Dyn2-mEGFP scaffolds, we normalize the mEGFP integrated fluorescence value against the Rh-DOPE signal on the constricted regions of the NT. Finally, each value was normalized against the mean fluorescence of Dyn2-mEGFP scaffolds (Fig. 5.10 a, F_{helix}).

5.5.5 Quantification of membrane fission efficiency by Dyn2

To quantify the membrane fission efficiency by Dyn2, the protein was added at the desired concentration (20 nM or 0.5 µM) followed by the addition of GTP to a final concentration of 2 mM.

The quantification of fission probability was done by counting the number of broken NTs in the field of view upon Dyn2 and GTP addition to the microscopy chamber.

5.5.6 *In vitro* reconstitution of ER-like membranous network

The formation of the membranous network resembling the tubular ER begins with the co-reconstitution of Rtnl1 and Atl into LUV membranes as previously described. To test the necessity of both Rtnl1 and Atl to reconstitute the membrane network, two populations of fluorescently labeled proteo-liposomes were prepared in working buffer, one with purified Atl (ratio of Atl to lipid 1:400) and the other with purified Atl and Rtnl1 (ratios of protein to lipid 1:400 and 1:150, respectively). After proteo-liposomes reconstitution, each population of proteo-liposomes was diluted in working buffer to a final concentration of 0.2 mM and in the presence of 2 mM GTP, and transferred to a microscopy chamber previously sealed with a homemade PDMS chamber to prevent evaporation. The sealed samples were incubated for 12 hours at 37ºC before visualization using an inverted microscope.

5.5.7 Fluorescence-based quantification of LUVs-aggregates

0.2 mM LUVs were incubated with 0.5 µM Dyn2 or Dyn2-mEGFP for 10-15 min (unless indicated otherwise) in an 0.5 mL vial. After incubation, the samples were deposited on a coverglass previously blocked with bovine serum albumin (BSA) to prevent the adhesion of lipids to the bottom of the coverslip.

For the analysis, 5 images per field of view (10-15 field of views in total) were acquired and averaged using the Z-stack Average option in ImageJ software. Further analysis of LUVs and aggregates in pixel^2 was performed using a constant threshold and Analyze Particles algorithm in ImageJ software[200].

5.5.8 Single-molecule fluorescence calibration

To count individual Dyn2-mEGFP molecules based on fluorescence measurements, we performed single-molecule fluorescence calibration of single mEGFP molecules as follows.

The surface of the coverslip was cleaned by sonication with pure ethanol for 30 min, and then rinsed 5 times with Milli-Q water, followed by 30-45 s of air plasma cleaning. The mEGFP stock was diluted in PBS 1X to a final concentration of 1 nM and sonicated for 10 s to avoid big aggregates[176]. Upon sonication, 1 nM mEGFP solution was added to the observation chamber. Images of mEGFP molecules were recorded using a 2x2 binning in a Nikon Eclipse Ti-e inverted microscope equipped with a 100x/1.49 NA oil objective, an Andor Zyla 4.2 sCMOS camera controlled by μManager software, a LED excitation system. Sample imaging was performed at light powers between 10 and 20% at 1 sec of exposure time for 3-5 minutes (Fig. 5.11 a). Upon acquisition, the open-source image processing software Icy[201] was used to detect individual mEGFP molecules bound to the coverslip and to determine the position of the fluorescence peak (Fig. 5.11 a, b). Background fluorescence per pixel unit was calculated as the mean fluorescence per pixel measured in 4 randomly positioned ROIs without mEGFP molecules using imageJ software (Fig. 5.11b). The mEGFP fluorescence was then measured and normalized as total integrated fluorescence over 4x4 pixel squares, centered on the fluorescence peak (Fig. 5.11 a, b, red squares). The distribution of mEGFP fluorescence intensity is shown in Fig. 5.11 c.

We further verified the single-molecule nature of the measured fluorescence by fluorescence lost after photobleaching (FRAP). By applying a high excitation power (40%), we observed a stepwise decrease in mEGFP fluorescence (Fig. 5.10 d), which is characteristic of single-molecule photobleaching.

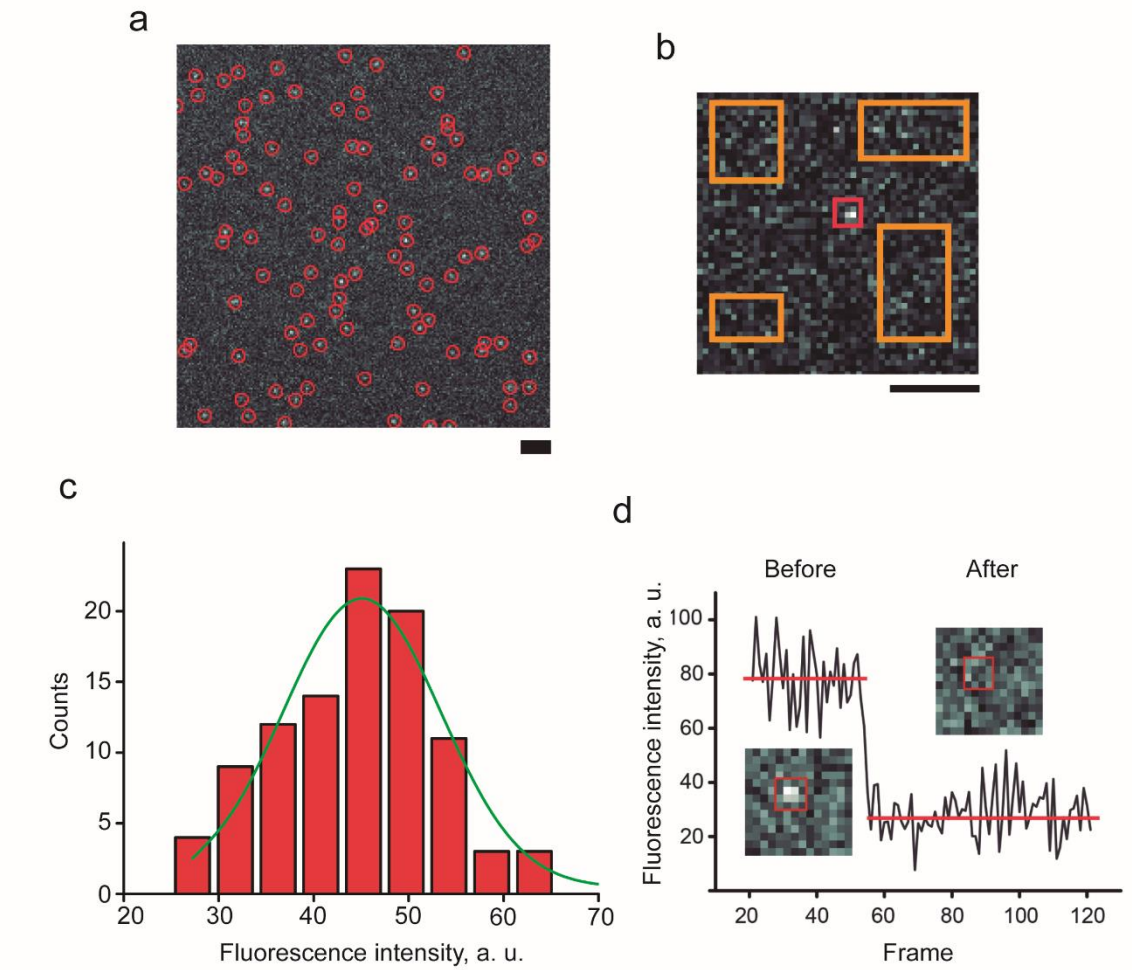

Figure 5.11. Single-molecule fluorescence calibration of mEGFP molecules. (a) Representative fluorescence micrograph of individual mEGFP molecules over the microscopy coverslip (red squares). **(b)** 4x4 pixel ROIs centered on the mEGFP molecules (red) and rectangular ROIs randomly selected at different areas of the coverslip (orange) were analyzed to calculate the fluorescence corresponding to mEGFP molecules and to the background. Scale bar is 1 µm. **(c)** Histogram showing the distribution of the mEGFP fluorescence intensity. The line in green shows a Gaussian fit. The normality of the distribution was further confirmed by Anderson-Darling test (A=0.5154). **(d)** Representative plot showing the stepwise photobleaching that corresponds to a single mEGFP molecule. The inserts show the fluorescence from a mEGFP molecule before and after photobleaching (red squares). Scale bars are 1 µm.

5.5.9 Stoichiometry of sub-helical Dyn2 complexes over lipid NTs

Lipid NTs were formed over SLBs (see NT forming by GSB rolling), and 10-20 nM bulk concentration of Dyn2-mEGFP was added to the chamber with a microinjection pump. In the membrane tethering experiments, Dyn2-mEGFP at 10-20 nM was added in the presence of 0.2 mM LUVs (doped with 0.1 mol% of Rh-DOPE to avoid cross-talk). Upon detection of binding of small Dyn2-mEGFP complexes to the lipid NTs, the reaction chamber was immediately washed with

the working buffer. The washing step was performed with 1-2 mM or without GTP to capture Dyn2-mEGFP complexes in the apo (nucleotide free) or ground (GTP) states, respectively.

Based on the total fluorescence intensity from a single mEGFP molecule calibration, the number of Dyn2-mEGFP molecules within the protein complexes were analyzed by taking into account the highest fluorescence signal recorded for a Dyn2-mEGFP spot. In the tethering experiments, only those spots showing co-localization of mEGFP and Rh fluorescence signal moving along the NT axis were considered. Background subtraction was done the same way as previously described for the calibration process. Calculation of the number of molecules was done by dividing the integrated fluorescence intensity of a fluorescent Dyn2-mEGFP spot by the unitary mEGFP fluorescence value.

5.5.10 Force measurements with optical tweezers

These experiments used a counter-rotating dual-beam optical tweezers device equipped with light-momentum force sensors that can measure force directly[202]. Two lasers are positioned to the same focus through opposing objective lenses of the microscope, creating a single optical trap. Proteo-lipid NTs were generated in situ as follows.

a) GSBs or proteo-GSBs were prepared over 5 μm polystyrene beads in working buffer, as explained previously (see Formation of GSBs on silica and polystyrene beads, steps a) and b)).

b) The 5 μm polystyrene bead was held in the optical trap and brought into contact with a 2 μm streptavidin-covered bead immobilized by aspiration in a micropipette tip. The two beads were separated at an initial constant draw rate of 0.1 μm/s to form a NT.

c) Cycles of extension-shortening were performed on individual tubes at different pulling speeds. Below 8 μm s^{-1}, the trap was linearly displaced at a constant calibrated speed. For higher velocities, the pipette was displaced away from the optical trap by a coarse positioner and draw rates were calculated offline as distance change per unit of time. The data was

collected with high force (< 1 pN), position (1-10 nm), and temporal (500 Hz) resolution. A similar experimental design was performed with pure lipid films to test the behavior of protein-free lipid NTs under force.

5.6 Structural characterization

5.6.1 Equipment and materials

Field Emission Scanning Electron Microscope (FESEM), JEM-2200FS/CR, JEOL Inc., Tokyo, Japan	
CCD Camera	16 megapixels, (4096 x 4096 pixels), 895 model, US4000, GATAN, USA
Software	JEM-toolbox, TEMography.com, Japan
Sample preparation	
Automatic vitrification robot	Vitrobot, FEI, the Netherlands
300 mesh holey carbon grids	R2/1, Quantifoil®, Quantifoil Instruments GmbH, Germany
High vacuum coating system for glow discharge	MED 020, BALTEC, Switzerland
Talos Arctica Cryo-TEM	
Direct detector	K2 Summit direct electron detector, GATAN, USA
Software	SerialEM, bio3d, Colorado, USA
Data analysis software	

Sample preparation	
10 nm BSA-conjugated gold beads	Aurion, the Netherlands
200 mesh holey carbon grids	R2/1, Quantifoil®, Quantifoil Instruments GmbH, Germany
Manual plunge-freezer	MPI Martinsried
Data analysis softwares	
EMAN2	2, version 2.9, NIH, USA
IMOD	bio3d, Colorado, USA

5.6.2 CryoEM of membrane-bound Dyn2

Samples for CryoEM studies were prepared by 10-15 min incubation of 0.5 µM of Dyn2 at 37ºC with 0.2 mM LUVs. Then, 4 µL sample was pipetted onto a R2/1 Cu 300 mesh grids, previously hydrophilized by plasma cleaning using a high vacuum coating system for glow discharge during 30 sec and 7.5 mA (set up to 5.3 mA). CryoEM grids were vitrified in liquid ethane using a Vitrobot system. Images were collected in a JEM-2200FS/CR transmission electron microscope, operated at 200 kV and equipped with an UltraScan 4000 SP (4008x4008 px) cooled slow-scan CCD camera. CryoEM image acquisition was performed at 400,000x magnification using a defocus range of 3-5 µm.

5.6.3 CryoET of Atl proteo-liposomes

After Atl proteo-liposomes reconstitution, 5 µL of the 0.2 mM proteo-liposomes were pipetted directly onto a glow-discharged 200 mesh holey carbon grid. 1 µL of a suspension containing 10 nm BSA-conjugated gold beads was added to each grid. The grids were manually blotted from the backside for 3 s with a manual plunge-freezer. Afterward, the grids were immediately immersed in a mixture of liquid ethane-propane (37% ethane).

SerialEM software[203] was used to collect 45 tilt-series at a Talos Arctica operating at 200 kV, with an angular step of 3°, starting from 0° in a symmetric dose collection until -60/60°, alternating every 12 degrees from positive to negative tilt in a semi dose-symmetric mode. Images were acquired using a K2 Summit direct electron detector, and the dose per frame was 0.293 $e^-/Å^2$, for a total dose of 120 $e^-/Å^2$ per tomogram. Each of the tilts was formed by a movie of 10 frames. The magnification during imaging acquisition was 18,050 with a giving pixel size of 2.77 Å.

Acquired images were aligned using Motioncor2 1.2.1. Tomograms were reconstructed in IMOD[204] or EMAN2 software with a SIRT-like filter for visualization. The tomograms were CTF–corrected with CTF plotter.

6. Bibliography

1. Ramachandran R, Schmid SL. The dynamin superfamily. *Curr Biol*. 2018;28(8):R411-R416. doi:10.1016/j.cub.2017.12.013
2. Chernomordik L V, Kozlov MM. Protein-Lipid Interplay in Fusion and Fission of Biological Membranes. *Annu Rev Biochem*. 2003;72(1):175-207. doi:10.1146/annurev.biochem.72.121801.161504
3. Kozlovsky Y, Kozlov MM. Membrane fission: model for intermediate structures. *Biophys J*. 2003;85(1):85-96. doi:10.1016/S0006-3495(03)74457-9
4. Shnyrova A, Frolov VA, Zimmerberg J. ER Biogenesis: Self-Assembly of Tubular Topology by Protein Hairpins. *Curr Biol*. 2008;18(11):R474-R476. doi:10.1016/j.cub.2008.04.031
5. Pinot M, Vanni S, Pagnotta S, et al. Polyunsaturated phospholipids facilitate membrane deformation and fission by endocytic proteins. *Science (80-)*. 2014;345(6197):693-697. doi:10.1126/science.1255288
6. Roux A, Uyhazi K, Frost A, De Camilli P. GTP-dependent twisting of dynamin implicates constriction and tension in membrane fission. *Nature*. 2006;441(7092):528-531. doi:10.1038/nature04718
7. Chan DC. Fusion and fission: interlinked processes critical for mitochondrial health. *Annu Rev Genet*. 2012;46:265-287. doi:10.1146/annurev-genet-110410-132529
8. Jones DM, Alvarez LA, Nolan R, et al. Dynamin-2 Stabilizes the HIV-1 Fusion Pore with a Low Oligomeric State. *Cell Rep*. 2017;18(2):443-453. doi:10.1016/j.celrep.2016.12.032
9. González-Jamett AM, Momboisse F, Haro-Acuña V, Bevilacqua JA, Caviedes P, Cárdenas AM. Dynamin-2 Function and Dysfunction Along the Secretory Pathway. *Front Endocrinol (Lausanne)*. 2013;4:126. doi:10.3389/fendo.2013.00126
10. Powers RE, Wang S, Liu TY, Rapoport TA. Reconstitution of the tubular endoplasmic reticulum network with purified components. *Nature*. 2017;543(7644):257-260. doi:10.1038/nature21387
11. Sabatini DD. George Palade 1912–2008. *Nat Cell Biol*. 2008;10(12):1374. doi:10.1038/ncb1208-1374
12. Dayel MJ, Horn EFY, Verkman AS. Diffusion of green fluorescent protein in the aqueous-phase lumen of endoplasmic reticulum. *Biophys J*.

1999;76(5):2843-2851. doi:10.1016/S0006-3495(99)77438-2

13. Ellenberg J, Siggia ED, Moreira JE, et al. Nuclear Membrane Dynamics and Reassembly in Living Cells: Targeting of an Inner Nuclear Membrane Protein in Interphase and Mitosis . *J Cell Biol*. 1997;138(6):1193-1206. doi:10.1083/jcb.138.6.1193
14. Lee C, Chen LB. Dynamic behavior of endoplasmic reticulum in living cells. *Cell*. 1988;54(1):37-46. doi:https://doi.org/10.1016/0092-8674(88)90177-8
15. Westrate LM, Lee JE, Prinz WA, Voeltz GK. Form follows function: the importance of endoplasmic reticulum shape. *Annu Rev Biochem*. 2015;84:791-811. doi:10.1146/annurev-biochem-072711-163501
16. Park SH, Blackstone C. Further assembly required: construction and dynamics of the endoplasmic reticulum network. *EMBO Rep*. 2010;11(7):515-521. doi:https://doi.org/10.1038/embor.2010.92
17. Jan CH, Williams CC, Weissman JS. Principles of ER cotranslational translocation revealed by proximity-specific ribosome profiling. *Science*. 2014;346(6210):1257521. doi:10.1126/science.1257521
18. Reid DW, Nicchitta C V. Diversity and selectivity in mRNA translation on the endoplasmic reticulum. *Nat Rev Mol Cell Biol*. 2015;16(4):221-231. doi:10.1038/nrm3958
19. Terasaki M, Shemesh T, Kasthuri N, et al. Stacked Endoplasmic Reticulum Sheets Are Connected by Helicoidal Membrane Motifs. *Cell*. 2013;154(2):285-296. doi:10.1016/j.cell.2013.06.031
20. Jaffe LF. Sources of calcium in egg activation: a review and hypothesis. *Dev Biol*. 1983;99(2):265-276. doi:10.1016/0012-1606(83)90276-2
21. Eisen A, Reynolds GT. Source and sinks for the calcium released during fertilization of single sea urchin eggs. *J Cell Biol*. 1985;100(5):1522-1527. doi:10.1083/jcb.100.5.1522
22. Clapham DE. Calcium Signaling. *Cell*. 2007;131(6):1047-1058. doi:https://doi.org/10.1016/j.cell.2007.11.028
23. Gilkey JC, Jaffe LF, Ridgway EB, Reynolds GT. A free calcium wave traverses the activating egg of the medaka, Oryzias latipes. *J Cell Biol*. 1978;76(2):448-466. doi:10.1083/jcb.76.2.448
24. Busa WB, Nuccitelli R. An elevated free cytosolic Ca2+ wave follows fertilization in eggs of the frog, Xenopus laevis. *J Cell Biol*.

1985;100(4):1325-1329. doi:10.1083/jcb.100.4.1325

25. Mulkey RM, Zucker RS. Action potentials must admit calcium to evoke transmitter release. *Nature*. 1991;350(6314):153-155. doi:10.1038/350153a0
26. Schwarz DS, Blower MD. The endoplasmic reticulum: structure, function and response to cellular signaling. *Cell Mol Life Sci*. 2016;73(1):79-94. doi:10.1007/s00018-015-2052-6
27. van Meer G, Voelker DR, Feigenson GW. Membrane lipids: where they are and how they behave. *Nat Rev Mol Cell Biol*. 2008;9(2):112-124. doi:10.1038/nrm2330
28. van der Veen JN, Kennelly JP, Wan S, Vance JE, Vance DE, Jacobs RL. The critical role of phosphatidylcholine and phosphatidylethanolamine metabolism in health and disease. *Biochim Biophys Acta - Biomembr*. 2017;1859(9, Part B):1558-1572. doi:https://doi.org/10.1016/j.bbamem.2017.04.006
29. Kučerka N, Tristram-Nagle S, Nagle JF. Closer Look at Structure of Fully Hydrated Fluid Phase DPPC Bilayers. *Biophys J*. 2006;90(11):L83-L85. doi:https://doi.org/10.1529/biophysj.106.086017
30. van den Brink-van der Laan E, Killian JA, de Kruijff B. Nonbilayer lipids affect peripheral and integral membrane proteins via changes in the lateral pressure profile. *Biochim Biophys Acta*. 2004;1666(1-2):275-288. doi:10.1016/j.bbamem.2004.06.010
31. Shi Z, Baumgart T. Membrane tension and peripheral protein density mediate membrane shape transitions. *Nat Commun*. 2015;6(1):5974. doi:10.1038/ncomms6974
32. Kruijff B de. Lipid polymorphism and biomembrane function. *Curr Opin Chem Biol*. 1997;1(4):564-569. doi:https://doi.org/10.1016/S1367-5931(97)80053-1
33. Di Paolo G, De Camilli P. Phosphoinositides in cell regulation and membrane dynamics. *Nature*. 2006;443(7112):651-657. doi:10.1038/nature05185
34. Guo Y, Li D, Zhang S, et al. Visualizing Intracellular Organelle and Cytoskeletal Interactions at Nanoscale Resolution on Millisecond Timescales. *Cell*. 2018;175(5):1430-1442.e17.

doi:10.1016/j.cell.2018.09.057

35. Hamada T, Ueda H, Kawase T, Hara-Nishimura I. Microtubules contribute to tubule elongation and anchoring of endoplasmic reticulum, resulting in high network complexity in Arabidopsis. *Plant Physiol*. 2014;166(4):1869-1876. doi:10.1104/pp.114.252320
36. Du Y, Ferro-Novick S, Novick P. Dynamics and inheritance of the endoplasmic reticulum. *J Cell Sci*. 2004;117(14):2871-2878. doi:10.1242/jcs.01286
37. Terasaki M, Chen LB, Fujiwara K. Microtubules and the endoplasmic reticulum are highly interdependent structures. *J Cell Biol*. 1986;103(4):1557-1568. doi:10.1083/jcb.103.4.1557
38. Phillips MJ, Voeltz GK. Structure and function of ER membrane contact sites with other organelles. *Nat Rev Mol Cell Biol*. 2016;17(2):69-82. doi:10.1038/nrm.2015.8
39. Vance JE, Aasman EJ, Szarka R. Brefeldin A does not inhibit the movement of phosphatidylethanolamine from its sites for synthesis to the cell surface. *J Biol Chem*. 1991;266(13):8241-8247.
40. Wirtz KWA, Zilversmit DB. Exchange of Phospholipids between Liver Mitochondria and Microsomes in Vitro. *J Biol Chem*. 1968;243(13):3596-3602. doi:10.1016/S0021-9258(19)34182-1
41. Lev S. Non-vesicular lipid transport by lipid-transfer proteins and beyond. *Nat Rev Mol Cell Biol*. 2010;11(10):739-750. doi:10.1038/nrm2971
42. Dennis EA, Kennedy EP. Intracellular sites of lipid synthesis and the biogenesis of mitochondria. *J Lipid Res*. 1972;13(2):263-267.
43. Osman C, Voelker DR, Langer T. Making heads or tails of phospholipids in mitochondria. *J Cell Biol*. 2011;192(1):7-16. doi:10.1083/jcb.201006159
44. Balla T, Sengupta N, Kim YJ. Lipid synthesis and transport are coupled to regulate membrane lipid dynamics in the endoplasmic reticulum. *Biochim Biophys Acta - Mol Cell Biol Lipids*. 2020;1865(1):158461. doi:https://doi.org/10.1016/j.bbalip.2019.05.005
45. Chen S, Novick P, Ferro-Novick S. ER structure and function. *Curr Opin Cell Biol*. 2013;25(4):428-433. doi:10.1016/j.ceb.2013.02.006
46. Nixon-Abell J, Obara CJ, Weigel A V, et al. Increased spatiotemporal resolution reveals highly dynamic dense tubular matrices in the peripheral

ER. *Science*. 2016;354(6311):aaf3928. doi:10.1126/science.aaf3928

47. Lee C, Chen LB. Dynamic behavior of endoplasmic reticulum in living cells. *Cell*. 1988;54(1):37-46. doi:10.1016/0092-8674(88)90177-8
48. Dreier L, Rapoport TA. In Vitro Formation of the Endoplasmic Reticulum Occurs Independently of Microtubules by a Controlled Fusion Reaction. *J Cell Biol*. 2000;148(5):883-898. doi:10.1083/jcb.148.5.883
49. Puhka M, Vihinen H, Joensuu M, Jokitalo E. Endoplasmic reticulum remains continuous and undergoes sheet-to-tubule transformation during cell division in mammalian cells . *J Cell Biol*. 2007;179(5):895-909. doi:10.1083/jcb.200705112
50. Khaminets A, Heinrich T, Mari M, et al. Regulation of endoplasmic reticulum turnover by selective autophagy. *Nature*. 2015;522(7556):354-358. doi:10.1038/nature14498
51. Grumati P, Morozzi G, Hölper S, et al. Full length RTN3 regulates turnover of tubular endoplasmic reticulum via selective autophagy. Zhang H, ed. *Elife*. 2017;6:e25555. doi:10.7554/eLife.25555
52. Shibata Y, Shemesh T, Prinz WA, Palazzo AF, Kozlov MM, Rapoport TA. Mechanisms determining the morphology of the peripheral ER. *Cell*. 2010;143(5):774-788. doi:10.1016/j.cell.2010.11.007
53. Senda T, Yoshinaga-Hirabayashi T. Intermembrane bridges within membrane organelles revealed by quick-freeze deep-etch electron microscopy. *Anat Rec*. 1998;251(3):339-345. doi:10.1002/(SICI)1097-0185(199807)251:3<339::AID-AR9>3.0.CO;2-Q
54. Klopfenstein DR, Kappeler F, Hauri HP. A novel direct interaction of endoplasmic reticulum with microtubules. *EMBO J*. 1998;17(21):6168-6177. doi:10.1093/emboj/17.21.6168
55. Klopfenstein DR, Klumperman J, Lustig A, Kammerer RA, Oorschot V, Hauri HP. Subdomain-specific localization of CLIMP-63 (p63) in the endoplasmic reticulum is mediated by its luminal alpha-helical segment. *J Cell Biol*. 2001;153(6):1287-1300. doi:10.1083/jcb.153.6.1287
56. Shibata Y, Voss C, Rist JM, et al. The reticulon and DP1/Yop1p proteins form immobile oligomers in the tubular endoplasmic reticulum. *J Biol Chem*. 2008;283(27):18892-18904. doi:10.1074/jbc.M800986200
57. Schweitzer Y, Shemesh T, Kozlov MM. A Model for Shaping Membrane

Sheets by Protein Scaffolds. *Biophys J*. 2015;109(3):564-573. doi:10.1016/j.bpj.2015.06.001

58. Voeltz GK, Prinz WA, Shibata Y, Rist JM, Rapoport TA. A class of membrane proteins shaping the tubular endoplasmic reticulum. *Cell*. 2006;124(3):573-586. doi:10.1016/j.cell.2005.11.047
59. Hu J, Shibata Y, Voss C, et al. Membrane proteins of the endoplasmic reticulum induce high-curvature tubules. *Science (80-)*. 2008;319(5867):1247-1250. doi:10.1126/science.1153634
60. Wang N, Rapoport TA. Reconstituting the reticular ER network - mechanistic implications and open questions. *J Cell Sci*. 2019;132(4). doi:10.1242/jcs.227611
61. Zurek N, Sparks L, Voeltz G. Reticulon short hairpin transmembrane domains are used to shape ER tubules. *Traffic*. 2011;12(1):28-41. doi:10.1111/j.1600-0854.2010.01134.x
62. Brady JP, Claridge JK, Smith PG, Schnell JR. A conserved amphipathic helix is required for membrane tubule formation by Yop1p. *Proc Natl Acad Sci U S A*. 2015;112(7):E639-48. doi:10.1073/pnas.1415882112
63. Rigaud J-L, Lévy D. Reconstitution of membrane proteins into liposomes. *Methods Enzymol*. 2003;372:65-86. doi:10.1016/S0076-6879(03)72004-7
64. Chen YJ, Zhang P, Egelman EH, Hinshaw JE. The stalk region of dynamin drives the constriction of dynamin tubes. *Nat Struct Mol Biol*. 2004;11(6):574-575. doi:10.1038/nsmb762
65. Berman SB, Pineda FJ, Hardwick JM. Mitochondrial fission and fusion dynamics: the long and short of it. *Cell Death Differ*. 2008;15(7):1147-1152. doi:10.1038/cdd.2008.57
66. Qian W, Choi S, Gibson GA, Watkins SC, Bakkenist CJ, Van Houten B. Mitochondrial hyperfusion induced by loss of the fission protein Drp1 causes ATM-dependent G2/M arrest and aneuploidy through DNA replication stress. *J Cell Sci*. 2012;125(23):5745-5757. doi:10.1242/jcs.109769
67. Knott AB, Perkins G, Schwarzenbacher R, Bossy-Wetzel E. Mitochondrial fragmentation in neurodegeneration. *Nat Rev Neurosci*. 2008;9(7):505-518. doi:10.1038/nrn2417
68. Escobar-Henriques M, Anton F. Mechanistic perspective of mitochondrial

fusion: Tubulation vs. fragmentation. *Biochim Biophys Acta - Mol Cell Res*. 2013;1833(1):162-175. doi:https://doi.org/10.1016/j.bbamcr.2012.07.016

69. Lü L, Niu L, Hu J. “At last in” the physiological roles of the tubular ER network. *Biophys Reports*. 2020;6(4):105-114. doi:10.1007/s41048-020-00113-y
70. Orso G, Pendin D, Liu S, et al. Homotypic fusion of ER membranes requires the dynamin-like GTPase Atlastin. *Nature*. 2009;460(7258):978-983. doi:10.1038/nature08280
71. Chen S, Desai T, McNew JA, Gerard P, Novick PJ, Ferro-Novick S. Lunapark stabilizes nascent three-way junctions in the endoplasmic reticulum. *Proc Natl Acad Sci*. 2015;112(2):418 LP - 423. doi:10.1073/pnas.1423026112
72. Niu L, Ma T, Yang F, et al. Atlastin-mediated membrane tethering is critical for cargo mobility and exit from the endoplasmic reticulum. *Proc Natl Acad Sci U S A*. 2019;116(28):14029-14038. doi:10.1073/pnas.1908409116
73. Warnock DE, Hinshaw JE, Schmid SL. Dynamin self-assembly stimulates its GTPase activity. *J Biol Chem*. 1996;271(37):22310-22314. doi:10.1074/jbc.271.37.22310
74. Pendin D, Tosetto J, Moss TJ, et al. GTP-dependent packing of a three-helix bundle is required for atlastin-mediated fusion. *Proc Natl Acad Sci U S A*. 2011;108(39):16283-16288. doi:10.1073/pnas.1106421108
75. Bian X, Klemm RW, Liu TY, et al. Structures of the atlastin GTPase provide insight into homotypic fusion of endoplasmic reticulum membranes. *Proc Natl Acad Sci U S A*. 2011;108(10):3976-3981. doi:10.1073/pnas.1101643108
76. Rismanchi N, Soderblom C, Stadler J, Zhu PP, Blackstone C. Atlastin GTPases are required for Golgi apparatus and ER morphogenesis. *Hum Mol Genet*. 2008;17(11):1591-1604. doi:10.1093/hmg/ddn046
77. Zheng J, Cahill SM, Lemmon MA, Fushman D, Schlessinger J, Cowburn D. Identification of the Binding Site for Acidic Phospholipids on the PH Domain of Dynamin: Implications for Stimulation of GTPase Activity. *J Mol Biol*. 1996;255(1):14-21. doi:https://doi.org/10.1006/jmbi.1996.0002
78. Byrnes LJ, Sondermann H. Structural basis for the nucleotide-dependent dimerization of the large G protein atlastin-1/SPG3A. *Proc Natl Acad Sci U*

S A. 2011;108(6):2216-2221. doi:10.1073/pnas.1012792108

79. Chappie JS, Acharya S, Liu Y-W, Leonard M, Pucadyil TJ, Schmid SL. An Intramolecular Signaling Element that Modulates Dynamin Function In Vitro and In Vivo. *Mol Biol Cell*. 2009;20(15):3561-3571. doi:10.1091/mbc.e09-04-0318
80. Reubold TF, Faelber K, Plattner N, et al. Crystal structure of the dynamin tetramer. *Nature*. 2015;525(7569):404-408. doi:10.1038/nature14880
81. Bashkirov P V., Akimov SA, Evseev AI, Schmid SL, Zimmerberg J, Frolov VA. GTPase Cycle of Dynamin Is Coupled to Membrane Squeeze and Release, Leading to Spontaneous Fission. *Cell*. 2008;135(7):1276-1286. doi:10.1016/j.cell.2008.11.028
82. Orso G, Pendin D, Liu S, et al. Homotypic fusion of ER membranes requires the dynamin-like GTPase Atlastin. *Nature*. 2009;460(7258):978-983. doi:10.1038/nature08280
83. Moss TJ, Daga A, McNew JA. Fusing a lasting relationship between ER tubules. *Trends Cell Biol*. 2011;21(7):416-423. doi:10.1016/j.tcb.2011.03.009
84. Wang S, Tukachinsky H, Romano FB, Rapoport TA. Cooperation of the ER-shaping proteins atlastin, lunapark, and reticulons to generate a tubular membrane network. Kozlov M, ed. *Elife*. 2016;5:e18605. doi:10.7554/eLife.18605
85. Chen S, Novick P, Ferro-Novick S. ER network formation requires a balance of the dynamin-like GTPase Sey1p and the Lunapark family member Lnp1p. *Nat Cell Biol*. 2012;14(7):707-716. doi:10.1038/ncb2523
86. Lee M, Ko YJ, Moon Y, et al. SNAREs support atlastin-mediated homotypic ER fusion in Saccharomyces cerevisiae. *J Cell Biol*. 2015;210(3):451-470. doi:10.1083/jcb.201501043
87. Kucharz K, Lauritzen M. CaMKII-dependent endoplasmic reticulum fission by whisker stimulation and during cortical spreading depolarization. *Brain*. 2018;141(4):1049-1062. doi:10.1093/brain/awy036
88. Terasaki M, Jaffe LA, Hunnicutt GR, Hammer JA 3rd. Structural change of the endoplasmic reticulum during fertilization: evidence for loss of membrane continuity using the green fluorescent protein. *Dev Biol*. 1996;179(2):320-328. doi:10.1006/dbio.1996.0263

89. Subramanian K, Meyer T. Calcium-induced restructuring of nuclear envelope and endoplasmic reticulum calcium stores. *Cell*. 1997;89(6):963-971. doi:10.1016/s0092-8674(00)80281-0

90. Bhaskara RM, Grumati P, Garcia-Pardo J, et al. Curvature induction and membrane remodeling by FAM134B reticulon homology domain assist selective ER-phagy. *Nat Commun*. 2019;10(1):2370. doi:10.1038/s41467-019-10345-3

91. Sainia SG, Liu C, Zhang P, Lee TH. Membrane tethering by the atlastin GTPase depends on GTP hydrolysis but not on forming the cross-over configuration. *Mol Biol Cell*. 2014;25(24):3942-3953. doi:10.1091/mbc.E14-08-1284

92. Kim KT, Moon Y, Jang Y, et al. Molecular mechanisms of atlastin-mediated ER membrane fusion revealed by a FRET-based single-vesicle fusion assay. *Sci Rep*. 2017;7(1):8700. doi:10.1038/s41598-017-09162-9

93. Frolov VA, Escalada A, Akimov SA, Shnyrova A V. Geometry of membrane fission. *Chem Phys Lipids*. 2015;185:129-140. doi:10.1016/j.chemphyslip.2014.07.006

94. Renard H-F, Simunovic M, Lemière J, et al. Endophilin-A2 functions in membrane scission in clathrin-independent endocytosis. *Nature*. 2015;517(7535):493-496. doi:10.1038/nature14064

95. Simunovic M, Manneville J-B, Renard H-F, et al. Friction Mediates Scission of Tubular Membranes Scaffolded by BAR Proteins. *Cell*. 2017;170(1):172-184.e11. doi:10.1016/j.cell.2017.05.047

96. Roux A. The physics of membrane tubes: soft templates for studying cellular membranes. *Soft Matter*. 2013;9(29):6726-6736. doi:10.1039/C3SM50514F

97. Upadhyaya A, Sheetz MP. Tension in tubulovesicular networks of Golgi and endoplasmic reticulum membranes. *Biophys J*. 2004;86(5):2923-2928. doi:10.1016/S0006-3495(04)74343-X

98. Ben M'barek K, Ajjaji D, Chorlay A, Vanni S, Forêt L, Thiam AR. ER Membrane Phospholipids and Surface Tension Control Cellular Lipid Droplet Formation. *Dev Cell*. 2017;41(6):591-604.e7. doi:10.1016/j.devcel.2017.05.012

99. Wu H, Carvalho P, Voeltz GK. Here, there, and everywhere: The

importance of ER membrane contact sites. *Science (80-)*. 2018;361(6401):eaan5835. doi:10.1126/science.aan5835

100. Diz-Muñoz A, Fletcher DA, Weiner OD. Use the force: membrane tension as an organizer of cell shape and motility. *Trends Cell Biol*. 2013;23(2):47-53. doi:10.1016/j.tcb.2012.09.006
101. O'Sullivan NC, Jahn TR, Reid E, O'Kane CJ. Reticulon-like-1, the Drosophila orthologue of the hereditary spastic paraplegia gene reticulon 2, is required for organization of endoplasmic reticulum and of distal motor axons. *Hum Mol Genet*. 2012;21(15):3356-3365. doi:10.1093/hmg/dds167
102. Lin C, White RR, Sparkes I, Ashwin P. Modeling Endoplasmic Reticulum Network Maintenance in a Plant Cell. *Biophys J*. 2017;113(1):214-222. doi:10.1016/j.bpj.2017.05.046
103. Rigaud JL, Pitard B, Levy D. Reconstitution of membrane proteins into liposomes: application to energy-transducing membrane proteins. *Biochim Biophys Acta*. 1995;1231(3):223-246. doi:10.1016/0005-2728(95)00091-v
104. Velasco-Olmo A, Ormaetxea Gisasola J, Martinez Galvez JMJM, Vera Lillo J, Shnyrova AVAVA V. Combining patch-clamping and fluorescence microscopy for quantitative reconstitution of cellular membrane processes with Giant Suspended Bilayers. *Sci Rep*. 2019;9(1):7255. doi:10.1038/s41598-019-43561-4
105. Jain NK, Roy I. Effect of trehalose on protein structure. *Protein Sci*. 2009;18(1):24-36. doi:10.1002/pro.3
106. Dar S, Kamerkar SC, Pucadyil TJ. A high-throughput platform for real-time analysis of membrane fission reactions reveals dynamin function. *Nat Cell Biol*. 2015;17(12):1588-1596. doi:10.1038/ncb3254
107. Terasaki M. Axonal endoplasmic reticulum is very narrow. *J Cell Sci*. 2018;131(4). doi:10.1242/jcs.210450
108. Schroeder LK, Barentine AES, Merta H, et al. Dynamic nanoscale morphology of the ER surveyed by STED microscopy. *J Cell Biol*. 2019;218(1):83-96. doi:10.1083/jcb.201809107
109. Shim S-H, Xia C, Zhong G, et al. Super-resolution fluorescence imaging of organelles in live cells with photoswitchable membrane probes. *Proc Natl Acad Sci U S A*. 2012;109(35):13978-13983. doi:10.1073/pnas.1201882109

110. Capraro BR, Yoon Y, Cho W, Baumgart T. Curvature sensing by the epsin N-terminal homology domain measured on cylindrical lipid membrane tethers. *J Am Chem Soc*. 2010;132(4):1200-1201. doi:10.1021/ja907936c
111. Aimon S, Callan-Jones A, Berthaud A, Pinot M, Toombes GES, Bassereau P. Membrane shape modulates transmembrane protein distribution. *Dev Cell*. 2014;28(2):212-218. doi:10.1016/j.devcel.2013.12.012
112. Pendin D, McNew JA, Daga A. Balancing ER dynamics: shaping, bending, severing, and mending membranes. *Curr Opin Cell Biol*. 2011;23(4):435-442. doi:10.1016/j.ceb.2011.04.007
113. Morlot S, Galli V, Klein M, et al. Membrane shape at the edge of the dynamin helix sets location and duration of the fission reaction. *Cell*. 2012;151(3):619-629. doi:10.1016/j.cell.2012.09.017
114. Drury JL, Dembo M. Aspiration of Human Neutrophils: Effects of Shear Thinning and Cortical Dissipation. *Biophys J*. 2001;81(6):3166-3177. doi:https://doi.org/10.1016/S0006-3495(01)75953-X
115. Heinrich V, Leung A, Evans E. Nano- to microscale dynamics of P-selectin detachment from leukocyte interfaces. II. Tether flow terminated by P-selectin dissociation from PSGL-1. *Biophys J*. 2005;88(3):2299-2308. doi:10.1529/biophysj.104.051706
116. Bassereau P, Jin R, Baumgart T, et al. The 2018 biomembrane curvature and remodeling roadmap. *J Phys D Appl Phys*. 2018;51(34). doi:10.1088/1361-6463/aacb98
117. Hu J, Shibata Y, Zhu PP, et al. A Class of Dynamin-like GTPases Involved in the Generation of the Tubular ER Network. *Cell*. 2009;138(3):549-561. doi:10.1016/j.cell.2009.05.025
118. Sugiura S, Mima J. Physiological lipid composition is vital for homotypic ER membrane fusion mediated by the dynamin-related GTPase Sey1p. *Sci Rep*. 2016;6(1):20407. doi:10.1038/srep20407
119. Moss TJ, Andreazza C, Verma A, Daga A, McNew JA. Membrane fusion by the GTPase atlastin requires a conserved C-terminal cytoplasmic tail and dimerization through the middle domain. *Proc Natl Acad Sci U S A*. 2011;108(27):11133-11138. doi:10.1073/pnas.1105056108
120. Saini SG, Liu C, Zhang P, Lee TH. Membrane tethering by the atlastin GTPase depends on GTP hydrolysis but not on forming the cross-over

configuration. *Mol Biol Cell*. 2014;25(24):3942-3953. doi:10.1091/mbc.e14-08-1284

121. Kuzmin PI, Zimmerberg J, Chizmadzhev YA, Cohen FS. A quantitative model for membrane fusion based on low-energy intermediates. *Proc Natl Acad Sci*. 2001;98(13):7235 LP - 7240. doi:10.1073/pnas.121191898
122. de Saint Basile G, Ménasché G, Fischer A. Molecular mechanisms of biogenesis and exocytosis of cytotoxic granules. *Nat Rev Immunol*. 2010;10(8):568-579. doi:10.1038/nri2803
123. Shi L, Shen Q-T, Kiel A, et al. SNARE proteins: one to fuse and three to keep the nascent fusion pore open. *Science*. 2012;335(6074):1355-1359. doi:10.1126/science.1214984
124. Montecucco C, Schiavo G, Pantano S. SNARE complexes and neuroexocytosis: how many, how close? *Trends Biochem Sci*. 2005;30(7):367-372. doi:10.1016/j.tibs.2005.05.002
125. Schmid SL, Frolov VA. Dynamin: Functional Design of a Membrane Fission Catalyst. *Annu Rev Cell Dev Biol*. 2011;27(1):79-105. doi:10.1146/annurev-cellbio-100109-104016
126. Praefcke GJK, McMahon HT. The dynamin superfamily: universal membrane tubulation and fission molecules? *Nat Rev Mol Cell Biol*. 2004;5(2):133-147. doi:10.1038/nrm1313
127. Daumke O, Praefcke GJK. Invited review: Mechanisms of GTP hydrolysis and conformational transitions in the dynamin superfamily. *Biopolymers*. 2016;105(8):580-593. doi:10.1002/bip.22855
128. Shnyrova A V, Bashkirov P V, Akimov SA, et al. Geometric catalysis of membrane fission driven by flexible dynamin rings. *Science*. 2013;339(6126):1433-1436. doi:10.1126/science.1233920
129. Hoeller D, Volarevic S, Dikic I. Compartmentalization of growth factor receptor signalling. *Curr Opin Cell Biol*. 2005;17(2):107-111. doi:10.1016/j.ceb.2005.01.001
130. Marsh M, Helenius A. Virus entry: open sesame. *Cell*. 2006;124(4):729-740. doi:10.1016/j.cell.2006.02.007
131. Doherty GJ, McMahon HT. Mechanisms of Endocytosis. *Annu Rev Biochem*. 2009;78(1):857-902. doi:10.1146/annurev.biochem.78.081307.110540

132. Antonny B, Burd C, De Camilli P, et al. Membrane fission by dynamin: what we know and what we need to know. *EMBO J*. 2016;35(21):2270-2284. doi:10.15252/embj.201694613
133. Koenig JH, Ikeda K. Disappearance and reformation of synaptic vesicle membrane upon transmitter release observed under reversible blockage of membrane retrieval. *J Neurosci*. 1989;9(11):3844-3860. doi:10.1523/jneurosci.09-11-03844.1989
134. Tsuruhara T, Koenig JH, Ikeda K. Synchronized endocytosis studied in the oocyte of a temperature-sensitive mutant of Drosophila melanogaster. *Cell Tissue Res*. 1990;259(2):199-207. doi:10.1007/BF00318441
135. Ferguson SM, Raimondi A, Paradise S, et al. Coordinated actions of actin and BAR proteins upstream of dynamin at endocytic clathrin-coated pits. *Dev Cell*. 2009;17(6):811-822. doi:10.1016/j.devcel.2009.11.005
136. Sundborger A, Soderblom C, Vorontsova O, Evergren E, Hinshaw JE, Shupliakov O. An endophilin-dynamin complex promotes budding of clathrin-coated vesicles during synaptic vesicle recycling. *J Cell Sci*. 2011;124(Pt 1):133-143. doi:10.1242/jcs.072686
137. Roux A, Koster G, Lenz M, et al. Membrane curvature controls dynamin polymerization. *Proc Natl Acad Sci*. 2010;107(9):4141-4146. doi:10.1073/PNAS.0913734107
138. Bhave M, Mettlen M, Wang X, Schmid SL. Early and nonredundant functions of dynamin isoforms in clathrin-mediated endocytosis. *Mol Biol Cell*. 2020;31(18):2035-2047. doi:10.1091/mbc.E20-06-0363
139. Srinivasan S, Burckhardt CJ, Bhave M, et al. A noncanonical role for dynamin-1 in regulating early stages of clathrin-mediated endocytosis in non-neuronal cells. Hughson F, ed. *PLOS Biol*. 2018;16(4):e2005377. doi:10.1371/journal.pbio.2005377
140. Cárdenas AM, Marengo FD. Rapid endocytosis and vesicle recycling in neuroendocrine cells. *Cell Mol Neurobiol*. 2010;30(8):1365-1370. doi:10.1007/s10571-010-9579-8
141. Cao H, Weller S, Orth JD, et al. Actin and Arf1-dependent recruitment of a cortactin-dynamin complex to the Golgi regulates post-Golgi transport. *Nat Cell Biol*. 2005;7(5):483-492. doi:10.1038/ncb1246
142. Mesaki K, Tanabe K, Obayashi M, Oe N, Takei K. Fission of tubular

endosomes triggers endosomal acidification and movement. *PLoS One*. 2011;6(5):e19764. doi:10.1371/journal.pone.0019764

143. Nicoziani P, Vilhardt F, Llorente A, et al. Role for dynamin in late endosome dynamics and trafficking of the cation-independent mannose 6-phosphate receptor. *Mol Biol Cell*. 2000;11(2):481-495. doi:10.1091/mbc.11.2.481
144. Lee JE, Westrate LM, Wu H, Page C, Voeltz GK. Multiple dynamin family members collaborate to drive mitochondrial division. *Nature*. 2016;540(7631):139-143. doi:10.1038/nature20555
145. Kraus F, Ryan MT. The constriction and scission machineries involved in mitochondrial fission. *J Cell Sci*. 2017;130(18):2953-2960. doi:10.1242/jcs.199562
146. Liu Y-W, Neumann S, Ramachandran R, Ferguson SM, Pucadyil TJ, Schmid SL. Differential curvature sensing and generating activities of dynamin isoforms provide opportunities for tissue-specific regulation. *Proc Natl Acad Sci*. 2011;108(26):E234-E242. doi:10.1073/pnas.1102710108
147. Hinshaw JE, Schmid SL. Dynamin self-assembles into rings suggesting a mechanism for coated vesicle budding. *Nature*. 1995;374(6518):190-192. doi:10.1038/374190a0
148. Ramachandran R, Surka M, Chappie JS, et al. The dynamin middle domain is critical for tetramerization and higher-order self-assembly. *EMBO J*. 2007;26(2):559-566. doi:10.1038/sj.emboj.7601491
149. Niemann HH, Knetsch MLW, Scherer A, Manstein DJ, Kull FJ. Crystal structure of a dynamin GTPase domain in both nucleotide-free and GDP-bound forms. *EMBO J*. 2001;20(21):5813-5821. doi:10.1093/emboj/20.21.5813
150. Reubold TF, Eschenburg S, Becker A, et al. Crystal structure of the GTPase domain of rat dynamin 1. *Proc Natl Acad Sci U S A*. 2005;102(37):13093-13098. doi:10.1073/pnas.0506491102
151. Sweitzer SM, Hinshaw JE. Dynamin undergoes a GTP-dependent conformational change causing vesiculation. *Cell*. 1998;93(6):1021-1029. doi:10.1016/S0092-8674(00)81207-6
152. Chappie JS, Acharya S, Leonard M, Schmid SL, Dyda F. G domain dimerization controls dynamin's assembly-stimulated GTPase activity. *Nature*. 2010;465(7297):435-440. doi:10.1038/nature09032

153. Chappie JSS, Mears JAA, Fang S, et al. A pseudoatomic model of the dynamin polymer identifies a hydrolysis-dependent powerstroke. *Cell*. 2011;147(1):209-222. doi:10.1016/j.cell.2011.09.003
154. Stowell MHB, Marks B, Wigge P, McMahon HT. Nucleotide-dependent conformational changes in dynamin: Evidence for a mechanochemical molecular spring. *Nat Cell Biol*. 1999;1(1):27-32. doi:10.1038/8997
155. Smirnova E, Shurland DL, Newman-Smith ED, Pishvaee B, Van Der Bliek AM. A model for dynamin self-assembly based on binding between three different protein domains. *J Biol Chem*. 1999;274(21):14942-14947. doi:10.1074/jbc.274.21.14942
156. Ford MGJ, Jenni S, Nunnari J. The crystal structure of dynamin. *Nature*. 2011;477(7366):561-566. doi:10.1038/nature10441
157. Ferguson KM, Lemmon MA, Schlessinger J, Sigler PB. Crystal structure at 2.2 Å resolution of the pleckstrin homology domain from human dynamin. *Cell*. 1994;79(2):199-209. doi:10.1016/0092-8674(94)90190-2
158. Harlan JE, Hajduk PJ, Yoon HS, Fesik SW. Pleckstrin homology domains bind to phosphatidylinositol-4,5-bisphosphate. *Nature*. 1994;371(6493):168-170. doi:10.1038/371168a0
159. Ramachandran R, Schmid SL. Real-time detection reveals that effectors couple dynamin's GTP-dependent conformational changes to the membrane. *EMBO J*. 2008;27(1):27-37. doi:10.1038/sj.emboj.7601961
160. Ramachandran R, Pucadyil TJ, Liu Y-W, et al. Membrane insertion of the pleckstrin homology domain variable loop 1 is critical for dynamin-catalyzed vesicle scission. *Mol Biol Cell*. 2009;20(22):4630-4639. doi:10.1091/mbc.e09-08-0683
161. Carr JF, Hinshaw JE. Dynamin Assembles into Spirals under Physiological Salt Conditions upon the Addition of GDP and γ-Phosphate Analogues *. *J Biol Chem*. 1997;272(44):28030-28035. doi:10.1074/jbc.272.44.28030
162. Carr JF, Hinshaw JE. Dynamin assembles into spirals under physiological salt conditions upon the addition of GDP and γ-phosphate analogues. *J Biol Chem*. 1997;272(44):28030-28035. doi:10.1074/jbc.272.44.28030
163. Zhang P, Hinshaw JE. Three-dimensional reconstruction of dynamin in the constricted state. *Nat Cell Biol*. 2001;3(10):922-926. doi:10.1038/ncb1001-

922

164. Muhlberg AB, Warnock DE, Schmid SL. Domain structure and intramolecular regulation of dynamin GTPase. *EMBO J*. 1997;16(22):6676-6683. doi:10.1093/emboj/16.22.6676
165. Ramachandran R, Surka M, Chappie JS, et al. The dynamin middle domain is critical for tetramerization and higher-order self-assembly. *EMBO J*. 2007;26(2):559-566. doi:10.1038/sj.emboj.7601491
166. Kong L, Sochacki KA, Wang H, et al. Cryo-EM of the dynamin polymer assembled on lipid membrane. *Nature*. 2018;560(7717):258-262. doi:10.1038/s41586-018-0378-6
167. Faelber K, Posor Y, Gao S, et al. Crystal structure of nucleotide-free dynamin. *Nature*. 2011;477(7366):556-562. doi:10.1038/nature10369
168. Kong L, Sochacki KA, Wang H, et al. Cryo-EM of the dynamin polymer assembled on lipid membrane. *Nature*. 2018;560(7717):258-262. doi:10.1038/s41586-018-0378-6
169. Sundborger AC, Fang S, Heymann JA, Ray P, Chappie JS, Hinshaw JE. A dynamin mutant defines a superconstricted prefission state. *Cell Rep*. 2014;8(3):734-742. doi:10.1016/j.celrep.2014.06.054
170. Mattila JP, Shnyrova A V., Sundborger AC, et al. A hemi-fission intermediate links two mechanistically distinct stages of membrane fission. *Nature*. 2015;524(7563):109-113. doi:10.1038/nature14509
171. Kadosh A, Colom A, Yellin B, Roux A, Shemesh T. The tilted helix model of dynamin oligomers. *Proc Natl Acad Sci U S A*. 2019;116(26):2845-12850. doi:10.1073/pnas.1903769116
172. Pannuzzo M, McDargh ZA, Deserno M. The role of scaffold reshaping and disassembly in dynamin driven membrane fission. Kozlov MM, Malhotra V, eds. *Elife*. 2018;7:e39441. doi:10.7554/eLife.39441
173. Colom A, Redondo-Morata L, Chiaruttini N, Roux A, Scheuring S. Dynamic remodeling of the dynamin helix during membrane constriction. *Proc Natl Acad Sci U S A*. 2017;114(21):5449-5454. doi:10.1073/pnas.1619578114
174. Hinshaw JE, Schmid SL. Hinshaw and Schmid 1995. 1995;374(March):190-192.
175. Cocucci E, Gaudin R, Kirchhausen T. Dynamin recruitment and membrane scission at the neck of a clathrin-coated pit. *Mol Biol Cell*.

2014;25(22):3595-3609. doi:10.1091/mbc.E14-07-1240

176. Grassart A, Cheng AT, Hong SH, et al. Actin and dynamin2 dynamics and interplay during clathrin-mediated endocytosis. *J Cell Biol*. 2014;205(5):721-735. doi:10.1083/jcb.201403041
177. Sundborger AC, Fang S, Heymann JA, Ray P, Chappie JS, Hinshaw JE. A dynamin mutant defines a superconstricted prefission state. *Cell Rep*. 2014;8(3):734-742. doi:10.1016/j.celrep.2014.06.054
178. Loerke D, Mettlen M, Yarar D, et al. Cargo and dynamin regulate clathrin-coated pit maturation. *PLoS Biol*. 2009;7(3):e57. doi:10.1371/journal.pbio.1000057
179. Chernomordik L V, Kozlov MM. Mechanics of membrane fusion. *Nat Struct Mol Biol*. 2008;15(7):675-683. doi:10.1038/nsmb.1455
180. Beltrán-Heredia E, Tsai F-C, Salinas-Almaguer S, Cao FJ, Bassereau P, Monroy F. Membrane curvature induces cardiolipin sorting. *Commun Biol*. 2019;2(1):225. doi:10.1038/s42003-019-0471-x
181. Chen Y-F, Tsang K-Y, Chang W-F, Fan Z-A. Differential dependencies on [Ca2+] and temperature of the monolayer spontaneous curvatures of DOPE, DOPA and cardiolipin: effects of modulating the strength of the inter-headgroup repulsion. *Soft Matter*. 2015;11(20):4041-4053. doi:10.1039/C5SM00577A
182. Renner LD, Weibel DB. Cardiolipin microdomains localize to negatively curved regions of Escherichia coli membranes. *Proc Natl Acad Sci*. 2011;108(15):6264 LP - 6269. doi:10.1073/pnas.1015757108
183. Nichols-Smith S, Kuhl T. Electrostatic interactions between model mitochondrial membranes. *Colloids Surf B Biointerfaces*. 2005;41(2-3):121-127. doi:10.1016/j.colsurfb.2004.11.003
184. Zacharias DA, Violin JD, Newton AC, Tsien RY. Partitioning of lipid-modified monomeric GFPs into membrane microdomains of live cells. *Science*. 2002;296(5569):913-916. doi:10.1126/science.1068539
185. Ferguson SM, De Camilli P. *Dynamin, a Membrane-Remodelling GTPase*. Vol 13. Nature Publishing Group; 2012:75-88. doi:10.1038/nrm3266
186. Merrifield CJ, Feldman ME, Wan L, Almers W. Imaging actin and dynamin recruitment during invagination of single clathrin-coated pits. *Nat Cell Biol*.

2002;4(9):691-698. doi:10.1038/ncb837

187. Liu J, Noel JK, Low HH. Structural basis for membrane tethering by a bacterial dynamin-like pair. *Nat Commun*. 2018;9(1):3345. doi:10.1038/s41467-018-05523-8
188. Jensen MB, Bhatia VK, Jao CC, et al. Membrane Curvature Sensing by Amphipathic Helices: A SINGLE LIPOSOME STUDY USING α-SYNUCLEIN AND ANNEXIN B12 *. *J Biol Chem*. 2011;286(49):42603-42614. doi:10.1074/jbc.M111.271130
189. Ramachandran R. Mitochondrial dynamics: The dynamin superfamily and execution by collusion. *Semin Cell Dev Biol*. 2018;76:201-212. doi:10.1016/j.semcdb.2017.07.039
190. Traut TW. Physiological concentrations of purines and pyrimidines. *Mol Cell Biochem*. 1994;140(1):1-22. doi:10.1007/BF00928361
191. Frolov VA, Cho M-S, Bronk P, Reese TS, Zimmerberg J. Multiple Local Contact Sites are Induced by GPI-Linked Influenza Hemagglutinin During Hemifusion and Flickering Pore Formation. *Traffic*. 2000;1(8):622-630. doi:https://doi.org/10.1034/j.1600-0854.2000.010806.x
192. Vetter IR, Wittinghofer A. The guanine nucleotide-binding switch in three dimensions. *Science*. 2001;294(5545):1299-1304. doi:10.1126/science.1062023
193. Jahn R, Lang T, Südhof TC. Membrane Fusion. *Cell*. 2003;112(4):519-533. doi:10.1016/S0092-8674(03)00112-0
194. Yoshida Y, Kinuta M, Abe T, et al. The stimulatory action of amphiphysin on dynamin function is dependent on lipid bilayer curvature. *EMBO J*. 2004;23(17):3483-3491. doi:https://doi.org/10.1038/sj.emboj.7600355
195. Edelstein A, Amodaj N, Hoover K, Vale R, Stuurman N. Computer Control of Microscopes Using μManager. *Curr Protoc Mol Biol*. 2010;92(1):14.20.1-14.20.17. doi:doi:10.1002/0471142727.mb1420s92
196. Abràmoff MD, Magalhães PJ, Ram SJ. Image processing with ImageJ Part II. *Biophotonics Int*. 2005;11(7):36-43.
197. Leonard M, Doo Song B, Ramachandran R, Schmid SL. Robust Colorimetric Assays for Dynamin's Basal and Stimulated GTPase Activities. In: ; 2005:490-503. doi:10.1016/S0076-6879(05)04043-7
198. Geertsma ER, Nik Mahmood NAB, Schuurman-Wolters GK, Poolman B.

Membrane reconstitution of ABC transporters and assays of translocator function. *Nat Protoc*. 2008;3(2):256-266. doi:10.1038/nprot.2007.519

199. Pucadyil TJ, Schmid SL. Supported bilayers with excess membrane reservoir: a template for reconstituting membrane budding and fission. *Biophys J*. 2010;99(2):517-525. doi:10.1016/j.bpj.2010.04.036
200. Schindelin J, Arganda-Carreras I, Frise E, et al. Fiji: an open-source platform for biological-image analysis. *Nat Methods*. 2012;9(7):676-682. doi:10.1038/nmeth.2019
201. de Chaumont F, Dallongeville S, Chenouard N, et al. Icy: an open bioimage informatics platform for extended reproducible research. *Nat Methods*. 2012;9(7):690-696. doi:10.1038/nmeth.2075
202. Smith SB, Cui Y, Bustamante C. Optical-trap force transducer that operates by direct measurement of light momentum. *Methods Enzymol*. 2003;361:134-162. doi:10.1016/s0076-6879(03)61009-8
203. Mastronarde DN. Automated electron microscope tomography using robust prediction of specimen movements. *J Struct Biol*. 2005;152(1):36-51. doi:https://doi.org/10.1016/j.jsb.2005.07.007
204. Kremer JR, Mastronarde DN, McIntosh JR. Computer visualization of three-dimensional image data using IMOD. *J Struct Biol*. 1996;116(1):71-76. doi:10.1006/jsbi.1996.0013

Appendix

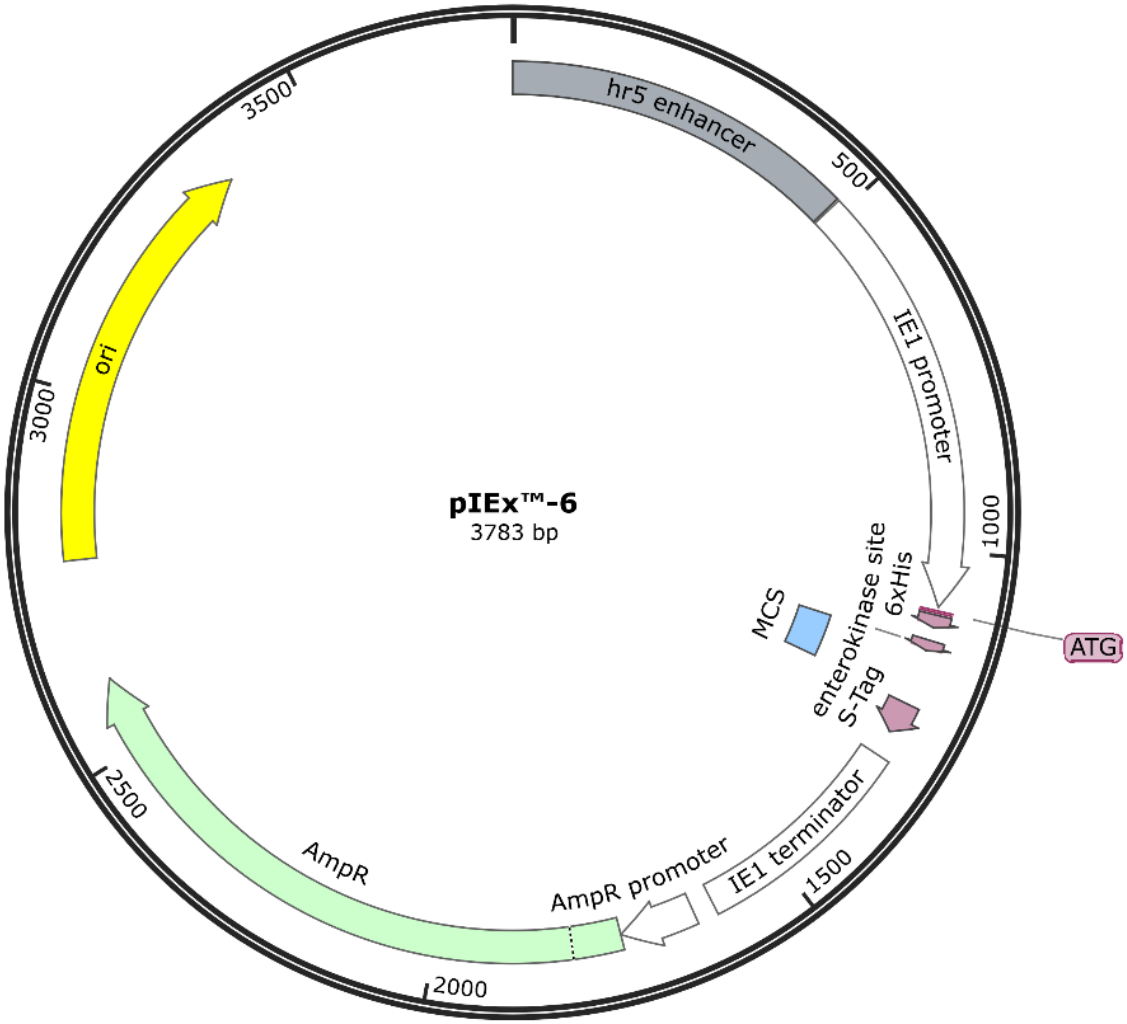

Nucleotide sequence for Dyn2 expression

ATGGGCAACCGCGGGATGGAAGAGCTGATCCCGCTGGTCAACAAACT
GCAGGACGCCTTCAGCTCCATCGGCCAGAGCTGCCACCTGGACCTGCCG
CAGATCGCTGTAGTGGGCGGCCAGAGCGCCGGCAAGAGCTCGGTGCTGG
AGAACTTCGTGGGCCGGGACTTCCTTCCCCGCGGTTCAGGAATCGTCACC
CGGCGGCCTCTCATTCTGCAGCTCATCTTCTCAAAAACAGAACATGCCGA
GTTTTTGCACTGCAAGTCCAAAAAGTTTACAGACTTTGATGAAGTCCGGCA
GGAGATTGAAGCAGAGACCGACAGGGTCACGGGGACCAACAAAGGCATC

TCCCCAGTGCCCATCAACCTTCGAGTCTACTCGCCACACGTGTTGAACTTG
ACCCTCATCGACCTCCCGGGTATCACCAAGGTGCCTGTGGGCGACCAGC
CTCCAGACATCGAGTACCAGATCAAGGACATGATCCTGCAGTTCATCAGC
CGGGAGAGCAGCCTCATTCTGGCTGTCACGCCCGCCAACATGGACCTGG
CCAACTCCGACGCCCTCAAGCTGGCCAAGGAAGTCGATCCCCAAGGCCTA
CGGACCATCGGTGTCATCACCAAGCTTGACCTGATGGACGAGGGCACCGA
CGCCAGGGACGTCTTGGAGAACAAGTTGCTCCCGTTGAGAAGAGGCTACA
TTGGCGTGGTGAACCGCAGCCAGAAGGATATTGAGGGCAAGAAGGACATC
CGTGCAGCACTGGCAGCTGAGAGGAAGTTCTTCCTCTCCCACCCGGCCTA
CCGGCACATGGCCGACCGCATGGGCACGCCACATCTGCAGAAGACGCTG
AATCAGCAACTGACCAACCACATCCGGGAGTCGCTGCCGGCCCTACGTAG
CAAACTACAGAGCCAGCTGCTGTCCCTGGAGAAGGAGGTGGAGGAGTAC
AAGAACTTTCGGCCCGACGACCCCACCCGCAAAACCAAAGCCCTGCTGCA
GATGGTCCAGCAGTTTGGGGTGGATTTTGAGAAGAGGATCGAGGGCTCAG
GAGATCAGGTGGACACTCTGGAGCTCTCCGGGGGCGCCCGAATCAATCG
CATCTTCCACGAGCGGTTCCCATTTGAGCTGGTGAAGATGGAGTTTGACG
AGAAGGACTTACGACGGGAGATCAGCTATGCCATTAAGAACATCCATGGA
GTCAGGACCGGGCTTTTCACCCCGGACTTGGCATTCGAGGCCATTGTGAA
AAAGCAGGTCGTCAAGCTGAAAGAGCCCTGTCTGAAATGTGTCGACCTGG
TTATCCAGGAGCTAATCAATACAGTTAGGCAGTGTACCAGTAAGCTCAGTT
CCTACCCCCGGTTGCGAGAGGAGACAGAGCGAATCGTCACCACTTACATC
CGGGAACGGGAGGGGAGAACGAAGGACCAGATTCTTCTGCTGATCGACA
TTGAGCAGTCCTACATCAACACGAACCATGAGGACTTCATCGGGTTTGCCA
ATGCCCAGCAGAGGAGCACGCAGCTGAACAAGAAGAGAGCCATCCCCAAT
CAGGGGGAGATCCTGGTGATCCGCAGGGGCTGGCTGACCATCAACAACA
TCAGCCTGATGAAAGGCGGCTCCAAGGAGTACTGGTTTGTGCTGACTGCC
GAGTCACTGTCCTGGTACAAGGATGAGGAGGAGAAAGAGAAGAAGTACAT
GCTGCCTCTGGACAACCTCAAGATCCGTGATGTGGAGAAGGGCTTCATGT
CCAACAAGCACGTCTTCGCCATCTTCAACACGGAGCAGAGAAACGTCTAC
AAGGACCTGCGGCAGATCGAGCTGGCCTGTGACTCCCAGGAAGACGTGG
ACAGCTGGAAGGCCTCGTTCCTCCGAGCTGGCGTCTACCCCGAGAAGGA
CCAGGCAGAAAACGAGGATGGGGCCCAGGAGAACACCTTCTCCATGGAC
CCCCAACTGGAGCGGCAGGTGGAGACCATTCGCAACCTGGTGGACTCATA
CGTGGCCATCATCAACAAGTCCATCCGCGACCTCATGCCAAAGACCATCA

TGCACCTCATGATCAACAATACGAAGGCCTTCATCCACCACGAGCTGCTG
GCCTACCTATACTCCTCGGCAGACCAGAGCAGCCTCATGGAGGAGTCGGC
TGACCAGGCACAGCGGCGGGACGACATGCTGCGCATGTACCATGCCCTC
AAGGAGGCGCTCAACATCATCGGTGACATCAGCACCAGCACTGTGTCCAC
GCCTGTACCCCCGCCTGTCGATGACACCTGGCTCCAGAGCGCCAGCAGC
CACAGCCCCACTCCACAGCGCCGACCGGTGTCCAGCATACACCCCCCTG
GCCGGCCCCCAGCAGTGAGGGGCCCCACTCCAGGGCCCCCCCTGATTCC
TGTTCCCGTGGGGGCAGCAGCCTCCTTCTCGGCGCCCCCAATCCCATCCC
GGCCTGGACCCCAGAGCGTGTTTGCCAACAGTGACCTCTTCCCAGCCCCG
CCTCAGATCCCATCTCGGCCAGTTCGGATCCCCCCAGGGATTCCCCCAGG
AGTGCCCAGCAGAAGACCCCCTGCTGCGCCCAGCCGGCCCACCATTATC
CGCCCAGCCGAGCCATCCCTGCTCGAC

Nucleotide sequence for Dyn2-mEGFP expression

ATGGGCAACCGCGGGATGGAAGAGCTGATCCCGCTGGTCAACAAACT
GCAGGACGCCTTCAGCTCCATCGGCCAGAGCTGCCACCTGGACCTGCCG
CAGATCGCTGTAGTGGGCGGCCAGAGCGCCGGCAAGAGCTCGGTGCTGG
AGAACTTCGTGGGCCGGGACTTCCTTCCCCGCGGTTCAGGAATCGTCACC
CGGCGGCCTCTCATTCTGCAGCTCATCTTCTCAAAAACAGAACATGCCGA
GTTTTTGCACTGCAAGTCCAAAAAGTTTACAGACTTTGATGAAGTCCGGCA
GGAGATTGAAGCAGAGACCGACAGGGTCACGGGGACCAACAAAGGCATC
TCCCCAGTGCCCATCAACCTTCGAGTCTACTCGCCACACGTGTTGAACTTG
ACCCTCATCGACCTCCCGGGTATCACCAAGGTGCCTGTGGGCGACCAGC
CTCCAGACATCGAGTACCAGATCAAGGACATGATCCTGCAGTTCATCAGC
CGGGAGAGCAGCCTCATTCTGGCTGTCACGCCCGCCAACATGGACCTGG
CCAACTCCGACGCCCTCAAGCTGGCCAAGGAAGTCGATCCCCAAGGCCTA
CGGACCATCGGTGTCATCACCAAGCTTGACCTGATGGACGAGGGCACCGA
CGCCAGGGACGTCTTGGAGAACAAGTTGCTCCCGTTGAGAAGAGGCTACA
TTGGCGTGGTGAACCGCAGCCAGAAGGATATTGAGGGCAAGAAGGACATC
CGTGCAGCACTGGCAGCTGAGAGGAAGTTCTTCCTCTCCCACCCGGCCTA
CCGGCACATGGCCGACCGCATGGGCACGCCACATCTGCAGAAGACGCTG
AATCAGCAACTGACCAACCACATCCGGGAGTCGCTGCCGGCCCTACGTAG
CAAACTACAGAGCCAGCTGCTGTCCCTGGAGAAGGAGGTGGAGGAGTAC
AAGAACTTTCGGCCCGACGACCCCACCCGCAAAACCAAAGCCCTGCTGCA

GATGGTCCAGCAGTTTGGGGTGGATTTTGAGAAGAGGATCGAGGGCTCAG
GAGATCAGGTGGACACTCTGGAGCTCTCCGGGGGCGCCCGAATCAATCG
CATCTTCCACGAGCGGTTCCCATTTGAGCTGGTGAAGATGGAGTTTGACG
AGAAGGACTTACGACGGGAGATCAGCTATGCCATTAAGAACATCCATGGA
GTCAGGACCGGGCTTTTCACCCCGGACTTGGCATTCGAGGCCATTGTGAA
AAAGCAGGTCGTCAAGCTGAAAGAGCCCTGTCTGAAATGTGTCGACCTGG
TTATCCAGGAGCTAATCAATACAGTTAGGCAGTGTACCAGTAAGCTCAGTT
CCTACCCCCGGTTGCGAGAGGAGACAGAGCGAATCGTCACCACTTACATC
CGGGAACGGGAGGGGAGAACGAAGGACCAGATTCTTCTGCTGATCGACA
TTGAGCAGTCCTACATCAACACGAACCATGAGGACTTCATCGGGTTTGCCA
ATGCCCAGCAGAGGAGCACGCAGCTGAACAAGAAGAGAGCCATCCCCAAT
CAGGGGGAGATCCTGGTGATCCGCAGGGGCTGGCTGACCATCAACAACA
TCAGCCTGATGAAAGGCGGCTCCAAGGAGTACTGGTTTGTGCTGACTGCC
GAGTCACTGTCCTGGTACAAGGATGAGGAGGAGAAAGAGAAGAAGTACAT
GCTGCCTCTGGACAACCTCAAGATCCGTGATGTGGAGAAGGGCTTCATGT
CCAACAAGCACGTCTTCGCCATCTTCAACACGGAGCAGAGAAACGTCTAC
AAGGACCTGCGGCAGATCGAGCTGGCCTGTGACTCCCAGGAAGACGTGG
ACAGCTGGAAGGCCTCGTTCCTCCGAGCTGGCGTCTACCCCGAGAAGGA
CCAGGCAGAAAACGAGGATGGGGCCCAGGAGAACACCTTCTCCATGGAC
CCCCAACTGGAGCGGCAGGTGGAGACCATTCGCAACCTGGTGGACTCATA
CGTGGCCATCATCAACAAGTCCATCCGCGACCTCATGCCAAAGACCATCA
TGCACCTCATGATCAACAATACGAAGGCCTTCATCCACCACGAGCTGCTG
GCCTACCTATACTCCTCGGCAGACCAGAGCAGCCTCATGGAGGAGTCGGC
TGACCAGGCACAGCGGCGGGACGACATGCTGCGCATGTACCATGCCCTC
AAGGAGGCGCTCAACATCATCGGTGACATCAGCACCAGCACTGTGTCCAC
GCCTGTACCCCCGCCTGTCGATGACACCTGGCTCCAGAGCGCCAGCAGC
CACAGCCCCACTCCACAGCGCCGACCGGTGTCCAGCATACACCCCCCTG
GCCGGCCCCCAGCAGTGAGGGGCCCCACTCCAGGGCCCCCCCTGATTCC
TGTTCCCGTGGGGGCAGCAGCCTCCTTCTCGGCGCCCCCAATCCCATCCC
GGCCTGGACCCCAGAGCGTGTTTGCCAACAGTGACCTCTTCCCAGCCCCG
CCTCAGATCCCATCTCGGCCAGTTCGGATCCCCCCAGGGATTCCCCCAGG
AGTGCCCAGCAGAAGACCCCCTGCTGCGCCCAGCCGGCCCACCATTATC
CGCCCAGCCGAGCCATCCCTGCTCGACATGGTGAGCAAGGGCGAGGAGC
TGTTCACCGGGGTGGTGCCCATCCTGGTCGAGCTGGACGGCGACGTAAA

CGGCCACAAGTTCAGCGTGTCCGGCGAGGGCGAGGGCGATGCCACCTAC
GGCAAGCTGACCCTGAAGTTCATCTGCACCACCGGCAAGCTGCCCGTGCC
CTGGCCCACCCTCGTGACCACCCTGACCTACGGCGTGCAGTGCTTCAGCC
GCTACCCCGACCACATGAAGCAGCACGACTTCTTCAAGTCCGCCATGCCC
GAAGGCTACGTCCAGGAGCGCACCATCTTCTTCAAGGACGACGGCAACTA
CAAGACCCGCGCCGAGGTGAAGTTCGAGGGCGACACCCTGGTGAACCGC
ATCGAGCTGAAGGGCATCGACTTCAAGGAGGACGGCAACATCCTGGGGC
ACAAGCTGGAGTACAACTACAACAGCCACAACGTCTATATCATGGCCGACA
AGCAGAAGAACGGCATCAAGGTGAACTTCAAGATCCGCCACAACATCGAG
GACGGCAGCGTGCAGCTCGCCGACCACTACCAGCAGAACACCCCCATCG
GCGACGGCCCCGTGCTGCTGCCCGACAACCACTACCTGAGCACCCAGTC
CAAGCTGAGCAAAGACCCCAACGAGAAGCGCGATCACATGGTCCTGCTGG
AGTTCGTGACCGCCGCCGGGATCACTCTCGGCATGGACGAGCTGTACAA
G

*mEGFP

Nucleotide sequence for Atl expression

ATGGGCGGATCGGCAGTGCAGGTGATCAACGCCTCCGAGGAGCACAC
ATTTGTGCTCAACGAGGATGCGCTGAGTGAGGTCCTAATGCGGGATGAGG
TCAAGGATCGGTTCGTCTGCGTTGTCTCCGTGGCTGGAGCCTTCCGAAAG
GGCAAGAGCTTCCTGCTGGACTTTTTTCTGCGCTATATGTATTCAAAGTAT
GTGCATCACGATGCGACAGACTGGCTGGGAGGCGAATCAGATCCGCTGG
AGGGTTTCTCCTGGCGCGGCGGATCTGAGCGCGACACCACCGGCATTCT
CATGTGGTCCGACATATTCCTGCACGACTATCCCAACGGCGACAAGATAG
CCATCATTCTGCTGGACACACAGGGCGCCTTCGACAGCCAGAGCACGGTG
CGCGATTGTGCCACCGTTTTTGCGTTGAGCACAATGCTGTCCTCGGTGCA
GATATACAACCTGTCACAGAACATCCAGGAGGACGACCTGCAGCACCTGC
AGCTCTTCACTGAGTATGGTCGCCTCGCGCTGGCCGACACCGGCAAAAAG
CCGTTCCAGCGTCTGCAGTTCCTCGTCCGGGACTGGAGCTTTCCCTACGA
GGCGGAATATGGTGCACTGGGCGGGGATAAGATTCTGAAACGACGTCTG
GAGGTGTCCGACAAACAGCACCCAGAACTACAGTCCCTGCGTCGCCACAT
TTCGTCCTGTTTCACGGAGGTGGCCTGCTTCCTGATGCCCCATCCAGGTC
TCAATGTGGCCACCAATCCTAAATTTGACGGTCGGCTGCAGGACATCACG

CCCGAGTTTAAGAGTAGCCTGCGCTCCCTGGTGCCCATGCTGCTGGCACC
GGACAACCTTGTCTACAAGGAGATCAGCGGACAGCGGGTGCGGGCCCGC
GATCTCATCCAGTACTTCCAATCGTACATGAACATCTACAAGGGCAACGAG
CTGCCCGAGCCGAAGAGCATGCTGGTGGCCACCGCAGAGGCTAACCATT
TGACTGCCGTGGCCGCCGCCAAGGAGCTGTACGGACAGCTCATGGAGGA
GGTGTGCGGTGGAACGCGGCCGTACTTAAGCACCGCCCATCTCCAGACG
GAGCACCTGCGGGTGAAGGACAAGGCACTGTTCCAGTTCGCCGCCAAGC
GCAAGATGGGTGGTGAGGAGTTCACCGAGAAATTCCGCAAGCAACTGGAA
GATGATCTTGAGGAGGTCTTCACCAACTACCAAGCACACAACGAGAGCAA
GAACATCTTTAAGGCAGCACGGACACCGGCGGTGTACTTCGCCTGCGCCG
TCATCATGTACATCCTTAGCGGCATCTTTGGATTGGTGGGTCTCTATACGT
TCGCCAACTTCTGCAACCTGGTTATGGGTGTGGCGCTTCTAACGCTGGCT
CTGTGGGCCTACATTAGATATAGCGGAGAGCTCAGCGACTTTGGCGGCAA
GTTGGATGACTTTGCAACGCTATTGTGGGAGAAATTCATGCGACCCATCTA
TCACGGCTGCATGGAGAAGGGCATCCACCATGTTGCCACTCATGCGACCG
AAATGGCTGTCGGCGGAGGCGCAGCCTCCTACCGCTCCCAGACCTCGGT
GAATGCGTCCAATGGCAAGGTGAAGCGGTCA

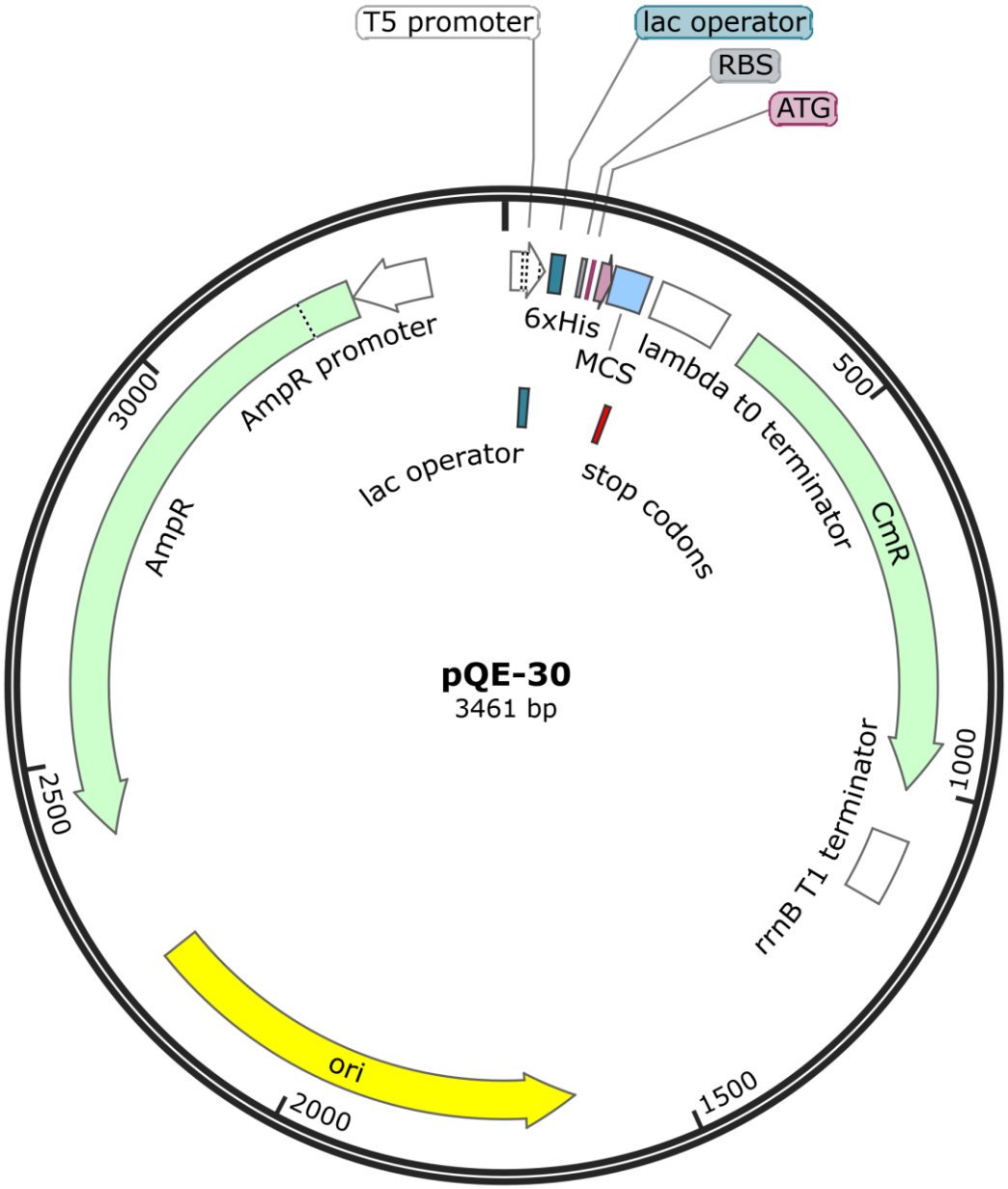
T5 promoter
lac operator
RBS
ATG
6xHis
MCS
lambda t0 terminator
CmR
rrnB T1 terminator
ori
AmpR
AmpR promoter
lac operator
stop codons
pQE-30
3461 bp
500
1000
1500
2000
2500
3000

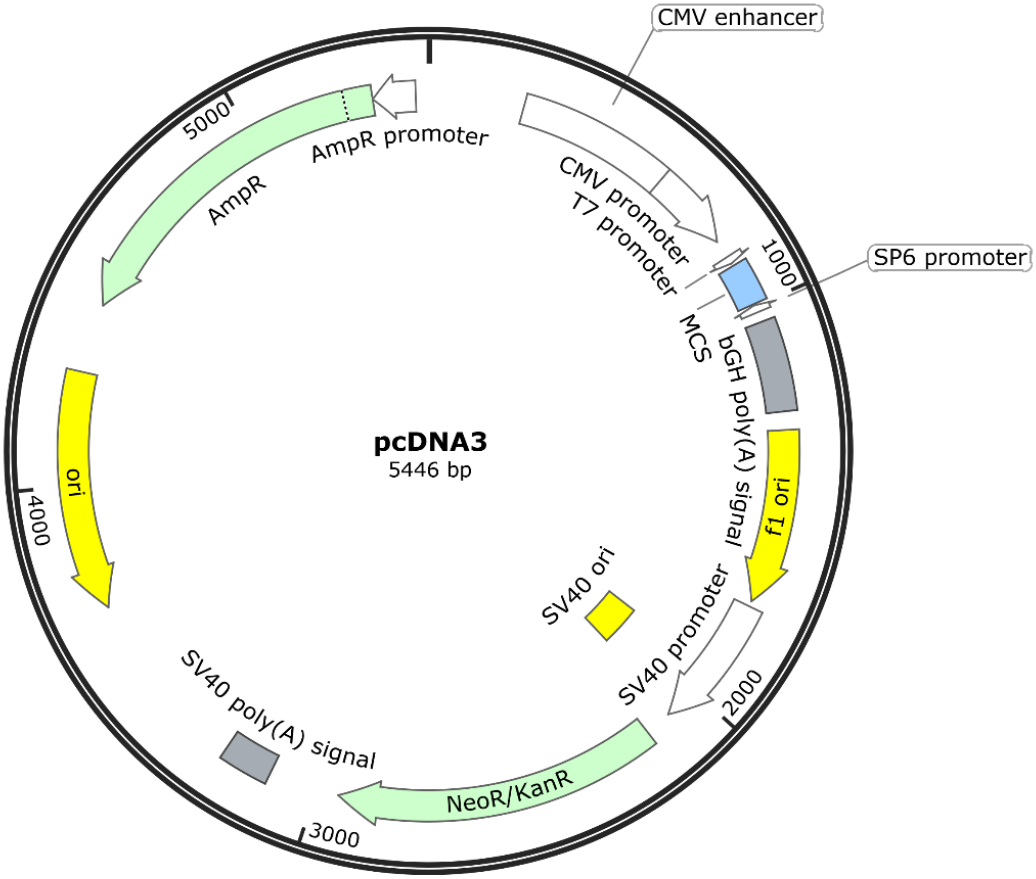

Nucleotide sequence for Rtnl1 expression

ATGTCCGCATTTGGTGAAACCGGTCAGAATGGCGTGTGCAAGCAGCGCCC
ATTGATTTGCTCCATACTCGATCCCAATGCCTGGTTTAAGCCCGAACGTTTGCA
CCCGCAAGTGGAATCCCTTATCTACTGGCGCGATGTGAAGAAATCCGGCATTG
TCTTCGGCGCTGGCCTGATCACACTGGCGGCCATCTCCAGCTTCTCGGTGATC
AGCGTGTTCGCCTACTTGTCGCTCCTAACCCTCTTCGGCACCGTCGCCTTCAG
AATCTACAAATCTGTGACACAGGCCGTGCAAAAGACAAACGAGGGTCACCCCT
TTAAGGATTACCTGGAGCTGGATCTGACGCTGTCGCACGAAAAGGTACAGAAC
ATTGCCGGCGTGGCTGTGGCACATATCAATGGCTTCATCTCCGAGCTGAGGC
GTCTGTTTCTTGTTGAGGATATCATCGATTCGATCAAGTTCGGCGTCATTCTGT
GGGTCTTCACCTACGTGGGTGCCTGGTTCAATGGCATGACTCTGGTCATCTTG
GCCTTTGTCTCGCTGTTTACCTTGCCCAAGGTCTACGAGAACAACAAGCAATC
GATCGACACTCACTTGGATCTGGTGCGCAGCAAATTGACAGAAATCACCGACA

AGATCCGAGTGGCCATCCCCATTGGCAACAAGAAGCCCGAGGCCGCTGCCGA
GTCTGAGAAGGACAAG

Nucleotide sequence for mGFP-Rtnl1 expression

GTGAGCAAGGGCGAGGAGCTGTTCACCGGGGTGGTGCCCATCCTGGTCG
AGCTGGACGGCGACGTAAACGGCCACAAGTTCAGCGTGTCCGGCGAGGGCG
AGGGCGATGCCACCTACGGCAAGCTGACCCTGAAGTTCATCTGCACCACCGG
CAAGCTGCCCGTGCCCTGGCCCACCCTCGTGACCACCCTGACCTACGGCGTG
CAGTGCTTCAGCCGCTACCCCGACCACATGAAGCAGCACGACTTCTTCAAGTC
CGCCATGCCCGAAGGCTACGTCCAGGAGCGCACCATCTTCTTCAAGGACGAC
GGCAACTACAAGACCCGCGCCGAGGTGAAGTTCGAGGGCGACACCCTGGTGA
ACCGCATCGAGCTGAAGGGCATCGACTTCAAGGAGGACGGCAACATCCTGGG
GCACAAGCTGGAGTACAACTACAACAGCCACAACGTCTATATCATGGCCGACA
AGCAGAAGAACGGCATCAAGGTGAACTTCAAGATCCGCCACAACATCGAGGA
CGGCAGCGTGCAGCTCGCCGACCACTACCAGCAGAACACCCCCATCGGCGAC
GGCCCCGTGCTGCTGCCCGACAACCACTACCTGAGCACCCAGTCCAAGCTGA
GCAAAGACCCCAACGAGAAGCGCGATCACATGGTCCTGCTGGAGTTCGTGAC
CGCCGCCGGGATCACTCTCGGCATGGACGAGCTGTACAAGATGTCCGCATTT
GGTGAAACCGGTCAGAATGGCGTGTGCAAGCAGCGCCCATTGATTTGCTCCAT
ACTCGATCCCAATGCCTGGTTTAAGCCCGAACGTTTGCACCCGCAAGTGGAAT
CCCTTATCTACTGGCGCGATGTGAAGAAATCCGGCATTGTCTTCGGCGCTGGC
CTGATCACACTGGCGGCCATCTCCAGCTTCTCGGTGATCAGCGTGTTCGCCTA
CTTGTCGCTCCTAACCCTCTTCGGCACCGTCGCCTTCAGAATCTACAAATCTGT
GACACAGGCCGTGCAAAAGACAAACGAGGGTCACCCCTTTAAGGATTACCTG
GAGCTGGATCTGACGCTGTCGCACGAAAAGGTACAGAACATTGCCGGCGTGG
CTGTGGCACATATCAATGGCTTCATCTCCGAGCTGAGGCGTCTGTTTCTTGTT
GAGGATATCATCGATTCGATCAAGTTCGGCGTCATTCTGTGGGTCTTCACCTA
CGTGGGTGCCTGGTTCAATGGCATGACTCTGGTCATCTTGGCCTTTGTCTCGC
TGTTTACCTTGCCCAAGGTCTACGAGAACAACAAGCAATCGATCGACACTCAC
TTGGATCTGGTGCGCAGCAAATTGACAGAAATCACCGACAAGATCCGAGTGGC
CATCCCCATTGGCAACAAGAAGCCCGAGGCCGCTGCCGAGTCTGAGAAGGAC
AAG

*mGFP